optica

Volume 1 • Issue 4 • October 2014

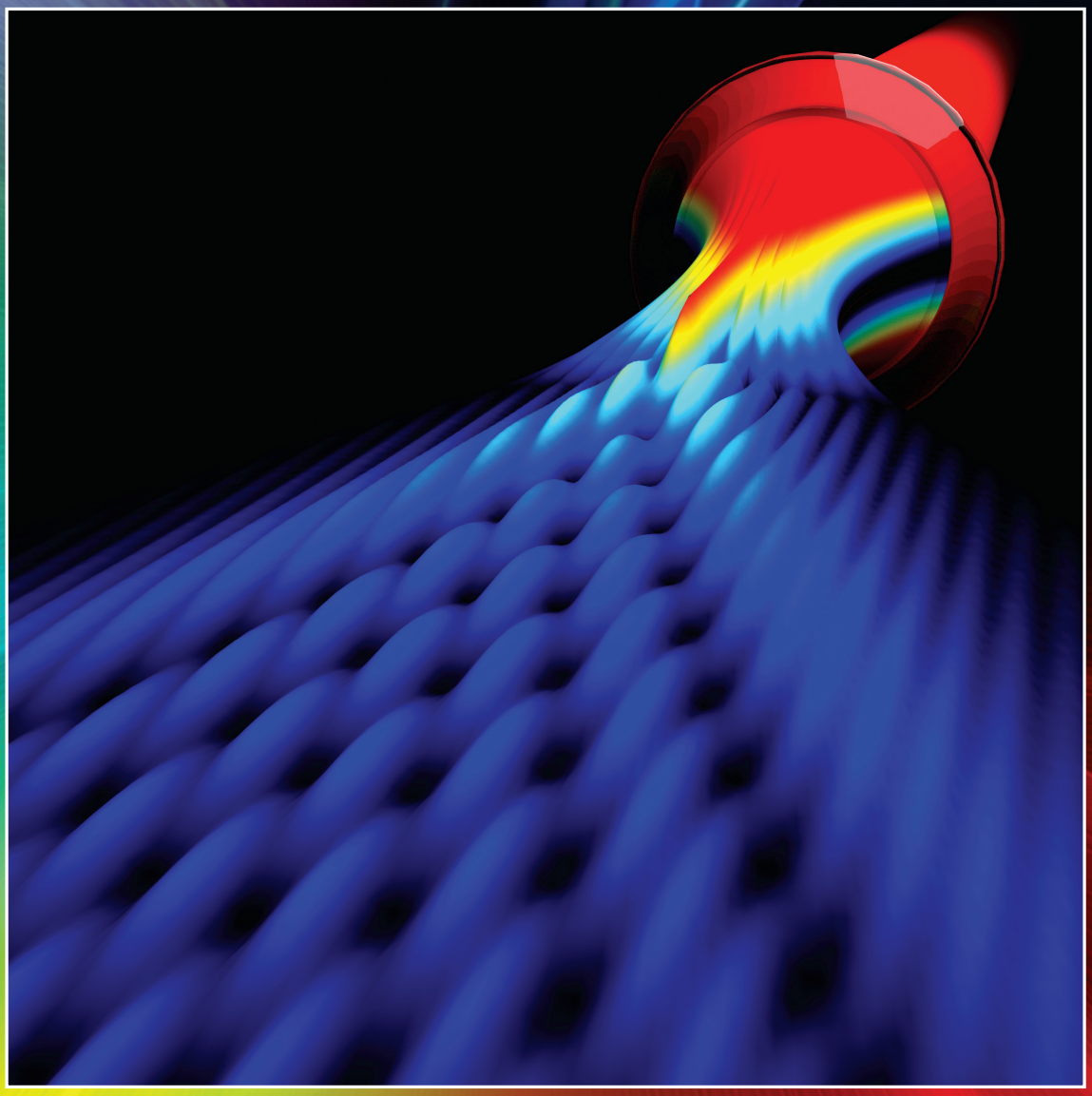

OSA®
The Optical Society

ISSN: 2334-2536

optica.osa.org

Research Article Vol. 1, No. 4 / October 2014 / Optica 192

Ultrafast nonequilibrium carrier dynamics in semiconductor laser mode locking

I. Kilen,[1] J. Hader,[2] J. V. Moloney,[1,2,*] and S. W. Koch[3]

[1]Department of Mathematics, Program in Applied Mathematics, University of Arizona, Tucson, Arizona 85721, USA

[2]College of Optical Sciences, University of Arizona, Tucson, Arizona 85721, USA

[3]Department of Physics, University of Marburg, 35032 Marburg, Germany

*Corresponding author: jml@acms.arizona.edu

Received 2 July 2014; revised 15 August 2014; accepted 20 August 2014 (Doc. ID 215263); published 22 September 2014

Semiconductor disk lasers have been shown to be ideal as wavelength-agile, high-brightness sources for producing high average power under various pulsed mode-locking scenarios. Systematic microscopic modeling reveals that ultrafast nonequilibrium kinetic hole burning in electron/hole carrier distributions dictates the outcome of femtosecond duration mode-locked pulse formation. The existence of a large reservoir of unsaturated carriers within the inverted distributions leads to the emergence of multiple pulse waveforms (not necessarily harmonically mode-locked pulse trains) that inefficiently draw on these carrier reservoirs. The concept of gain is no longer meaningful in this limit, and the dynamical inversion of electrons and holes primarily in the active medium establishes the final dynamical state of the system. The simulation results explain much of the generic behavior observed in key recent experiments and point to the difficulty of pushing semiconductor mode-locked lasers to pulse durations below 100 fs.

OCIS codes: (140.3430) Laser theory; (140.7270) Vertical emitting lasers; (140.5960) Semiconductor lasers; (140.7090) Ultrafast lasers.

http://dx.doi.org/10.1364/OPTICA.1.000192

1. INTRODUCTION

Optically pumped vertical external cavity surface emitting lasers (VECSELs) or disk lasers have been shown to be ideal as wavelength-agile, high-brightness sources for numerous applications including CW raw power [1,2], multi-watt single frequency [3], and high average power under various pulsed mode-locking scenarios. Specifically, mode locking has been observed with external semiconductor saturable absorber mirrors (SESAMs) [4–6], integrated quantum well and quantum dot SESAMs [7], and graphene [7,8] and carbon nanotube [9] saturable absorbers. To our knowledge, the shortest fundamental mode-locked pulse duration to date has been 107 fs, albeit at very low average power [10]. While shorter 60 fs pulses have been reported in [11] within longer few picosecond "pulse molecules," we will see that these might also be interpreted as simple interferences between time-shifted, mode-locked picosecond pulses. Rate equation level models using parameters extracted from experiments have proved successful in capturing the mode-locking behavior for longer-duration pulses [12]. As typical intraband carrier scattering times are on the order of 100 fs, it is expected that dynamically changing nonequilibrium distributions will not have a chance to relax to quasi-equilibrium Fermi–Dirac distributions during the pulse itself. The complexity of the nonequilibrium many-body dynamics has limited studies to date to relatively simple ones or multiple quantum-well (QW) single-pass geometries.

In this work, we present a simulation of microscopic many-body effects in the VECSEL gain medium and in the saturable QW absorber by solving the two-band Maxwell Semiconductor Bloch equations (MSBE) in the Hartree–Fock limit using microscopically motivated carrier relaxation and dephasing times. Our simulations show that 100 fs or sub-100 fs pulse mode locking is likely to not be possible in the resonant periodic gain (RPG) active structures under study in this work. Indeed, in Ref. [10], a nonuniform spacing of QWs was used in the low gain limit to broaden the linear net gain to achieve 107 fs pulses. In higher-gain situations, unused carriers can

2334-2536/14/040192-06$15/0$15.00

destabilize the pulse by seeding amplification in spectral windows that exist outside the direct interacting nonequilibrium system. The implications of this are profound and show that it will be extremely difficult to avoid dynamical pulse breakup under strong pump conditions. In particular, we show that the apparent 60 fs pulses observed in [11] are likely due to a pulse splitting into two relatively clean, longer-duration pulses that feed off independent carrier reservoirs in the inverted system. We also identify a clear pulse separation in time at higher pump levels that is consistent with predictions from a very recent record average power mode-locking experiment with a graphene mode-locking element.

2. MICROSCOPIC THEORY AND SIMULATION OF SHORT-CAVITY MODE LOCKING

The theoretical analysis of the VECSEL mode-locking dynamics requires the simulation of the light field $E(z,t)$ propagation inside the laser cavity as well as the nonlinear interaction of this cavity field with the material polarizations $P(z,t)$ of the optically active QW gain region and the QW saturable absorber (SESAM). Assuming that the cavity light field circulates in the z direction, perpendicular to the QW planes, Maxwell's wave equation can be written in the simple form

$$\left[\frac{\partial^2}{\partial z^2} - \frac{n^2}{c_0^2}\frac{\partial^2}{\partial t^2}\right] E(z,t) = \mu_0 \frac{\partial^2}{\partial t^2} P(z,t), \tag{1}$$

where the constants n and c_0 are the background refractive index and the vacuum velocity of light, respectively, and μ_0 denotes the vacuum permeability. The macroscopic polarization $P(z,t)$ is obtained by the summation of the microscopic polarizations $p_{\lambda,\nu,\mathbf{k}}$ over the crystal momentum $\mathbf{k}$ in the plane of the QWs. The dynamics of the microscopic polarization $p_{\lambda,\nu,\mathbf{k}}$ follow from the multiband semiconductor Bloch equations (SBEs) [13]

$$\begin{aligned}\frac{\partial}{\partial t} p_{\lambda,\nu,\mathbf{k}} &= -\frac{i}{\hbar}\sum_{\lambda_1,\nu_1}\left(e^e_{\lambda,\lambda_1,\mathbf{k}}\delta_{\nu,\nu_1} + e^h_{\nu,\nu_1,\mathbf{k}}\delta_{\lambda,\lambda_1}\right)p_{\lambda_1,\nu_1,\mathbf{k}} \\ &\quad - i\left(n^e_{\lambda,\mathbf{k}} + n^h_{\nu,\mathbf{k}} - 1\right)\Omega_{\lambda,\nu,\mathbf{k}} + \Gamma_{\lambda,\nu;\mathrm{deph}}, \\ \frac{\partial}{\partial t} n^{e(h)}_{\lambda(\nu),\mathbf{k}} &= -2\,\mathrm{Im}\left(\Omega_{\lambda,\nu,\mathbf{k}}\left(p_{\lambda,\nu,\mathbf{k}}\right)^{\star}\right) + \Gamma^{e(h)}_{\lambda(\nu);\mathrm{scatt}}.\end{aligned} \tag{2}$$

These equations couple the dynamics of the microscopic polarization $p_{\lambda,\nu,\mathbf{k}}$ and the occupation function $n^{e(h)}_{\lambda(\nu),\mathbf{k}}$, determining the probability that a state $\mathbf{k}$ in the conduction band λ (valence band ν) is occupied by an electron (hole). The renormalized single-particle energies in the Hartree–Fock approximation are

$$\begin{aligned} e^e_{\lambda,\lambda_1,\mathbf{k}} &= \varepsilon^e_{\lambda,\mathbf{k}}\delta_{\lambda,\lambda_1} - \sum_{\lambda_2,\mathbf{q}} V^{\lambda,\lambda_2,\lambda_1,\lambda_2}_{|\mathbf{k}-\mathbf{q}|} n^e_{\lambda_2,\mathbf{q}}, \\ e^h_{\nu,\nu_1,\mathbf{k}} &= \varepsilon^h_{\nu,\mathbf{k}}\delta_{\nu,\nu_1} - \sum_{\nu_2,\mathbf{q}} V^{\nu,\nu_2,\nu_1,\nu_2}_{|\mathbf{k}-\mathbf{q}|} n^h_{\nu_2,\mathbf{q}}, \end{aligned} \tag{3}$$

and the renormalized Rabi frequency is

$$\Omega_{\lambda,\nu,\mathbf{k}} = \omega_R + \frac{1}{\hbar}\sum_{\lambda_1,\nu_1,\mathbf{q}\neq\mathbf{k}} V^{\lambda,\nu_1,\nu,\lambda_1}_{|\mathbf{k}-\mathbf{q}|} p_{\lambda_1,\nu_1,\mathbf{q}}. \tag{4}$$

Here, $V(|\mathbf{k}-\mathbf{q}|)$ is the Coulomb potential and $\omega_R = d^{\lambda,\nu}_{\mathbf{k}} E(z,t)/\hbar$, where $d^{\lambda,\nu}_{\mathbf{k}}$ is the dipole-matrix element.

Contributions to the SBE that go beyond the Hartree–Fock approximation describe correlation effects such as dephasing of the polarization (Γ_{deph}), carrier scattering (Γ_{scatt}), and Coulomb screening. In the equation of motion for the carrier distributions [Eq. (2)], the correlation effects in the second Born–Markov approximation lead to Boltzmann-type scattering terms. Inclusion of these terms at this level would make simulation impossible, although we can use the full model with these correlation effects included to assess how quickly a kinetic hole can refill by taking nonequilibrium carrier distributions from the present simulation as initial data.

Together with the wave equation, the SBEs establish the MSBEs. Since the numerical evaluation of the microscopic scattering terms in each time step of a numerical laser dynamics simulation is excessively CPU time demanding, it is often necessary to include the correlation effects on the level of effective rates expressing the net effect of the underlying microscopic processes. In this limit, the dephasing of the polarization is described by a simple decay contribution with the characteristic dephasing time τ_{dep}; $\Gamma_{\lambda,\nu;\mathrm{deph}} = -p_{\lambda,\nu,\mathbf{k}}/\tau_{\mathrm{deph}}$ and, similarly, the carrier-scattering contribution modeling the equilibration of the carrier system follows from $\Gamma_{\lambda(\nu);\mathrm{scatt}} = -(n^{e(h)}_{\lambda(\nu),\mathbf{k}} - f^{e(h)}_{\lambda(\nu),\mathbf{k}})/\tau_{\mathrm{scatt}}$, where $f^{e(h)}_{\lambda(\nu),k}$ is the background quasi-equilibrium distribution of the optically pumped QW and τ_{scatt} governs the characteristic time scales of scattering events. To test our model [14,15] and to study the relevance of nonequilibrium effects, we restrict ourselves to a two-band model, postulating strong confinement of electrons and holes such that only the lowest sub-bands need to be taken into account. In addition, we limit consideration to a parabolic band structure where the transition energy, i.e., the difference between the conduction and valence band energy $\hbar\omega_{\mathbf{k}} = (\hbar^2\mathbf{k}^2/2m_e) + (\hbar^2\mathbf{k}^2/2m_h) + E_g$ is expressible in terms of the effective masses of the electrons m_e, holes m_h, and the bandgap energy E_g. As a sanity check, we employed a full multiband microscopic simulation in a single-pass setting that goes beyond the Hartree–Fock limit to assess the role of ultrafast correlations in the hot carriers (electron/hole) and carrier capture from the pumped barrier to inverted well states. While these can include further pulse-reshaping effects due to kinetic hole filling, we anticipate that the generic features observed in the simple two-band model will be preserved. This will be detailed in a future publication. In the low-gain limit, due to the presence of shallow kinetic holes, these correlations should not significantly affect the results.

We use this model to simulate mode locking in a linear one-dimensional cavity consisting of an AR-coated VECSEL chip consisting of a 10 quantum well RPG active medium and a SESAM at the other end of the cavity. A schematic of the modeled cavity is shown in Fig. 1. We effectively represent tighter focusing on the SESAM by appropriately adjusting the on-axis

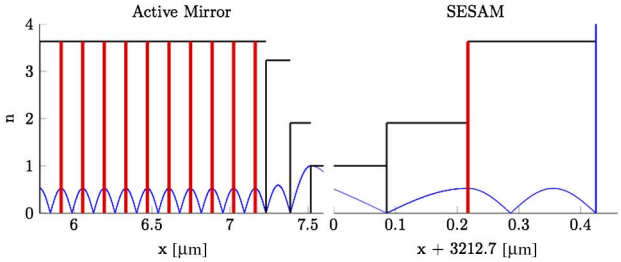

Fig. 1. Schematic of linear cavity with the 10 QW RPG VECSEL chip shown on the left (DBR to the left of this not shown) and a single QW SESAM with spacer and an output coupler. The empty cavity part of the simulation domain in the center is not shown.

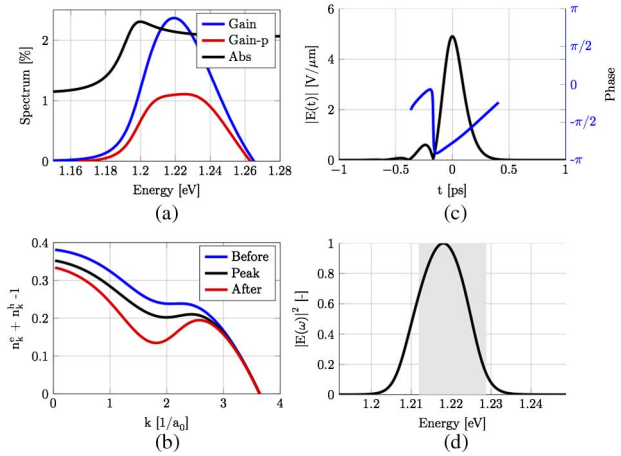

Fig. 2. (a) Plot of the equilibrium gain at a carrier density $n = 1.75 \times 10^{16}$ m^{-2} and at room temperature (blue). Included in this graph is the single QW absorption of the SESAM. The net roundtrip gain is interpreted as the difference of these two curves. (b) Instantaneous snapshots of the inversion in the active VECSEL structure immediately before (blue), at the peak (black), and immediately after the transit of the mode-locked pulse. (c) Plot of the final stable low-power, mode-locked pulse together with the phase across the pulse. (d) Spectrum of the mode-locked pulse. The shaded area shows that this pulse utilizes the full available linear net gain bandwidth.

intensity to represent a ten-fold intensity increase on the SESAM relative to that on the VECSEL chip.

The 10 QW RPG structure modeled here is identical to that employed in Refs. [1,2] to achieve greater than 100 W CW from a VECSEL structure. Details are given therein. We assume a single-layer AR coating on both the VECSEL chip and the SESAM. The VECSEL chip consists of 10 InGaAs QWs grown on an AlGaAs distributed Bragg reflector (DBR), and the SESAM consists of a single InGaAs QW attached to a 1% output coupling mirror. These two components are on opposite sides of a 3.2 cm linear cavity as shown in Fig. 1, with a roundtrip time of approximately 21 ps. We assume a 30 ps (0.5 ps) relaxation time for the QW populations in the VECSEL (SESAM) back to a reference 300 K quasi-equilibrium distribution and the same InGaAs/AlGaAs band structure parameters as for the RPG. The reference distribution density for the SESAM is kept at 5.0e14 [1/m^2], while the density of the QWs in the VECSEL are incremented for the different situations. We stress that the behavior discussed below is expected to be generic in RPG-grown VECSELs.

3. LOW-INVERSION MODE LOCKING

The concept of gain and gain bandwidth is heavily used in discussing and analyzing most mode-locking experiments. For example, a very useful picture that goes back to the seminal early work of Haus [16] utilizes the idea of net gain to estimate the expected characteristic pulse width in a mode-locked setting. This idea works rather well for a host of solid state materials such as fiber lasers, Ti:sapphire, etc. It has also been extensively used to model semiconductor laser mode locking, more recently in a rate equation model of a mode-locked VECSEL [12]. These parameterized models, which may work well for longer pulses, have the built-in assumption that the polarization dynamics is slaved to the driving field and can be adiabatically eliminated. Strictly, this assumption is untrue even for longer picosecond duration pulses, although it appears to work well. However, it is clear from Eq. (2) that the field is driven by the carrier inversion with the latter mediated by the polarization. Because of this, we will focus on the carrier (electron and hole) dynamics in interpreting the results of recent experiments and will only use the term "gain" as a historical reference. Rather than encountering "spectral hole burning," a concept associated with inhomogeneously broadened gain media, we will talk instead about "kinetic hole burning" in the respective carrier distributions.

The situation depicted in Fig. 2 represents a well-behaved dynamical system where the final low average and peak power mode-locked pulse train is stable. The mode-locked pulse has a FWHM of 204 fs and a time–bandwidth product of 0.5. Note the linear chirp across the main pulse and small leading edge subpulse. The pulse substructure is sensitive to the type and degree of dispersion of the single-layer AR coating. In the carrier inversion plots shown in Fig. 2(b), the inversion never bleaches out and simply cycles in a well-controlled fashion between the blue and red curves on each cavity roundtrip. The concept of gain is useful in this limit, as the pulse spectrum shows that the final pulse avails itself of the available linear net gain bandwidth [compare the intersection points of the blue (gain) and black (absorption) curves in Fig. 1(a)]. This low-power, pulsed, mode-locked behavior is akin to that observed in [10].

4. INTERMEDIATE INVERSION PULSE SPLITTING

As the carrier system is driven more strongly by the pump, we observe a fundamental change in the dynamics which cannot be interpreted successfully via a gain model. The key physical quantity of interest is now the inversion $(n^e_{\lambda,\mathbf{k}} + n^h_{\nu,\mathbf{k}} - 1)$ term driving the polarization in Eq. (2), and the dynamics are now unavoidably nonequilibrium. Under strong driving conditions, the initially weak circulating pulse grows and burns a single kinetic hole that recovers after the pulse has left the gain medium. As the pulse becomes stronger and stronger, this transient kinetic hole gets deeper until the inversion is driven

down to zero at pulse center, meaning that there are no carriers available to provide further amplification (gain) in this spectral window. Now, unsaturated carriers in regions spanning both sides of the central spectral window (in the k space) are available to provide amplification, and we observe the emergence of a double-pulse waveform that more effectively utilizes carriers in the inverted medium. In this case, we observe an unusual pulse waveform consisting of two slightly time-shifted, mode-locked pulses whose individual spectra beat to produce an interference or beating that might be misinterpreted as a pulse "molecule" of longer duration (350 fs here), containing a train of shorter (50 fs here) mode-locked pulses. Figure 3 summarizes this behavior in detail.

Figure 3(a) depicts the unsaturated (linear) gain and saturable absorber (SESAM) loss; the net linear gain of the system can be read off from this figure. In comparison to the single-pulse mode-locking scenario of Fig. 2, the dynamical behavior of the inversion now shows two kinetic holes, i.e., two minima in the carrier inversion. This results from the fact that the circulating pulse has evolved to a self-reproducing dynamical state that efficiently extracts carriers from two spectrally separate reservoirs. The interference between these two temporally split pulses could be misinterpreted as individual 50 fs mode-locked pulses within a ps duration "pulse molecule." We observe that this interference effect is rather robust at intermediate pump levels. Finally, inspection of the two separate spectral peaks in Fig. 3(b) shows that, while the full spectral gain bandwidth is spanned when compared to Fig. 3(a), now a large chunk in the middle is not utilized.

Instead, two well-separated spectral peaks emerge, with each associated with independent time-separated pulses. We note

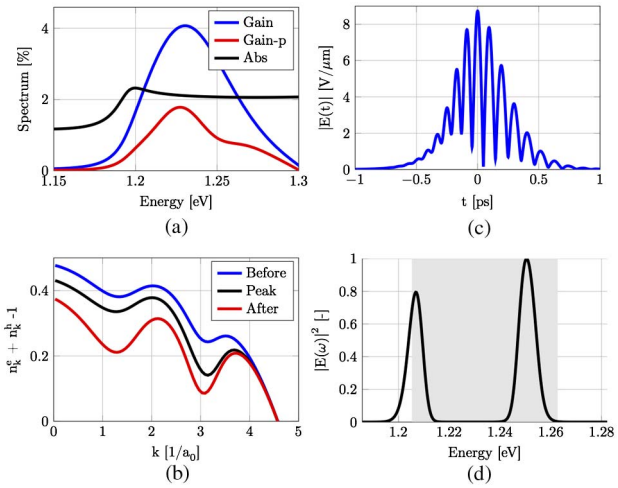

Fig. 3. (a) Similar plot to Fig. 1(a) except that the carriers are now driven more strongly by the pump with density $n = 2.4 \times 10^{16}$ m^{-2} and at room temperature. The net gain is again the difference between the blue (gain) and black (SESAM QW absorption). (b) The electron momentum resolved (k) inversion now shows a double depression and again cycles back and forth between the blue and black curve every roundtrip. (c) Mode-locked pulse waveform showing a beating between two slightly shifted sub-ps-duration pulses. (d) Split spectral peaks, each associated with slighted time-shifted single pulses.

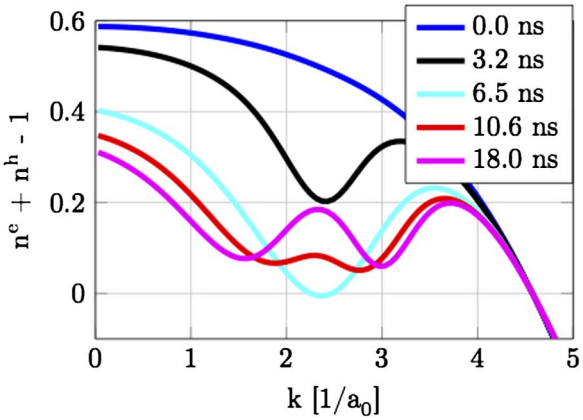

Fig. 4. Development of dual kinetic holes in the inversion starting from an initial Fermi distribution at $t = 0$. The inversion goes negative transiently prior to splitting into two kinetic holes.

here that we can indeed verify (not shown) that this modulated pulse waveform can be spectrally filtered and identified with individual approximate duration 235 fs pulses.

The inversion depicted in Fig. 3 captures an asymptotic, long-time dynamical state of the mode-locked cavity where the pulse has stabilized. However, the dynamical evolution to this final state is somewhat involved and the usual net gain interpretation has to be supplanted by a fully nonequilibrium, kinetic hole-burning one. Prior to the development of the dual split kinetic holes depicted in Fig. 3, we observe a dynamical transient growth of the pulse waveform to the point where the inversion in the vicinity of the central frequency is fully bleached and the subsequent evolution avails itself of unsaturated carrier reservoirs to the high- and low-frequency side of this central frequency. This picture is shown in Fig. 4.

5. HIGH-INVERSION PULSE SPLITTING

At even higher pump levels, there can be too much unsaturated gain for the absorber to clean up. This will drive the generation of new pulses in the cavity that can result in pulse trains, harmonically mode-locked pulses, etc. A special case is when one has the correct amount of absorption (and/or the faster recovery time); it is then possible to obtain a situation in which the time-separated pulses from Section 4 split into two time-shifted pulses. This splitting is simply a further manifestation of the interference observed in Section 4, but now the individual pulses become trapped in their own local potentials and essentially behave as independent mode-locked entities.

This behavior bears a close resemblance to a very recent experimental result that demonstrated up to 10 W of average power in a graphene mode-locked VECSEL. In this work it is argued, based on an observed two-peaked pulse spectrum for average powers exceeding 6 W, that pulse splitting into two temporally separated stable pulses with locally flat phases is the likely interpretation of the experimental data. This would mean that the 10 W average power would be shared between both pulses, say approximately 5 W in each pulse.

Figure 5 summarizes the mode-locked behavior at these higher carrier densities (pump levels). The main difference here

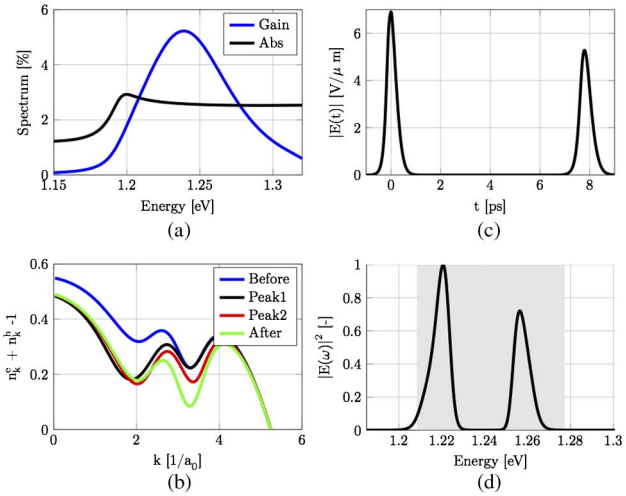

Fig. 5. (a) Linear gain and SESAM absorption spectrum at higher pump levels. (b) Strongly distorted nonequilibrium carrier inversions now show four curves, with the two intermediate ones at the peak of each time-separated pulse. (c) Time-separated, mode-locked pulses and (d) spectrum of both pulses.

is that both pulses no longer overlap but are well separated in time and spectrally. The nonequilibrium inversion has again bleached out in the center, causing two independent pulses to draw from separate carrier reservoirs. In our model, these behaviors are robust over a range of initial carrier densities. Again, by spectral filtering, we can show that each individual pulse is identified with a single peak in the above spectrum.

6. ROLE OF SATURABLE ABSORBER RELAXATION IN CLEANING UP PULSES

We now discuss the influence of the SESAM fast saturable decay rate on the mode-locked pulse behavior observed in the last two sections. If the absorber relaxes sufficiently fast (~500 fs), it can act to damp out any residual amplification resulting from

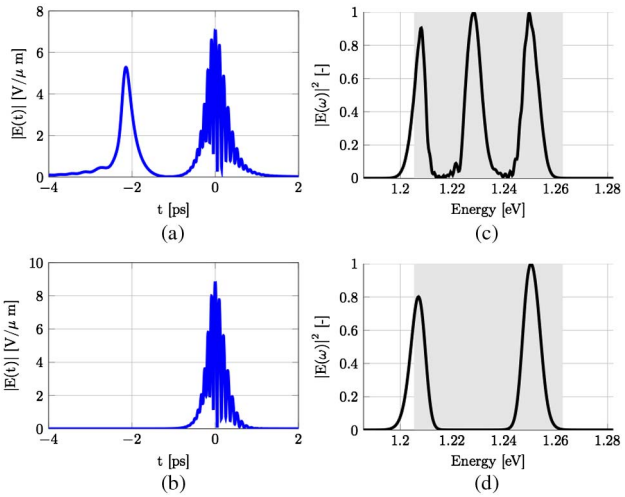

Fig. 6. (a) Emergence of mode-locked pulse train with a slow saturable absorber. (b) Cleaned up single pulse with fast saturable absorber. (c) Triple-peaked spectrum of mode-locked pulses. (d) Double-peaked spectrum of interfering mode-locked pulses (see Fig. 3).

unsaturated carriers in the active structure and consequently clean up the mode-locked pulse train. We illustrate this behavior for the case of the emergence of multiple pulses for a slow saturable absorber in Fig. 6. The triple-pulse waveform (two interfering as in Fig. 3) shown in Fig. 6 and its associated triple peak spectrum can be cleaned up if the saturable absorber relaxes fast enough to prevent the growth of the secondary pulses. We observe a clean mode-locked double pulse with a double spectral peak if we employ the faster saturable absorber in the cavity.

7. RESULTS AND CONCLUSIONS

Our microscopic simulations show that nonequilibrium carrier distributions within inverted QWs in a RPG VECSEL structure are so strongly modified under strong pumping conditions that the nonequilibrium gain saturation picture becomes irrelevant. Our results show that it will be challenging to generate high peak and average power mode-locked pulses from these semiconductor disk lasers. The underlying physics here is fundamentally different from that encountered in other solid state gain media (Ti:sapphire, Er-doped fiber, etc.) or in QD mode-locked VECSELs, as the carriers are free to move in the in-plane dimension. Here, when the carriers contributing to direct amplification are bleached out, the system self-adapts to form uncoupled carrier reservoirs that sustain independent multiple pulses in the cavity.

Our results show that, when bleached out at high pump levels, nonequilibrium carrier distributions dynamically adjust so as to promote independent carrier reservoirs that feed separate pulses within the cavity. These can, for example, create the illusion that a "pulse molecule" is formed, containing even shorter mode-locked pulse trains at certain pump levels. While this work isolates uniquely nonlinear nonequilibrium features that profoundly modify the nature of ultrafast mode locking in semiconductor disk lasers, we expect that these observations will apply to edge emitting structures. However, the latter will be further complicated by long gain paths in contrast to the very thin gain regime in the disk geometry.

Finally, we need to point out that there are many other players involved in influencing the final pulse waveforms. In this work, we have restricted our study to a two-band model and a fixed single-layer AR coating with its own intrinsic dispersion. It is clear that coatings designed for narrow-band CW lasers will exhibit strong dispersion away from the designed wavelength. The net dispersion in the cavity will involve contributions from the transient nonlinear field-induced refractive index in addition to from linear dispersive elements such as DBRs, AR coatings, and mirrors. It is anticipated that these contributions can likewise be optimized to reduce nonlinear chirp and produce ultrashort bandwidth-limited pulses.

FUNDING INFORMATION

Air Force Office of Scientific Research (AFOSR) (FA9550-14-1-0062).

REFERENCES

1. B. Heinen, T.-L. Wang, M. Sparenberg, A. Weber, B. Kunert, J. Hader, S. W. Koch, J. V. Moloney, M. Koch, and W. Stolz,

"106 W continuous-wave output power from vertical-external-cavity surface-emitting laser," Electron. Lett. **48**, 516 (2012).
2. T.-L. Wang, B. Heinen, J. Hader, C. Dineen, M. Sparenberg, A. Weber, B. Kunert, S. W. Koch, J. V. Moloney, M. Koch, and W. Stolz, "Quantum design strategy pushes high-power vertical external cavity surface emitting lasers beyond 100 W," Laser Photon. Rev. **6**, L12–L14 (2012).
3. A. Laurain, C. Mart, J. Hader, J. V. Moloney, B. Kunert, and W. Stolz, "15 W single frequency optically pumped semiconductor laser with sub-MHz linewidth," IEEE Photon. Technol. Lett. **26**, 131–133 (2014).
4. M. Scheller, T.-L. Wang, B. Kunert, W. Stolz, S. W. Koch, and J. V. Moloney, "Passively mode-locked VECSEL emitting 682 fs pulses with 5.1 W of average output power," Electron. Lett. **48**, 588–589 (2012).
5. K. G. Wilcox, A. C. Tropper, H. E. Beere, D. A. Ritchie, B. Kunert, B. Heinen, and W. Stolz, "4.35 kW peak power femtosecond pulse mode-locked VECSEL for supercontinuum generation," Opt. Express **21**, 1599–1605 (2013).
6. M. Hoffmann, O. D. Sieber, V. J. Wittwer, I. L. Krestnikov, D. A. Livshits, Y. Barbarin, T. Südmeyer, and U. Keller, "Femtosecond high-power quantum dot vertical external cavity surface emitting laser," Opt. Express **19**, 8108–8116 (2011).
7. C. A. Zaugg, Z. Sun, V. J. Wittwer, D. Popa, S. Milana, T. S. Kulmala, R. S. Sundaram, M. Mangold, O. D. Sieber, M. Golling, Y. Lee, J. H. Ahn, A. C. Ferrari, and U. Keller, "Ultrafast and widely tuneable vertical-external-cavity surface-emitting laser, mode-locked by a graphene-integrated distributed Bragg reflector," Opt. Express **21**, 31548–31559 (2013).
8. S. Husaini and R. A. Bedford, "Antiresonant graphene saturable absorber mirror for mode-locking VECSELs," (private communication, 2013).
9. K. Seger, N. Meiser, S. Y. Choi, B. H. Jung, D.-I. Yeom, F. Rotermund, O. Okhotnikov, F. Laurell, and V. Pasiskevicius, "Carbon nanotube mode-locked optically-pumped semiconductor disk laser," Opt. Express **21**, 17806–17813 (2013).
10. P. Klopp, U. Griebner, M. Zorn, and M. Weyers, "Pulse repetition rate of 92 GHz or pulse duration shorter than 110 fs from a mode-locked semiconductor disk laser," Appl. Phys. Lett. **98**, 071103 (2011).
11. A. H. Quarterman, K. G. Wilcox, V. Apostolopoulos, Z. Mihoubi, S. P. Elsmere, I. Farrer, D. A. Ritchie, and A. Tropper, "A passively mode-locked external-cavity semiconductor laser emitting 60-fs pulses," Nat. Photonics **3**, 729–731 (2009).
12. O. D. Sieber, M. Hoffmann, V. J. Wittwer, M. Mangold, M. Golling, B. W. Tilma, T. Südmeyer, and U. Keller, "Experimentally verified pulse formation model for high-power femtosecond VECSELs," Appl. Phys. B **113**, 133–145 (2013).
13. H. Haug and S. W. Koch, *Quantum Theory of the Optical and Electronic Properties of Semiconductors* (World Scientific, 2009).
14. A. Baumner, S. W. Koch, and J. V. Moloney, "Non-equilibrium analysis of the two-color operation in semiconductor quantum-well lasers," Phys. Status Solidi B **248**, 843–846 (2011).
15. J. V. Moloney, I. Kilen, A. Bäumner, M. Scheller, and S. W. Koch, "Nonequilibrium and thermal effects in mode-locked VECSELs," Opt. Express **22**, 6422–6427 (2014).
16. H. A. Haus, "Mode-locking of lasers," IEEE J. Sel. Top. Quantum Electron. **6**, 1173–1185 (2000).

optica

The plasmonic memristor: a latching optical switch

C. Hoessbacher,[1,3] Y. Fedoryshyn,[1] A. Emboras,[1] A. Melikyan,[2] M. Kohl,[2] D. Hillerkuss,[1] C. Hafner,[1] and J. Leuthold[1,4]

[1]Institute of Electromagnetic Fields, ETH Zurich, 8092 Zurich, Switzerland

[2]Institutes IMT, Karlsruhe Institute of Technology (KIT), D-76131 Karlsruhe, Germany

[3]e-mail: choessbacher@ethz.ch

[4]e-mail: JuergLeuthold@ethz.ch

Received 8 July 2014; revised 18 August 2014; accepted 19 August 2014 (Doc. ID 216430); published 22 September 2014

Plasmonic memristors are electrically activated optical switches with a memory effect. This effect is important for a new generation of latching optical switches that maintain their state without power consumption. It is also of interest for new optical memories that can be activated by a single electrical write/erase impulse. The operation principle is based on the reversible formation of a conductive path in the dielectric layer of a plasmonic metal–insulator–metal waveguide. Extinction ratios of 12 dB (6 dB) are demonstrated in 10 μm (5 μm) long devices for operating voltages of ±2 V. With this, the devices feature the characteristics of electronic resistive random access memory, but for the field of plasmonics. Such plasmonic memristors are interesting in view of new applications in information storage and for low power circuit switching.

OCIS codes: (130.3120) Integrated optics devices; (240.6680) Surface plasmons; (130.4815) Optical switching devices; (250.5403) Plasmonics; (210.4680) Optical memories.

http://dx.doi.org/10.1364/OPTICA.1.000198

Integrated optically readable memories are key elements in the toolbox of next-generation information storage, as they permit one to replace electrical data buffers in optical communication systems [1]. Moreover, latching optical switches are needed for low power circuit switching [2].

Memory switching effects have been studied in electronics for many years [3–5]. One important example is the so-called resistive random access memory (RRAM or ReRAM) or memristor (memory resistor). RRAMs have attracted attention as possible candidates for future nonvolatile memories as an alternative for today's flash memories. Typical devices consist of a capacitor-like metal–insulator–metal (MIM) structure. The two states of RRAMs are accessed by applying a voltage between the two metals. Depending on the voltage, either a high-resistance or low-resistance nanometer-scale conductive path is formed in the insulator between the two metals.

In plasmonics, the signal is encoded as a surface plasmon polariton (SPP) that propagates along a metal–dielectric interface. The confinement of such SPP modes may be below the diffraction limit, which is why the field of plasmonics has triggered a number of suggestions for small-scale switch implementations [6–12]. Most interestingly, the typical structure of a RRAM device with its MIM layers also could serve as a plasmonic MIM waveguide and, thus, might pave the way for a new resistive switch in the field of plasmonics. Combining RRAMs with plasmonics allows one to relate the electrical and the optical world with new applications in circuit switching and memory concepts and ultimately could lead to the realization of a compact latching switch with electrical write/erase and optical readout functionality. Recently, optical switching with a 0.09 dB extinction for the first time indicated the feasibility of a plasmonic RRAM device [13]. The device consisted of a silver/amorphous silicon/p-silicon layer structure with the resistive switching being caused by the formation and annihilation of a metallic filament in the amorphous silicon layer. In another demonstration, a thermally induced insulator–metal phase transition based on vanadium dioxide was used to demonstrate plasmonic switching with a memory effect [14]. With this scheme, the authors showed a rather high extinction ratio of 10.3 dB with a device of 5 μm length. The device, however, requires relatively high electrical powers of about 28 mW for the thermally induced phase change.

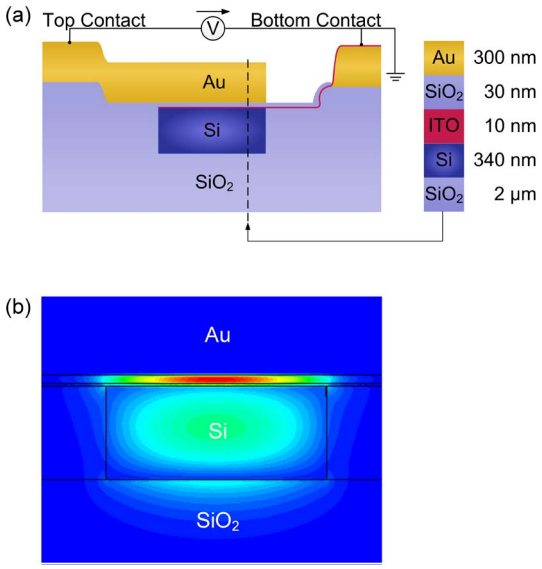

Fig. 1. (a) Cross-sectional view of the plasmonic memristor. The device comprises the typical memristor MIM layers that further serve as a plasmonic waveguide (gold/silicon dioxide/ITO) on top of a silicon photonic waveguide. (b) Electric field distribution of the quasi-TM fundamental mode in the hybrid plasmonic and SOI waveguide. The mode is highly confined in the 30 nm thin SiO_2 layer. When applying a voltage, a conductive path is formed in the insulating layer that strongly perturbs the plasmonic mode.

In this work, we present a plasmonic memristor with a high extinction ratio. More precisely, we demonstrate a latching optical switch based on the electrically induced creation and elimination of a conductive path in a gold/silicon dioxide/indium-tin oxide layer structure. The device is integrated with a silicon photonic waveguide and performs switching with an extinction ratio of 12 dB (6 dB) for a 10 µm (5 µm) long device. The operation power is consumed only when the state of the switch is changed and is below 200 nW.

The resistive switch consists of a hybrid waveguide with a plasmonic section on top of a silicon photonic strip waveguide (800 nm × 340 nm), as suggested in [9,11]. This hybrid approach allows for a simple fabrication process and can be easily integrated with a silicon photonic platform designed for TM polarization. Figure 1(a) shows the cross section of the device. The plasmonic waveguide itself is formed by a 30 nm thick silicon dioxide (SiO_2) layer sandwiched between a 10 nm thick indium-tin oxide (ITO) layer and a 300 nm thick gold (Au) layer. The ITO layer has a nominal carrier concentration of 10^{19} cm^{-3}. It is thin to enable coupling between the photonic and plasmonic sections. Figure 1(b) shows the corresponding electric field distribution of the quasi-TM fundamental mode at 1550 nm wavelength obtained with numerical simulations using the commercial software CST Microwave Studio. In this structure, a significant part of the electrical field is confined to the thin SiO_2 layer (39%). This is crucial for memristor performance, since the optical field has to interact with tiny nanofilaments in the insulator. Simulated propagation losses and coupling losses between the silicon photonic and the hybrid waveguide section are 0.2 dB/µm and 1.2 dB per interface, respectively. The ITO layer and the top metal further serve as bottom and top electrodes, respectively. They are connected to metal pads for contact with electrical probes. The ITO bottom electrode is contacted via a 300 nm thick Au layer at the side of the photonic waveguide; see Fig. 1(a). Light is coupled to the memristor by means of silicon strip waveguides with TM grating couplers at both ends.

The silicon photonic structures are fabricated on a silicon-on-insulator (SOI) substrate with a 340 nm thick silicon layer and 2 µm thick buried oxide layer using a single step e-beam lithography and an inductively couple plasma reactive-ion etching (ICP-RIE) process. The chip is then covered by a plasma-enhanced chemical vapor deposition (PECVD)-grown 500 nm thick SiO_2 layer acting as cladding for the photonic waveguide. Local openings in the SiO_2 on top of the photonic waveguides (1.6 µm wide) define the plasmonic sections of the devices. They are fabricated via photolithography and an RIE process. The 300 nm Au bottom contact is produced using photolithography, e-beam evaporation and a lift-off process. This contact is laterally offset with respect to the photonic waveguide. Next, the 10 nm ITO layer is RF-sputtered and structured using photolithography and lift-off. A 30 nm SiO_2 layer is RF-sputtered on top. A second 300 nm Au contact is deposited and structured similarly to the bottom one. Finally, the 30 nm oxide is opened locally using an RIE process to access the bottom contact pad. Figure 2 shows an optical microscope image of a fabricated device.

The device was characterized in two steps. First, we studied the quasi-static behavior. We measured the hysteresis of the current and the optical transmission while slowly sweeping the applied voltage. In a second step, we investigated the time-resolved switching process.

We measured the current and the optical transmission as a function of the applied voltage. As indicated in Fig. 1, the voltage was applied between the top and bottom electrodes. A compliance current of 100 nA was set to protect the device from permanent breakdown. Continuous-wave laser light at a wavelength of 1550 nm was coupled to the chip through grating couplers. The transmitted optical signal was measured with a powermeter.

The electrical behavior of a 5 µm long device with the laser being turned off is displayed in Fig. 3. The applied voltage was swept from −3 to 3 V and back in steps of 60 mV with

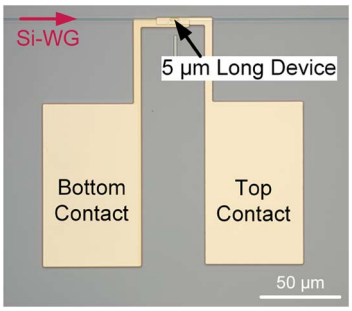

Fig. 2. Optical microscope image of the 5 µm long plasmonic switch. Light is coupled by means of a silicon waveguide (Si-WG) to the plasmonic memristor. The golden squares are the electrical contact pads.

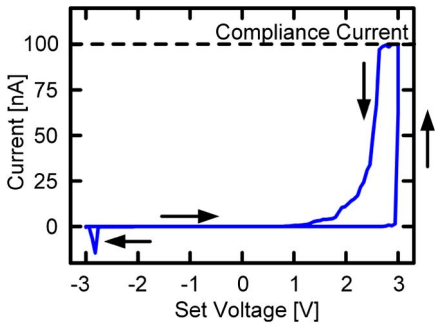

Fig. 3. Electrical current–voltage characteristic of the plasmonic memristor. The response indicates a hysteresis as it is typical for resistive switching memory cells. An abrupt increase of the current is found with a threshold around 2.9 V. Note that the set voltage differs from the actual (measured) voltage in the compliance limit.

a duration of 2 s per step. We observed a sudden increase of the current at a threshold of ~2.9 V. Here, the current reached its compliance limit. When scanning back, the current decreased while showing a hysteresis. This hysteresis is typical for RRAM devices [5].

Figure 4(a) shows the normalized optical transmission for 50 consecutive measurement cycles below threshold (±2 V, 20 mV per step, 2 s per step, total duration of 13.3 min per cycle). We started at −2 V in the ON state. While gradually increasing the voltage, the optical signal decreased. When decreasing the voltage, the optical transmission increased again, while being lower than for the forward sweep direction. This hysteresis indicates the memory effect of the switch. The device returned to its initial state after completion of each measurement cycle. This shows excellent repeatability of the switching effect. The difference between the ON and OFF states (extinction ratio) was 6 dB. The latching extinction ratio between the latched states was 3.5 dB. Since the device was operated below threshold, no significant current was measured and no hysteresis was observed in the I–V curve. Therefore, peak operating power during switching is below 200 nW.

The dependence of the extinction ratio on the device length was investigated, as well. From Fig. 4(b) one can see that increasing the length from 5 to 10 μm increases the extinction ratio from 6 to 12 dB. Thus, the extinction ratio increases with increasing device length. While two devices with different lengths do not yet provide sufficient statistics, the result at least indicates a trend.

Propagation losses in the hybrid waveguide section of 1 dB/μm and coupling losses between the silicon photonic and the hybrid waveguide of 6.5 dB per interface were determined through cut-back measurements. The experimentally determined losses are higher than the simulated ones due to fabrication imperfections. When opening the silicon dioxide cladding to define the plasmonic section, the structure was overetched. This resulted in a step between the silicon photonic and the hybrid waveguide sections, explaining the high coupling losses. The same process step led to surface roughness at the top of the silicon waveguide that contributed to the propagation losses. Furthermore, layer imperfection, in particular in the sputter-deposited silicon dioxide layer,

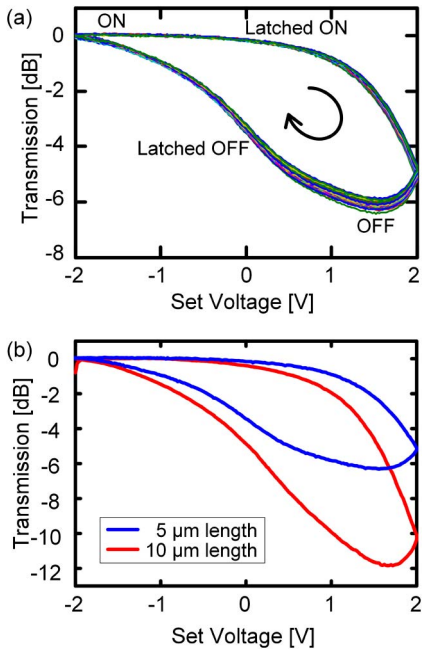

Fig. 4. Quasi-static performance of the plasmonic memristor. (a) Latching optical switch behavior for a 5 μm long device: 50 measurement cycles of the normalized optical transmission as a function of the set voltage showing hysteresis and an extinction ratio of 6 dB. (b) Latching optical switch behavior of a 10 μm long device showing an extinction ratio of 12 dB. During these measurements below threshold, no hysteresis was observed in the I–V curve.

influenced the propagation losses. Better control of the fabrication process will avoid this problem for future devices.

The results of Figs. 3 and 4 can be explained as follows. When a positive voltage is applied, a conductive path is formed in the oxide layer. As this conductive path is bridging the two electrodes, the current increases. For the reverse scanning direction, the conductive path is eliminated, so that the current decreases. Since the plasmonic signal is highly confined in the insulating layer, it is quite sensitive to the alteration of the insulating layer. This is why the switch may be operated below threshold. Even before electrical switching, the plasmonic mode is strongly perturbed by the conductive path, thus reducing the optical transmission.

A change of the ITO refractive index due to carrier accumulation/depletion was also said to influence the optical transmission [9,11]. However, theoretical calculations predict low extinction ratios (~1 dB) [9], so this effect is considered to be small compared to the resistive switching.

The physical nature of the resistive switching mechanism was reviewed in literature and is still not fully understood [3,5]. Yet, it is known that defects in insulating layers, such as metals and oxygen vacancies, play an important role in resistive switching devices, as they enable the formation and elimination of the conductive path. In the present device, the sputter-deposited SiO_2 that is used as an insulating layer is expected to contain a large number of defects [15]. For comparison, a sample with PEVCD SiO_2 was fabricated showing much lower extinction ratios and no hysteresis in the voltage-transmission curve. The switching mechanism

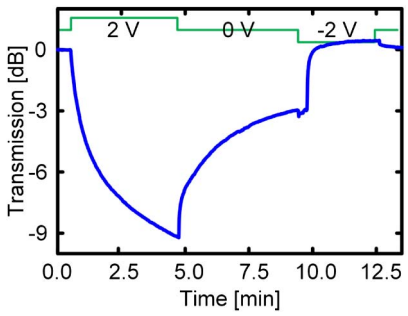

Fig. 5. Dynamic behavior for a 5 min switching process. A voltage of 2 V was applied for 5 min, before switching the voltage off again (green). A latching extinction ratio of 3 dB was observed. By applying a voltage of −2 V. The device was reset to its initial state.

might be explained by positively charged ions being injected from the top electrode. The ions thereby form narrow conductive filaments. This metal filament type of resistive switching was even observed with *in situ* transmission electron microscopy studies [15]. The layer thicknesses of the present plasmonic memristor are too small to resolve nanofilaments in a scanning electron microscopy study. However, needle-like gold filaments were reported in a very similar structure with a 100 nm thin sputter-deposited silicon dioxide layer in the supplement file of reference [16]. Another switching mechanism suggested in the literature is based on a conductive path of oxygen vacancies that is formed in the oxide layer. In that sense, silicon dioxide might be utilized by locally enriching silicon inside the silicon oxide matrix [15,17–20].

To further assess the device, we studied the dynamic behavior of the switch. Here, we determined the step response of the device at both minute and millisecond time scales. Moreover, a megahertz modulation was applied to the device.

The slow switching process is depicted in Fig. 5. A voltage of 2 V was applied to a 5 μm long device for 5 min, before switching the voltage off again. The optical signal measured with a power meter showed a latching extinction ratio of 3 dB. After that, the device was reset to its initial state by a negative voltage of −2 V.

Furthermore, a 5 ms long electrical impulse of 2 V was applied to the optical memristor (see Fig. 6). Here, the optical response of a 20 μm long device was measured with a photodiode and a real-time oscilloscope. Despite the short duration, a latching switching behavior was found as well. The latching extinction ratio was ∼0.6 dB, however. Thus, the extinction ratio increases with the duration of the pulse that is applied. The energy required for a transition is as little as 60 μJ or 1 nJ, depending on the switching duration.

To further investigate the switching speed, a sinusoidal modulation in the megahertz regime was applied to the device and detected with a photodiode and a lock-in amplifier. This revealed a relatively flat frequency response between 40 kHz and 10 MHz. The 3 dB bandwidth at an operation with ±2 V with respect the amplitude at 40 kHz is 30 MHz (see Fig. 7, blue triangles). However, subnanosecond switching times have been reported for electronic memristors [21].

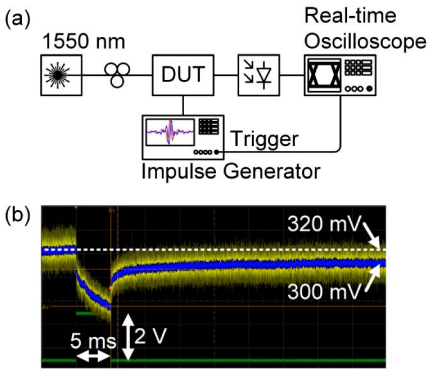

Fig. 6. Dynamic behavior for a 5 ms switching process. (a) Measurement setup: an electrical impulse was sent to the device under test (DUT) while measuring the optical response with a photodiode on a real-time oscilloscope. (b) Screenshot of the real-time oscilloscope showing the switching process (yellow) for a 5 ms long electrical impulse of 2 V (green). The blue line is the measured signal after a low-pass filter. A latching extinction ratio of ∼0.6 dB was observed.

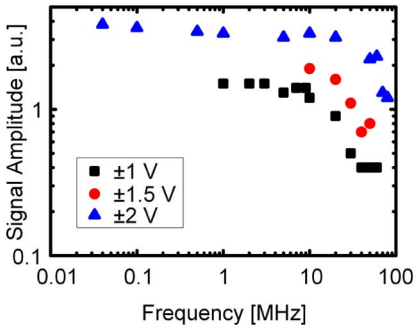

Fig. 7. Megahertz frequency response of the plasmonic memristor. A sinusoidal signal was applied to a 5 μm long device using an arbitrary waveform generator. The optical signal was detected with a photodiode and a lock-in amplifier.

Higher speeds thus should be doable for plasmonic memristors with optimized dimensions and material compositions.

In conclusion, we demonstrated a latching optical switch that combines the memristor concept with plasmonics. The switch exploits the formation and elimination of a conductive path in the insulating layer of a metal–insulator–metal layer stack. The conductive path leads to an attenuation of the optical mode in the OFF state and is ruptured when switching to the ON state. The plasmonic switch is integrated with a silicon photonic waveguide. Optical extinction ratios of 12 dB at 1550 nm wavelength are shown for 10 μm long devices. The operation power is consumed only when the state of the switch is changed and is below 200 nW with operating voltages in the range of ±2 V and currents below 100 nA. Tests with 50 write cycles and sinusoidal modulation in the megahertz regime demonstrate excellent repeatability of the switching mechanism.

FUNDING INFORMATION

European Commission (EC) project NAVOLCHI (288869).

ACKNOWLEDGMENTS

This work was partly carried out in the Binnig and Rohrer Nanotechnology Center as well as in the FIRST cleanroom facility at the ETH Zurich.

REFERENCES

1. C. A. Barrios and M. Lipson, J. Lightwave Technol. **24**, 2898 (2006).
2. C. H. Ji, Y. Yee, J. Choi, S. H. Kim, and J. U. Bu, IEEE J. Sel. Top. Quantum Electron. **10**, 545 (2004).
3. A. Sawa, Mater. Today **11**(6), 28 (2008).
4. D. B. Strukov, G. S. Snider, D. R. Stewart, and R. S. Williams, Nature **453**, 80 (2008).
5. R. Waser, R. Dittmann, G. Staikov, and K. Szot, Adv. Mater. **21**, 2632 (2009).
6. R. M. Briggs, J. Grandidier, S. P. Burgos, E. Feigenbaum, and H. A. Atwater, Nano Lett. **10**, 4851 (2010).
7. W. Cai, J. S. White, and M. L. Brongersma, Nano Lett. **9**, 4403 (2009).
8. G. Gagnon, N. Lahoud, G. A. Mattiussi, and P. Berini, J. Lightwave Technol. **24**, 4391 (2006).
9. A. Melikyan, N. Lindenmann, S. Walheim, P. M. Leufke, S. Ulrich, J. Ye, P. Vincze, H. Hahn, T. Schimmel, C. Koos, W. Freude, and J. Leuthold, Opt. Express **19**, 8855 (2011).
10. T. Nikolajsen, K. Leosson, and S. I. Bozhevolnyi, Appl. Phys. Lett. **85**, 5833 (2004).
11. V. J. Sorger, N. D. Lanzillotti-Kimura, R.-M. Ma, and X. Zhang, Nanophotonics **1**, 17 (2012).
12. A. Melikyan, L. Alloatti, A. Muslija, D. Hillerkuss, P. C. Schindler, J. Li, R. Palmer, D. Korn, S. Muehlbrandt, D. Van Thourhout, B. Chen, R. Dinu, M. Sommer, C. Koos, M. Kohl, W. Freude, and J. Leuthold, Nat. Photonics **8**, 229 (2014).
13. A. Emboras, I. Goykhman, B. Desiatov, N. Mazurski, L. Stern, J. Shappir, and U. Levy, Nano Lett. **13**, 6151 (2013).
14. A. Joushaghani, B. A. Kruger, S. Paradis, D. Alain, J. S. Aitchison, and J. K. S. Poon, Appl. Phys. Lett. **102**, 061101 (2013).
15. Y. Yang, P. Gao, S. Gaba, T. Chang, X. Pan, and W. Lu, Nat. Commun. **3**, 732 (2012).
16. E. Feigenbaum, K. Diest, and H. A. Atwater, Nano Lett. **10**, 2111 (2010).
17. M. Cavallini, Z. Hemmatian, A. Riminucci, M. Prezioso, V. Morandi, and M. Murgia, Adv. Mater. **24**, 1197 (2012).
18. A. Mehonic, S. Cueff, M. Wojdak, S. Hudziak, C. Labbe, R. Rizk, and A. J. Kenyon, Nanotechnology **23**, 455201 (2012).
19. A. Mehonic, A. Vrajitoarea, S. Cueff, S. Hudziak, H. Howe, C. Labbe, R. Rizk, M. Pepper, and A. J. Kenyon, Sci. Rep. **3**, 2708 (2013).
20. J. Yao, L. Zhong, D. Natelson, and J. M. Tour, Sci. Rep. **2**, 242 (2012).
21. A. C. Torrezan, J. P. Strachan, G. Medeiros-Ribeiro, and R. S. Williams, Nanotechnology **22**, 485203 (2011).

Research Article Vol. 1, No. 4 / October 2014 / Optica 203

Experimental realization of an optical antenna designed for collecting 99% of photons from a quantum emitter

X.-L. Chu,[1,2] T. J. K. Brenner,[1,3] X.-W. Chen,[1,2] Y. Ghosh,[4] J. A. Hollingsworth,[4] V. Sandoghdar,[1,2] and S. Götzinger[1,2,*]

[1]Max Planck Institute for the Science of Light, 91058 Erlangen, Germany

[2]Department of Physics, Friedrich Alexander University of Erlangen-Nürnberg, 91058 Erlangen, Germany

[3]Institute of Physics & Astronomy, University of Potsdam, 14476 Potsdam-Golm, Germany

[4]Materials Physics & Applications: Center for Integrated Nanotechnologies, Los Alamos National Laboratory, Los Alamos, New Mexico 87545, USA

*Corresponding author: stephan.goetzinger@mpl.mpg.de

Received 21 May 2014; revised 11 August 2014; accepted 20 August 2014 (Doc. ID 212480); published 25 September 2014

A light source that emits single photons at well-defined times and into a well-defined mode would be a decisive asset for quantum information processing, quantum metrology, and sub-shot-noise detection of absorption. One of the central challenges in the realization of such a deterministic device based on a single quantum emitter concerns the collection of the photons, which are radiated into a 4π solid angle. Here, we present the fabrication and characterization of an optical antenna designed to convert the dipolar radiation of an arbitrarily oriented quantum emitter to a directional beam with more than 99% efficiency. Our approach is extremely versatile and can be used for more efficient detection of nanoscopic emitters ranging from semiconductor quantum dots to dye molecules, color centers, or rare-earth ions in various environments. Having addressed the issue of collection efficiency, we also discuss the photophysical limitations of the existing quantum emitters for the realization of a deterministic single-photon source.

OCIS codes: (270.0270) Quantum optics; (030.5260) Photon counting; (310.0310) Thin films; (350.4238) Nanophotonics and photonic crystals.

http://dx.doi.org/10.1364/OPTICA.1.000203

There is a great deal of interest in the optics community in efficient collection of light from atoms, molecules, quantum dots, or other nanoscopic emitters [1–3]. One of the motivations concerns the detection of weak traces of fluorescence in biophotonics, where studies of chromophores with low quantum yield [4] or imaging of fast dynamical phenomena [5,6] are desirable. Similarly, spectroscopy of weakly emitting quantum systems such as rare-earth ions [7] and color centers can benefit from higher count rates. Another fascinating prospect is in the realization of a new primary intensity standard based on a known flux of single photons obtained from an isolated quantum emitter through pulsed excitation [8]. A very different area of interest is in quantum optics with prominent applications in sub-shot-noise detection [9], quantum communication [10], and quantum computation [1]. In these applications losses quickly compromise the performance. For example, it is often stated that efficiencies on the order of 99% are required for practical linear optics quantum computing [3]. In quantum key distribution, low losses are desirable both for increased data transmission rates and for higher security of the connection.

Many different approaches have been explored for achieving high collection efficiency from single emitters. For example, a

deep parabolic mirror has been used to extract light from an atom in a trap [11]; however, this solution is incompatible with most applications in the condensed phase. Another strategy has been to manipulate the density of states in microcavities [12,13], but the need for operation under resonance conditions and the difficulty of fabrication have hampered collection efficiencies close to unity. Novel geometries using nanowires and their combination with cavity arrangements also hold promise for high collection efficiency [14–16], but practical combination of these solutions with generic emitters is nontrivial and yet to be demonstrated. Recently, plasmonic nanostructures have also been combined with concepts from antenna theory and near-field optics to introduce directionality to the radiation pattern of emitters [17,18]. Unfortunately, however, near-field coupling to metals is intrinsically accompanied by substantial losses.

Three years ago, we devised a new antenna concept based on planar dielectric structures [19]. In that work, we experimentally demonstrated 96% collection efficiency from a single molecule that was oriented normal to the antenna plane. The noise on the light generated by a perfect emitter in such an antenna is reduced to 20% of the shot-noise value. This can be deduced from $\sqrt{xN(1-x)}$, which describes the fluctuation in the number of detected photons with an average value N and loss factor x [9]. Improvements beyond a certain noise level become increasingly more difficult to achieve. For example, a collection efficiency of 99% would reduce the noise to only about 10% of the shot-noise value, corresponding to 10 dB intensity squeezing.

Motivated by the need for low-noise light sources and the desire to generalize our planar dielectric antenna to arbitrarily oriented emitters, we proposed a metallo-dielectric antenna design for reaching collection efficiencies exceeding 99% for any orientation of the emitter dipole moment [20]. In this article we report on the first fabrication and characterization, to the best of our knowledge, of such an antenna and elaborate on the subtleties involved in the realization of a single-photon source with 99% efficiency.

Figure 1(a) sketches the main ingredients of a planar metallo-dielectric antenna. The general requirement of $n_1 > n_2 > n_3$ remains the same as the previously discussed dielectric antenna [19]. However, to capture and redirect any leakage in the direction normal to the antenna plane, we add a mirror on the far side of the n_3 medium. The simplest experimental realization of this structure is to use a metallic mirror at a large enough distance from the $n_2 - n_3$ interface to avoid coupling to surface plasmons.

In this work, we have chosen to perform our experiments with semiconductor nanocrystals. In particular, we have used "giant" CdSe/CdS core/thick-shell quantum dots [21] featuring nearly complete suppression of blinking and fluorescence intermittency [22]. Figure 1(b) displays the schematics of our experimental arrangement. The first component of the antenna consists of a sapphire cover glass (refractive index $n_1 = 1.78$). We then coat this substrate with 200 nm of PMMA (refractive index 1.49) and spin cast quantum dots on this layer at a very small surface coverage. Next, a 150 nm thick layer of PVA (refractive index 1.5) is coated on top.

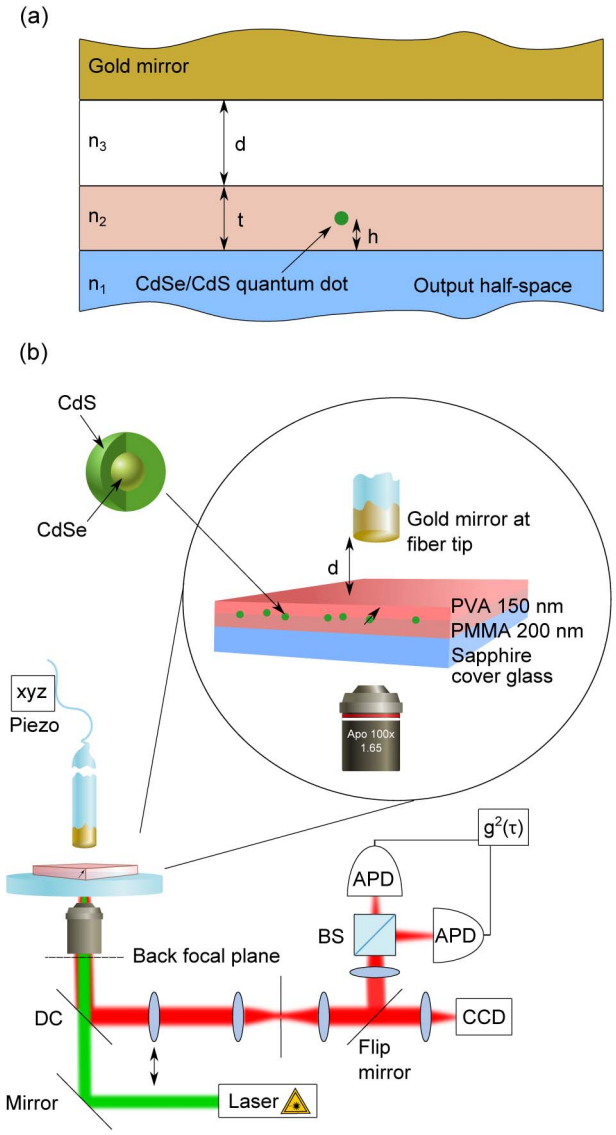

Fig. 1. (a) Layer arrangement of the metallo-dielectric antenna. (b) Schematic diagram of the experimental setup. CdSe/CdS giant quantum dots are embedded in between two polymer layers (PMMA and PVA) of the same index of refraction, and a gold-coated end of a fiber is placed at variable separations from the top. A laser beam (wavelength 532 nm) illuminates the sample through a 100x microscope objective. The emitted fluorescence is collected by the same objective and guided to two avalanche photodiodes (APDs) to measure the second-order correlation function $g^2(\tau)$ or to a CCD camera for back-focal-plane imaging. BS, beam splitter; DC, dichromatic mirror.

Considering the similarity of the refractive indices of PVA and PMMA, we can treat these combined layers as the second antenna medium with $n_2 = 1.5$. The thickness of this medium is measured using atomic force microscopy. The third medium consists of air with $n_3 = 1$. In this proof-of-principle demonstration, we have decided to place the metallic mirror at the cleaved end of a thinned optical fiber so that we could vary its position at will. Quantum dots are excited by a laser at $\lambda = 532$ nm (CW or pulsed), and their fluorescence is collected using the same microscope objective (Olympus Apo 100×, NA 1.65). The resulting emission centered at the wavelength

of 637 nm is detected on a CCD camera or analyzed using a Hanbury Brown and Twiss coincidence setup. The overall detection efficiency of the setup amounts to 35%.

The key function of the antenna is to redistribute the radiated power by an emitter into a solid angle that can be collected by a commercial microscope objective. To investigate the angular emission pattern of a single quantum dot, we imaged its intensity distribution at the back focal plane of the objective. Figures 2(a) and 2(b) display the experimental outcome and its theoretical fit, respectively, for the dielectric part of the antenna without the gold mirror. To arrive at Fig. 2(b), we first determined the ratio between the axial and in-plane dipole contributions by fitting the data in Fig. 2(c), which plots the detected power integrated over the azimuthal angle ϕ as a function of the polar emission angle θ [see Fig. 2(a)]. The agreement between the experimental (red) and theoretical (blue) traces is excellent. The slight deviation at angles beyond 62° is caused by the unfortunate position of a small scattering impurity on the detection optics [see, for example, Fig. 2(f)]. Once the in-plane dipole contribution was extracted, it was further separated into x and y components by fitting the image in Fig. 2(a). We remark that the semiconductor nanocrystals used in our experiments are known to exhibit a two-dimensional dipole moment [23]. Due to its arbitrary orientation with respect to the optical axis it has to be described by three independent orthogonal components, where the z axis is aligned with the optical axis. In the case presented in Fig. 2, the axial, x, and y components amounted to 44%, 21%, and 35%, respectively.

Figures 2(d)–2(o) present the polarization dependence of the emission pattern obtained by placing a polarizer in the

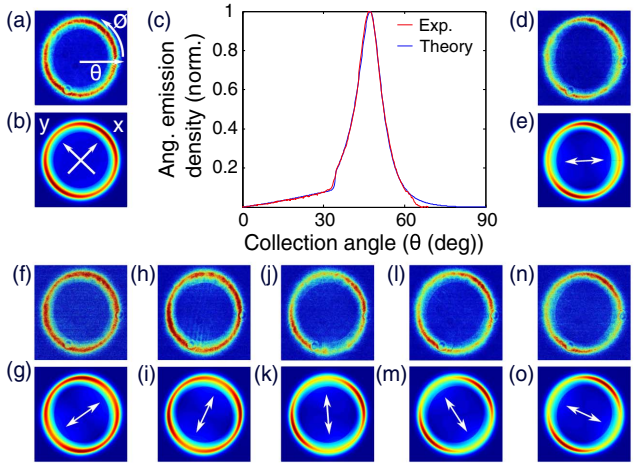

Fig. 2. Characterization of the angular emission from a single quantum dot in a dielectric antenna before the gold mirror was added. (a) Power distribution of the emission in the back focal plane of the microscope objective. (b) Theoretical fit to the image in (a), yielding information about the emission dipole moments (see text for more information). (c) Signal in (a) integrated over the angle ϕ plotted as a function of the polar angle θ as indicated in (a). (d), (f), (h), (j), (l), (n) Experimental measurements as in (a) but for six different settings of a polarizer angle in the detection path at 30° increments. (e), (g), (i), (k), (m), (o) Corresponding theoretical predictions (not fits). The white arrows indicate the orientation of the polarizer in each case.

detection path. In Figs. 2(d), 2(f), 2(h), 2(j), 2(l), and 2(n) we incremented the orientation of the polarizer in steps of 30°. Figures 2(e), 2(g), 2(i), 2(k), 2(m), and 2(o) plot the corresponding theoretical predictions based on the dipole orientations deduced from the fit in Fig. 2(b). The excellent agreement between the measured and calculated angular intensity distributions for all polarization projections without additional fitting confirms the robustness of our analysis and the assignment of the quantum dot emission dipoles.

The insets in Fig. 3(a) display the experimental (top) back-focal-plane images of another quantum dot without the gold mirror [i.e., similar to the case in Fig. 2(a)] as well as the theoretical fit to it (bottom), while the main graph in the figure shows the integration over ϕ. We now introduce the gold-coated end of an optical fiber with a diameter of about 15 μm. By using a piezoelectric scanner, we could place the mirror at different separations from the dielectric part of the antenna. The top insets in Figs. 3(b)–3(e) display the measured back-focal-plane fluorescence distribution for separations of 225, 284, 355, and 680 nm. The lower insets present the theoretical predictions. We emphasize that once the data in Fig. 3(a) were fitted, the following calculated images were obtained by merely considering a gold mirror at the corresponding measured separation. The main parts of the figures show the detected power integrated over ϕ as a function of θ. These data reveal that for a large mirror-slab distance, the part of the quantum dot emission reflected from the mirror interferes with the downward emission to yield the observed modulations. The remarkably good agreement between the experiment (red) and theory (blue) verifies the predicted contribution of the metallic mirror.

To quantify the effect of the gold mirror further, we compared the photon flux with and without it. The leakage out of the far side of the dielectric part of the antenna amounts to 4% for an axially oriented dipole and 12% for dipole moments in the antenna plane. We found that the detected fluorescence signal was consistently 10% larger in the presence of the mirror. This is in very good agreement with the expected effect of 9.5% for this quantum dot, which had 31% and 69% of its emission dipole in the axial and planar components, respectively. We note that the quantum dot was excited via total internal reflection through the microscope objective to avoid fluorescence from the gold mirror.

The studies presented above let us conclude that the antenna fully meets its design specification, chosen to yield more than 99% collection efficiency within a half angle of 68° accessible to a microscope objective with a numerical aperture of 1.65. This addresses an outstanding bottleneck in the realization of deterministic single-photon sources. What is now required is to excite a quantum emitter using short pulses at a well-defined repetition rate. However, a successful execution of this scheme also requires an emitter that has a fluorescence stability better than 99%. An ideal two-level atom would satisfy this condition because it emits as many photons per unit time as excitation pulses if these were spaced sufficiently far apart with respect to the spontaneous emission lifetime. Unfortunately, a thorough examination of the existing quantum

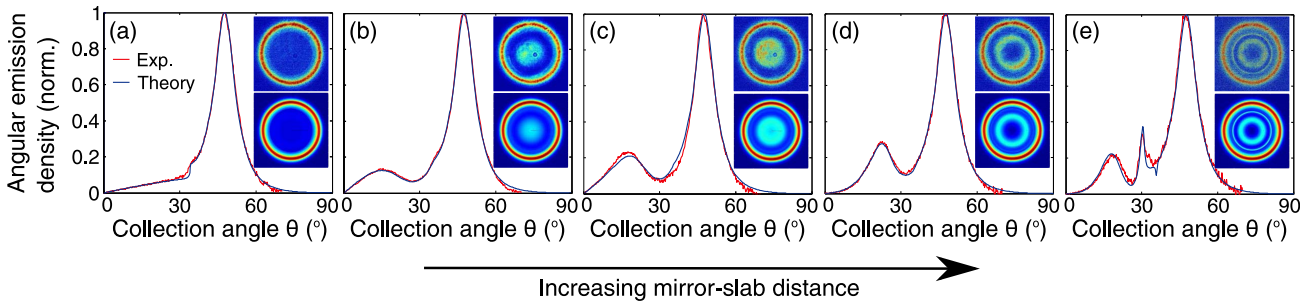

Fig. 3. Theoretical and measured angular fluorescence signal of a single quantum dot in the antenna structure. Insets: measured (top) back-focal-plane image and theoretical (bottom) simulations. (a) No metallic mirror. (b)–(e) In the presence of a gold mirror placed at distances of $d = 225$, 284, 355, and 680 nm, respectively, from the top surface of the dielectric antenna.

emitters led us to the conclusion that this task is currently beyond reach due to limited photophysical properties.

Over the past two decades, molecules, quantum dots, and color centers have been explored as single-photon sources [9], whereby the term single-photon source has become unanimous with a system that never emits two photons at a time. However, scientists are yet to demonstrate a source that would deliver a photon at an expected time. Several issues have to be considered, and in each system one or more of these pose problems. First, a nonunity quantum yield would introduce randomly missing photons. This issue is exacerbated by the difficulty of determining quantum efficiencies with 1% accuracy. Second, limited photostability is prohibitive for practical applications and long-term usage. Third, at high excitation intensities the supporting medium often fluoresces at the level of a few percent. Fourth, intermittent transitions such as intersystem crossing or blinking introduce randomness. Fifth, multiphoton absorption or multi-excitonic behavior might compromise the two-level character of the emitter at high excitation rates. Each and every one of these effects compromise and directly affect the quality of the single-photon source and its properties, such as intensity squeezing.

Conventional dye molecules fall short of these requirements because of bleaching and blinking, although selected systems have been shown to be unusually photostable [24,25]. Atoms and ions in the gas phase are not favorable because of the difficulty in trapping and integration into compact devices. Color centers in bulk diamond can be extremely photostable [26], but they also suffer from intersystem crossing and blinking. In addition, color centers in nanocrystals have a large inhomogeneity in terms of quantum yield and fluorescence lifetime. Another alternative has been discussed in the context of semiconductor quantum dots. Here one usually distinguishes between epitaxially grown nanostructures and chemically produced nanocrystals such as CdSe/CdS core-shell dots. The former offer excellent suppression of two-photon emission, but they might confront various undesired states involving dark or charged excitons [27,28]. Furthermore, good optical properties of these dots only emerge at cryogenic temperatures. Standard core-shell nanocrystals suffer from severe blinking, which makes precise power calibration impossible. Giant core-shell nanocrystals solve the blinking problem by suppressing Auger recombination, but at high pump intensities they can undergo transitions to biexciton and higher-order multi-exciton states, resulting in deviations from a strong two-photon emission suppression. Recent progress in the detection of a single rare-earth ion promises a viable alternative; however, much work still remains to be done to characterize the photophysics of these species at the single emitter level [7,29].

In this work, we have chosen giant quantum dots for their strong photostability and access to several dipole moment components. Although these dots do not blink in the common sense of experiencing on–off-states, Figs. 4(a) and 4(c) show that the fluorescence can fluctuate about a mean value at weak excitation and flicker among different on-levels [30] under strong illumination. Furthermore, it has been previously shown that significant suppression of Auger recombination in giant quantum dots leads to efficient room-temperature biexciton [31] and multiple-exciton emission [32]. Figure 5 displays the second-order autocorrelation function determined from Hanbury Brown and Twiss measurements at low [Fig. 5(a)] and high [Fig. 5(b)] excitation powers. While

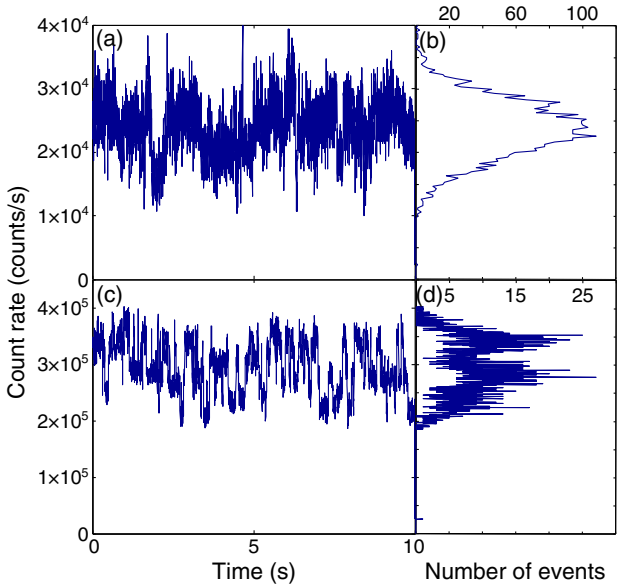

Fig. 4. (a), (c) Time traces of a single quantum dot with 1 ms resolution and 10 s acquisition time under an excitation power of (a) 40 nW and (c) 1 μW. (b), (d) Distribution of the fluorescence signal corresponding to (a) and (c), respectively.

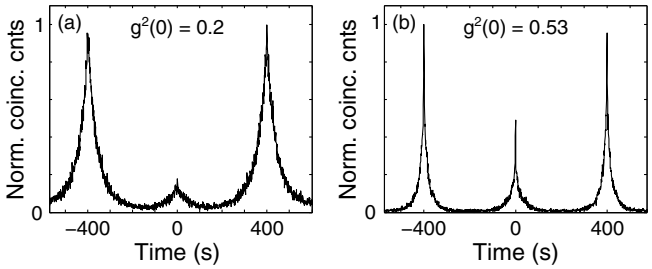

Fig. 5. Antibunching curves recorded from a quantum dot coupled to the antenna at excitation (pulsed) powers of (a) 40 nW and (b) 1.19 μW. The bin size was 3.2 ns.

antibunching is clearly observed in the former case, $g^{(2)}(\tau = 0)$ grows above 0.5 at high powers. We note that we have verified that the reduction of the antibunching is not due to residual background. We emphasize that the relatively low photon count rates are the result of a weak excitation of the quantum dot in order to avoid multi-excitonic emission.

In conclusion, we have demonstrated a planar metallo-dielectric antenna that redistributes the photons from an emitter in excellent agreement with its theoretical design, which predicts a collection efficiency larger than 99%. Such an antenna provides a crucial building block of an ultrabright single-photon source that can deliver up to several tens of millions of photons per second at deterministic times. Here, it will be crucial to reduce losses in the emission and detection processes also to the percent level. Although the photophysics of quantum emitters and the quantum yield of detectors currently do not meet this standard, the enormous recent progress in the development of efficient single-photon counters [33] and the synthesis of novel emitters [34,35] promises to address these issues.

FUNDING INFORMATION

European Research Council [Advanced Grant (SINGLE-ION)]; Max Planck Society; European Metrology Research Programme (EMRP) [project SIQUTE (contract EXL02)].

ACKNOWLEDGMENTS

Giant quantum dots were synthesized at the Center for Integrated Nanotechnologies, a U.S. Department of Energy, Office of Basic Energy Sciences user facility. Los Alamos National Laboratory, an affirmative action equal opportunity employer, is operated by Los Alamos National Security, LLC, for the National Nuclear Security Administration of the U.S. Department of Energy under contract DE-AC52-06NA25396.

REFERENCES

1. J. L. O'Brien, "Optical quantum computing," Science **318**, 1567–1570 (2007).
2. S. Scheel, "Single-photon sources—an introduction," J. Mod. Opt. **56**, 141–160 (2009).
3. S. Buckley, K. Rivoire, and J. Vuckovic, "Engineered quantum dot single-photon sources," Rep. Prog. Phys. **75**, 126503 (2012).
4. J. R. Lakowicz, *Principles of Fluorescence Spectroscopy* (Springer, 2004).
5. V. Vogel, ed., *Nanotechnology, Volume 5: Nanomedicine* (Wiley-VCH, 2009).
6. C.-L. Hsieh, S. Spindler, J. Ehrig, and V. Sandoghdar, "Tracking single particles on supported lipid membranes: multimobility diffusion and nanoscopic confinement," J. Phys. Chem. B **118**, 1545–1554 (2014).
7. T. Utikal, E. Eichhammer, L. Petersen, A. Renn, S. Götzinger, and V. Sandoghdar, "Spectroscopic detection and state preparation of a single praseodymium ion in a crystal," Nat. Commun. **5**, 3627 (2014).
8. J. Y. Cheung, C. J. Chunnilall, E. R. Woolliams, N. P. Fox, J. R. Mountford, J. Wang, and P. J. Thomas, "The quantum candela: a re-definition of the standard units for optical radiation," J. Mod. Opt. **54**, 373–396 (2007).
9. B. Lounis and M. Orrit, "Single-photon sources," Rep. Prog. Phys. **68**, 11291179 (2005).
10. N. Gisin, G. Ribordy, W. Tittel, and H. Zbinden, "Quantum cryptography," Rev. Mod. Phys. **74**, 145–195 (2002).
11. A. Golla, B. Chalopin, M. Bader, I. Harder, K. Mantel, R. Maiwald, N. Lindlein, M. Sondermann, and G. Leuchs, "Generation of a wave packet tailored to efficient free space excitation of a single atoms," Eur. Phys. J. D **66**, 190–199 (2012).
12. W. Barnes, G. Björk, J. Gérard, P. Jonsson, J. Wasey, P. Worthing, and V. Zwiller, "Solid-state single photon sources: light collection strategies," Eur. Phys. J. D **18**, 197–210 (2002).
13. O. Gazzano, S. M. de Vasconcellos, C. Arnold, A. Nowak, E. Galopin, I. Sagnes, L. Lanco, A. Lemaitre, and P. Senellart, "Bright solid-state sources of indistinguishable single photons," Nat. Commun. **4**, 1425 (2013).
14. J. Claudon, J. Bleuse, N. S. Malik, M. Bazin, P. Jaffrennou, N. Gregersen, C. Sauvan, P. Lalanne, and J.-M. Gerard, "A highly efficient single-photon source based on a quantum dot in a photonic nanowire," Nat. Photonics **4**, 174–177 (2010).
15. M. Khajavikhan, A. Simic, M. Katz, J. H. Lee, B. Slutsky, A. Mizrahi, V. Lomakin, and Y. Fainman, "Thresholdless nanoscale coaxial lasers," Nature **482**, 204–207 (2012).
16. M. Munsch, N. S. Malik, E. Duput, A. Delga, J. Bleuse, J.-M. Gerard, and J. Claudon, "Dielectric GaAs antenna ensuring an efficient broadband coupling between an InAs quantum dot and a Gaussian optical beam," Phys. Rev. Lett. **110**, 177402 (2013).
17. S. Kühn, G. Mori, M. Agio, and V. Sandoghdar, "Modification of single molecule fluorescence close to a nanostructure: radiation pattern, spontaneous emission and quenching," Mol. Phys. **106**, 893–908 (2008).
18. A. G. Curto, G. Volpe, T. H. Taminiau, M. P. Kreuzer, R. Quidant, and N. F. van Hulst, "Unidirectional emission of a quantum dot coupled to a nanoantenna," Science **329**, 930–933 (2010).
19. K. G. Lee, X. W. Chen, H. Eghlidi, P. Kukura, R. Lettow, A. Renn, V. Sandoghdar, and S. Götzinger, "A planar dielectric antenna for directional single-photon emission and near-unity collection efficiency," Nat. Photonics **5**, 166–169 (2011).
20. X.-W. Chen, S. Götzinger, and V. Sandoghdar, "99% efficiency in collecting photons from a single emitter," Opt. Lett. **36**, 3545–3547 (2011).
21. Y. Chen, J. Vela, H. Htoon, J. L. Casson, D. J. Werder, D. A. Bussian, V. I. Klimov, and J. A. Hollingsworth, "Giant multishell CdSe nanocrystal quantum dots with suppressed blinking," J. Am. Chem. Soc. **130**, 5026–5027 (2008).
22. Y. Ghosh, B. Mangum, J. L. Casson, D. J. Williams, H. Htoon, and J. A. Hollingsworth, "New insights into the complexities of shell growth and the strong influence of particle volume in non-blinking 'giant' core/shell nanocrystal quantum dots," J. Am. Chem. Soc. **134**, 9634–9643 (2012).
23. I. Chung, K. T. Shimizu, and M. G. Bawendi, "Room temperature measurements of the 3D orientation of single CdSe quantum dots using polarization microscopy," Proc. Natl. Acad. Sci. USA **100**, 405–408 (2003).
24. R. J. Pfab, J. Zimmermann, C. Hettich, I. Gerhardt, A. Renn, and V. Sandoghdar, "Aligned terrylene molecules in a spin-coated ultrathin

crystalline film of *p*-terphenyl," Chem. Phys. Lett. **387**, 490–495 (2004).
25. C. Toninelli, K. Early, J. Bremi, A. Renn, S. Götzinger, and V. Sandoghdar, "Near-infrared single-photons from aligned molecules in ultrathin crystalline films at room temperature," Opt. Express **18**, 6577–6582 (2010).
26. F. Jelezko and J. Wrachtrup, "Single defect centres in diamond: a review," Phys. Status Solidi A **203**, 3207–3225 (2006).
27. P. Michler, ed., *Single Quantum Dots: Fundamentals, Applications and New Concepts* (Springer, 2003).
28. S. Strauf, N. G. Stoltz, M. T. Rakher, L. Coldren, P. M. Petroff, and D. Bouwmeester, "High-frequency single photon source with polarization control," Nat. Photonics **1**, 704–708 (2007).
29. R. Kolesov, K. Xia, R. Reuter, R. Stöhr, A. Zappe, J. Meijer, P. R. Hemmer, and J. Wrachtrup, "Optical detection of a single rare-earth ion in a crystal," Nat. Commun. **3**, 1029 (2012).
30. C. Galland, Y. Ghosh, A. Steinbrück, M. Sykora, J. A. Hollingsworth, V. I. Klimov, and H. Htoon, "Two types of luminescence blinking revealed by spectroelectrochemistry of single quantum dots," Nature **479**, 203–207 (2011).
31. Y.-S. Park, A. Malko, J. Vela, Y. Chen, Y. Ghosh, F. Garcia-Santamaria, J. A. Hollingsworth, V. I. Klimov, and H. Htoon, "Near-unity quantum yields of biexciton emission from CdSe/CdS nanocrystals measured using single-particle spectroscopy," Phys. Rev. Lett. **106**, 1874018 (2011).
32. H. Htoon, A. V. Malko, D. Bussian, J. Vela, Y. Chen, J. A. Hollingsworth, and V. I. Klimov, "Highly emissive multiexcitons in steady-state photoluminescence of individual "giant" CdSe/CdS core/shell nanocrystals," Nano Lett. **10**, 2401–2407 (2010).
33. F. Marsili, V. B. Verma, J. A. Stern, S. Harrington, A. E. Lita, T. Gerrits, I. Vayshenker, B. Beak, M. D. Shaw, R. P. Mirin, and S. W. Nam, "Detecting single infrared photons with 93% system efficiency," Nat. Photonics **7**, 210–214 (2013).
34. B. D. Mangum, S. Sampat, Y. Ghosh, J. A. Hollingsworth, H. Htoon, and A. V. Malko, "Influence of core size on biexciton quantum yield in giant CdSe/CdS nanocrystals," Nanoscale **6**, 3712–3720 (2014).
35. B. D. Mangum, F. Wang, A. Dennis, J. A. Hollingsworth, and H. Htoon, "Competition between Auger recombination and hot electron trapping in blinking of type II InP/CdS nanocrystals," Small **10**, 2892–2901 (2014).

Research Article Vol. 1, No. 4 / October 2014 / Optica 209

Extended depth-of-field imaging and ranging in a snapshot

PAUL ZAMMIT, ANDREW R. HARVEY,* AND GUILLEM CARLES

University of Glasgow, University Avenue, Glasgow, G12 8QQ, UK

**Corresponding author: andy.harvey@glasgow.ac.uk*

Received 19 June 2014; revised 12 August 2014; accepted 23 August 2014 (Doc. ID 214358); published 26 September 2014

Traditional approaches to imaging require that an increase in depth of field is associated with a reduction in numerical aperture, and hence with a reduction in resolution and optical throughput. In their seminal work, Dowski and Cathey reported how the asymmetric point-spread function generated by a cubic-phase aberration encodes the detected image such that digital recovery can yield images with an extended depth of field without sacrificing resolution [Appl. Opt. 34, 1859 (1995)]. Unfortunately recovered images are generally visibly degraded by artifacts arising from subtle variations in point-spread functions with defocus. We report a technique that involves determination of the spatially variant translation of image components that accompanies defocus to enable determination of spatially variant defocus. This in turn enables recovery of artifact-free, extended depth-of-field images together with a two-dimensional defocus and range map of the imaged scene. We demonstrate the technique for high-quality macroscopic and microscopic imaging of scenes presenting an extended defocus of up to two waves, and for generation of defocus maps with an uncertainty of 0.036 waves.

OCIS codes: (110.0110) Imaging systems; (110.6880) Three-dimensional image acquisition; (110.1758) Computational imaging; (110.7348) Wavefront encoding.

http://dx.doi.org/10.1364/OPTICA.1.000209

1. INTRODUCTION

We report here a new modality of hybrid imaging that provides three-dimensional image ranging with an extended depth-of-field (DOF) and with enhanced image quality. Perhaps the earliest demonstration of the benefit of hybrid imaging was the report by Häusler in 1972 [1] of combining time-sequential, swept-focus imaging of a deep object with post-detection image recovery to yield a sharp image with extended DOF. The average modulation-transfer function (MTF) of swept-focus imaging exhibits no nulls and the absence of phase effects enabled simple recovery using coherent optical processing based on a photographic transparency, which provided more convenient recovery than digital computation at that time. The seminal 1995 paper by Dowski and Cathey [2] showed that a cubic optical phase function introduced into the exit pupil of an imaging system yields a point-spread function (PSF) that is approximately invariant to defocus, exhibits no nulls in the MTF, and therefore enables digital recovery of a high-quality image for an extended DOF [3]. Control of focus-related aberrations is a major challenge in lens design, and so hybrid imaging using cubic or other antisymmetric phase functions such as trefoil [4] has been exploited for simplification of lens design and manufacture in miniaturization of zoom lenses [5] and thermal imaging [6], particularly for infinite-conjugate imaging.

Although the MTF for a cubic phase function is approximately invariant with defocus, there is translation of the PSF and strong phase modulation on the optical-transfer function (OTF) [7,8]. Image recovery with a single kernel therefore introduces phase mismatches between the coding optical phase-transfer function (PTF) and the PTF of the digital filter used for image recovery, leading to range-dependent translation and image-replication artifacts [9]. It is perhaps for these reasons that practical exploitation of this so-called wavefront coding (WC) technique appears to have slowed in recent years.

Attempts have been made to reduce the impact of these phase-induced artifacts: algorithms based on wavelet transforms

have been used to estimate the magnitude of the image-replication artifacts for a single image and to parametrically estimate the optimal kernel for artifact-free image recovery [10]. For practical three-dimensional scenes, however, this requires accurate segmentation of scene components corresponding to objects at different ranges. Mo *et al.* proposed to use a deconvolution kernel based on the average optical PTF over the selected DOF together with a PTF-based optimization technique [11]; however, artifacts remain in simulated recovered images. Similarly, nonlinear filtering instead of the conventional Wiener filter has also succeeded in suppressing artifacts, but not eradicating them [12].

Radially symmetric phase functions have also been proposed for increase of DOF, including quartic and logarithmic phase functions [13] and the logarithmic asphere [14], and these enable recovery of images without phase-induced artifacts but with higher levels of noise amplification than for the antisymmetric functions [15] for reasons that appear to be fundamentally associated with the antisymmetry [7].

We report here theory and experimental results for a generalized technique we call Complementary Kernel Matching (CKM), which exploits the range-dependent translation of two images recorded with dissimilar imaging PSFs obtained from cubic phase functions, followed by inference of defocus and recovery of an image with the correct kernel and hence without translation or image-replication artifacts. By measuring translation, rather than artifact magnitude as used in [10], more robust determination of range is accomplished and furthermore this is achieved on a per-pixel basis, without the need for segmentation of image components. It is, however, necessary to record two images with dissimilar optical modulations and we present methods to achieve this in both time-sequential and snapshot modes.

The CKM technique involves both recovery of an extended-DOF image and simultaneously determination of a depth map. Estimation of a depth map from variations in image quality associated with a range-variant PSF has previously been demonstrated using shape from defocus of a conventional PSF using a sequence of defocused images [16]; Quirin and Piestun proposed a technique to estimate depth from two snapshots taken with two different engineered PSFs [17], where one PSF yields depth information and the other yields an extended-DOF image; Blanchard and Greenaway extracted depth information using a diffractive optical element to generate multiple defocused images on a single camera array and solved the intensity-transport equation to determine depth [18]. When the scene consists of point sources, the form of the PSF is directly measurable and this enables range measurement in particle image velocimetry [19,20] and three-dimensional stochastic optical reconstruction microscopy (STORM) [21,22]. The principle of the CKM technique we describe differs in that it exploits range-dependent translation of image pixels rather than blurring, offers the unique advantages of combining extended DOF with snapshot operation, is inherently achromatic, and is relatively simple to implement.

In the following sections, the theory of CKM is developed, simulation results are presented, and finally, an experimental evaluation of the technique and the obtained results are presented and analyzed. Although we consider here only the cubic function for generation of the encoding function, the principle is expected to be applicable to various other masks. CKM is based on the use of phase masks that produce images exhibiting detectable changes with defocus. The robustness of the technique benefits from the image-domain translation associated with some asymmetric phase functions, such as cubic functions, which is not present for radially symmetric or trefoil phase functions.

2. THEORY AND SIMULATION

Complementary Kernel matching imaging is based on recording two independent images with two phase masks providing complementary PSFs, that is, imaging kernels. We restrict our analysis initially to complex-conjugate pairs of the cubic phase function, ψ and ψ^*, where $\psi = \exp(2\pi i\phi)$ and $\phi = \alpha(x^3 + y^3)$ which, when combined with defocus W_{20}, provides the two pupil functions

$$P^{\pm} = \exp[2\pi i(W_{20}(x^2 + y^2) \pm \phi)], \tag{1}$$

where α determines the strengths of the phase mask and (x, y) are the normalized pupil coordinates. This choice is motivated solely by the fact that the complex conjugate is easily generated by simply rotating the CPM half a revolution in the pupil plane. However, CKM requires only two PSFs which respond differently to defocus, and we present initially only a specific and idealized example of a more general principle. As will be seen, the technique is robust even when P^+ and P^- are not simply related by complex conjugation.

Simple image recovery, using a Wiener filter for example, of the intensity distribution recorded using the phase functions P^+ and P^-, yields images exhibiting both artifacts and translation when the optical defocus W_{20} is dissimilar to the defocus, $\tilde{W}_{20}$, used for the recovery kernel. Translation, ρ, is parallel to the $\xi = \eta$ direction in the image plane and is proportional to $(\tilde{W}_{20}^2 - W_{20}^2)/\alpha$ for the phase function ψ and proportionate to $-(\tilde{W}_{20}^2 - W_{20}^2)/\alpha$ for ψ^* [2,7,9,23]. The value of optical defocus, W_{20}, used to record an image can thus be determined by identifying the matching $\tilde{W}_{20}$ that produces no displacement between the recovered images corresponding to ψ and ψ^*. In these circumstances, recovered images will also be free of phase-error artifacts.

More generally we write $W_{20}(\xi, \eta)$ to indicate that image defocus varies according to the range of scene components, and this leads to a spatially varying shift $\rho(\xi, \eta)$. Estimation of $\rho(\xi, \eta)$, based on a map of the disparity (as used to characterize stereopsis for example) between the images recorded with the phase masks ψ and ψ^* enables determination of a spatially varying $\tilde{W}_{20}(\xi, \eta)$ that enables recovery of an artifact-free image. Furthermore, $\tilde{W}_{20}(\xi, \eta)$ yields an estimate of the depth map of the scene.

If $r_+^{\tilde{W}_{20}, W_{20}}$ and $r_-^{\tilde{W}_{20}, W_{20}}$ are the images restored using the deconvolving PSF corresponding to P^+ and P^-, with uniform

defocus $\tilde{W}_{20}$ and image defocus $W_{20}(\xi,\eta)$, the spatial-shifting properties lead to a disparity between them such that

$$r_{+}^{\tilde{W}_{20},W_{20}}\left(\xi-\frac{\rho(\xi,\eta)}{\sqrt{2}},\eta-\frac{\rho(\xi,\eta)}{\sqrt{2}}\right)=r_{-}^{\tilde{W}_{20},W_{20}}\left(\xi+\frac{\rho(\xi,\eta)}{\sqrt{2}},\eta+\frac{\rho(\xi,\eta)}{\sqrt{2}}\right), \quad (2)$$

where $\rho(\xi,\eta)$ is the scalar value describing a spatially variant displacement of scene components in the $\xi=\eta$ direction according to the mismatch between $\tilde{W}_{20}$ and $W_{20}(\xi,\eta)$. The effect of a spatially variant displacement of the recovered scene is illustrated for a simulated image of a spoke target in Fig. 1, for which $W_{20}(\xi,\eta)$ spatially varies with segment from zero to three waves as the orientations of the segment spokes varies from zero through 2π clockwise. Red arrows indicating disparities in $r_{+}^{\tilde{W}_{20}=0,W_{20}}$ and $r_{-}^{\tilde{W}_{20}=0,W_{20}}$ are superimposed on the recovered images.

Additional to the shifts, phase-mismatch artifacts are apparent from mismatches between W_{20} and $\tilde{W}_{20}$. In consequence, Eq. (2) does not strictly hold. Nevertheless, calculation of the disparity map $2\rho(\xi,\eta)$ is possible since the shift is by far the dominant effect. Conversely, and more interesting, for spatially variant deconvolution with $\tilde{W}_{20}(\xi,\eta)=W_{20}(\xi,\eta)$, $\rho(\xi,\eta)$ vanishes and therefore phase artifacts are not present in Eq. (2). The recovered image is then, in the absence of noise, free of phase-induced artifacts.

Rather than calculating the disparity map which results from the recovery using uniform $\tilde{W}_{20}$, it is more convenient to seek the spatially variant $\tilde{W}_{20}(\xi,\eta)$ that produces a null disparity map, since the artifacts will be suppressed as the solution is approached, that is, we calculate $\tilde{W}_{20}(\xi,\eta)$ that minimizes the difference between $r_{+}^{\tilde{W}_{20},W_{20}(\xi,\eta)}(\xi,\eta)$ and $r_{-}^{\tilde{W}_{20},W_{20}(\xi,\eta)}(\xi,\eta)$. Calculation of $\tilde{W}_{20}$ may be performed on a per-pixel basis, but to improve robustness, evaluation in a small neighborhood of each pixel is desirable to reduce sensitivity to noise. We perform this neighborhood evaluation using a smoothed representation of the difference image

$$\tilde{W}_{20}^{\sigma}(\xi,\eta)=\underset{\tilde{W}_{20}}{\arg\min}\left\{\mathcal{G}_{\sigma}\left[\left(r_{+}^{\tilde{W}_{20},W_{20}}(\xi,\eta)-r_{-}^{\tilde{W}_{20},W_{20}}(\xi,\eta)\right)^{2}\right]\right\}, \quad (3)$$

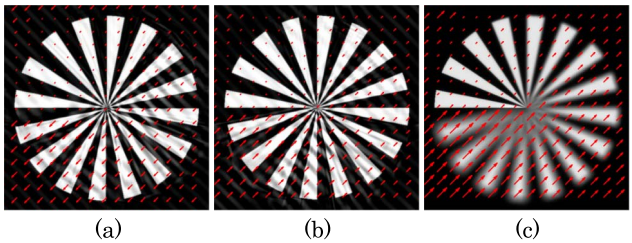

(a) (b) (c)

Fig. 1. Disparity maps. (a) $r_{+}^{\tilde{W}_{20}=0,W_{20}}$ with negative disparity (arrows pointing from upper-right to lower-left corner). (b) $r_{-}^{\tilde{W}_{20}=0,W_{20}}$ with positive disparity (arrows pointing from lower-left to upper-right corner). (c) Resultant disparity, $2\rho(\xi,\eta)$ (i.e., difference in the previous two) superimposed on the conventional image.

where $\mathcal{G}_{\sigma}$ is a Gaussian low-pass filter. The standard deviation σ is a compromise between noise robustness and the size of the response function that tends to segment the image according to $W_{20}(\xi,\eta)$. When $\tilde{W}_{20}^{\sigma}(\xi,\eta)=W_{20}(\xi,\eta)\ \ \forall\ \xi,\eta$, $r_{+}^{\tilde{W}_{20},W_{20}}=r_{-}^{\tilde{W}_{20},W_{20}}$ and each recovered image will be artifact-free. If σ is large, evaluation of Eq. (3) becomes less sensitive to noise and to scene features, but at the expense of lower lateral resolution for detection of spatial changes in defocus; for example, for discriminating between one object in front of another.

We reconstruct the deconvolved image by Wiener filtering based on the spatially varying PSF corresponding to the values of $\tilde{W}_{20}(\xi,\eta)$ that minimize the metric in Eq. (3). We denote this image obtained by $r_{\pm}^{\tilde{W}_{20}^{\sigma}(\xi,\eta),W_{20}(\xi,\eta)}$ to indicate that a neighborhood of size σ is used and to highlight the field dependence on both the imaging and recovery kernels, $W_{20}(\xi,\eta)$ and $\tilde{W}_{20}^{\sigma}(\xi,\eta)$, respectively. In practice, this reconstruction strategy can result in local changes in contrast which manifest as slightly brighter or darker patches in the recovered image. This effect is removed by averaging the images obtained for a range of values of σ. These changes in contrast are quite abrupt and hence introduce nonphysical frequency components beyond the optical cutoff frequency, and these we attenuate using a low-pass filter with negligible effect on the image quality. The final reconstructed image can thus be written as

$$r(\xi,\eta)=\mathcal{F}\left(\sum_{i=1}^{n}\frac{r_{+}^{\tilde{W}_{20}^{\sigma_i}(\xi,\eta),W_{20}(\xi,\eta)}+r_{-}^{\tilde{W}_{20}^{\sigma_i}(\xi,\eta),W_{20}(\xi,\eta)}}{2n},\nu_c\right), \quad (4)$$

where for clarity the ξ,η dependence of r_{+} and r_{-} has been suppressed but is implicit, $\mathcal{F}(\cdot,\nu_c)$ is an ideal low-pass filter, and ν_c is the optical cutoff frequency. Note that reconstruction in Eq. (4) follows from the set of images $r_{+}^{\tilde{W}_{20}^{\sigma_i}(\xi,\eta),W_{20}(\xi,\eta)}$ and $r_{-}^{\tilde{W}_{20}^{\sigma_i}(\xi,\eta),W_{20}(\xi,\eta)}$ calculated using Eq. (3) for a range of n different σ_i values.

Simulation results obtained from the application of this algorithm for the recovery of simulated images are shown in Fig. 2. A reference diffraction-limited image is shown in Fig. 2(a) and blurring by uniform defocus $W_{20}=4$ is shown in Fig. 2(b). The image in Fig. 2(c) is obtained by conventional image recovery with $\tilde{W}_{20}=0$ as typically employed for WC, while the image in Fig. 2(d) was recovered using the CKM method. Detected images included zero-mean, white Gaussian noise with 46 dB signal-to-noise ratio. The variation with $\tilde{W}_{20}$ of the argument of the argmin function in Eq. (3) is depicted in Fig. 2(e), where the minimum indicates the correct detected defocus at $\tilde{W}_{20}=W_{20}=4$. By comparing Figs. 2(c) and 2(d), it is apparent that through CKM, the phase-modulation artifacts that are generally observed in WC image recovery [9] have been eliminated, thus enabling a higher quality, artifact-free recovery to be obtained. Similar results were robustly obtained for a range of scene types and noise levels.

We illustrate the ability to recover images with varying defocus across the field of view in Fig. 3. Conventional in-focus images of a spoke target and fishing boat are shown

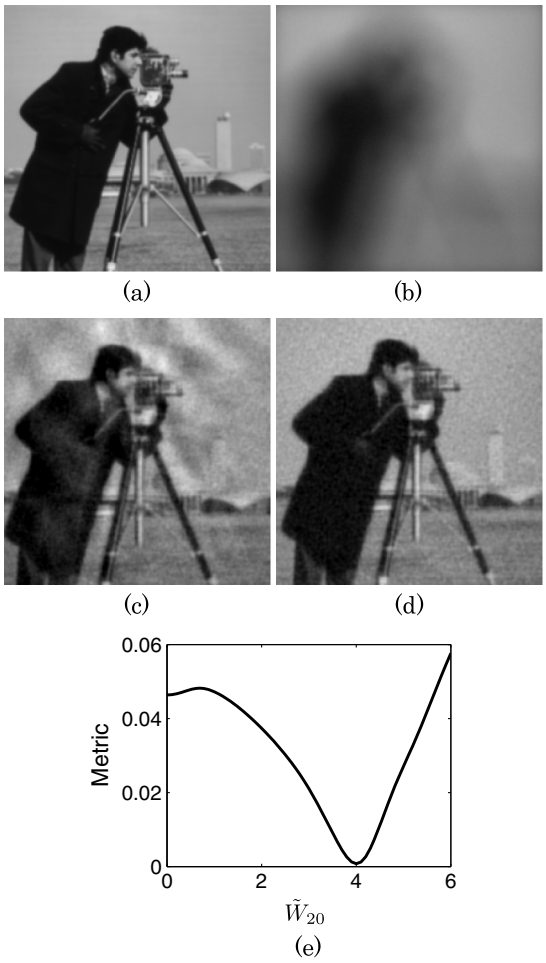

Fig. 2. Uniform four waves of defocus. (a) Diffraction-limited reference. (b) Conventional optics imaging. (c) WC with $\alpha = 5$. (d) CKM with $\alpha = 5$. (e) Calculated metric for defocus detection.

in column (a); simulations of the effects of spatially varying defocus $W_{20}(\xi, \eta)$ for conventional imaging are shown in column (b), where $W_{20}(\xi, \eta)$ varies with orientation of the spokes for the spoke target (as for Fig. 1) and varies linearly with elevation from positive to negative defocus for the fishing boat; conventional image recovery of images recorded with a cubic phase mask and $\tilde{W}_{20} = 0$ is shown in column (c) and with CKM recovery in column (d). The presence of artifacts for conventional WC image recovery and their absence in CKM is clearly evident. Furthermore, the CKM algorithm also yields a defocus map and hence also a range map. Although the raw defocus map $\tilde{W}^{\sigma}_{20}(\xi, \eta)$ can be noisy where regions without texture give rise to ambiguity, restored image are nevertheless free of phase-induced artifacts.

The two images corresponding to ψ and ψ^* can be recorded time-sequentially, for example, by rotating a phase mask through an angle of π, or in a snapshot by using one of the configurations shown in Fig. 4. In Fig. 4(a), the pupil and its conjugate are implemented in two distinct optical paths and using one detector for each image, while in (b) a minor modification enables a single detector array to be used. It is important to note that CKM image recovery involves individual calibration of the PSFs for P^{+} and P^{-}, and hence is unaffected if practical implementations, such as those depicted in Fig. 4, yield two PSFs that do not correspond to the ideal phase conjugation between the two phase functions. This will arise, for example, for small dissimilarities in the aberrations between

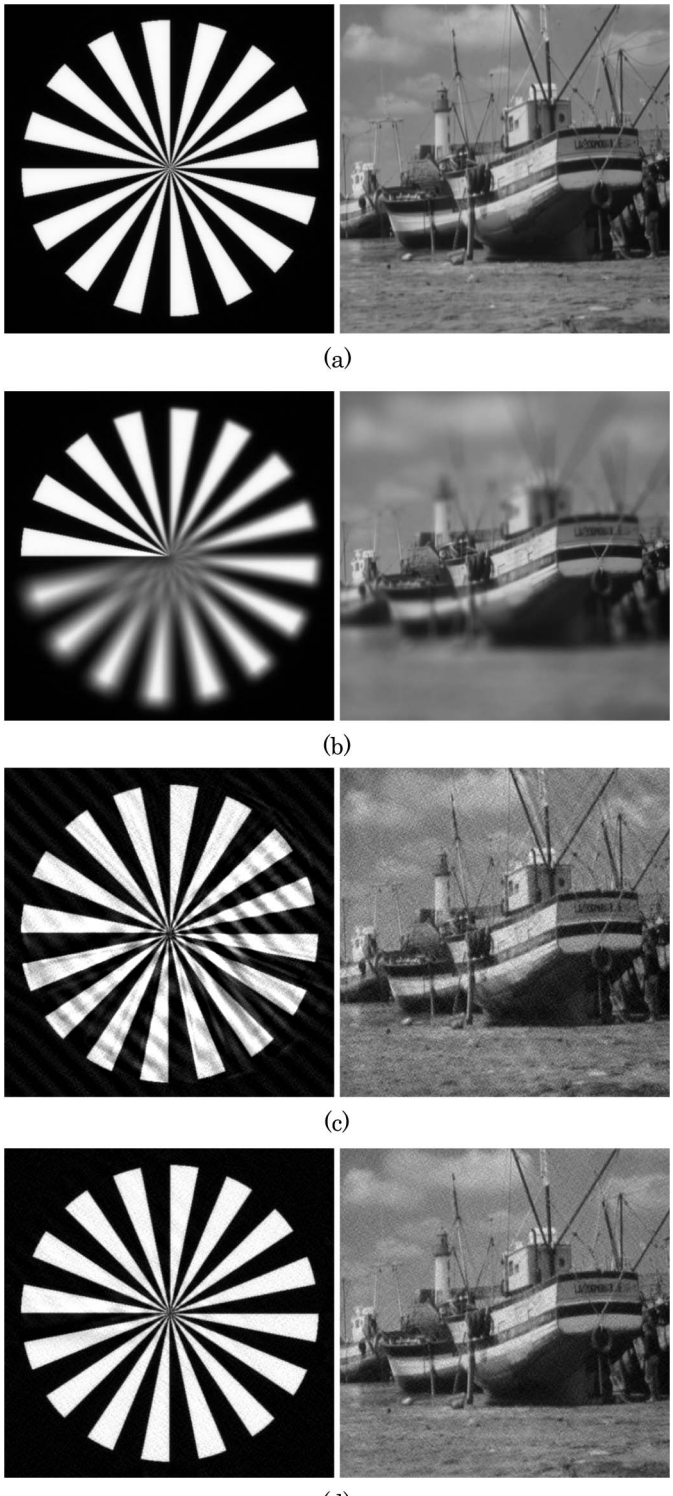

Fig. 3. Images with varying amounts of defocus up to three waves; spoke target shows angular step change in defocus and boat image shows continuous vertical defocus change. (a) Diffraction-limited reference. (b) Conventional optics imaging. (c) WC with $\alpha = 4$. (d) CKM with $\alpha = 4$.

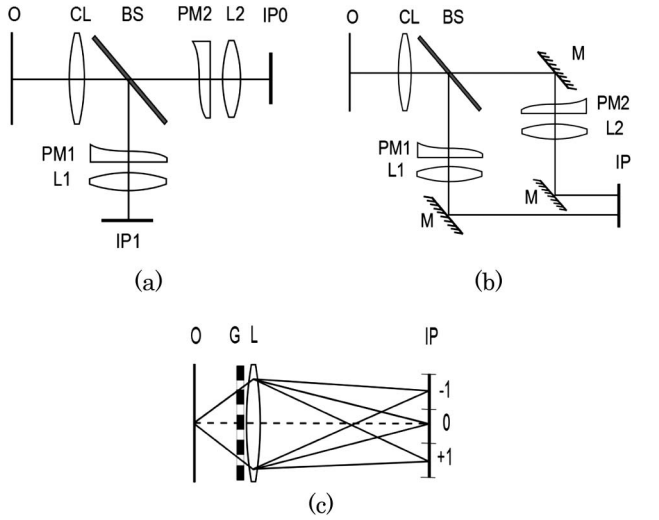

Fig. 4. Possible layouts for a single-snapshot acquisition. (a) Dual-detector system. (b), (c) Single detector systems. O, object; CL, collimating lens; BS, beam splitter; PM, phase mask; L, lens; IP, image plane; M, Mirror; G, Grating.

the imaging systems. Figure 4(c) depicts a scheme similar to that reported by Blanchard and Greenaway for producing conjugate wavefronts [18]: a dislocated grating located in the pupil of an imaging system yields three diffraction orders that are captured by a single imaging detector (the light from higher orders is lost). Encoding of ψ into the grating spatial modulation yields replicated images at the detector encoded with PSFs due to ψ and ψ^* in the $+1$ and -1 diffraction orders. The zero-order image corresponds to a nonmodulated pupil and is not used. The ± 1 diffraction orders thus yield equivalent images to those provided by Figs. 4(a) and 4(b) but with the advantage of a common lens for both images recorded for ψ and ψ^*, thus simplifying the calibration process. This method offers a convenient simultaneous recording of images for ψ and ψ^* phase masks with a single detector array, but is inefficient in its use of light and of detector pixels (the zero order is not used), and in its simplest form requires imaging with narrow-band light, although some achromatization is possible [24].

For our proof-of-concept demonstration, we report here a time-sequential implementation of ψ and ψ^* using a Spatial Light Modulator (SLM) [25], which proves convenient for calibration.

3. EXPERIMENTAL DEMONSTRATION

A. Experimental Setup

We demonstrate the CKM technique using a conventional finite-conjugate imaging configuration employing an SLM to time-sequentially implement the phase functions ψ and ψ^* and indeed the more general phase functions P^+ and P^- that include defocus, W_{20}. This is intended as a proof of principle, and we will report a snapshot implementation in the near future. A mechanical time-sequential implementation is also possible: for example, by rotation of a refractive cubic-phase mask through π radians about the optic axis to switch between ψ and ψ^*; however,

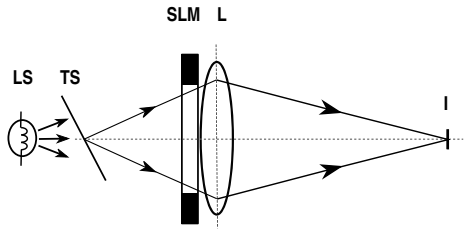

Fig. 5. Experimental setup. L, imaging lens; LS, light source; TS, tilted slide; SLM, spatial light modulator; I, detector.

practical implementation introduces significant error into the measurement of ρ associated with uncertainties in the deviation of the images by the phase mask. Furthermore, accurate calibration of the variation of ρ and PSF with W_{20} based on defocus of the system PSF can be more readily achieved with an SLM than by mechanical defocus of, for example, a pinhole.

The experimental setup is shown in Fig. 5. Using object and image distances of 350 and 1650 mm, an f/15 singlet lens of focal length 300 mm forms an in-focus image with a nominal magnification of approximately 5 on a *Hamamatsu Orca* CCD detector. A polarizer, quarter-wave plate, and analyzer are used with the SLM [25,26], yielding a maximum phase modulation of $3\pi/2$ with total amplitude modulation of <4% using illumination at a wavelength of 543 nm. An iris placed adjacent to the SLM ensures that the SLM is in the aperture stop of the system, so that phase coding is independent of field angle.

As described below, the CKM method is demonstrated for imaging of three-dimensional test targets involving significant defocus. Calibration of the variation of PSF intensity distribution and displacements ρ with W_{20}, as required for accurate image recovery and estimation of $W_{20}(\xi, \eta)$, was achieved by recording the image of a 1 μm pinhole located in the object plane of the imaging system. Two hundred PSFs were recorded for pupil functions P^+ and P^- implemented with the SLM, that is, for encoding functions for ψ and ψ^*, and for defocus varying equidistantly in the range $-3 \le W_{20} \le 3$. The variations of ρ with W_{20}, as determined by correlation of each PSF with the reference (in-focus) PSF for P^+ and P^- together with least-square fits of quadratic functions, are shown in Fig. 6.

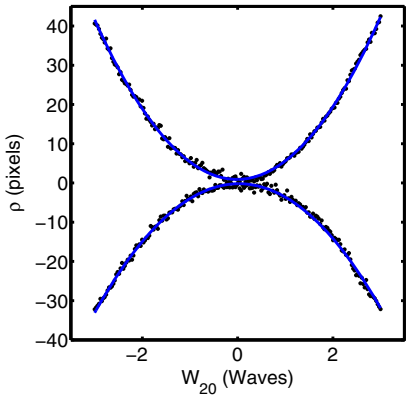

Fig. 6. Calibration process. Measured translation, ρ, against W_{20} for ψ (negative curve) and for ψ^* (positive curve). Fitted quadratic curves shown as blue solid lines and data as black dots.

The quadratic fits were used to improve the estimate of the noise-free PSF position that was subsequently used in image recovery.

The best-fit quadratic functions correspond to an α that is approximately 21% greater for P^+ than for P^-. Measurement with a Shack–Hartman sensor of the phase fronts produced by the SLM yields best-fit cubic wavefronts for P^+ and P^- that correspond to values of α comparable to this measured asymmetry. Although this asymmetry could be removed by a pixel-wise calibration of the SLM phase function, it is more interesting to demonstrate that the technique is robust to such aberrations.

B. Results—Artifact Removal

As a pertinent demonstration of this technique, we present the application of CKM to imaging of microscope slides. Shown in Fig. 7 is an image of a section of the petiole of a leaf and in Fig. 8, a sample of seeds and a pine-leaf section. To provide appreciable range of defocus, the object in Fig. 7(a) was tilted to provide a linear variation in defocus in the vertical direction, and the two samples in Fig. 8(a) were separated by a glass slide of constant thickness. In each case, the defocus is $W_{20} \approx 1.6$.

Figures 7(b) and 8(b) show the corresponding images captured by means of a WC system with $\tilde{W}_{20} = 0$ in the recovery, where the out-of-focus regions of the scene exhibit clear phase-error artifacts. For the images captured and reconstructed with a CKM system shown in Figs. 7(c) and 8(c), however, the artifacts are effectively eliminated, which in turn enables image details to be more readily discerned. In addition, Fig. 8(d) shows the image recovered using a commercial focus-stack algorithm (Helicon focus V5.3) generated using 201 images taken over a defocus range of $-3 \le W_{20} \le 3$ at steps of 0.03 waves. Comparing Figs. 8(c) and 8(d) one can observe that, using just two recorded images, the CKM technique demonstrates comparable image quality to that obtained with the 201-image focus-stack algorithm. In the near future, we will demonstrate this using a single snapshot.

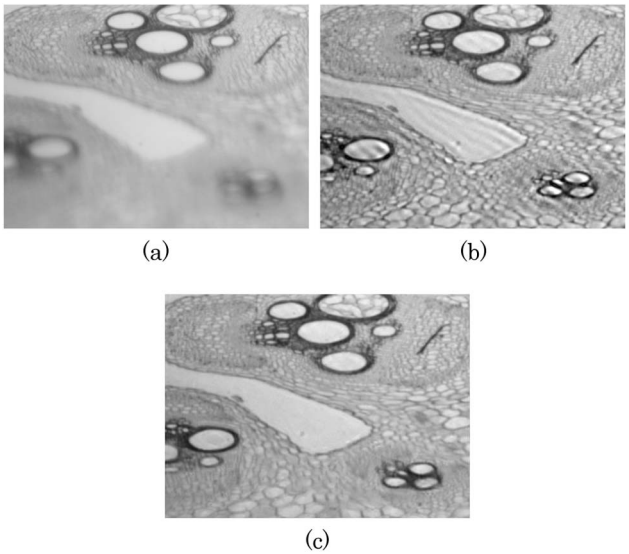

(a) (b) (c)

Fig. 7. Tilted petiole section captured with (a) conventional imaging system, (b) WC system, and (c) CKM system.

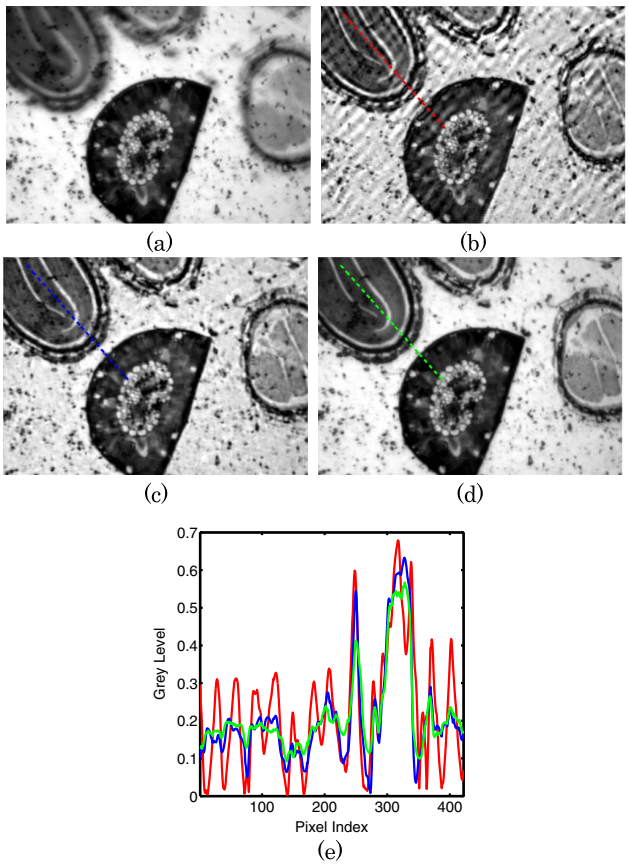

(a) (b) (c) (d) (e)

Fig. 8. Step-defocus pine-leaf section and seeds. (a) Conventional imaging system, (b) WC system, (c) CKM system, and (d) focus stack. (e) Line profile taken along the lines with the corresponding color in (b)–(d). Red is for the WC system, blue is for the CKM system, and green is for the focus stack.

The line plots shown in Fig. 8(e) correspond to a mid-height intensity horizontal profile taken along the dashed lines shown in Figs. 8(b), 8(c), and 8(d). While strong artifactual oscillations are evident on the traditional WC profile, these are absent in the CKM images. The commercial focus-stack reconstruction algorithm employs some form of smoothing which we do not use in the CKM recovery, as can be observed by comparing Figs. 8(d) to 8(c). This explains why some peaks are shallower than the corresponding peaks in the CKM recovery.

C. Results—Depth Estimation

As stated previously, the CKM technique involves evaluation of defocus in a small region of an image so that it is possible to reconstruct a scene in 3D provided sufficient texture is present. We assessed the use of CKM image reconstruction for three-dimensional ranging by imaging a calibration target consisting of a regularly spaced array of disks tilted at an angle of approximately 65° with respect to the nominal image plane, introducing defocus of $0.3 \le W_{20} \le 2.0$. Images of the calibration target captured with a conventional imaging system, WC system, and CKM system are shown in Figs. 9(a), 9(b), and 9(c), respectively.

To reconstruct the scene in three dimensions, the defocus map was averaged over the region of each disk, and textureless

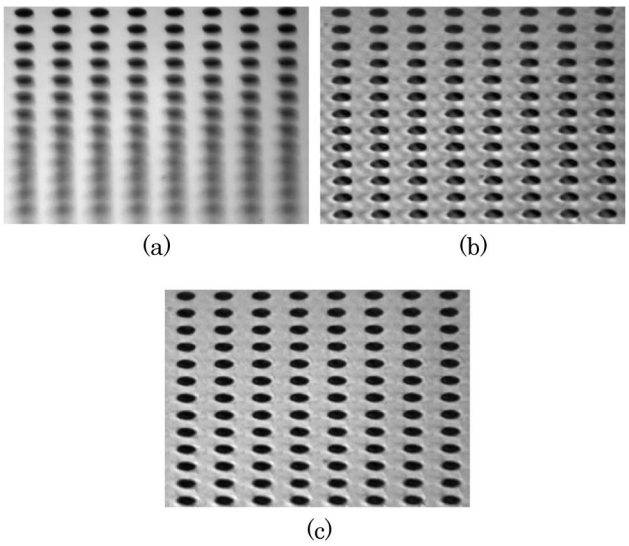

Fig. 9. Tilted distortion target captured with (a) conventional imaging system, (b) WC system, and (c) CKM system.

areas which do not provide defocus information were masked. The calibration target was aligned such that there is effectively uniform defocus along each row of disks and a linear variation in defocus along each column. A ground truth slope was calculated by centroiding several disks and taking the ratio between their average horizontal to vertical separation. This was found to be 1.976 ± 0.002, that is, approximately $\tan(65°)$ as expected.

Measurements of the range of each disk using the snapshot CKM measurement of defocus and based on a time-sequentially recorded focus stack were performed. For the focus-stack measurement, an image-sharpness criterion was used to select the plane of best focus, as the SLM was used to vary the focus of the image in steps of 0.03 waves. The range of each disk as computed by both the CKM and the focus stack are shown plotted in Fig. 10(b). Additionally, for illustration purposes, a three-dimensional reconstruction of the calibration target as computed by the CKM method is shown in Fig. 10(a).

The gradients of the least-square linear fits are 2.00 ± 0.01 for the CKM technique and 1.95 ± 0.02 for the focus-stack measurement. That is, the CKM measurement is 1.2% greater than the ground truth while the focus-stack measurement is 1.3% smaller. These results suggest that the ranging accuracy of CKM is comparable to the accuracy for focus stacking. For this specific target, the uncertainty in range for the CKM technique is 40 μm, which corresponds to an uncertainty in W_{20} of 0.036 waves of defocus (slightly larger than the quantization step) and to 1.84% of the depth range. The corresponding uncertainty for the focus stack was found to be approximately twice as much. If implemented on a typical microscope with a numerical aperture of 0.65 and a typical DOF of 1 μm, this would correspond to a depth resolution of approximately 5% of the conventional DOF for the CKM and 10% for the focus stack. This implies that the performance of CKM is comparable to that of a focus stack. We therefore conclude that the CKM technique can be employed to capture three-dimensional range-resolved images with extended DOF using

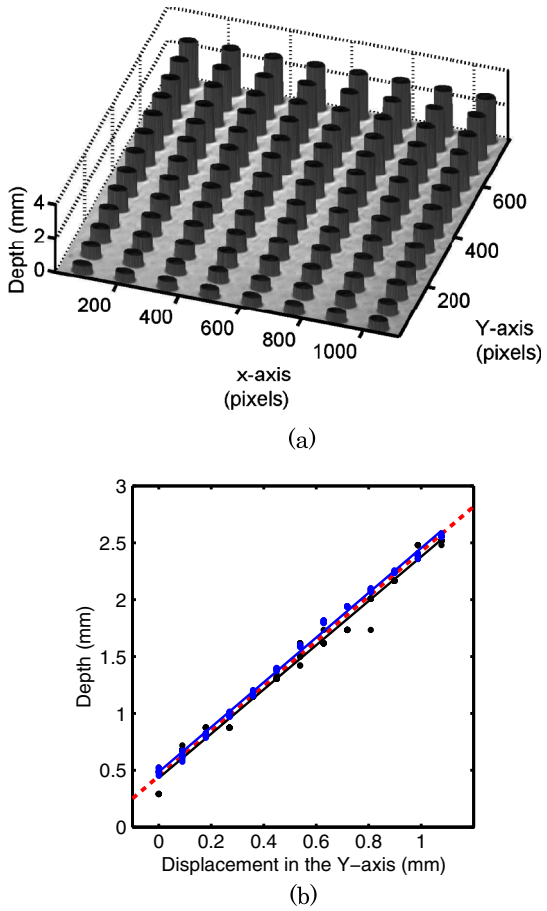

Fig. 10. Tilted distortion target. (a) 3D reconstruction. (b) Slope estimate by CKM (blue curve), slope estimate by focus stacking (black curve), and ground truth slope (red broken line).

just two data acquisitions and, in principle, using one of the techniques shown in Fig. 4 in a single snapshot. This is pertinent to a wide range of time-resolved imaging applications, including extended DOF microscopy or particle image velocimetry [19].

4. CONCLUSIONS

We report to our knowledge the first demonstration of artifact-free, extended-DOF imaging with simultaneous ranging using hybrid-imaging techniques. In previously reported approaches to hybrid imaging, a range of phase functions have been reported that tend to fall into two classes: either the antisymmetric cubic and trefoil masks (or qualitatively similar shapes) or symmetric masks [14,13], and these provide complementary advantages. While the former offers a superior trade-off between enhanced DOF and noise amplification [15], the spatial-phase effects introduced by the asymmetry introduce highly problematic artifacts and also range-dependent image shifts [9] that are absent for symmetric phase functions. Here we demonstrate that, by recording images with complementary OTF characteristics, it is possible to benefit from the enhanced DOF of an antisymmetric mask but without introducing image artifacts, and combined with the enhancement of three-dimensional ranging. This so-called complementary

kernel imaging constitutes a new paradigm for hybrid imaging that builds on the early use of multiple kernels by Hausler [1]. As reported here, CKM exploits translation of the PSF with defocus, and this translation provides robust image recovery. Translation does not occur with the radially symmetric phase masks [14,13] or the trefoil mask [4]; however, the presence of defocus-related phase-induced image artifacts for the trefoil and other masks does suggest CKM is applicable provided the image recovery is sensitive to defocus. In this case, CKM would not rely on translation but on a distortion and blurring combination. Indeed, two different phase mask types might be implemented, benefiting from complementary advantages.

The CKM method has been verified both by simulation and by experiment. Simulation results show suppression of restoration artifacts even at relatively low signal-to-noise ratios. Experimental results show that high-quality, artifact-free images can be obtained even for large defocus. In addition, CKM provides a means of 3D image reconstruction and, following proper calibration, range measurement. Future work will transfer this technique to high-numerical-aperture imaging, use of broadband refractive phase masks, and snapshot operation.

FUNDING INFORMATION

Engineering and Physical Sciences Research Council (EPSRC) (EP/K503058/1).

REFERENCES

1. G. Hausler, "A method to increase the depth of focus by two step image processing," Opt. Commun. **6**, 38–42 (1972).
2. J. Edward, R. Dowski, and W. T. Cathey, "Extended depth of field through wave-front coding," Appl. Opt. **34**, 1859–1866 (1995).
3. S. Bradburn, W. T. Cathey, and E. R. Dowski, "Realizations of focus invariance in optical–digital systems with wave-front coding," Appl. Opt. **36**, 9157–9166 (1997).
4. S. Prasad, T. C. Torgersen, V. P. Pauca, R. J. Plemmons, and J. van der Gracht, "Engineering the pupil phase to improve image quality," Proc. SPIE **5108**, 1–12 (2003).
5. M. Demenikov, E. Findlay, and A. R. Harvey, "Miniaturization of zoom lenses with a single moving element," Opt. Express **17**, 6118–6127 (2009).
6. G. Muyo, A. Singh, M. Andersson, D. Huckridge, A. Wood, and A. R. Harvey, "Infrared imaging with a wavefront-coded singlet lens," Opt. Express **17**, 21118–21123 (2009).
7. G. Muyo and A. R. Harvey, "Decomposition of the optical transfer function: wavefront coding imaging systems," Opt. Lett. **30**, 2715–2717 (2005).
8. M. Somayaji, V. R. Bhakta, and M. P. Christensen, "Experimental evidence of the theoretical spatial frequency response of cubic phase mask wavefront coding imaging systems," Opt. Express **20**, 1878–1895 (2012).
9. M. Demenikov and A. R. Harvey, "Image artifacts in hybrid imaging systems with a cubic phase mask," Opt. Express **18**, 8207–8212 (2010).
10. M. Demenikov and A. R. Harvey, "Parametric blind-deconvolution algorithm to remove image artifacts in hybrid imaging systems," Opt. Express **18**, 18035–18040 (2010).
11. X. Mo and J. Wang, "Phase transfer function based method to alleviate image artifacts in wavefront coding imaging system," Proc. SPIE **8907**, 89074H (2013).
12. R. N. Zahreddine, R. H. Cormack, and C. J. Cogswell, "Noise removal in extended depth of field microscope images through nonlinear signal processing," Appl. Opt. **52**, D1–D11 (2013).
13. S. Mezouari and A. R. Harvey, "Phase pupil functions for reduction of defocus and spherical aberrations," Opt. Lett. **28**, 771–773 (2003).
14. N. George and W. Chi, "Extended depth of field using a logarithmic asphere," J. Opt. A **5**, S157–S163 (2003).
15. T. Vettenburg, N. Bustin, and A. R. Harvey, "Fidelity optimization for aberration-tolerant hybrid imaging systems," Opt. Express **18**, 9220–9228 (2010).
16. P. Favaro and S. Soatto, "A geometric approach to shape from defocus," IEEE Trans. Pattern Anal. Mach. Intell. **27**, 406–417 (2005).
17. S. Quirin and R. Piestun, "Depth estimation and image recovery using broadband, incoherent illumination with engineered point spread," Appl. Opt. **52**, A367–A376 (2013).
18. P. M. Blanchard and A. H. Greenaway, "Simultaneous multiplane imaging with a distorted diffraction grating," Appl. Opt. **38**, 6692–6699 (1999).
19. A. K. Prasad, "Stereoscopic particle image velocimetry," Exp. Fluids **29**, 103–116 (2000).
20. F. Pereira and M. Gharib, "Defocusing digital particle image velocimetry and the three-dimensional characterization of two-phase flows," Meas. Sci. Technol. **13**, 683–694 (2002).
21. B. Huang, W. Wang, M. Bates, and X. Zhuang, "Three-dimensional super-resolution imaging by stochastic optical reconstruction microscopy," Science **319**, 810–813 (2008).
22. J. He, X. Zhuang, S. A. Jones, and S.-H. Shim, "Fast, three-dimensional super-resolution imaging of live cells," Nat. Methods **8**, 499–505 (2011).
23. G. Carles, "Analysis of the cubic-phase wavefront-coding function: physical insight and selection of optimal coding strength," Opt. Lasers Eng. **50**, 1377–1382 (2012).
24. Y. Feng, P. A. Dalgarno, D. Lee, Y. Yang, R. R. Thomson, and A. H. Greenaway, "Chromatically-corrected, high-efficiency, multi-colour, multi-plane 3D imaging," Opt. Express **20**, 20705–20714 (2012).
25. G. Carles, G. Muyo, S. Bosch, and A. Harvey, "Use of a spatial light modulator as an adaptable phase mask for wavefront coding," J. Mod. Opt. **57**, 893–900 (2010).
26. B. Das, S. Vyas, J. Joseph, P. Senthilkumaran, and K. Singh, "Transmission type twisted nematic liquid crystal display for three gray-level phase-modulated holographic data storage systems," Opt. Lasers Eng. **47**, 1150–1159 (2009).

Research Article Vol. 1, No. 4 / October 2014 / Optica 217

Multiview optical resolution photoacoustic microscopy

Liren Zhu,[1,†] Lei Li,[1,2,†] Liang Gao,[1] and Lihong V. Wang[1,*]

[1]Optical Imaging Laboratory, Department of Biomedical Engineering, Washington University in St. Louis, St. Louis, Missouri 63130, USA

[2]Department of Electrical and System Engineering, Washington University in St. Louis, St. Louis, Missouri 63130, USA

*Corresponding author: lhwang@biomed.wustl.edu

Received 27 June 2014; revised 26 August 2014; accepted 26 August 2014 (Doc. ID 214941); published 29 September 2014

Optical resolution photoacoustic microscopy (OR-PAM), while providing high lateral resolution, has been limited by its relatively poor acoustically determined axial resolution. Although this limitation has been tackled in recent works by using either broadband acoustic detection or nonlinear photoacoustic effects, a flexible solution with three-dimensional optical resolution in reflection mode remains desired. Herein we present a multiview OR-PAM technique. By imaging the sample from multiple view angles and reconstructing the data using a multiview deconvolution method, we have experimentally demonstrated an isotropic optical resolution in three dimensions.

OCIS codes: (170.3880) Medical and biological imaging; (170.5120) Photoacoustic imaging; (180.6900) Three-dimensional microscopy; (100.1830) Deconvolution.

http://dx.doi.org/10.1364/OPTICA.1.000217

1. INTRODUCTION

Small and quasi-transparent model organisms, such as zebrafish and Drosophila embryos, are widely used in developmental biology [1] and neurophysiology [2]. Due to their significance, many efforts have recently been made in imaging these small model animals with photoacoustic microscopy [3,4]. Optical resolution photoacoustic microscopy (OR-PAM) provides high-resolution images of biological samples with various endogenous or exogenous contrasts [5–7]. Although the high lateral resolution and label-free imaging capability makes OR-PAM an appealing choice, its relatively poor axial resolution has limited its applications.

Conventional OR-PAM systems achieve optical resolution by focusing light within the acoustic focal zone, providing down to submicrometer level lateral resolution [8]. However, optical focusing cannot provide adequate axial resolution in most practical cases [9]. OR-PAM relies on time-of-flight detection of acoustic signals to provide axial resolution. The acoustically determined axial resolution is limited by the bandwidth of the acoustic detection, and the typical value is usually around tens of micrometers [10], an order of magnitude worse than the lateral resolution. Many works have focused on enhancing the axial resolution of OR-PAM. Improved acoustic temporal resolution has been reported through the use of broadband detectors, such as high-frequency transducers [10] and optical ultrasound detectors [11]. However, these methods require custom designed hardware, and suffer from the severe attenuation of high-frequency ultrasonic waves in biological tissue and coupling media, limiting the imaging depth and the working distance. Meanwhile, optical sectioning has been achieved in OR-PAM through photoacoustic nonlinearity [12,13]. However, in these optically sectioned PAM techniques, because depth scanning is required to acquire A-line signals, the imaging speed is reduced.

In this article, we propose to improve resolution isotropy and to provide optical resolution in three dimensions (3D) by imaging the sample from multiple view angles and numerically integrating the information acquired from each angle. Multiview deconvolution has been proven effective in other optical imaging modalities, particularly in light-sheet fluorescence microscopy (LSFM) [14,15]. By introducing the multiview imaging approach into OR-PAM, we developed multiview optical resolution photoacoustic microscopy (MV-OR-PAM) and have achieved optical-diffraction-limited resolution in 3D.

2. THEORY AND SIMULATION

In a conventional OR-PAM system, a 3D image of an object is blurred by the effects of both diffraction-limited optical focusing and bandwidth-limited acoustic detection. Here the effect of acoustic focusing in the lateral direction is negligible due to the fact that the dimension of the acoustic focal spot of a typical focused transducer is usually much larger than that of the optical focal spot. Additionally, along the axial direction within the acoustic focal zone, the acoustic detection in OR-PAM is linear and shift-invariant [10]. Mathematically, denoting $f(\mathbf{r}, z)$ as the object function we want to image, $g_o(\mathbf{r}, z)$ as the optical fluence distribution, $g_a(\mathbf{r}, z)$ as the impulse response of the transducer, and $I(\mathbf{r}, z)$ as the final 3D image in acoustic pressure before taking the envelopes of the received photoacoustic signals, the image formation can be described as

$$I(\mathbf{r}, z) = [f(\mathbf{r}, z) *_{\mathbf{r}} g_o(\mathbf{r}, z)] *_z g_a(z). \quad (1)$$

Here, $\mathbf{r}$ is a vector representing two-dimensional (2D) coordinates (x, y), z is the coordinate along the axial direction, $*_{\mathbf{r}}$ denotes the 2D convolution in the lateral directions, and $*_z$ denotes convolution along the z direction. Assuming the optical fluence along the axial direction within the optical depth of focus is uniform, the concatenating convolutions in the lateral and axial directions become a 3D convolution,

$$I(\mathbf{r}, z) = f(\mathbf{r}, z) * g(\mathbf{r}, z), \quad (2)$$

where $g(\mathbf{r}, z)$ is the overall 3D point spread function (PSF) of the system and $g(\mathbf{r}, z) = g_o(\mathbf{r}, z = z_f) \cdot g_a(z)$. Here z_f is the depth of the focal plane. In a conventional OR-PAM system, the lab coordinate system is identical to the local-coordinate system attached to the sample. In MV-OR-PAM, a sequence of low-axial-resolution 3D images is acquired at different view angles by rotating the sample as illustrated in Figs. 1(a) and 1(b). In the local-coordinate system attached to the sample, the acoustically defined, low-resolution axis varies with the view angle. Therefore, the 3D image in each view is blurred by a local-coordinate PSF transformed from the original global-coordinate PSF, $g(\mathbf{r}, z)$. Hereafter, we denote $(\mathbf{r}, z)$ as the coordinates in the local system and $(\mathbf{r}_0, z_0)$ as the coordinates in the lab system. Provided that the transforms from the lab coordinate system at each view v to the local-coordinate system, T_v, and the original untransformed PSF, $g(\mathbf{r}, z)$, are known *a priori*, a multiview imaging problem can be formulated as

$$I_v(\mathbf{r}, z) = f(\mathbf{r}, z) * T_v\{g(\mathbf{r}_0, z_0)\}(\mathbf{r}, z). \quad (3)$$

Here, $I_v(\mathbf{r}, z)$ is the measurement at view v. The underlying object function $f(\mathbf{r}, z)$ can be recovered with multiview deconvolution methods. The multiview extension of the Lucy–Richardson algorithm is chosen for its simplicity and performance demonstrated in other optical imaging modalities [16,17].

We simulated the principle of MV-OR-PAM, with the results shown in Fig. 1. Two point targets were placed 2 μm apart along the z axis and imaged at angle 0° [Fig. 1(a)].

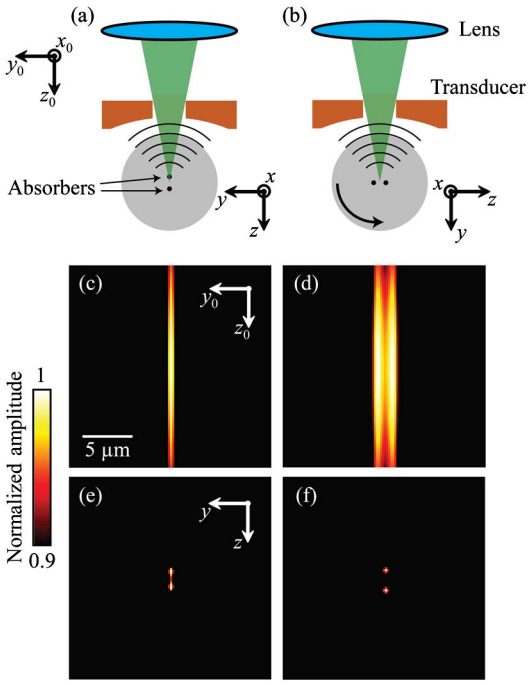

Fig. 1. Principle and simulation of MV-OR-PAM. (a) Imaging two closely located (2 μm apart) point absorbers at angle 0° when the lab coordinate system is identical to the sample's local-coordinate system. (b) Rotate the sample by 90° and image it again. Notice the orientations of the absorbers and the local system are changed. (c), (d) Acquired images from (a) and (b) under the global-coordinate system. (e) Reconstructed image using MV-OR-PAM under the local-coordinate system. (f) Ground truth image (blurred for display) of the two absorbers.

The entire object was then rotated 90° around the x axis and imaged again [Fig. 1(b)]. At each view angle, the object was first convolved in the x, y directions with a 3D Gaussian illumination function that has full widths at half-maximum (FWHMs) of 2.0 μm × 2.0 μm × 57.0 μm. The resultant 3D volume was then convolved with a typical ultrasound transducer's impulse response, which is a Gaussian derivative function in the z direction, with a FWHM of 50.0 μm. We then took the envelope on each A-line to form single-view images at angle 0° [Fig. 1(c)] and angle 90° [Fig. 1(d)]. The final reconstructed image [Fig. 1(e)] was calculated by applying the independent multiview Lucy–Richardson algorithm [15] on these two volumes over 15 iterations. Compared to the ground truth image [Fig. 1(f)], the signals from the two point sources originally mixed together in the upright view become resolvable in the reconstructed image. This indicates that MV-OR-PAM is able to recover the information missing in one view by integrating information from another view. Although envelope extraction, strictly speaking, violates the linearity of deconvolution, our analysis revealed that it is still a good approximation when measurements from multiple view angles are used and the PSF is much wider along the depth direction than the lateral directions (see Appendix A).

We also studied the effect of the number of views on the improvement of axial resolution and resolution isotropy through simulation. Different numbers of views were equally spaced within a 180° range. A point target located on the focal

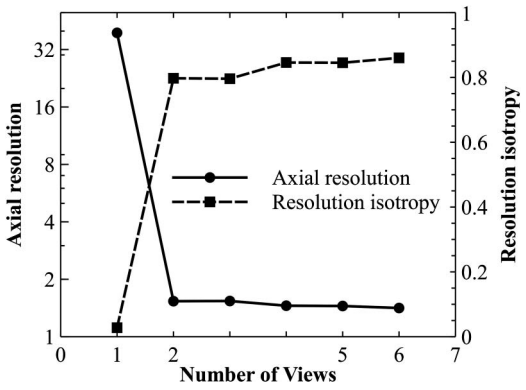

Fig. 2. Simulating the effect of the number of views on axial resolution and resolution isotropy. Views were spaced evenly within a 180° angle. Notice the left y axis is log scaled.

plane was imaged. The reconstructed B-scans were fitted to a 2D elliptical Gaussian function. The FWHMs of the major and minor axes were measured as resolution values. The resolution isotropy was quantified as the ratio between the resolution values along the minor axis and the major axis. The results are shown in Fig. 2. Both axial resolution and resolution isotropy are significantly improved when the first additional view is added, but further increases in the number of views result in a diminished advantage. In a practical situation, however, the inclusion of more views will increase the overall signal-to-noise ratio (SNR) at the expense of data acquisition speed.

3. EXPERIMENTAL SETUP AND METHODS

In order to experimentally validate MV-OR-PAM, we constructed an OR-PAM system with a subsystem that can rotate the sample during imaging. The original OR-PAM system has been detailed in [18]. Briefly, the system (Fig. 3) employs a 532 nm pulsed laser (SPOT-10-200-532, Elforlight). After attenuation by a variable neutral density filter, the laser beam was focused by a lens with a focal length of 200.0 mm. The focused light is spatially filtered by a 50-μm-diameter pinhole (P50C, Thorlabs) and coupled into a single-mode optical fiber through a fiber coupler. The fiber output is collimated by a doublet (F.L. = 25.0 mm, AC127-025-A, Thorlabs) and then focused by another identical doublet. A compensation lens (F.L. = 100.0 mm, LA1207-A, Thorlabs) corrects for water immersion, and a ring transducer (35 MHz center frequency, 25 MHz bandwidth) detects PA signals. The lateral resolution of the system is limited by the effective numerical aperture of the optical system and has been experimentally quantified as 2.6 μm [18].

Prior to imaging, the object to be imaged was immobilized in 3% agar gel and mounted in a sample holding tube. As shown in Fig. 3, the tube is connected to a rotating shaft driven by a stepper motor. The shaft passes through a spring-loaded PTFE seal (13125K68, McMaster-Carr) to ensure water tightness and is supported by several bearings. A 2D raster scan along the x and y directions was performed at each view angle. Then, the sample was rotated by a preset angle around the x

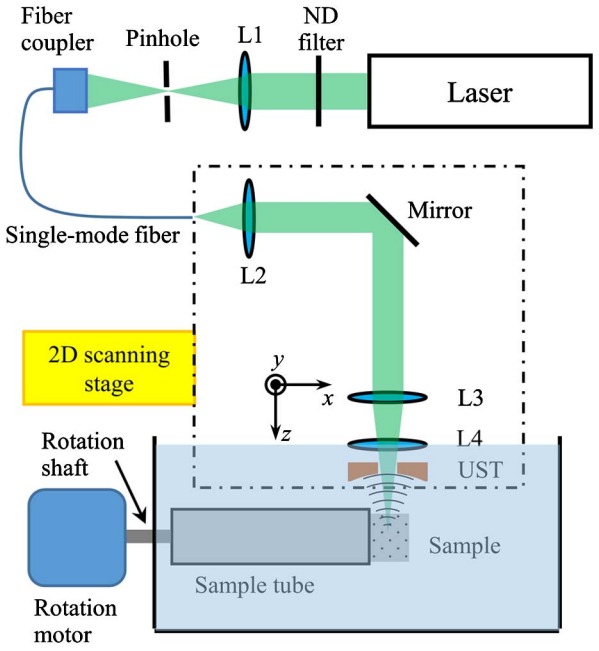

Fig. 3. Schematic of the MV-OR-PAM system. L1, condenser lens; L2, fiber collimator lens; L3, objective lens; L4, compensation lens; UST, ultrasound transducer. Both optical and acoustic axes are along the z direction under the lab coordinate system, and the rotation axis is along the x direction of the lab coordinate system.

axis and scanned again. Each 2D scan generated a 3D dataset with an optical-diffraction-limited lateral resolution and an acoustic-bandwidth-determined axial resolution.

Before reconstruction, we coregistered the 3D datasets acquired from different view angles to the local-coordinate system of the sample. Subresolution absorbing beads (silanized iron oxide beads, 2 μm average diameter, Thermo Scientific) were uniformly mixed in agar as registration markers. The beads were segmented and localized using an algorithm modified from that described in [19], and the parameters were optimized empirically by matching the number of segmented beads per unit volume with the expected number concentration of the suspension. To ensure reliable segmentation, high-frequency noises in the images were suppressed with a 2D Gaussian filter with an isotropic standard deviation of 2.55 μm along the lateral directions. The beads were then segmented using a difference-of-Gaussians filter with standard deviations of 6.25 and 7.38 μm. Local minima in the 3.75 μm × 3.75 μm × 3.75 μm neighborhood were considered as beads, and their positions were extracted by fitting a 3D quadratic function to this neighborhood in the original 3D image. The bead locations were then processed to generate a 3D affine transform from each view to the first view. After successful coregistration, the reconstruction was performed using an independent multiview Lucy–Richardson algorithm [15]. Bead images with a lateral FWHM close to 2.6 μm (the experimentally quantified resolution value) were considered as good estimations of the 3D PSF of the system and were normalized and averaged to be the PSF used in the reconstruction algorithm. Furthermore, we applied Tikhonov

regularization (regularization parameter = 0.006) to account for noises in the images [20].

4. RESULTS AND DISCUSSION

We imaged the subresolution beads to quantify the improvement of resolution isotropy in MV-OR-PAM. 3D images were acquired at two views 50° apart, and then coregistered and reconstructed with 15 iterations. The B-scan images of a single bead from conventional, single-view OR-PAM and MV-OR-PAM are shown in Figs. 4(a) and 4(b). Figure 4(c) shows the overlap of the two views. In Figs. 4(d) and 4(e), the data points extracted from Figs. 4(a) and 4(b) were fitted with normalized Gaussian functions. We then quantified resolutions based on the FWHM of these Gaussian functions. The lateral resolutions of the single-view image and reconstructed image were estimated as 2.6 and 2.0 μm, respectively. This slight improvement in lateral resolution is due to the deconvolution of the reconstruction algorithm. The axial resolutions, defined along the worst-resolution axis, were 42.2 and 4.7 μm for the single-view image and the reconstructed image, respectively. Thus we achieved a nine-fold improvement in axial resolution. Resolution isotropy, quantified as the ratio between the best-axis resolution and worst-axis resolution, was improved by a factor of 7 (from 0.060 to 0.41). Figures 4(f) and 4(g) and Media 1 show volumetric renderings of both the single-view OR-PAM image and the image acquired by MV-OR-PAM.

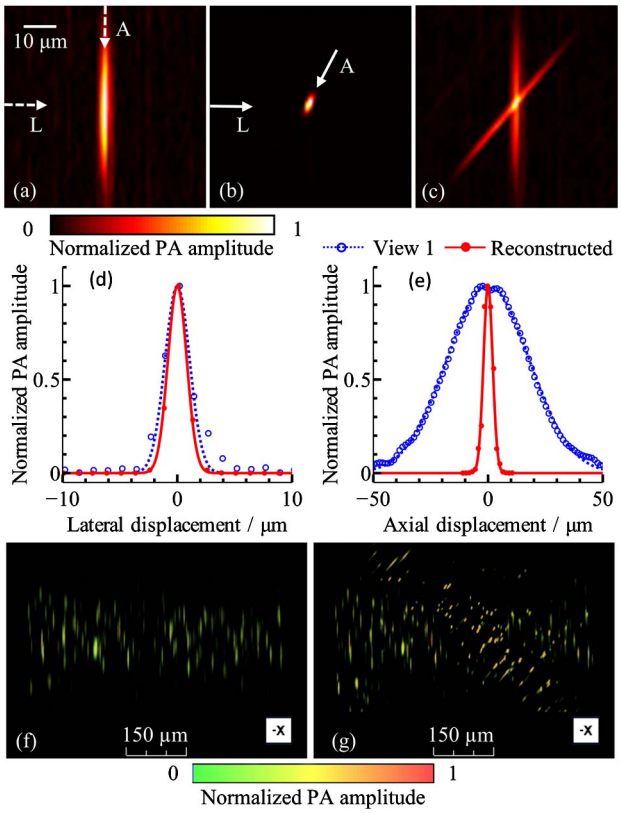

Fig. 4. Quantification of improvement of axial resolution and resolution isotropy. Image slices perpendicular to rotation axis (original B-scan plane) from (a) single-view and (b) reconstructed 3D volume data. (c) Arithmetic fusion of the two views at the same area as in (a) and (b), showing overlap between the two views. (d) Lateral line profiles from single-view and reconstructed volume, indicated by the horizontal arrows marked as "L" in panels (a) and (b). (e) Axial line profiles extracted along the depth direction from single-view image (a) and along the worst-resolution direction from the reconstructed image (b), both marked as "A". (f), (g) Volumetric rendering of single-view dataset and reconstructed dataset. See Media 1 for a full view angle rendering of these two datasets.

To further validate MV-OR-PAM in biological imaging applications, we imaged a wild-type zebrafish embryo six days postfertilization (dpf) *ex vivo*. Zebrafish husbandry was described in our previous work [21]. All animal work was performed in compliance with Washington University's institutional animal protocols. Before imaging, the embryo was anaesthetized with tricaine and fixed with 4% paraformaldehyde (PFA) and 1X phosphate buffered saline (PBS). Two images were acquired with angles approximately 90° apart, with a field of view (FOV) of 0.5 mm by 3.0 mm and a step size of 2.5 μm for both the x and y directions. The sample was rotated with respect to the x axis in the local-coordinate system.

Figures 5(a) and 5(b) show the maximum amplitude projections along the y axis of the single-view image at angle 0° and

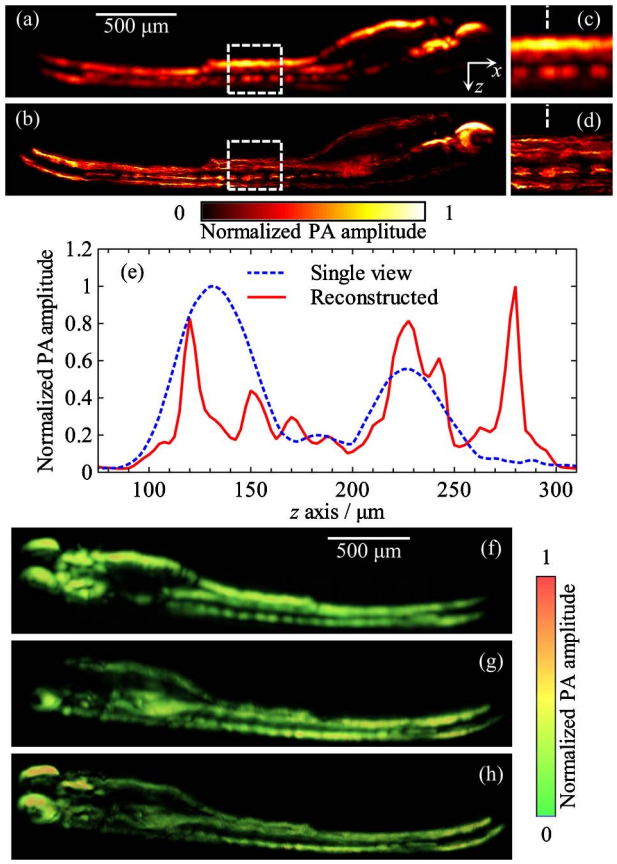

Fig. 5. Single-view and reconstructed images of zebrafish *ex vivo*. (a), (b) MAP images along the y axis of the single-view image at 0° and the reconstructed image of MV-OR-PAM, respectively. (c), (d) Close-up of the region marked by the white, dashed boxes from panels (a) and (b), respectively. (e) Signal profiles along the white, dashed lines in panels (c) and (d). (f), (g) Volumetric rendering of the two single-view images at 0° and 90°, respectively. (h) Volumetric rendering of the reconstructed image from the same angle as in (f) and (g). See Media 2 for a full view angle rendering of these three datasets.

the reconstructed image, respectively. Figures 5(c) and 5(d) show the corresponding close-up features within the white dashed boxes. Figure 5(e) shows the signal amplitudes along the white dashed lines in Figs. 5(c) and 5(d). Because the z axis is the depth direction, features along this direction are severely blurred in both single-view images, Figs. 5(a) and 5(c). However, they can be easily discriminated in the reconstructed images, Figs. 5(b) and 5(d). In addition, the PA signals are weak at the bottom of the embryo in the single-view image [Fig. 5(a)] because upper structures absorb most of the laser energy. In contrast, these signals are recovered in the reconstructed image [Fig. 5(b)]. Figures 5(f)–5(h) and Media 2 show volumetric renderings of two single-view 3D images and the reconstructed 3D image, respectively. Compared with either single-view image, the reconstructed image shows significant improvement in spatial resolution and information completeness.

A previous study demonstrated that one-dimensional deconvolution along the depth direction can also improve axial resolution and resolution isotropy by a factor of two in OR-PAM [10]. Compared with this approach, MV-OR-PAM has achieved greater improvements in axial resolution (nine-fold) and resolution isotropy (seven-fold). This is because the complementary information provided by additional views facilitates solving the ill-posed deconvolution problem [15,22]. Furthermore, previous studies also show that the introduction of additional views can significantly reduce the computational cost [14,15].

Making use of the flexibility of fiber delivery, instead of rotating the sample, rotating the imaging head would be a straightforward next step, which will make MV-OR-PAM available for more biological applications, such as high-resolution functional brain imaging and tumor model study in mouse brains and ears. Since we have demonstrated that two views are enough to achieve adequate resolution improvement, another option is to employ a dual-axis design, as in Ref. [13], with two near-orthogonal optical and acoustic paths. In both cases, the spatial transforms between images acquired at each view angle can be calibrated beforehand, and the reconstruction procedure is directly applicable.

5. CONCLUSION

To summarize, we have developed MV-OR-PAM with improved axial resolution and resolution isotropy, and we have demonstrated this technique by imaging a subresolution microsphere phantom and a 6 dpf zebrafish embryo *ex vivo*. An optical resolution of 4.7 μm was experimentally quantified in 3D. Compared with the acoustically determined value in conventional OR-PAM, a nine-fold improvement in axial resolution and a seven-fold improvement in resolution isotropy have been achieved. In addition, our simulation and experimental results indicate that two nearly orthogonal views are sufficient to accomplish quasi-isotropic resolution in 3D; therefore, the high imaging speed of OR-PAM can be retained. MV-OR-PAM is expected to open up new areas of investigation in imaging translucent animals such as zebrafish and Drosophila embryos with high 3D resolution.

APPENDIX A

The original Lucy–Richardson deconvolution algorithm and the multiview extended version of it assume that the image, the PSF, and the underlying object function are probability distributions, and therefore should be nonnegative. This assumption imposes a unique problem in applying the multiview Lucy–Richardson deconvolution algorithm to photoacoustic images, as the PA signals are bipolar. By taking the envelope of each A-line before reconstruction, bipolar signals become unipolar, but the strict linearity of the algorithm is breached. This breach could induce error in deconvolution along the depth direction, if only one view is used. However, since the PSF of OR-PAM is highly anisotropic, even small errors along the A-line direction in one view cause a huge penalty in the near-orthogonal view or views. Therefore, the iterative algorithm will be driven toward a more accurate estimation.

For two orthogonal views acquired at 0° and 90°, the update equations at each iteration r are as follows:

$$u_0 = \frac{I_0}{\hat{f}^{(r)} * g_0} * g_0', \tag{A1}$$

$$u_{90} = \frac{I_{90}}{\hat{f}^{(r)} * g_{90}} * g_{90}', \tag{A2}$$

$$\hat{f}^{(r+1)} = \hat{f}^{(r)} \cdot u_0 \cdot u_{90}, \tag{A3}$$

where u_0 and u_{90} denote the updated terms from 0° and 90°, I is the measurement, g is the PSF, g' is the flipped PSF, and $\hat{f}$ is the estimation of the object function. The entire iteration procedure will converge toward an estimation that results in both u_0 and u_{90} close to 1. The nonlinearity caused by envelope extraction, however, makes u_0 alone favor an inaccurate $\hat{f}$ along the depth direction of I_0. But in OR-PAM the 3D PSF is much wider along the depth direction than along the lateral directions, so g_0 is much wider than g_{90} along this particular direction. Thus an inaccurate $\hat{f}$, favorable for u_0, will generate a large u_{90}, driving the final result to a more accurate estimation. On the contrary, an accurate $\hat{f}$, favorable for u_{90}, will produce a small u_0.

The above analysis, along with our simulation and experimental results, shows that our method is viable for OR-PAM.

FUNDING INFORMATION

National Institutes of Health (NIH) (DP1 EB016986, R01 CA159959, R01 CA186567, R01 EB016963).

ACKNOWLEDGMENTS

The authors thank Prof. James Ballard for his close reading of the manuscript and an author of Ref. [15], Dr. Stephan Preibisch, for discussion of multiview deconvolution algorithms. We also thank Sarah DeGenova and Kelly Monk for helping

prepare the zebrafish embryos. L. V. Wang has a financial interest in Microphotoacoustics, Inc., and Endra, Inc., which, however, did not support this work.

†These authors contributed equally to this work.

REFERENCES

1. D. J. Grunwald and J. S. Eisen, "Headwaters of the zebrafish—emergence of a new model vertebrate," Nat. Rev. Genet. **3**, 717–724 (2002).
2. H. J. Bellen, C. Tong, and H. Tsuda, "100 years of Drosophila research and its impact on vertebrate neuroscience: a history lesson for the future," Nat. Rev. Neurosci. **11**, 514–522 (2010).
3. D. Razansky, M. Distel, C. Vinegoni, R. Ma, N. Perrimon, R. W. Köster, and V. Ntziachristos, "Multispectral opto-acoustic tomography of deep-seated fluorescent proteins in vivo," Nat. Photonics **3**, 412–417 (2009).
4. S. Ye, R. Yang, J. Xiong, K. K. Shung, Q. Zhou, C. Li, and Q. Ren, "Label-free imaging of zebrafish larvae in vivo by photoacoustic microscopy," Biomed. Opt. Express **3**, 360–365 (2012).
5. L. H. V. Wang and S. Hu, "Photoacoustic tomography: in vivo imaging from organelles to organs," Science **335**, 1458–1462 (2012).
6. L. V. Wang and L. Gao, "Photoacoustic microscopy and computed tomography: from bench to bedside," Annu. Rev. Biomed. Eng. **16**, 155–185 (2014).
7. S. Hu and L. H. V. Wang, "Optical-resolution photoacoustic microscopy: auscultation of biological systems at the cellular level," Biophys. J. **105**, 841–847 (2013).
8. C. Zhang, K. Maslov, S. Hu, R. M. Chen, Q. F. Zhou, K. K. Shung, and L. H. V. Wang, "Reflection-mode submicron-resolution in vivo photoacoustic microscopy," J. Biomed. Opt. **17**, 020501 (2012).
9. L. V. Wang and H. Wu, *Biomedical Optics: Principles and Imaging* (Wiley, 2012).
10. C. Zhang, K. Maslov, J. J. Yao, and L. H. V. Wang, "In vivo photoacoustic microscopy with 7.6-μm axial resolution using a commercial 125-MHz ultrasonic transducer," J. Biomed. Opt. **17**, 116016 (2012).
11. Z. X. Xie, S. L. Chen, T. Ling, L. J. Guo, P. L. Carson, and X. D. Wang, "Pure optical photoacoustic microscopy," Opt. Express **19**, 9027–9034 (2011).
12. R. L. Shelton, S. P. Mattison, and B. E. Applegate, "Volumetric imaging of erythrocytes using label-free multiphoton photoacoustic microscopy," J. Biophotonics, doi: 10.1002/jbio.201300059 (posted online August 21, 2013).
13. L. Zhu, L. Gao, L. Li, L. Wang, T. Ma, Q. Zhou, K. K. Shung, and L. V. Wang, "Cross-optical-beam nonlinear photoacoustic microscopy," Proc. SPIE **8943**, 89433H (2014).
14. Y. Wu, P. Wawrzusin, J. Senseney, R. S. Fischer, R. Christensen, A. Santella, A. G. York, P. W. Winter, C. M. Waterman, and Z. Bao, "Spatially isotropic four-dimensional imaging with dual-view plane illumination microscopy," Nat. Biotechnol. **31**, 1032–1038 (2013).
15. S. Preibisch, F. Amat, E. Stamataki, M. Sarov, E. Myers, and P. Tomancak, "Efficient Bayesian-based multi-view deconvolution," Nat. Methods **11**, 645–648 (2014).
16. W. H. Richardson, "Bayesian-based iterative method of image restoration," J. Opt. Soc. Am. **62**, 55–59 (1972).
17. L. Lucy, "An iterative technique for the rectification of observed distributions," Astron. J. **79**, 745–754 (1974).
18. L. Li, C. Yeh, S. Hu, L. Wang, B. T. Soetikno, R. Chen, Q. Zhou, K. K. Shung, K. I. Maslov, and L. V. Wang, "Fully motorized optical-resolution photoacoustic microscopy," Opt. Lett. **39**, 2117–2120 (2014).
19. S. Preibisch, S. Saalfeld, J. Schindelin, and P. Tomancak, "Software for bead-based registration of selective plane illumination microscopy data," Nat. Methods **7**, 418–419 (2010).
20. A. N. Tikhonov, V. I. Arsenin, and F. John, *Solutions of Ill-Posed Problems* (Winston, 1977).
21. L. Gao, L. Zhu, C. Li, and L. V. Wang, "Nonlinear light-sheet fluorescence microscopy by photobleaching imprinting," J. R. Soc. Interface **11**, 20130851 (2014).
22. U. Krzic, "Multiple-view microscopy with light-sheet based fluorescence microscope," Ph.D. thesis (Heidelberg University, 2009).

optica

Decoupled and simultaneous three-dimensional imaging and optical manipulation through a single objective

Arran Curran,[1,*] Simon Tuohy,[2] Dirk G. A. L. Aarts,[1] Martin J. Booth,[2] Tony Wilson,[2] and Roel P. A. Dullens[1]

[1]Department of Chemistry, Physical and Theoretical Chemistry Laboratory, University of Oxford, South Parks Road, Oxford OX1 3QZ, UK

[2]Department of Engineering Science, University of Oxford, Parks Road, Oxford OX1 3PJ, UK

*Corresponding author: arran.curran@chem.ox.ac.uk

Received 15 May 2014; revised 22 August 2014; accepted 23 August 2014 (Doc. ID 212157); published 1 October 2014

The combination of optical manipulation and three-dimensional imaging is a central technique in fields ranging from medicine to physics. Using the objective lens simultaneously for optical trapping and imaging, however, inherently confines the trapping and imaging planes to the same focal plane. Here, we combine remote refocusing microscopy and optical trapping to optically decouple the imaging and trapping planes, achieving aberration-free three-dimensional imaging and simultaneous, decoupled optical trapping without the need for feedback or aberration corrections. We demonstrate our approach by directly imaging the flow field around optically trapped spheres in three dimensions. Due to its compatibility with other imaging and optical manipulation techniques, our approach is relevant to the wide range of fields that combine imaging and optical manipulation, such as physical chemistry, cell biology, and soft matter.

OCIS codes: (350.4855) Optical tweezers or optical manipulation; (180.0180) Microscopy; (180.1790) Confocal microscopy.

http://dx.doi.org/10.1364/OPTICA.1.000223

The combination of optical manipulation and microscopy is of paramount importance in medicine, biology, chemistry, and physics [1–8]. Optical manipulation experiments generally require simultaneous imaging for data acquisition, and usually the same objective lens is used for optical trapping and imaging. This leaves space around the sample free for techniques such as microfluidics, holographic microscopy, rheology, or atomic force microscopy [4,9–12]. However, it does pose a fundamental restriction on which part of the sample may be imaged while trapping, since the imaging and trapping planes are inherently coupled to the same focal plane.

To overcome this restriction, two objectives have been positioned nose-to-nose, on opposite sides of the sample, with one providing the optical trapping, and the other the imaging [13–15]. In this way the trapping and imaging planes are mechanically decoupled, which allows for independent imaging of optically trapped particles in three dimensions. However, this configuration requires thin samples and limits access to the sample. Another approach to decouple the imaging and trapping planes is to use wavefront engineering and computational feedback. Mechanical or digital wavefront engineering of either the imaging or trapping wavefront can offset its relative axial position [16–18], though aberrations in the refocused plane are inevitable. In the case of mechanical refocusing the axial depth is limited ~10 μm [19]. In digital refocusing, aberration corrections can increase this depth to ~30 μm for optical trapping [20,21], though the low optical efficiency [22] limits its applicability in simultaneous three-dimensional (3D) imaging. Digital holographic microscopy has become an increasingly popular technique for 3D tracking and is easily combined with optical trapping [10,23]. Nevertheless, the imaging and trapping planes are not decoupled and the sample still needs to be accessible from both sides. In addition, it is prohibitively difficult to apply holographic microscopy to dense and turbid samples due to the complexity of the resulting holograms.

In this Letter, we present a unique approach that facilitates 3D holographic optical trapping and simultaneous, decoupled imaging using a single microscope objective at the sample. By remotely refocusing the imaging plane [19] it is optically decoupled from the trapping plane, and we are able to image in 3D while simultaneously optically manipulating the system, without the need for any digital feedback or aberration correction. Figure 1(a) shows the schematic of our setup, which is composed of the remote refocusing component, the CMOS camera or confocal scan head, holographic optical trapping, and a single objective inverted microscope (see Supplement 1). Importantly, a wide variety of other imaging and trapping techniques can be easily incorporated in our setup, which underlines the general applicability of our approach. Our setup is designed to optically manipulate the sample while simultaneously imaging the volume around the manipulated region using a single objective at the sample.

The key to optically decoupling the imaging and trapping planes is the aberration-free remote refocusing component [19], which is highlighted in Fig. 1(b) for brightfield and confocal modes. In brightfield mode, the light from the sample, collected by O1, is relayed to O2, which produces a low magnification 3D image of the sample. This 3D image is then reimaged with a high magnification onto the CMOS camera by O3. In this way we remotely image our sample, where the axial displacement of objective O3 controls the position of the imaging plane within the sample. Importantly, the remote refocusing component fully retains the properties of the chosen imaging mode. When used in confocal mode, the translation of O3 dynamically changes the axial position of the confocal illumination and imaging planes, thereby retaining the optical sectioning of the sample, as shown in Fig. 1(b). The maximum axial depth in our system is 66 μm and is limited by the travel of O3 (see Supplement 1). We characterize the remote refocusing by measuring the point spread functions generated at the sample for different axial positions of objective O3 (see Supplement 1). Figure 1(c) shows the intensity distributions at O1 when O3 is positioned at an axial position of $z = -50$, 0, and $+50$ μm, respectively. In each case the intensity distribution is that of a diffraction limited spot, which demonstrates the aberration-free remote refocusing in our system [19].

Figure 2 shows the remote refocusing microscope operating in brightfield and confocal mode, respectively. Figure 2(a) presents brightfield images of a 10 μm, grid while Fig. 2(b) shows confocal images of a colloidal monolayer (see Supplement 1). In each image O3 is positioned at $z = -50$, 0, and $+50$ μm, from left to right, respectively, which refocuses the imaging plane in the sample to an axial depth of $+33$, 0, and -33 μm relative to the nominal focal plane of O1. At each position of O3, the sample stage is then adjusted to bring the grid or colloidal monolayer back into focus. Both imaging modes show excellent contrast and resolution for the full range of remote refocusing. A minor reduction in the collected fluorescence can be seen at $z = \pm 33$ μm due to the reduced collection of the objectives when operating away from their focal planes. This has little effect in the brightfield images.

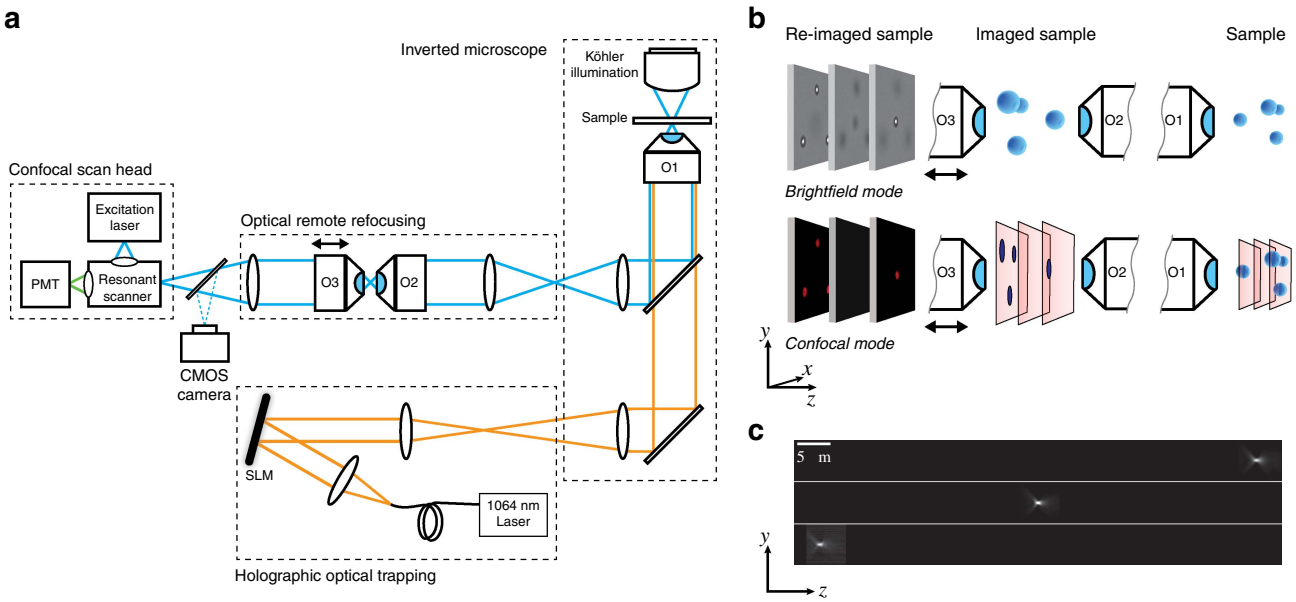

Fig. 1. Experimental setup combining 3D remote refocusing microscopy and optical manipulation. (a) Schematic diagram of the experimental setup, which consists of four main units: a single objective inverted microscope, remote refocusing, holographic optical trapping, and a CMOS camera or a confocal scan head containing the resonant scanner, the excitation laser, and the photo-multiplier tube (PMT). The flip mirror in front of the CMOS camera and the confocal scan head determines which imaging mode is used. (b) Simplified schematic of the optical remote refocusing technique in brightfield and confocal modes. In brightfield, a low magnification 3D image of the sample is created by O2, which is subsequently reimaged by O3 onto the CMOS camera. In confocal mode, the translation of O3 changes the axial position of the illumination and imaging focal planes, resulting in optical sectioning of the sample. (c) *xz* profiles of the intensity distribution of a focused laser beam formed by O1 at the sample plane. The three panels correspond to O3 being positioned at $z = -50$ (top), 0 (middle), and $+50$ μm (bottom), respectively. Each intensity profile is normalized to the maximum pixel value.

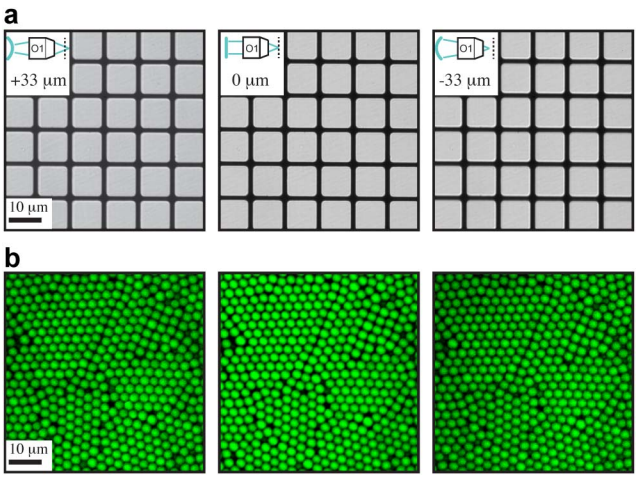

Fig. 2. Remote refocusing microscopy. (a) Brightfield images of a 10 μm grid positioned at axial depth of $z = +33$, 0, and −33 μm relative to the nominal focal plane of O1. The images are then brought into focus by positioning O3 at $z = -50$, 0, and +50 μm, respectively. (b) Confocal images of a colloidal monolayer for the same axial positions as in (a).

To illustrate the simultaneous and decoupled 3D imaging and optical trapping capabilities, we image four particles that are trapped at the vertices of a tetrahedron. Three vertices of the tetrahedron are placed in the same *xy* plane, separated by 20 μm. The fourth vertex is positioned 17 μm above this plane. Figure 3(a) shows a sequence of five brightfield images with axial increments of 5 μm and starting 5 μm below the base of the tetrahedron. Figure 3(b) presents confocal images at the same resolution, field of view, and axial position as the brightfield images in Fig. 3(a). The tetrahedral geometry is obvious from both the brightfield and confocal images, where the optical sectioning of the confocal imaging is reflected by the absence of the out-of-focus contributions that are present in the brightfield images. Figure 3(c) presents a 3D view of the tetrahedron as observed in confocal mode, which shows the capability of our system to image around a static optically trapped network using only a single objective at the sample.

More challenging, we directly image the 3D flow field around optically trapped particles using our remote refocusing microscope in confocal mode. As the flow profile around a sphere is well known [24,25] and relevant for active systems such as swimming bacteria [26], it forms an ideal proof-of-principle case study for our setup. First, we trap a single 10 μm diameter sphere in a dilute dispersion of small ∼500 nm diameter fluorescent tracer particles and subsequently flow the tracer suspension past the trapped sphere

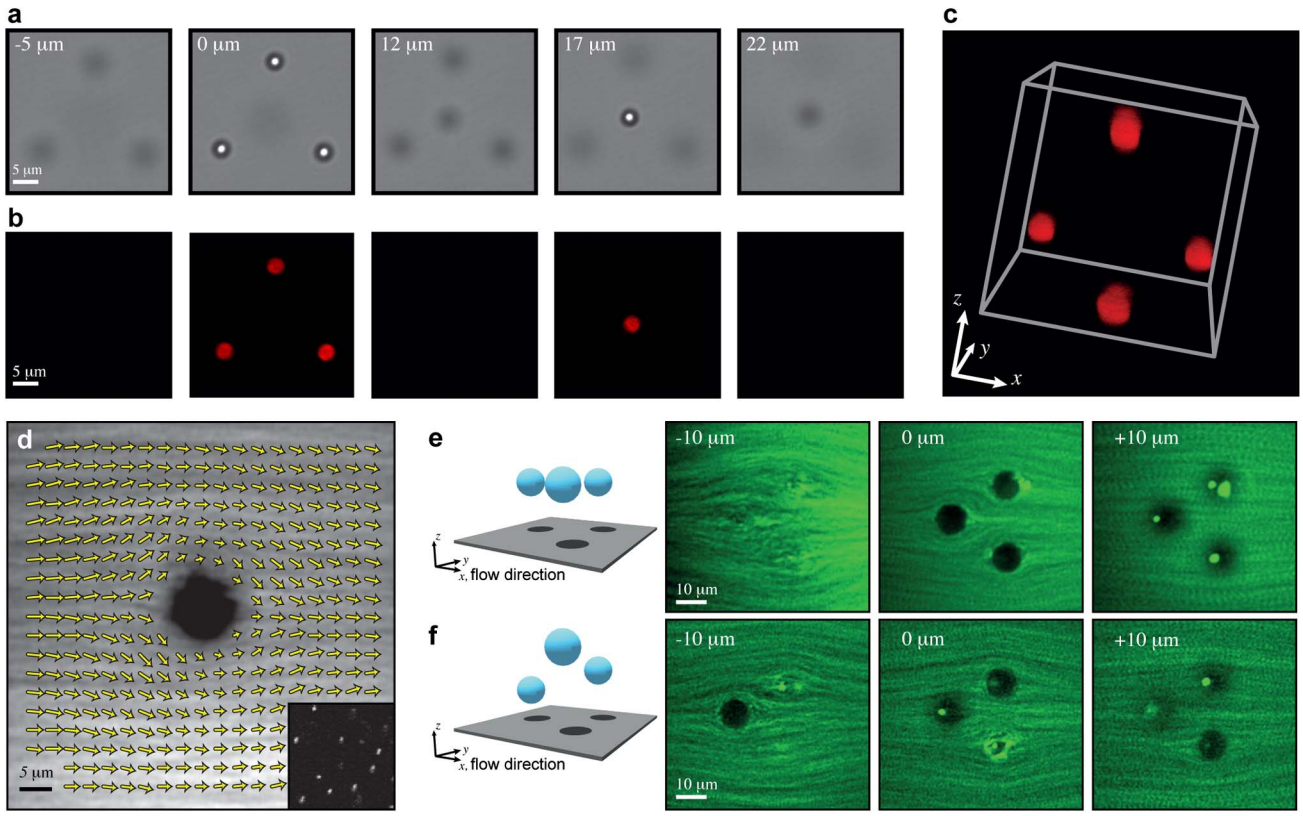

Fig. 3. Decoupled and simultaneous 3D imaging and optical manipulation. Colloids optically trapped at the vertices of the tetrahedron. (a) Brightfield images with axial increments of 5 μm and starting 5 μm below the base of the tetrahedron. (b) Corresponding confocal images at the same resolution, field of view, and axial position. (c) 3D image of the tetrahedron as observed by the confocal scan head. (d) Confocal image showing the flow profile of ∼500 nm diameter particles around a single 10 μm diameter optically trapped sphere. The image is averaged over 5000 frames (the inset shows a region of 19 μm × 19 μm of a single frame) with the measured velocity field overlaid. For clarity we normalize the velocity component in *x* by the bulk flow velocity. (e) and (f) Flow fields around three optically trapped spheres, which are trapped either (e) in the same plane ($z = 0$ μm) or (f) in three different planes ($z = -10$, 0, and 10 μm), as detailed in the illustrations.

(see Supplement 1). With the confocal scan head we then image the flow profile around the large sphere as is shown in Fig. 3(d). Here, we present an image averaged over 5000 frames captured while the flowing tracer particles move around the larger trapped sphere. The inset shows a small region of a single confocal frame in which the tracer particles are readily observed. Using standard particle tracking algorithms [27] the particle trajectories are used to compute the velocity field, which is overlaid on the data in Fig. 3(d). For clarity, we normalize the velocity component in the x direction by the bulk flow velocity, i.e., far away from the trapped sphere. In Figs. 3(e) and 3(f) we show the flow profiles around three optically trapped spheres, where they are trapped either at the same height (e) or at three different heights (f). These flow profiles corroborate the capability of our system to simultaneously and independently perform quantitative imaging and optical manipulation in 3D while also exhibiting how our system may be used to address fundamental hydrodynamic problems. While the Stokes flow around a single sphere is well established, the flow profile around a network of particles in the limit of small particle–particle separation is less obvious as it may not be described by the superposition of the Stokes flow around single spheres [28]. In addition, the complex 3D flow profiles in active systems could be elucidated directly, for example, by trapping motile bacteria such as Chlamydomonas and simultaneously imaging the flow field [26].

In summary, we have developed a unique method to optically decouple 3D imaging from optical trapping. By remotely refocusing the sample, only a single objective at the sample is required, which allows access for further experimental techniques such as rheology or microfluidics. Our system is capable of aberration-free 3D imaging with an axial range of 66 μm, while simultaneously manipulating the sample with optical tweezers. Because our simple yet powerful technique is compatible with other optical manipulation and imaging techniques, we believe it is directly relevant to the wide range of experiments that use optical manipulation and simultaneous imaging.

FUNDING INFORMATION

European Research Council (ERC) (ERC Starting Grant 279541-IMCOLMAT).

ACKNOWLEDGMENTS

The authors thank Yanyan Liu for the tracer particles used in the flow experiments.

See Supplement 1 for supporting content.

REFERENCES

1. A. Ashkin, J. M. Dziedzic, and T. Yamane, Nature **330**, 769 (1987).
2. D. G. Grier, Nature **424**, 810 (2003).
3. M. P. MacDonald, G. C. Spalding, and K. Dholakia, Nature **426**, 421 (2003).
4. J. Enger, M. Goksör, K. Ramser, P. Hagberg, and D. Hanstorp, Lab On Chip **4**, 196 (2004).
5. M. W. Berns and K. O. Greulich, *Laser Manipulation of Cells and Tissues* (Academic, 2007).
6. H. Kress, J.-G. Park, C. O. Mejean, J. D. Forster, J. Park, S. S. Walse, Y. Zhang, D. Wu, O. D. Weiner, T. M. Fahmy, and E. R. Dufresne, Nat. Methods **6**, 905 (2009).
7. M. Padgett and R. Bowman, Nat. Photonics **5**, 343 (2011).
8. N. R. Guydosh and S. M. Block, Nature **461**, 125 (2009).
9. J. Sheng, E. Malkiel, and J. Katz, Appl. Opt. **45**, 3893 (2006).
10. S.-H. Lee and D. G. Grier, Opt. Express **15**, 1505 (2007).
11. Y. L. Wu, J. H. J. Brand, J. L. A. van Gemert, J. Verkerk, H. Wisman, A. van Blaaderen, and A. Imhof, Rev. Sci. Instrum. **78**, 103902 (2007).
12. O. Chaudhuri, S. H. Parekh, W. A. Lam, and D. A. Fletcher, Nat. Methods **6**, 383 (2009).
13. D. L. J. Vossen, A. van der Horst, M. Dogterom, and A. van Blaaderen, Rev. Sci. Instrum. **75**, 2960 (2004).
14. W. T. M. Irvine, M. J. Bowick, and P. M. Chaikin, Nat. Mater. **11**, 948 (2012).
15. M. Yevnin, D. Kasimov, Y. Gluckman, Y. Ebenstein, and Y. Roichman, Biomed. Opt. Express **4**, 2087 (2013).
16. A. Hoffmann, G. Meyer zu Hörste, G. Pilarczyk, S. Monajembashi, V. Uhl, and K. O. Greulich, Appl. Phys. B **71**, 747 (2000).
17. Y. Yasuno, S. Makita, T. Yatagai, T. Wiesendanger, A. Ruprecht, and H. Tiziani, Opt. Express **11**, 54 (2003).
18. S. A. Khan and N. A. Riza, Opt. Commun. **265**, 461 (2006).
19. E. J. Botcherby, R. Juskaitis, M. J. Booth, and T. Wilson, Opt. Lett. **32**, 2007 (2007).
20. K. D. Wulff, D. G. Cole, R. L. Clark, and R. Di Leonardo, Opt. Express **14**, 4170 (2006).
21. M. Dienerowitz, G. Gibson, R. Bowman, and M. Padgett, Opt. Express **19**, 24589 (2011).
22. G. Sinclair, P. Jordan, J. Leach, M. J. Padgett, and J. Cooper, J. Mod. Opt. **51**, 409 (2004).
23. B. Kemper, A. Barroso, M. Woerdemann, L. Dewenter, A. Vollmer, R. Schubert, A. Mellmann, A. G. von Bally, and C. Denz, J. Biophotonics **6**, 260 (2013).
24. S. Taneda, J. Phys. Soc. Jpn. **46**, 1935 (1979).
25. J. Happel and H. Brenner, *Low Reynolds Number Hydrodynamics* (Kluwer Academic, 1983).
26. M. Polin, I. Tuval, K. Drescher, J. P. Gollub, and R. E. Goldstein, Science **325**, 487 (2009).
27. J. C. Crocker and D. G. Grier, J. Colloid Interface Sci. **179**, 298 (1996).
28. C. Scholz, F. Wirner, Y. Li, and C. Bechinger, Exp. Fluids **53**, 1327 (2012).

Research Article Vol. 1, No. 4 / October 2014 / Optica 227

Focusing on moving targets through scattering samples

EDWARD HAOJIANG ZHOU,[1] HAOWEN RUAN,[1] CHANGHUEI YANG,[1,4] AND BENJAMIN JUDKEWITZ[1,2,3]

[1]Departments of Electrical Engineering and Bioengineering, California Institute of Technology, Pasadena, California 91125, USA

[2]Exzellenzcluster NeuroCure, Charité Berlin, Humboldt University, 10117 Berlin, Germany

[3]e-mail: benjamin.judkewitz@charite.de

[4]e-mail: chyang@caltech.edu

Received 21 July 2014; revised 12 August 2014; accepted 23 August 2014 (Doc. ID 217492); published 1 October 2014

Focusing light through scattering media has been a longstanding goal of biomedical optics. While wavefront shaping and optical time-reversal techniques can in principle be used to focus light across scattering media, achieving this within a scattering medium with a noninvasive and efficient reference beacon, or guide star, remains an important challenge. Here, we show optical time-reversal focusing using a new technique termed Time Reversal by Analysis of Changing wavefronts from Kinetic targets (TRACK). By taking the difference between time-varying scattering fields caused by a moving object and applying optical time reversal, light can be focused back to the location previously occupied by the object. We demonstrate this approach with discretely moved objects as well as with particles in an aqueous flow, and obtain a focal peak-to-background strength of 204 in our demonstration experiments. We further demonstrate that the generated focus can be used to noninvasively count particles in a flow-cytometry configuration—even when the particles are hidden behind a strong diffuser. By achieving optical time reversal and focusing noninvasively without any external guide stars, using just the intrinsic characteristics of the sample, this work paves the way to a range of scattering media imaging applications, including underwater and atmospheric focusing as well as noninvasive *in vivo* flow cytometry.

OCIS codes: (110.0113) Imaging through turbid media; (070.5040) Phase conjugation; (110.0180) Microscopy.

http://dx.doi.org/10.1364/OPTICA.1.000227

1. INTRODUCTION

Focusing light through highly scattering media is an important challenge in biomedical imaging, colloidal optics, and astronomy. When light propagates through strongly scattering samples, refractive index inhomogeneities scatter the light field in many directions. This was long thought of as a randomizing process, which precludes the formation of a sharp focus. However, by taking advantage of the deterministic nature of scattering, researchers in the field of complex wavefront shaping have demonstrated that light can be focused at an arbitrary location within and across scattering media—by shaping the input wavefront reaching the sample [1,2]. Because appropriate input wavefronts are complex and because they depend on sample structure as well as target location, determining them remains a key challenge.

With direct optical access to the input plane and the focusing plane, wavefronts can be found with one of three strategies: iterative optimization [1,3–5], optical time reversal [6], or measuring and inverting the sample transmission matrix [7,8]. When there is no direct access to the target plane, e.g., when the target plane is hidden within the sample, physical guide stars such as beads can be placed within the sample and used as reference beacons [9–11]. Because this requires invasive insertion, recent research has focused on virtual, ultrasound-based guide stars relying on the acousto-optic [12–16] or the photo-acoustic effect [17–20]. However, all of these

strategies are either limited by the acoustic resolution (tens of micrometers at best) or require many measurements, thereby increasing the recording time by orders of magnitude. Thus far, near-instantaneous time reversal at optical resolutions remains elusive.

Here we introduce a new all-optical method, termed Time Reversal by Analysis of Changing wavefronts from Kinetic targets (TRACK), which achieves precise optical time reversal to a target hidden behind a scattering sample—without the need for acoustic guide stars. Unlike previous techniques, this method uses the motion of the target itself to serve as a guide star.

2. RESULTS

A. Principle

To test whether we can noninvasively focus light through a scattering sample without using any extrinsic guide star, we constructed the setup diagrammed in Fig. 1. We interpret optical scattering through our diffuser as a linear process described by a complex spatial transmission matrix, $T(x_a, x_b)$ [1]. This matrix defines the transformation of the optical field at an input plane with coordinates x_a directly before the diffuser to an output plane with coordinates x_b behind the diffuser, where we have a moving target with a reflectivity function $R(x_b)$. We assume that our digital phase-conjugation system is set up such that we can discretely measure and control the optical field along the input plane coordinates x_a.

Our detect-and-refocus process is composed of four primary steps. First, we illuminate the scatterer with an input wave, $U(x_a)$, to reflect light off our target. $U(x_a)$ transforms into a speckle field at the output plane as defined by the transmission matrix: $S(x_b) = T(x_a, x_b)U(x_a)$. A portion of the speckle field $S(x_b)$ will hit our target object with reflectivity function $R(x_b)$. The target object's backreflected optical field is thus the product $E_1(x_b) = R(x_b)S(x_b)$. Note that $R(x_b) = 0$ and hence $E_1(x_b) = 0$ everywhere except along the target's finite spatial extent. We also assume $S(x_b) \neq 0$ somewhere along our target to ensure a nonzero reflected signal.

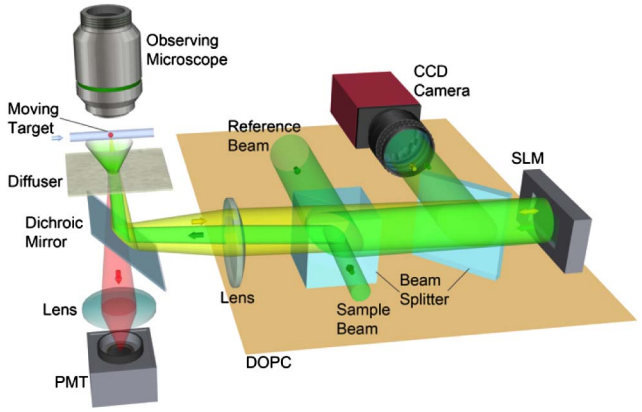

Fig. 1. Concise setup including sample and digital phase conjugation: varying backscattered wavefronts due to a target's movement are captured by off-axis holography. The phase of the wavefront difference is time reversed by the digital optical phase-conjugation (DOPC) system. Diffuse light is focused back to the previous position of the target.

Second, we measure the entire backscattered optical field at the input plane, $M_1(x_a)$, as depicted in Fig. 2(a). Following linear optics, we split the backscattered field $M_1(x_a)$ into a sum of two components: one reflected from our target object at the output plane, $E_1'(x_a)$, and one originating from all other locations within the sample volume, $B(x_a)$. The target-dependent component $E_1'(x_a)$ is defined as the target-reflected optical field at the output plane, $E_1(x_b)$, after it has backscattered to the input plane. Following the common assumption of a lossless scattering process, we may use our transmission matrix to express $E_1'(x_a)$ as

$$E_1'(x_a) = T^t(x_a, x_b)E_1(x_b), \tag{1}$$

where T^t, the transpose of T, represents the reverse process of scattering from the output to the input plane. The total measured field at the input plane is thus the sum

$$M_1(x_a) = T^t(x_a, x_b)E_1(x_b) + B(x_a), \tag{2}$$

where again $B(x_a)$ is the background optical field arising from all other locations within the sample.

Third, we measure a second backscattered field at the input plane, $M_2(x_a)$, after the reflective target object physically shifts a finite distance Δ across the output plane. This measurement is depicted in Fig. 2(b). A spatially shifted target will generate a new reflected field, $E_2(x_b) = R(x_b - \Delta)S(x_b)$, which will again transform to the input plane via our transmission matrix and combine with a background field contribution to yield

$$M_2(x_a) = T^t(x_a, x_b)E_2(x_b) + B(x_a). \tag{3}$$

Equation (3) implicitly assumes that T and $B(x_a)$ remain the same as for the first measurement, requiring the scattering sample to be stationary (apart from target motion) at the time scale of the measurement interval.

Fourth, we digitally subtract our two measurements to effectively remove any background contribution and isolate the target-reflected signal:

$$M_2(x_a) - M_1(x_a) = T^t(x_a, x_b)[E_2(x_b) - E_1(x_b)]. \tag{4}$$

We compute the phase conjugate of this subtraction and display it on our digital optical phase-conjugation (DOPC) setup's spatial light modulator (SLM) to create the following field at the input plane: $T^\dagger(x_a, x_b)[E_2(x_b) - E_1(x_b)]^*$, where $\dagger$ denotes a conjugate transpose and $*$ a complex conjugate. This field scatters from the sample's input to output plane to form our final target-focused field, $E_f(x_b)$, as shown in Fig. 2(c):

$$\begin{aligned} E_f(x_b) &= T(x_a, x_b)T^\dagger(x_a, x_b)[E_2(x_b) - E_1(x_b)]^* \\ &\approx [E_2(x_b) - E_1(x_b)]^*. \end{aligned} \tag{5}$$

Here, we assume a complete scattering process to form the approximation $T(x_a, x_b)T^\dagger(x_a, x_b) \approx I$, the identity matrix. Conjugated light thus forms the field $E_2 - E_1$ at the sample plane, implying light is focused to both shifted target positions. If the target was originally off the laser speckle field (i.e., E_1 is

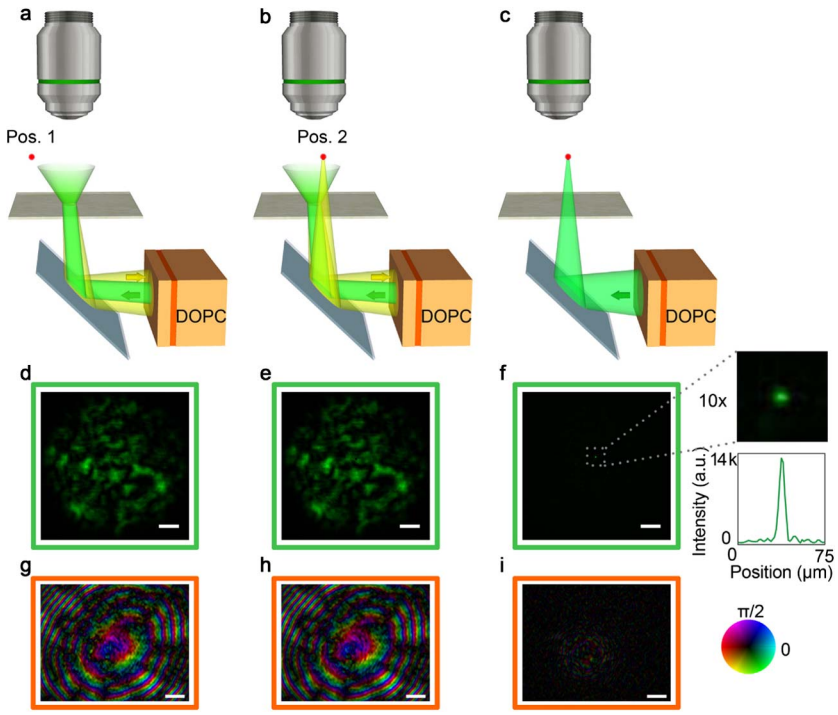

Fig. 2. Focusing on a moving target through a scattering sample: (a) target at position 1 (far off the illuminated field of view); (b) target at position 2 (within the illuminated field of view); (c) light is focused behind the diffuser; (d)–(f) corresponding images recorded with the observing microscope; (g) and (h) phase maps recorded at the camera imaging the SLM surface; (i) difference of field in (g) and field in (h). The cross-section intensity distribution in (f) indicates a PBR of 204. Scale bars in (d)–(f) are 100 μm. Scale bars in (g)–(i) all stand for 1 mm.

zero everywhere), a focus will appear only at its second location, which corresponds to our ability to refocus onto a moving object.

B. Direct Observation of Optical Focusing in Reflection Mode

Our reflection-mode TRACK setup is diagramed in Fig. 1. To record backscattered light at the SLM plane, a camera was pixel-to-pixel aligned to image the SLM surface, and wavefronts were measured by off-axis holography [21,22]. For demonstration, we created a sample consisting of 10 μm diameter polystyrene beads behind a highly diffusing tape. The beads were placed on a glass slide 7 mm behind the diffuser, whose movement was two-dimensionally controlled by a piezo stage. To confirm the formation of a focus through scattering media, an observing microscope (OM) was set up to image the target plane from the back. Importantly, this microscope was only used for validation of successful focusing, but not to derive wavefronts or create the foci.

We started by recording a backscattered wavefront without any targets behind the diffuser [Fig. 2(g)] and compared it to the wavefront measured when a target was inside the illuminated field of view [Fig. 2(h)]. As expected, both wavefronts were dominated by backscattering from the entire diffuser, while the relative difference of the wavefronts was 15% (relative average amplitude) [Fig. 2(i)]. When we time reversed the difference wavefront by digital phase conjugation, the OM recorded a high-contrast focus at the location of the target. Figure 2(f) includes a plot of the intensity profile (horizontal section across the peak), which shows a peak-to-background ratio (PBR) of 204.

C. Moving Target Tracking behind Scattering Media

If we keep repeating this experiment with a continuously moving target, light will be focused dynamically on the target. In other words, we can track the moving target through the scattering medium. To confirm this experimentally, we recorded a background wavefront at the SLM plane (with no target bead in the illuminated area), and subsequently moved a target bead to multiple locations within the illuminated area. At each position of the target [as shown in Figs. 3(a)–3(c)], after recording the wavefront, we subtracted the background wavefront from the current wavefront and time reversed the result such that it focused on the current location of the target [as shown in Figs. 3(d)–3(f)]. A detailed timing diagram of the system is included in Fig. S7 in (Supplement 1). In this experiment, a 50 μm diameter retro-reflective target bead was 14 mm behind the diffuser.

D. Optical Flow Cytometry in Scattering Media

To mimic an *in vivo* flow-cytometry scenario, we placed a microfluidic channel behind the diffuser. Two kinds of beads were used in this experiment: nonfluorescent polystyrene beads as guide stars and fluorescent beads to be counted in a flow-cytometry-type setup. Repeating the first experiment ("direct observation of optical focusing," above) in a microfluidic channel, we recorded two scattering fields with a guide star bead outside and inside the illuminated area [Fig. 4(a) and

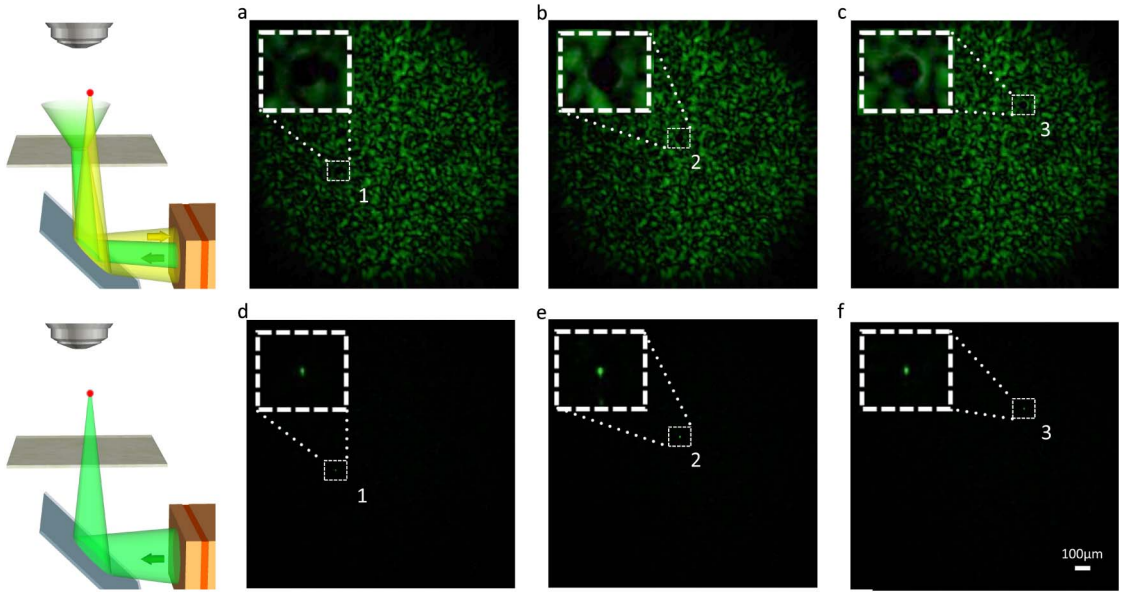

Fig. 3. Target tracking: images taken with the observing microscope. (a)–(c) Images of targets at positions 1–3 in the laser speckle; (d)–(f) phase-conjugate foci at corresponding positions.

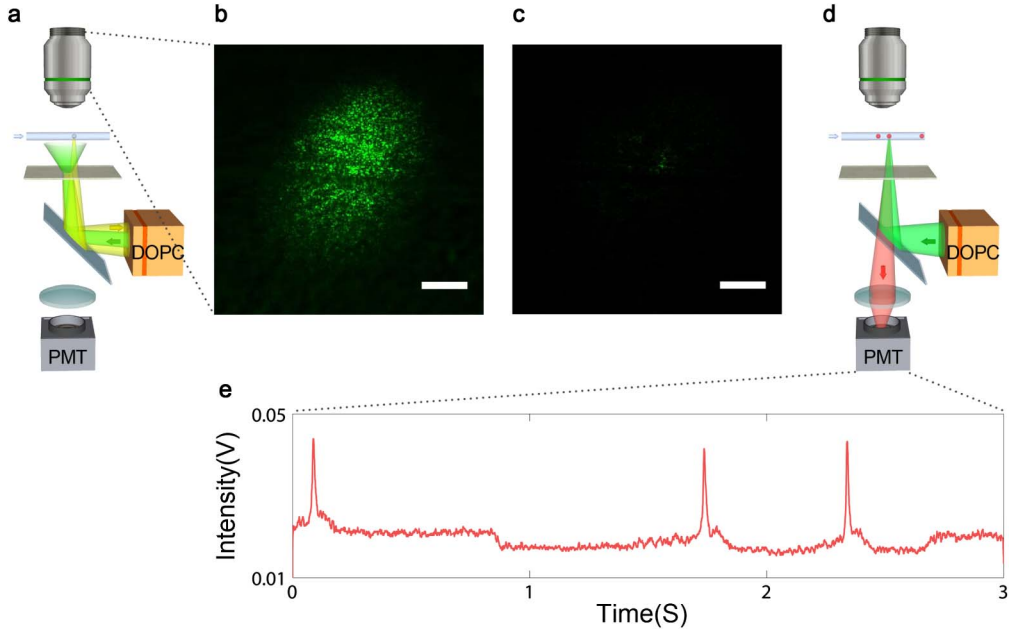

Fig. 4. Optical flow cytometry in scattering media: (a) schematic of the recording step, in which a focus is established as above; (b) laser speckle shining on the microfluidic channel as imaged by the observing camera; (c) time-reversed focus established with the help of the first bead; (d) schematic of the particle counting setup; (e) signal captured on the PMT with clear signals caused by fluorescent beads passing the focus. Both scale bars stand for 100 μm (Media 1).

Media 1]. We then phase conjugated the difference wavefront and observed a focus at the exact position of the guide bead [as shown in Fig. 4(c) and Media 1]. From the cross-section intensity distribution, we measured a PBR of 134 and a full width half-maximum (FWHM) of 8.9 μm. After formation of the focus, fluorescence beads were flown at a speed of 5 cm/s, and the time-varying fluorescence signal was recorded by a single-channel photomultiplier tube (PMT). The PMT trace contained clearly detectable signals that corresponded to fluorescent beads passing the focus. Illumination, phase conjugation, and fluorescence detection by the PMT all occurred on the same side of the scattering sample in a reflection geometry.

3. DISCUSSION

In this work we provided, to the best of our knowledge, the first demonstration of time-reversed optical focusing through

scattering media by using the motion of a target object as a guide star—a technique we call TRACK. We would like to use this section to note some points of consideration associated with this work.

First, TRACK will focus on all backscattering targets that moved between the two wavefront recordings. If the goal is to focus on a single target or bead, only one moving backscattering bead should be within the illuminated area.

Second, we would like to point out that our experimental setup associated with the experimental findings shown in Figs. 2–4 contains a microscope objective and camera (outlined in green in Fig. 1) that allowed us to directly observe the space after the diffuser. We used that imaging system to directly observe and verify that the TRACK focus was achieved. In practical applications, it is unlikely that such an observation perspective would be available. In most of the application scenarios, our only access to the target of interest would be on one side of the diffusing medium, in a reflection geometry. A good case in point would be the task of reflection-mode focusing of light through skin and into a blood vessel. The reflection-mode focusing results presented here show that focusing light in this geometry is feasible. For example, upon creating the time-reversed optical focus (Fig. 4), we can observe the passage of fluorescent beads through the microfluidic channel by simply observing the upticks in fluorescence scattered back through the diffuser.

Another important trade-off space this method introduces is an intrinsic relationship between focus spot size and achievable PBR. Mathematically, these two quantities are related to each other through the number of optical modes that the DOPC can capture and control during playback [23]:

$$\mathrm{PBR}_{\mathrm{phase\text{-}only}} \approx \frac{\pi}{4} \cdot \frac{N_{\mathrm{SLM}}}{N_{\mathrm{target}}}, \tag{6}$$

where N_{SLM} indicates modes on the SLM from the scattering of the target and N_{target} represents the number of modes modulated by the target in the speckle plane. The above formula contains a $\pi/4$ factor because the DOPC in this set of experiments is a phase-only modulator system. For the experimental setup used for Fig. 2, the above formula predicts a focus PBR of 390—a quantity that is consistent with our experimental result of 204, indicating a time-reversal efficiency of >50%. The above formula leads to an interesting consequence. By using smaller target objects, we can effectively create a tighter optical focus and simultaneously boost the PBR. However, we caution that the use of ever smaller target objects will lead to a weaker initial scattering signal arriving at the DOPC and in turn degrade the time-reversed wavefront in the presence of noise. This will then reduce the focus PBR.

As the different sets of experimental results reported in Figs. 3 and 4 show, this method can be used to create a time-reversed focus that tracks with the target object or to create a fixed and static focus at a specific location along the trajectory of the object. Each of these focusing types is useful for different applications: dynamic tracking can potentially be useful for following moving targets in deep ocean or convective atmosphere environments, while the static focus would be most useful for flow-cytometry-type applications.

4. METHODS

A. Setup

All data were collected by a self-built optical system schematically described in Fig. S1 in Supplement 1. In the setup, we used a 532 nm fiber-coupled semiconductor laser. The polarization of the beam was made horizontal (by a half-wave plate and polarizing beam splitter), which is in accordance with SLM modulation polarization. Beam splitter 1 split the incoming light into two beams, the sample beam and the reference beam.

The sample beam was expanded by a laser expander for a suitable size of laser spot at the sample. Reflected by mirrors and beam splitter 2, the sample beam passed through lens 2 and was eventually reflected to the sample by a dichroic mirror, which was at a 45° angle to the horizontal plane. The sample was placed close to the focal plane of lens 2. Light backscattered by the sample was collimated to the SLM by lens 2.

The reference beam passed through a neutral density filter and was coupled into a single-mode fiber for spatial filtering. After exiting the fiber, the beam was collimated by lens 1. Scattered light and reference light were combined by beam splitter 3 before reaching the DOPC system.

Polystyrene beads were obtained from Life Technology. Retro-reflective beads, which consisted of aluminum coated 50 μm glass spheres, were obtained from Cospheric.

To create samples we used adhesive backed, highly diffusing films (3M Scotch model no. 810, ~60 μm thick), which did not transmit a detectable ballistic component (measured with a detection threshold of 10^{-8} of the illumination power). We used it as a random phase plate diffuser whose angle scattering distribution is plotted in Fig. S3 in Supplement 1. To show that our results can be extended to biological samples, we performed TRACK experiments through a 0.5 mm thick section of *ex vivo* chicken muscle tissue (scattering coefficient μ_s: 30 mm^{-1} and anisotropy parameter g: 0.965 [14]). The results of this experiment are shown in Fig. S2 in Supplement 1.

B. Backscattered Field Capture and Phase Retrieval

The backscattered field was recorded in a single-shot measurement by digital off-axis holography. In the DOPC system, the SLM surface was imaged on a CCD camera with a precision of single pixel-to-pixel alignment. The camera captured the interference pattern between the backscattered field and the reference field at the SLM surface. Then 2D fast Fourier transform (FFT) was applied to the captured images. In accordance with off-axis holography, an angle was set between the reference beam and the sample beam to separate the zero order, +1 order, and −1 order of the interference pattern in the Fourier spectrum. By filtering out the DC term and −1 term and back transforming the spectrum, the scattered field from the sample was retrieved. For time reversal, this field was conjugated, and (since we used a phase-only SLM) the phase of the result was displayed on the SLM.

C. Fluorescence Signal Capture

In the flow-cytometry experiment, we used orange fluorescent (540/560) polystyrene microspheres obtained from Life Technology. As shown in Fig. 4(c), orange fluorescence from the beads propagated through the diffuser along with diffuse backscattered light at 532 nm. Colors were separated by the dichroic mirror (a 532 edge pass filter, model Di02-R532-25 × 36 from Semrock). Underneath the dichroic mirror, a lens images the surface of the diffuser to a compact PMT. The fluorescence spectrum of the sample and the transmission spectrum of edge pass filter are shown in Fig. S6 in Supplement 1. A median filter was used to filter the signal shown in Fig. 4(e).

D. Reference Phase Correction

In digital phase conjugation, reference beam and SLM curvature will affect the conjugate phase map and thus the time-reversal PBR. By digitally modulating the SLM curvature to iteratively maximize the reflection from the SLM back into the single-mode fiber in the reference beam arm, we can compensate for SLM curvature as well as reference beam phase errors [14]. A threefold enhancement is observed.

E. Quality Assurance Setup

To assure the pixel-to-pixel alignment between the camera and SLM and the performance of the DOPC system, a quality assurance arm was configured in the sample arm including two flipping mirrors, beam splitter 2, mirror 2, and camera 2 (Fig. S1 in Supplement 1). When flip mirror 1 and flip mirror 2 were flipped up, the system was changed from the reflective mode to the transmission mode. When applying time reversal, we expected to observe a focus on camera 2. By tuning the position and tilting of the SLM, we optimized the intensity of the focus. In this way, a day-to-day precise alignment of the DOPC system was guaranteed.

FUNDING INFORMATION

GIST-Caltech (CG2012); NIH (1DP2OD007307-01); Wellcome Trust (WT092197).

ACKNOWLEDGMENTS

We thank Roarke Horstmeyer and Chen Xu for carefully reading our manuscript and providing helpful advice. B. J. was supported by a Sir Henry Wellcome postdoctoral fellowship.

See Supplement 1 for supporting content.

REFERENCES

1. I. M. Vellekoop and A. P. Mosk, "Focusing coherent light through opaque strongly scattering media," Opt. Lett. **32**, 2309–2311 (2007).
2. A. P. Mosk, A. Lagendijk, G. Lerosey, and M. Fink, "Controlling waves in space and time for imaging and focusing in complex media," Nat. Photonics **6**, 283–292 (2012).
3. I. M. Vellekoop, A. Lagendijk, and A. Mosk, "Exploiting disorder for perfect focusing," Nat. Photonics **4**, 320–322 (2010).
4. D. B. Conkey, A. M. Caravaca-Aguirre, and R. Piestun, "High-speed focusing of light through dynamic turbid media," in *Imaging and Applied Optics Technical Papers*, OSA Technical Digest (online) (Optical Society of America, 2012), paper CTu4B.6.
5. H. Yılmaz, W. L. Vos, and A. P. Mosk, "Optimal control of light propagation through multiple-scattering media in the presence of noise," Biomed. Opt. Express **4**, 1759–1768 (2013).
6. Z. Yaqoob, D. Psaltis, M. S. Feld, and C. Yang, "Optical phase conjugation for turbidity suppression in biological samples," Nat. Photonics **2**, 110–115 (2008).
7. S. Popoff, G. Lerosey, M. Fink, A. C. Boccara, and S. Gigan, "Image transmission through an opaque material," Nat. Commun. **1**, 81 (2010).
8. Y. Choi, C. Yoon, M. Kim, T. Yang, C. Fang-Yen, R. Dasari, K. Lee, and W. Choi, "Scanner-free and wide-field endoscopic imaging by using a single multimode optical fiber," Phys. Rev. Lett. **109**, 203901 (2012).
9. C.-L. Hsieh, Y. Pu, R. Grange, and D. Psaltis, "Digital phase conjugation of second harmonic radiation emitted by nanoparticles in turbid media," Opt. Express **18**, 12283–12290 (2010).
10. I. M. Vellekoop, M. Cui, and C. Yang, "Digital optical phase conjugation of fluorescence in turbid tissue," Appl. Phys. Lett. **101**, 81108 (2012).
11. X. Tao, J. Crest, S. Kotadia, O. Azucena, D. C. Chen, W. Sullivan, and J. Kubby, "Live imaging using adaptive optics with fluorescent protein guide-stars," Opt. Express **20**, 15969–15982 (2012).
12. X. Xu, H. Liu, and L. V. Wang, "Time-reversed ultrasonically encoded optical focusing into scattering media," Nat. Photonics **5**, 154–157 (2011).
13. P. Lai, X. Xu, H. Liu, Y. Suzuki, and L. V. Wang, "Reflection-mode time-reversed ultrasonically encoded optical focusing into turbid media," J. Biomed. Opt. **16**, 080505 (2011).
14. Y. M. Wang, B. Judkewitz, C. A. DiMarzio, and C. Yang, "Deep-tissue focal fluorescence imaging with digitally time-reversed ultrasound-encoded light," Nat. Commun. **3**, 928 (2012).
15. K. Si, R. Fiolka, and M. Cui, "Fluorescence imaging beyond the ballistic regime by ultrasound pulse guided digital phase conjugation," Nat. Photonics **6**, 657–661 (2012).
16. B. Judkewitz, Y. M. Wang, R. Horstmeyer, A. Mathy, and C. Yang, "Speckle-scale focusing in the diffusive regime with time reversal of variance-encoded light (TROVE)," Nat. Photonics **7**, 300–305 (2013).
17. F. Kong, R. H. Silverman, L. Liu, P. V. Chitnis, K. K. Lee, and Y. C. Chen, "Photoacoustic-guided convergence of light through optically diffusive media," Opt. Lett. **36**, 2053–2055 (2011).
18. D. B. Conkey, A. M. Caravaca-Aguirre, J. D. Dove, H. Ju, T. W. Murray, and R. Piestun, "Super-resolution photoacoustic imaging through a scattering wall," arXiv:1310.5736 (2013).
19. P. Lai, L. Wang, J. W. Tay, and L. V. Wang, "Nonlinear photoacoustic wavefront shaping (PAWS) for single speckle-grain optical focusing in scattering media," arXiv:1402.0816 (2014).
20. T. Chaigne, O. Katz, A. C. Boccara, M. Fink, E. Bossy, and S. Gigan, "Controlling light in scattering media non-invasively using the photoacoustic transmission matrix," Nat. Photonics **8**, 58–64 (2014).
21. U. Schnars and W. Jüptner, "Direct recording of holograms by a CCD target and numerical reconstruction," Appl. Opt. **33**, 179–181 (1994).
22. E. Cuche, P. Marquet, and C. Depeursinge, "Spatial filtering for zero-order and twin-image elimination in digital off-axis holography," Appl. Opt. **39**, 4070–4075 (2000).
23. I. M. Vellekoop, "Controlling the propagation of light in disordered scattering media," Ph.D. thesis (University of Twente, 2008).

Review Article Vol. 1, No. 4 / October 2014 / Optica 233

Designing advanced very-large-mode-area fibers for power scaling of fiber-laser systems

Fabian Stutzki,[1,*] Florian Jansen,[1] Hans-Jürgen Otto,[1] Cesar Jauregui,[1] Jens Limpert,[1,2,3] and Andreas Tünnermann[1,2,3]

[1]Institute of Applied Physics, Abbe Center of Photonics, Friedrich-Schiller-Universität Jena, Albert-Einstein-Strasse 15, 07745 Jena, Germany

[2]Helmholtz-Institute Jena, Fröbelstieg 3, 07743 Jena, Germany

[3]Fraunhofer Institute for Applied Optics and Precision Engineering, Albert-Einstein-Str. 7, 07745 Jena, Germany

*Corresponding author: fabian.stutzki@uni-jena.de

Received 14 April 2014; revised 26 August 2014; accepted 7 September 2014 (Doc. ID 210193); published 9 October 2014

Fiber lasers are a highly regarded solid-state laser concept due to their high efficiency, beam quality, and easy thermal management. Unfortunately, the performance of high-power fiber-laser systems is challenged by the onset of detrimental nonlinear effects. Their impact can be reduced dramatically by employing fibers with larger mode-field areas. Even though this is an efficient way to mitigate nonlinear effects, maintaining effective single-mode operation, and with it high beam quality, becomes increasingly difficult as the core is enlarged. In this paper the demands and challenges for the design of a very-large-mode-area (VLMA) fiber are discussed. The benefits of using higher-order mode delocalization as the working principle of active double-clad VLMA fibers are described. Finally, a new low-symmetry large-pitch fiber, which is expected to improve the performance of state-of-the-art fiber-laser systems by increasing higher-order mode delocalization, is proposed and thoroughly analyzed.

OCIS codes: (060.2280) Fiber design and fabrication; (060.2400) Fiber properties; (060.2430) Fibers, single-mode; (060.4005) Microstructured fibers; (060.5295) Photonic crystal fibers.

http://dx.doi.org/10.1364/OPTICA.1.000233

1. INTRODUCTION

The characteristics of a rare-earth-doped fiber are directly responsible for the performance of a fiber-laser system at high average powers and for its ability to maintain diffraction-limited beam quality and high efficiency [1]. One of the main challenges for high-power fiber-laser systems—especially for pulsed ones—is the onset of detrimental nonlinear effects such as stimulated Brillouin scattering, stimulated Raman scattering, and self-phase modulation [2]. Crucially, the impact of all these nonlinear effects scales inversely with the effective mode-field area. Consequently, scaling the mode-field area is the most effective mitigation strategy for nonlinear effects in optical fibers. Additionally, the impact of nonlinear effects can be further mitigated by using shorter fiber lengths. For MW-level-peak-power fiber-laser systems this has led to the development of rod-type fibers with mode-field diameters (MFDs) of more than 50 μm and typical fiber lengths of about 1 m [2,3], most commonly employing a double-cladding structure for the guidance of a high-power low-brightness pump radiation. In practice, these active fibers support the propagation of a few modes, but they can be adjusted to effectively operate with a single mode to enable high beam quality and beam-pointing stability. Unfortunately, operating few-mode fibers in an effective single mode becomes increasingly difficult as the core size is enlarged. Therefore, fiber designs that aim at scaling the MFD of the fundamental mode (FM) to sizes beyond 50 times the signal wavelength [known as very-large-mode-area (VLMA) fibers], while still maintaining nearly diffraction-limited beam quality, have to incorporate mechanisms that enforce effective single-mode operation. Over the last decade many mechanisms have been proposed and incorporated into advanced VLMA fiber designs with

the sole purpose of preferentially amplifying one single mode in a fiber. This can be done by introducing losses to the propagation of the higher-order modes (HOMs), by having structures that provide a higher amplification factor to the FM than to the HOM, or by propagating in a single HOM that ensures reduced mode coupling.

The main two exponents of the first strategy (i.e., HOM attenuation) are the so-called chirally coupled core (CCC) fibers [4] and the leakage-channel fibers (LCFs) [5]. The CCC fibers are characterized by having one or more satellite cores wrapped around the main signal core. This arrangement allows for a resonant coupling of the HOMs of the main core into the satellite core, where the radiation is lost due to very high bending losses. On the other hand, the LCFs rely on an open core structure that provides much higher leakage losses for the HOM than for the FM. This way, after the light has propagated a certain length through this fiber, only the FM will survive. In order to generate the leakage losses, the LCFs have to either dispose of a double-clad structure or exploit bending losses [6].

As mentioned above, the second strategy of enforcing effective single-mode operation is by preferentially amplifying the FM of a fiber. One implementation of this idea is implementing doped areas that are smaller than the fiber core so that the overlap of the HOMs with this doped region (and with it the gain) is significantly reduced with respect to the overlap/gain of the FM [7–9]. However, the most recent and successful implementation of the preferential amplification of the FM in double-clad VLMA fiber is based on a concept known as HOM delocalization [10]. In this approach the fibers are explicitly designed to deform HOMs from the core region. This results in a double benefit: on the one hand the HOMs are more difficult to excite with a Gaussian beam (which are the typical beams found in fiber-laser systems), and, on the other hand, the amplification factor of the HOMs is substantially reduced. Even though, as mentioned above, there are other approaches that can be successfully exploited to achieve single-mode operation in VLMA fibers, the concept of HOM delocalization is one of the newest and most promising ones, and, therefore, it will be thoroughly discussed in this paper. There are currently two main representatives of this approach: the distributed mode filtering (DMF) rod [11], which achieves delocalization by resonantly coupling the HOMs outside of the core, and the large-pitch fibers (LPFs) [10], in which the delocalization of the HOMs is assisted by avoided crossing [12]. Recently a new fiber design that also exploits HOM delocalization assisted by avoided crossings has been proposed: multitrench fiber (MTF) [13]. However, to the best of our knowledge, no experimental demonstration of VLMA MTFs has been published so far.

The underlying idea of the last strategy (i.e., HOM propagation) employs the fact that nearest-neighbor mode coupling in multimode fibers is reduced when propagating in a single HOM, typically a LP_{0m} mode of high order, instead of the FM. At the same time, bend resistance is greatly increased. Thus, in HOM fibers long-period gratings are used to couple light from the FM to the HOM and, after amplification, vice versa [14,15].

Among all the different VLMA fiber designs proposed so far, the LPF concept [10] is the one that currently holds most of the performance records for pulsed VLMA-fiber-laser systems with nearly diffraction-limited beam quality. For example, several hundred watts average power [16], up to 26 mJ pulse energy [17], and 3.8 GW peak power [18] have been demonstrated with these fibers. Moreover, recently a Tm-doped LPF design has been presented that possesses the largest MFD (~65 μm) published so far for effectively single-mode fibers around 2 μm emission wavelength [19]. These results justify why LPFs have become in recent years a reference in performance for pulsed fiber-laser systems, to the point that they are used as a benchmark to evaluate novel fiber designs.

The short length of high-peak-power fiber amplifiers combined with the high average power levels that are routinely delivered by these fibers can easily result in peak thermal loads of several 10 W/m. Such high thermal loads give rise to thermal effects that lead to a significant shrinking of the MFD in VLMA fibers [20]. More importantly, these high thermal loads ultimately result in the onset of mode instabilities [1,21]. Mode instabilities refer to the threshold-like degradation of the output beam of an active fiber observed once a certain average power threshold (in the range of some 100 W or even kW) has been reached. Mode instabilities are firmly believed to be induced by the interplay of thermal effects and modal interference in the active fiber [22–24]. The strong impact of thermal effects in the performance of VLMA fibers illustrated by the examples cited above implies that the influence of the thermal load in high-power fiber amplifiers has to be included as an integral part of the evaluation of any future high-power fiber design.

In the first part of this paper the challenges for mode-area scaling while maintaining single-mode operation are investigated employing common step-index fibers (SIFs) as an example. The next part focuses on maintaining effective single-mode operation in few-mode fibers. Based on this general discussion, the benefits of HOM delocalization are analyzed. Finally, an improved LPF with reduced symmetry is proposed that is expected to offer better performance than the standard LPF design.

2. MODE-FIELD-AREA SCALING

In the following, some general laws of mode-field-area scaling are pointed out. These considerations will be illustrated for a SIF, but they can be easily transferred to other fiber designs and are, therefore, general. Furthermore, the shape of the FM (intensity profile) and its size relative to the core will be used as parameters that have to be maintained during scaling (in the following referred to as normalized mode shape). By doing this, a similar confinement to the core, a similar amplification characteristic, and a similar beam quality at the output of the fiber are ensured independently of the core size. However, when scaling the fiber this way, other mode properties, such as the effective indices or the propagation losses, will necessarily change with the core size.

As is widely known, the core of a SIF has a slightly higher refractive index than the surrounding cladding, which allows

for optical guidance based on total internal reflection. The guiding properties of a SIF can be characterized by the V parameter that is derived from the core diameter $2a$, the wavelength λ, and the numerical aperture NA, according to the following equation:

$$V = \frac{2\pi a}{\lambda} \cdot \mathrm{NA} \approx \frac{2\pi a}{\lambda} \cdot \sqrt{2n_{\mathrm{core}} \cdot \Delta n}. \quad (1)$$

Fibers with a V parameter less than 2.405 and an infinitely extended cladding are strictly single-mode, i.e., the core guides exclusively a nearly Gaussian FM [25]. All SIFs that share a specific V parameter possess modes with identical normalized mode shape regardless of their wavelength, core size, or core–cladding index step. Therefore, scaling should be performed with a constant V parameter, which implies that the MFD increases linearly with the core diameter. In order to increase the mode area while leaving the V parameter constant, the NA has to be decreased linearly; i.e., scaling the core size by a factor of 2 requires the NA to be halved. Additionally, in the weakly guiding approximation, the core–cladding index step Δn is proportional to NA^2. Thus, linearly scaling the core diameter implies a quadratically decreasing index step Δn to maintain a given V parameter.

The validity of this scaling law is not limited to the intentionally designed index steps between the core and cladding of a SIF, but it is also applicable to any other index change [25]. In any waveguide, an index change can be induced by various effects, such as bending [6], the thermal load [26,27], the Kerr nonlinearity, or the so-called resonantly induced refractive index changes [28]. All these effects have to be scaled accordingly, as will be highlighted in the next paragraphs. Even though all of these effects can alter the waveguide properties during operation, the first two are the most common, and therefore our following discussion will revolve around them.

The influence of bending was comprehensively studied in [6], and it has already been shown that mode-area scaling requires the bending radius to be scaled proportional to NA^{-3} [29]. This means that doubling the core diameter and increasing the bending radius by a factor of 2^3 yields equivalent normalized mode shapes, as this scales the applied index profile quadratically. The cubic behavior of the bending radius highlights the need for straight rod-type structures for MFDs beyond 50 μm [2,10]. By keeping the fiber straight, the rod-type design avoids any bending-induced mode deformations and reduces mode mixing due to microbendings [30].

The thermally induced index changes that occur in active fibers due to quantum-defect heating during amplification can be approximated by a parabolic index gradient inside the doped area and a logarithmic decay outside of this region [26,28]. With constant material parameters and geometries, the thermal load caused by optical amplification in an active fiber is directly proportional to the thermally induced index gradient. In terms of mode-area scaling, this index gradient has to be treated identically to the index step of SIFs; i.e., the thermal load decreases quadratically when scaling the core size. In other words, doubling the core diameter and reducing the thermal load by a factor of 4, leads to identical normalized mode shapes. This dependence has been experimentally verified in [20].

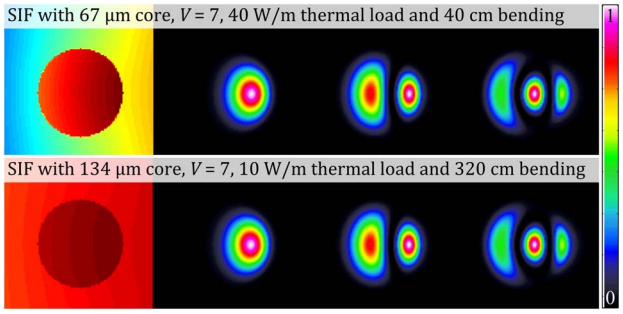

Fig. 1. Modes of a SIF with $V = 7$ and core diameters of 67 and 134 μm, respectively, under the influence of thermal load and bending.

In Fig. 1, these scaling laws are exemplarily illustrated for a SIF with $V = 7$ under thermal load and bending. So, as mentioned before, in order to scale the MFD by a factor of 2 (from 50 to 100 μm in the unbent case) while maintaining the same normalized mode shapes, the core diameter has to be doubled (from 67 to 134 μm in this case), and the index step has to be reduced by a factor of 4 to yield the same V parameter. Additionally, the thermal load also has to be reduced by a factor of 4, and, simultaneously, the bending radius has to be increased by a factor of 8. Applying these scaling principles leads to the same mode set, which is proportionally scaled. In consequence, it can be deduced that larger cores become increasingly more sensitive to perturbations.

The quadratically increasing influence of index changes when scaling the MFD is also valid for photonic-crystal fibers (PCFs). In particular, the tolerance to the index matching between the doped core material and the undoped surrounding cladding material of an active PCF becomes quadratically smaller for larger core diameters [31].

Finally, a general dependence of mode-area scaling on the wavelength can also be deduced from Eq. (1). For a given NA, the core diameter can be scaled linearly with the wavelength. For instance, a wavelength of 2 μm as used in Tm-doped fibers allows for a two times larger MFD compared to 1 μm while maintaining the same NA and V parameter.

All scaling properties are summarized in Table 1. For any mode-area-scalable fiber concept it is vital to study the absolute parameters that most severely alter the mode properties. In the case of active VLMA fibers these are the index-matching

Table 1. Scaling Factors of Relevant Fiber Parameters in Order to Maintain the Normalized Mode Shapes of a SIF with Constant V Parameter

Parameter	Scaling Factor (V = const)
Mode-field diameter	$\cdot x$
Core diameter	$\cdot x$
Mode-field area	$\cdot x^2$
Index contrast Δn	$/x^2$
Index-matching accuracy	$/x^2$
Bending radius	$\cdot x^3$
Thermal load	$/x^2$

accuracy (especially for PCFs), bending, and the thermo-optic effect. Furthermore, in general it is sufficient to calculate these effects for one distinct MFD, e.g., 50 μm, and apply the scaling properties for larger variants or different wavelengths.

3. EFFECTIVE SINGLE-MODE OPERATION

This section highlights different concepts for effective single-mode operation.

Single-clad SIFs can be strictly single-mode for $V < 2.405$. Theoretically, a SIF can be indefinitely scaled if the V parameter is kept constant, but this would require a linear reduction of the NA or a quadratic reduction of the index contrast, which has some technological limitations, in particular for doped cores. In practice, an accuracy of ± 0.01 can be achieved in the NA, which leads to few-mode guidance for MFDs of more than 20 μm at 1 μm wavelength, i.e., in Yb-doped fibers. A more accurate control of the NA can be achieved by index-guiding PCFs [32]. In these fibers averaging over the small low-index inclusions in the cladding leads to an effective NA, which allows for strictly single-mode (single-clad) fibers with up to 33 μm MFD [33]. For larger cores the scaling requires an even better control of the effective NA than what is achievable today, and, consequently, these fibers become few-mode again.

Effective single-mode operation can be enforced in multimode fibers by suppressing the HOMs as they propagate along the waveguide. A very strong suppression mechanism can arise from the differential modal propagation losses induced by an infinite or absorbing cladding (i.e., single-clad fibers) [34], by bending [6], or by resonances [4,35]. All these mechanisms are based on higher propagation losses for the HOMs compared to the FM. By choosing an appropriate fiber length the HOMs can be suppressed by, e.g., 20 dB, and effective single-mode operation is achieved. However, in general the propagation loss difference between different modes collapses for larger core sizes, which significantly reduces the efficiency of this discrimination mechanism as the core diameter is increased [6,31]. Additionally, since in these fibers the modal energy is typically lost at the outer fiber boundary, the propagation losses are strongly decreased if a thermally induced parabolic index profile is created during active operation, since the modes become progressively better confined around the fiber axis. Moreover, the propagation losses of straight double-clad fibers are negligible as the double-clad structure that strongly confines the pump also confines the signal radiation [34]. However, it can be argued that some sort of propagation losses for individual modes may be achieved by mode mixing [30], but their exact value can hardly be calculated. In conclusion, the HOM discrimination due to propagation losses is not scalable and cannot be applied to most high-power fiber designs.

Theoretically, effective single-mode operation can be realized in few-mode fibers only by adjusting the excitation conditions [30]. A fiber amplifier is typically seeded by an oscillator or amplifier delivering a nearly Gaussian beam profile. Therefore, the modal excitation with a Gaussian beam profile is of crucial interest. This Gaussian beam can be size-, position-, and angle-mismatched with respect to the ideal case, which leads to a multidimensional parameter space for the evaluation of the excitation. In a strictly single-mode fiber any mismatch will only decrease the power content in the FM, but in a multimode fiber this power can be coupled to guided HOMs. To illustrate this effect the excitation of the mode set of a SIF with V parameter of 7 is simulated for a size- and position-matched Gaussian beam, which is tilted by an increasing angle (Fig. 2). It can be seen that one distinct HOM, namely the LP_{11}, is predominantly excited for small angle mismatch. For larger angles LP_{02} and LP_{12} are excited as well. Modes of higher orders have progressively finer structured intensity profiles and phase patterns, which makes the accidental excitation of these modes by an incident Gaussian beam more and more unlikely. Pure excitation of the FM becomes increasingly difficult as the core size and, with it, the number of modes are scaled [30].

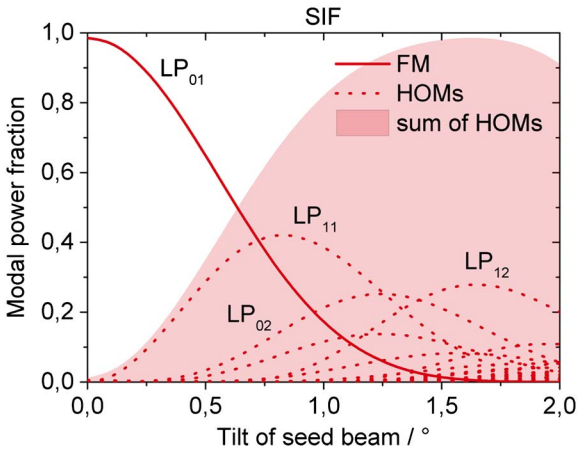

Fig. 2. Excitation of the modes of a SIF with $V = 7$ and 50 μm MFD as a function of the tilt of the incident mode-matched Gaussian beam. The solid line represents the power fraction in the FM, whereas the dashed lines represent the power fraction in each HOM. The shaded area illustrates the total power fraction contained in all the HOMs.

4. HOM DELOCALIZATION

As briefly mentioned in Section 1, a promising novel approach for effective single-mode operation is HOM delocalization. This concept influences simultaneously the excitation and amplification of modes inside a few-mode fiber. The LPF was the first representative of a fiber design exploiting HOM delocalization, and it showed a significant increase in the mode-instability threshold [10,16]. In the meantime this operation principle has been transferred to other fiber designs, namely the DMF fiber [11] and MTF [13], both based on resonant effects. These different approaches highlight the fundamental nature of this operation principle.

The principle of operation of HOM delocalization will be discussed in the following. Figure 3 illustrates the mode excitation of a fiber employing HOM delocalization, in this exemplary case and without loss of generality, and a LPF, a structure that is discussed in detail later. As the FM maintains a nearly Gaussian profile, its excitation is very similar for LPF (Fig. 3) and SIF (Fig. 2). However, the HOM excitation is fairly different. While for a SIF the HOM power content (shaded area) is distributed among only a few distinct modes, the strong HOM

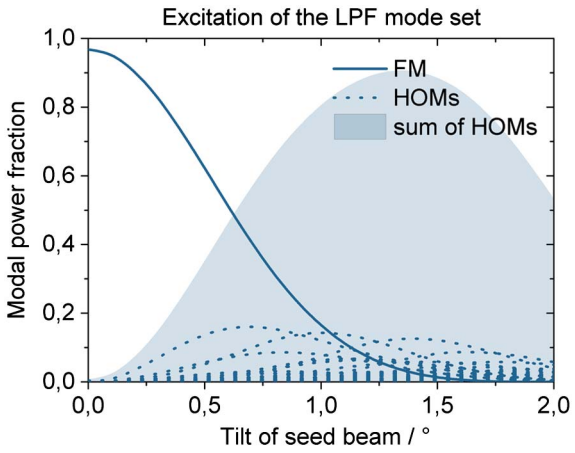

Fig. 3. Excitation of the modes of a LPF with 50 μm MFD as a function of an increasing tilt of the incident Gaussian beam. The solid line represents the power fraction in the FM, whereas the dashed lines represent the power fraction in each HOM. The shaded area illustrates the total power fraction contained in all the HOMs.

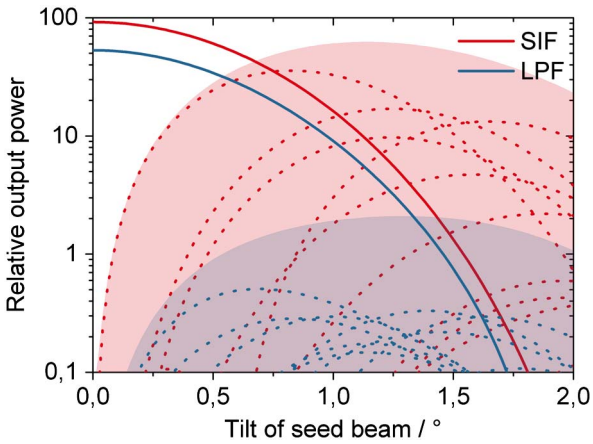

Fig. 4. Relative output power in the FM (solid lines) and the HOMs (dotted lines) for a SIF (red) and a LPF (blue). The combined power of all HOMs is shown as a shaded region.

deformations distribute the same overall HOM power content into many different HOMs. This difference seems to be negligible at first glance, but the combination of excitation and amplification reveals a very strong suppression of HOMs in a fiber amplifier.

The gain of an individual mode in an active fiber is mainly determined by the overlap γ of the mode with the doped region,

$$\gamma = \frac{\int I \mathrm{d}A_{\mathrm{doped}}}{\int I \mathrm{d}A}. \tag{2}$$

This parameter can be used to evaluate the quality of HOM suppression by analyzing the differential amplification of each relevant HOM with respect to the FM. In the simplest approximation the amplification of different modes can be calculated by assuming a small-signal gain behavior:

$$G = \exp(\gamma g_0 l). \tag{3}$$

It has to be noted that most high-power VLMA fibers are not operated in small-signal gain, but they operate near or above the saturation intensity instead [36]. However, even in saturated cases, the general conclusions extracted from the small-signal gain case are valid. Typical rod-type fibers possess a small-signal gain greater than 30 dB/m, but their effective gain is lowered to about 20 dB/m due to saturation effects. Consequently, the amplification characteristics of these fibers can be approximated, in the simplest case, by assuming an effective small signal gain of 20 dB ($g_0 l = 4.6$). In order to convey an idea of the impact of the different modal overlaps with the doped region, some examples can be calculated. Thus, while a mode with 100% overlap would experience an amplification factor of 100, modes with 85%, 40%, and 20% possess amplification factors of 50, 6, and just 3, respectively. Clearly, modes with lower overlap values can be dramatically suppressed at the output of the fiber (with respect to the power content of the FM) by differential gain.

The combination of excitation and amplification is illustrated in Fig. 4. The basis for this graph is the power fraction in each mode (taken from Figs. 2 and 3), which is amplified according to their individual doping overlap [Eqs. (2) and (3)]. The differential amplification of each mode leads to a very strong suppression of individual HOMs. Clearly, not only the power content of each individual mode but also the combined HOM content (shaded area) is dramatically reduced for the LPF employing HOM delocalization compared to a few-mode SIF. It should be noted that this evaluation is only an example to show the general strength of this effect. With higher gain values the suppression of HOMs is even stronger. Furthermore, effects such as thermal load may alter the overlap with the doped region of the modes during active operation, an effect that will be discussed later on.

Considering the excitation and amplification in combination brings an interesting fork in the design process of an active fiber. The question is which HOMs should be further considered in the design process. This is a crucial decision that determines how to optimize a given design. Interestingly the set of relevant HOMs is different if the fiber is going to be used as an oscillator or as an amplifier. In the first case the relevant HOMs are those exhibiting the higher overlap with the doped region, since these will see the highest gain. On the other hand, if the fiber is going to be used as an amplifier, many modes can be excluded due to their negligible "accidental" excitability. For instance, LP_{31}-like HOMs can have higher overlaps with the doped region than LP_{1m}-like HOMs [37], but these fine structured modes are difficult to excite with a Gaussian-like beam, and, therefore, they have no impact on the single-mode operation of a fiber amplifier.

Typically the LP_{1m}-like HOMs are the most relevant modes since they are the first to be strongly excited in a fiber with a slight misalignment of the seed beam. Furthermore, these modes usually appear during mode instabilities [1]. Therefore, the suppression of LP_{1m}-like HOMs is currently one of the main goals of advanced high-power VLMA fibers designed to be used primarily as amplifiers.

In conclusion, HOM delocalization can be a very strong mechanism to enforce effective single-mode operation of a fiber amplifier. A further refinement for HOM delocalizing fibers can be thought of: introducing absorptive regions in the pump core of these fibers. In such fibers the delocalized HOMs possess a large overlap with the absorbing material, whereas the FM will only have very limited contact with it. Thus, with proper gain/loss management [38], the HOMs can be suppressed further as they propagate along the fiber.

5. LARGE-PITCH FIBER

The LPF concept exploits the enormous design flexibility of PCFs [32,39] to achieve and maximize HOM delocalization. While the modal-sieve concept employing propagation losses can be used for HOM suppression of a single-clad PCF [40], this modal discrimination mechanism cannot be exploited any longer for double-clad fibers. Nevertheless, the low-index structure can still be arranged in such a way that an efficient HOM delocalization can be achieved. The principle of HOM deformation has already been discussed (Figs. 3 and 4), but the LPF structure employs additional features worthwhile to highlight.

The mode set of an exemplary LPF design for increasing thermal load is illustrated in Fig. 5. While for a SIF the LP_{11} typically possesses the highest overlap among the LP_{1m}-modes, a LP_{13}-like HOM has the highest overlap for the LPF structure. The exchange of mode orders has a very beneficial effect, when applying thermal load to this structure (i.e., in active operation). As all LP_{1m}-like HOMs share the same symmetry class they are involved in avoided crossings [12,41]. Therefore, the LP_{13}-like HOM is deformed and the LP_{12}-like HOM takes over its role as the most confined HOM for an increasing thermal load. A further increase of thermal load leads to the final LP_{11}-like HOM taking over the role as the HOM with the highest overlap. In consequence, avoided crossings can decrease the HOM overlap for a large range of thermal loads, and, therefore, the effect of HOM delocalization becomes even stronger. The evaluation of HOM delocalization as performed in Fig. 4 (i.e., a "cold" fiber) is a worst-case scenario for a LPF.

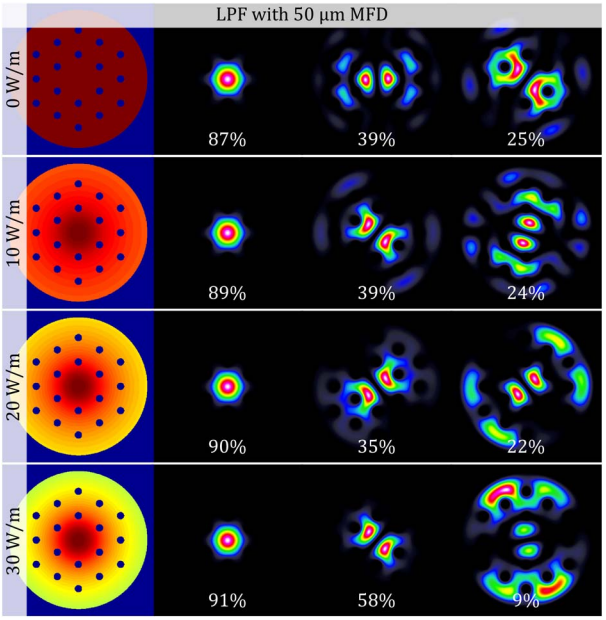

Fig. 5. Structure and modes of a LPF with 50 µm MFD at 1030 nm wavelength for increasing thermal load. The FM and two LP_{1m}-like HOMs with the largest overlap with the doped region are illustrated.

Another outstanding property of the LPF design is its scalability. The modal intensity profiles of a LPF behave, under proportional scaling of the structure, like those of an ideal SIF with a constant V parameter. This effect is well known for endlessly single-mode PCFs [40], where the effective V parameter of an approximately infinite PCF becomes independent of the hole-to-hole spacing (pitch) Λ for relative hole diameters $d/\Lambda > 0.1$ and $\Lambda > 10 \cdot \lambda$. Therefore, the LPF structure can be scaled proportionally to larger cores while, e.g., the normalized mode shapes are maintained. Additionally, this also implies that the LPF design operates over a very large wavelength region, since increasing the pitch is equivalent to decreasing the wavelength. This scalability is not a general feature of HOM delocalization but a special feature of the nonresonant design approach of the LPF.

6. LOW-SYMMETRY LARGE-PITCH FIBER

Despite the strong effective single-mode operation of a LPF, the thermal load will (for a high enough power) end up strongly modifying the waveguide and with it its guiding properties, in particular the amount of HOM delocalization. In this section we propose a new LPF design with increased HOM delocalization, which improves the performance at high thermal loads compared to the standard LPF.

The symmetry of a waveguide structure influences the symmetry of the guided modes [42]. Even though this is true for all modes, the FM is the one being least influenced by symmetry changes of the cladding; instead it will adapt itself to the inner core geometry. In contrast, the LP_{1m}-like HOMs prefer mirror symmetries. Thus, by altering the fiber symmetry, these classes of modes can be further deformed to increase the HOM delocalization [43].

On the way to less symmetric structures spirals are an interesting idea, which has been proposed by our group [44] and adopted by others [37,45]. In theory spiral structures can be asymmetric without any mirror or rotational symmetries, but the HOM delocalization is mainly affected by geometries with a structure size comparable to the transverse wavelength of the modes [39,43]. For some spiral structures it can be seen that the HOMs are swirled out of the core region, which can enhance the HOM delocalization.

A design implementing such a swirling structure, but still based on a hexagonal lattice for standard stack-and-draw technique, is proposed in Fig. 6. This low-symmetry LPF exploits holes of different diameters to increase HOM delocalization.

7. METHODOLOGY AND COMPARABILITY

The evaluation of fiber designs is a very difficult task since it involves sweeping a multidimensional parameter field. Furthermore, the simulation of a fiber amplifier can become very

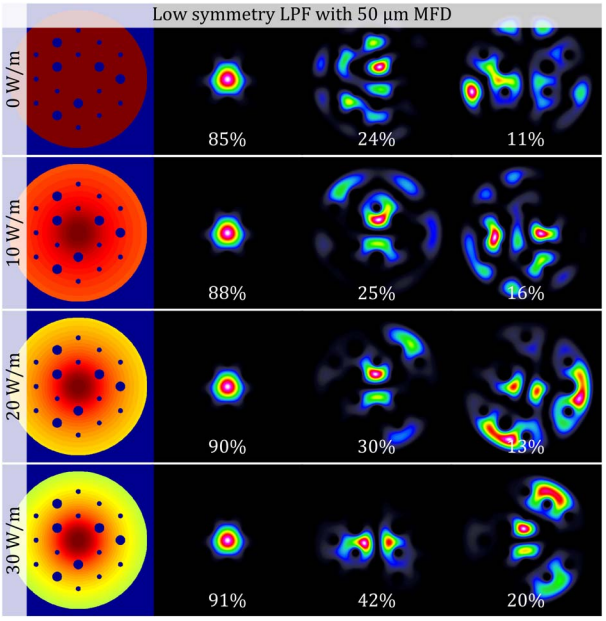

Fig. 6. Structure and modes of a low-symmetry LPF with 50 µm MFD (1030 nm wavelength) for increasing thermal load. The FM and the LP_{1m}-like HOMs with the highest overlap with the doped region are illustrated.

challenging and computationally intense as soon as effects such as thermal waveguide changes, mode coupling, and mode instabilities are included. In fact, the development of such simulation tools is a topic of ongoing research in several groups around the world. In many cases the inclusion of these effects requires some assumptions, which have not been understood in detail and/or have yet to be verified experimentally. Herein, we propose a simple, yet powerful, method to estimate the performance of new fiber designs, which can be deduced purely from the fiber design (i.e., there is no need to simulate the laser operation of the fiber). This method is based on the experimental observation showing that a reduced overlap of the HOMs with the doped region is beneficial in terms of the mode-instability threshold and that thermal waveguide changes have a strong impact on the guiding properties of a high-power fiber design. There are many additional parameters that can and should be considered for the design of a fiber amplifier or laser—such as the signal and pump wavelength, doping concentration, pump absorption, and fiber length—but again, this complicates the evaluation process and distracts from the fundamental operating principle of different fiber designs. In fact, none of this is strictly necessary to carry out an estimation of the performance level of a new fiber design. According to our simulations and experimental observations, the evolution of the modal overlap with the doped region with an increasing thermal load seems to be a very important property that allows performing such first estimations of the expected performance of a new high-power fiber design based on HOM delocalization.

For this evaluation the refractive index profile of a given fiber design is arranged and the doped area is defined. Based on the analytic approximations from [26,28] the thermally induced index change can be added and the corresponding mode set is calculated. Finally, Eq. (2) is used to calculate the overlap with the doped region for each mode.

Additionally to the methodology, the comparability of different fiber designs is also a very error-prone task. A proper choice of parameters is necessary to grant comparability among different fiber designs. As has been shown in the first part, the scaling laws require the MFD to be constant. Furthermore, for the design of an amplifier, the evolution of the signal power along the fiber (which ultimately determines the strength of nonlinear effects) should be comparable, by maintaining the doped area, pump-clad area, doping concentration, and FM overlap with the doped region. On the other hand, geometrical parameters such as the core diameter or the hole size do not have to be matched as they bear no meaning for physical effects.

For the following evaluation a MFD of 50 µm, a cladding diameter of 200 µm, a doped region with 50 µm diameter, and a FM overlap with a doped region of about 85% are fixed. These parameters are achieved for a LPF with a pitch of 35 µm and $d/\Lambda = 0.3$. For the low-symmetry LPF the relative hole diameters can be chosen as 0.2 and 0.4 for the smaller and larger holes, respectively. All simulations are performed at a wavelength of 1030 nm, which implies a Yb-doped fiber amplifier. Such systems have reached average output powers of 300 W with fiber lengths of 1 m. In the counter-pumped configuration an exponential evolution of the thermal load from some W/m up to about 40 W/m can be expected, which highlights the necessity to evaluate this thermal range.

With the scaling laws given above, this evaluation is equivalent to a fiber with, e.g., a two times larger core diameter and a four times smaller thermal load. More interestingly, this evaluation can be directly transferred to a Tm-based fiber amplifier with a signal around 2 µm and the same MFD but with four times higher thermal load—these values suit the experimental situation very well due to the increased quantum defect of Tm-doped silica pumped around 790 nm.

8. PERFORMANCE EVALUATION

Figure 7 depicts the evolution of the modal overlaps with increasing thermal load for the LPF fiber design (blue lines) and the low-symmetry LPF (green lines). As already illustrated in Fig. 3, the general trend of continually increased HOM overlap with increasing thermal load (e.g., as would be seen in a SIF) is interrupted by two avoided crossings. Over a large thermal load range (0–20 W/m) the performance of the LPF is even better than that of the "cold" fiber. Consequently the HOM overlap with the doped region averaged over the whole thermal load range considered herein is 45%. The proposed low-symmetry LPF (Fig. 6, green lines) allows us to enhance the HOM delocalization even further, leading to a mean HOM overlap of just 32%. In combination with the exponential gain evolution and excitation, this design is expected to show an even more robust effective single-mode operation and higher mode-instability threshold.

For the experimental realization of a fiber design the impact of manufacturing tolerances has to be studied as well. For a

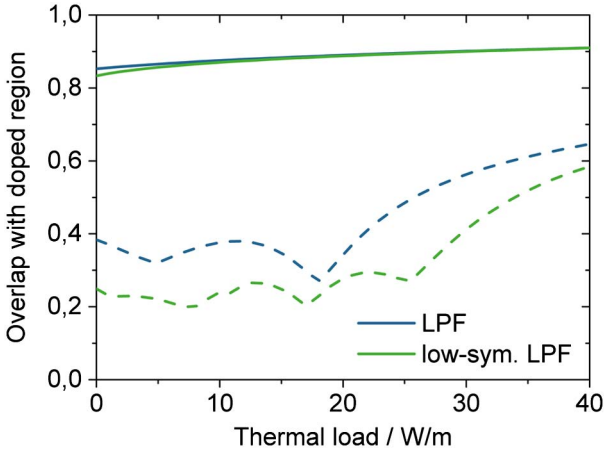

Fig. 7. Evolution of the modal overlap with the doped region for the FM (solid lines) and for the most relevant HOM (usually a LP_{1m}-like HOM and represented by dotted lines) with increasing thermal load for the LPF (blue) and for the low-symmetry LPF (green).

PCF the index matching between the doped region and the host material is crucial [31]. An index mismatching accuracy of −2e − 5 has been achieved experimentally [20]. Therefore, this accuracy has been assumed in the following evaluation, summarized in Fig. 8. A lower core index can deform the FM of the waveguide. Due to the combination of smaller and larger air holes the low-symmetry LPF is more sensitive to an index depression of the doped region than the standard LPF. This can affect the efficiency and beam quality of the low-symmetry fiber design for very low average powers (even though the relative air hole sizes can be fine-tuned to get rid of this effect at low powers). However, in high-power operation the thermal load necessary to overcome these deformations is easily reached and the index depression will hardly affect the performance. At the same time, the HOM suppression is improved as the HOMs are pushed out of the core region. Therefore, the index depression effectively shifts the region

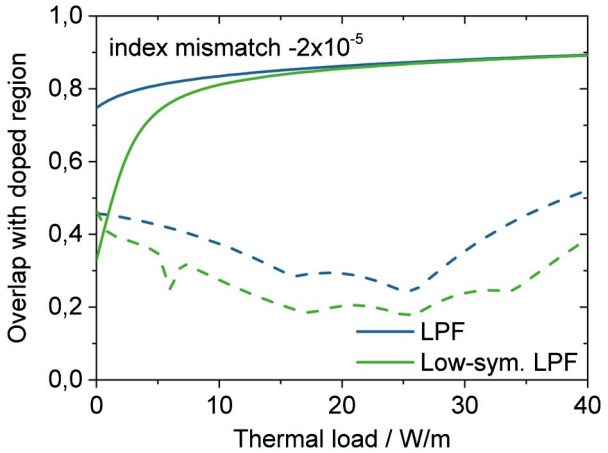

Fig. 8. Evolution of the modal overlap with the doped region for the FM (solid lines) and for the most relevant HOM (usually a LP_{1m}-like HOMs and represented by dotted lines) assuming a core index mismatch of −2e − 5 as a function of the thermal load for the LPF (blue) and for the low-symmetry LPF (green).

with strong HOM suppression to higher thermal loads compared to a perfectly matched fiber (Fig. 7). For the range of thermal loads studied herein the mean HOM overlap is 37% and 26% for the LPF and low-symmetry LPF, respectively. Therefore, the improved HOM delocalization especially for high thermal loads of the low-symmetry LPF is expected to outweigh any possible performance degradation at low powers.

Finally, and as mentioned above, the beam quality is a very important parameter. One might expect a decrease in beam quality for the asymmetric design, but due to the partly increased hole sizes, the FM confinement and beam quality are maintained with respect to the standard LPF. The calculated FM of both designs possesses a theoretical $M^2 < 1.2$.

9. CONCLUSION

Fiber-laser systems have shown their benefits regarding high efficiency, diffraction-limited beam quality, and easy thermal management. However, the long interaction length of the tightly confined light with the material of the fiber makes these waveguides very sensitive to nonlinear effects. Thus, the performance evolution of fiber-laser systems has been enabled by the development of fibers that can mitigate nonlinear effects. Over the years it has become clear that the most effective technique for the mitigation of nonlinear effects in an active fiber is scaling of the MFD. However, as highlighted in the paper, there are some physical laws that are obeyed when scaling the size of a fiber, and they result in the fiber becoming more and more sensitive to external perturbations. Additionally, with the current technological limitations fibers with very large MFDs (>50 μm) become few-mode. Therefore, in order to avoid a penalization in the beam quality and/or pointing stability of the radiation emitted by fiber-laser systems, advanced techniques are required to preserve effective single-mode operation even with VLMAs. From the techniques proposed so far so-called HOM delocalization seems to be the most robust and promising. In this technique, the inner structure of the fiber is designed in such a way that the HOMs are pushed away from the core and/or doped region of the fiber. As thoroughly discussed above, this brings a twofold benefit: on the one hand the HOMs have a lower overlap with the doped region and, therefore, undergo a significantly lower amplification factor than the FM; on the other hand, the delocalized HOMs cannot be efficiently excited by an incoming Gaussian beam, which results in the energy being spread over many HOMs instead of being concentrated in just one. The distribution of power in many HOMs, as has been shown in the paper, is advantageous since it results in a strong preferential amplification of the FM. Additionally, HOM delocalization is strongly suspected to be able to increase the mode-instability threshold in fiber-laser systems. HOM delocalization was first exploited in LPF and later incorporated in other designs such as the DMF rod or the MTF. Currently, the LPF design has enabled most of the performance records in ultrafast fiber-laser systems with several hundred watts average power, up to 26 mJ pulse energy, and 3.8 GW peak power. Another outstanding property of the LPF design is its

scalability: the LPF structure can be scaled proportionally to larger cores while the normalized mode shapes are maintained.

A further refinement of the LPF design has been presented in this paper, the so-called low-symmetry LPF. The inner structure of this design has a considerably reduced number of symmetries resulting in a stronger delocalization of the HOMs. For the first time, to the best of our knowledge, a comparative analysis of different fiber designs including index depressions of the doped region and a variable thermal load has been presented. From this study it can be expected that a low-symmetry LPF can achieve an improved delocalization of the HOMs over a broader thermal load range than the standard LPF, which should enable more robust effective single-mode operation.

FUNDING INFORMATION

German Federal Ministry of Education and Research (BMBF); European Research Council (ERC) (617173 ACOPS and240460 PECS); Thuringian Ministry for Economy, Labour and Technology (TMWAT, Project No. 2011 FGR 0103); European Social Fund (ESF).

REFERENCES

1. C. Jauregui, J. Limpert, and A. Tünnermann, "High-power fibre lasers," Nat. Photonics **7**, 861–867 (2013).
2. J. Limpert, F. Röser, and D. Schimpf, "High repetition rate gigawatt peak power fiber laser systems: challenges, design, and experiment," IEEE J. Sel. Top. Quantum Electron. **15**, 159–169 (2009).
3. J. Limpert, O. Schmidt, J. Rothhardt, F. Röser, T. Schreiber, A. Tünnermann, S. Ermeneux, P. Yvernault, and F. Salin, "Extended single-mode photonic crystal fiber lasers," Opt. Express **14**, 2715–2720 (2006).
4. X. Ma, C. Zhu, I.-N. Hu, A. Kaplan, and A. Galvanauskas, "Single-mode chirally-coupled-core fibers with larger than 50 μm diameter cores," Opt. Express **22**, 9206–9219 (2014).
5. L. Dong, H. A. McKay, L. Fu, M. Ohta, A. Marcinkevicius, S. Suzuki, and M. E. Fermann, "Ytterbium-doped all glass leakage channel fibers with highly fluorine-doped silica pump cladding," Opt. Express **17**, 8962–8969 (2009).
6. J. P. Koplow, D. A. V. Kliner, and L. Goldberg, "Single-mode operation of a coiled multimode fiber amplifier," Opt. Lett. **25**, 442–444 (2000).
7. J. R. Armitage, "Three-level fiber laser amplifier: a theoretical model," Appl. Opt **27**, 4831–4836 (1988).
8. B. G. Ward, "Finite element analysis of photonic crystal rods with inhomogeneous anisotropic refractive index tensor," IEEE J. Quantum Electron. **44**, 150–156 (2008).
9. T. Eidam, S. Hädrich, F. Jansen, F. Stutzki, J. Rothhardt, H. Carstens, C. Jauregui, J. Limpert, and A. Tünnermann, "Preferential gain photonic-crystal fiber for mode stabilization at high average powers," Opt. Express **19**, 8656–8661 (2011).
10. J. Limpert, F. Stutzki, F. Jansen, H.-J. Otto, T. Eidam, C. Jauregui, and A. Tünnermann, "Yb-doped large-pitch fibres: effective single-mode operation based on higher-order mode delocalisation," Light Sci. Appl. **1**, 1–5 (2012).
11. T. T. Alkeskjold, M. Laurila, J. Weirich, M. M. Johansen, C. B. Olausson, O. Lumholt, D. Noordegraaf, M. D. Maack, and C. Jakobsen, "Photonic crystal fiber amplifiers for high power ultrafast fiber lasers," Nanophotonics **2**, 369–381 (2013).
12. F. Jansen, F. Stutzki, C. Jauregui, J. Limpert, and A. Tünnermann, "Avoided crossings in photonic crystal fibers," Opt. Express **19**, 13578–13589 (2011).
13. D. Jain, C. Baskiotis, and J. K. Sahu, "Mode area scaling with multi-trench rod-type fibers," Opt. Express **21**, 1448–1455 (2013).
14. S. Ramachandran, J. W. Nicholson, S. Ghalmi, M. F. Yan, P. Wisk, E. Monberg, and F. V. Dimarcello, "Light propagation with ultralarge modal areas in optical fibers," Opt. Lett. **31**, 1797–1799 (2006).
15. X. Peng, K. Kim, M. Mielke, T. Booth, J. W. Nicholson, J. M. Fini, X. Liu, A. DeSantolo, P. S. Westbrook, R. S. Windeler, E. M. Monberg, F. V. DiMarcello, C. Headley, and D. J. DiGiovanni, "Higher-order mode fiber enables high energy chirped-pulse amplification," Opt. Express **21**, 32411–32416 (2013).
16. F. Stutzki, F. Jansen, T. Eidam, A. Steinmetz, C. Jauregui, J. Limpert, and A. Tünnermann, "High average power large-pitch fiber amplifier with robust single-mode operation," Opt. Lett. **36**, 689–691 (2011).
17. F. Stutzki, F. Jansen, A. Liem, C. Jauregui, J. Limpert, and A. Tünnermann, "26 mJ, 130 W *Q*-switched fiber-laser system with near-diffraction-limited beam quality," Opt. Lett. **37**, 1073–1075 (2012).
18. T. Eidam, J. Rothhardt, F. Stutzki, F. Jansen, S. Hädrich, H. Carstens, C. Jauregui, J. Limpert, and A. Tünnermann, "Fiber chirped-pulse amplification system emitting 3.8 GW peak power," Opt. Express **19**, 255–260 (2011).
19. F. Jansen, F. Stutzki, C. Jauregui, J. Limpert, and A. Tünnermann, "High-power very large mode-area thulium-doped fiber laser," Opt. Lett. **37**, 4546–4548 (2012).
20. F. Jansen, F. Stutzki, H.-J. Otto, T. Eidam, A. Liem, C. Jauregui, J. Limpert, and A. Tünnermann, "Thermally induced waveguide changes in active fibers," Opt. Express **20**, 3997–4008 (2012).
21. T. Eidam, C. Wirth, C. Jauregui, F. Stutzki, F. Jansen, H.-J. Otto, O. Schmidt, T. Schreiber, J. Limpert, and A. Tünnermann, "Experimental observations of the threshold-like onset of mode instabilities in high power fiber amplifiers," Opt. Express **19**, 13218–13224 (2011).
22. C. Jauregui, T. Eidam, H.-J. Otto, F. Stutzki, F. Jansen, J. Limpert, and A. Tünnermann, "Temperature-induced index gratings and their impact on mode instabilities in high-power fiber laser systems," Opt. Express **20**, 440–451 (2012).
23. A. V. Smith and J. J. Smith, "Mode instability in high power fiber amplifiers," Opt. Express **19**, 10180–10192 (2011).
24. B. Ward, C. Robin, and I. Dajani, "Origin of thermal modal instabilities in large mode area fiber amplifiers," Opt. Express **20**, 11407–11422 (2012).
25. A. Ghatak and K. Thyagarajan, *Introduction to Fiber Optics* (Cambridge University, 1998).
26. L. Zenteno, "High-power double-clad fiber lasers," J. Lightwave Technol. **11**, 1435–1446 (1993).
27. D. C. Brown and H. J. Hoffman, "Thermal, stress, and thermo-optic effects in high average power double-clad silica fiber lasers," IEEE J. Quantum Electron. **37**, 207–217 (2001).
28. M. J. F. Digonnet, R. W. Sadowski, H. J. Shaw, and R. H. Pantell, "Resonantly enhanced nonlinearity in doped fibers for low-power all-optical switching: a review," Opt. Fiber Technol. **3**, 44–64 (1997).
29. R. T. Schermer, "Mode scalability in bent optical fibers," Opt. Express **15**, 15674–15701 (2007).
30. M. E. Fermann, "Single-mode excitation of multimode fibers with ultrashort pulses," Opt. Lett. **23**, 52–54 (1998).
31. F. Jansen, F. Stutzki, H.-J. Otto, M. Baumgartl, C. Jauregui, J. Limpert, and A. Tünnermann, "The influence of index-depressions in core-pumped Yb-doped large pitch fibers," Opt. Express **18**, 26834–26842 (2010).
32. J. C. Knight, "Photonic crystal fibres," Nature **424**, 847–851 (2003).
33. J. Limpert, A. Liem, M. Reich, T. Schreiber, S. Nolte, H. Zellmer, A. Tünnermann, J. Broeng, A. Petersson, and C. Jakobsen, "Low-nonlinearity single-transverse-mode ytterbium-doped photonic crystal fiber amplifier," Opt. Express **12**, 1313–1319 (2004).
34. E. Snitzer, "Proposed fiber cavities for optical masers," J. Appl. Phys. **32**, 36–39 (1961).
35. S. Février, R. Jamier, J.-M. Blondy, S. L. Semjonov, M. E. Likhachev, M. M. Bubnov, E. M. Dianov, V. F. Khopin, M. Y. Salganskii, and A. N. Guryanov, "Low-loss singlemode large mode

area all-silica photonic bandgap fiber," Opt. Express **14**, 562–569 (2006).
36. J. R. Marciante, "Gain filtering for single-spatial-mode operation of large-mode-area fiber amplifiers," IEEE J. Sel. Top. Quantum Electron. **15**, 30–36 (2009).
37. R. Dauliat, D. Gaponov, A. Benoit, F. Salin, K. Schuster, R. Jamier, and P. Roy, "Inner cladding microstructuration based on symmetry reduction for improvement of singlemode robustness in VLMA fiber," Opt. Express **21**, 18927–18936 (2013).
38. J. Limpert, H. Zellmer, A. Tünnermann, T. Pertsch, and F. Lederer, "Suppression of higher order modes in a multimode fiber amplifier using efficient gain-loss-management (GLM)," in *Advanced Solid-State Lasers*, M. Fermann and L. Marshall, eds., Vol. **68** of Trends in Optics and Photonics Series (Optical Society of America, 2002), paper MB20.
39. P. S. J. Russell, "Photonic crystal fibers," Science **299**, 358–362 (2003).
40. T. A. Birks, J. C. Knight, and P. S. J. Russell, "Endlessly single-mode photonic crystal fiber," Opt. Lett. **22**, 961–963 (1997).
41. J. von Neumann and E. P. Wigner, "Über das Verhalten von Eigenwerten bei adiabatischen Prozessen," Phys. Z. **30**, 467–470 (1929).
42. P. R. McIsaac, "Symmetry-induced modal characteristics of uniform waveguides—I: summary of results," IEEE Trans. Microwave Theor. Tech. **23**, 421–429 (1975).
43. F. Stutzki, F. Jansen, C. Jauregui, J. Limpert, and A. Tünnermann, "Non-hexagonal large-pitch fibers for enhanced mode discrimination," Opt. Express **19**, 12081–12086 (2011).
44. J. Limpert, "Large-pitch fibers: pushing very large mode areas to highest powers," in *International Conference on Fibre Optics and Photonics*, OSA Technical Digest (online) (Optical Society of America, 2012), paper T2A.1.
45. E. Coscelli, C. Molardi, A. Cucinotta, and S. Selleri, "Symmetry-free Tm-doped photonic crystal fiber with enhanced mode area," IEEE J. Sel. Top. Quantum Electron. **20**, 4400207 (2014).

Research Article Vol. 1, No. 4 / October 2014 / Optica 243

Dynamics of cascaded resonant radiations in a dispersion-varying optical fiber

A. Bendahmane,[1] F. Braud,[1] M. Conforti,[1] B. Barviau,[1,2] A. Mussot,[1] and A. Kudlinski[1,*]

[1]Laboratoire PhLAM UMR CNRS 8523, IRCICA USR CNRS 3380, Université Lille1, 59655 Villeneuve d'Ascq, France

[2]CORIA UMR CNRS 6614, Université de Rouen, 76801 Saint Etienne du Rouvray, France

*Corresponding author: alexandre.kudlinski@univ-lille1.fr

Received 14 July 2014; revised 28 August 2014; accepted 4 September 2014 (Doc. ID 216876); published 14 October 2014

Temporal solitons propagating in the vicinity of a zero-dispersion wavelength in an optical fiber emit phase-matched resonant radiations (RRs) as a result of perturbations due to higher-order dispersion effects. These RRs propagate linearly and they usually rapidly spread out in time, thus having a very low peak power. Here, we show that the use of an engineered dispersion-varying optical fiber allows us to induce a completely new dynamics, in which a new physical mechanism—cascade of RRs—is discovered. It is explained by the fact that the RR is temporally recompressed thanks to the change of dispersion sign induced by the varying geometry along the fiber. In addition, we report the experimental evidence of physical processes that had remained unobserved experimentally so far, such as the emission of multiple RRs from a single soliton and the generation of a 500 nm continuum exclusively composed of polychromatic RRs.

OCIS codes: (190.4370) Nonlinear optics, fibers; (190.5530) Pulse propagation and temporal solitons; (320.7140) Ultrafast processes in fibers.

http://dx.doi.org/10.1364/OPTICA.1.000243

1. INTRODUCTION

Temporal solitons are fascinating localized structures in which dispersion is counterbalanced by nonlinearity [1]. In optical fibers, higher-order dispersion and/or nonlinear effects destabilize higher-order solitons, which leads to their fission into fundamental ones [2], which are much more robust and are only perturbed by these effects. An illustration of such a perturbation occurs when the soliton spectrum overlaps with the zero dispersion wavelength (ZDW) of the optical fiber [3]. In this situation, the soliton emits a resonant radiation (RR) (also termed dispersive wave or Cherenkov radiation) across the ZDW, mainly due to third-order dispersion [4]. The RR is generated at a higher (respectively, lower) frequency than the soliton if the third-order dispersion term is positive (respectively, negative). This results in the spectral recoil of the soliton toward lower (respectively, higher) frequencies as a consequence of the momentum conservation of the process. The generation of RRs is usually explained in terms of phase matching between the soliton and the RR [4]: $\beta_{\mathrm{RR}}(\omega) = \beta_S(\omega)$, with β_{RR} the propagation constant of the RR and β_S the one of the soliton at the frequency of the RR. After a Taylor expansion of the propagation constants up to the third order, this phase-matching relation becomes

$$\frac{\beta_2}{2}\Omega^2 + \frac{\beta_3}{6}\Omega^3 = \frac{\gamma P}{2}, \tag{1}$$

where β_2 and β_3 are the second- and third-order dispersion terms, $\Omega = \omega_S - \omega_{\mathrm{RR}}$ is the frequency separation between the soliton at ω_S and the RR at ω_{RR}, P is the soliton peak power, and γ is the fiber nonlinear coefficient.

The emission of RRs from solitons has been largely investigated in uniform optical fibers, particularly in the context of supercontinuum generation [5]. The generation of RRs may also occur for a Raman shifting soliton when it reaches a second ZDW at long wavelengths [6]. In this case, the soliton self-frequency shift (SSFS) is cancelled, because it is perfectly balanced by the spectral recoil due to the emission of a RR,

which is redshifted due to negative third-order dispersion [7]. Solitons and RRs may also interact and generate additional spectral components through nonlinear wave-mixing processes dictated by a wavenumber matching condition, interpreted in terms of four-wave mixing (FWM) [8,9]. Such interactions have been observed experimentally with ultrashort pulses [10,11] and within the context of cw supercontinuum generation [12]. Recently the concept of RR has been extended to account for a new resonance with a negative frequency part of the spectrum, which turns out to be extremely blueshifted [13]. Moreover, it has been shown that the emission of RR is not a prerogative of solitons, but it can be shed by other sources such as shock waves [14,15].

In axially varying fibers, the generation of RRs may lead to even much more complex scenarios due to the design flexibility offered by these waveguides. The spectral recoil accompanying the emission of a RR may, for instance, lead to a soliton blueshift [16–18] as a result of the nonuniform fiber dispersion [17]. Recently, it has been shown with numerical simulations that a single Raman shifting soliton can generate a polychromatic RR in a suitably engineered tapered fiber such that the ZDW remains close enough to the soliton spectrum throughout propagation [19]. Following the same idea, it has been shown numerically that multiple RRs can be generated from a single fundamental soliton in an axially segmented fiber by sequentially hitting the ZDW, which progressively shifts toward long wavelengths in order to follow the SSFS [20].

In this paper, we propose a detailed experimental and numerical study of the dynamics of RR generation in a dispersion-varying photonic crystal fiber (PCF) suitably tailored so that a Raman shifting soliton hits the long-wavelength second ZDW several times. This leads to a very rich and unprecedented dynamics in which (i) multiple RRs are emitted from a single fundamental soliton (each time the soliton hits the ZDW), (ii) each generated RR, which remains temporally localized as a result of varying dispersion, cascades its own new RR, and (iii) a continuum exclusively composed of RRs spanning over 500 nm is generated.

2. GENERATION OF CASCADED RESONANT RADIATIONS

We are interested here in a situation similar to the one described in [6], namely a soliton experiencing a Raman-induced SSFS until it reaches the second ZDW, where it stops and generates a RR across the ZDW. However, the important difference that is the key of our study is that the second ZDW evolves longitudinally so that the soliton or the RR hits it several times during propagation, which completely modifies the soliton/RR dynamics.

A. Fiber Properties

Figure 1(a) (left axis) shows the evolution of the fiber diameter recorded during the drawing process. The initial uniform section is 7 m long and is such that the dispersion is anomalous over the 1000–1450 nm spectral range, a second ZDW being located at 1450 nm, as can be seen from Fig. 1(a) (solid line, right axis). This is achieved for a hole-to-hole spacing Λ of 1.17 μm and a relative hole diameter d/Λ of 0.64, with two bigger holes (d/Λ of 0.87) located apart from the core. This ensures a polarization-maintaining behavior with an extinction ratio of about 20 dB over the spectral range of interest. The varying section has a cosine shape (starting from 7 m) and is obtained by varying the outer diameter during the fiber draw [Fig. 1(a), left axis]. This results in varying the hole-to-hole spacing while the relative hole diameter d/Λ is kept constant. The amplitude of the oscillating section has been designed such that the ZDW decreases from 1450 nm (for the largest diameter) to 1140 nm (for the smallest one), as shown in Fig. 1(a) (solid line, right axis). The period of the oscillation has been fixed to 5 m, but it is worth noting that the periodic nature of the modulation does not play any role here (only the fact that the second ZDW alternatively increases and decreases is important). Full dispersion curves (simulated with a finite element mode solver) corresponding to the maximum and minimum diameters are plotted in Fig. 1(b) in blue and red lines, respectively.

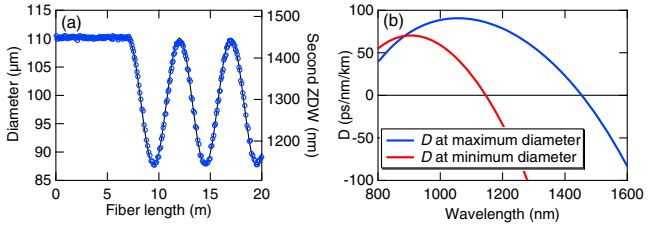

Fig. 1. (a) Left axis: evolution of the outer diameter of the dispersion-varying PCF versus length measured during the draw process (markers). Right axis: simulated evolution of the second ZDW versus fiber length (solid line). (b) Simulated dispersion curves for the maximum (blue line) and minimum (red line) fiber diameters.

B. Experimental Setup

Figure 2 shows the experimental setup used for all experiments. The femtosecond oscillator delivers pulses centered at 1027.5 nm at a repetition rate of 54 MHz. After passing through an optical isolator, half-wave plates, and a polarizer, they are launched into a 90/10 polarization-maintaining coupler. At the coupler output (i.e., at the PCF input), the pulses have been fully characterized using a frequency-resolved optical gating system. They have a Gaussian shape with a full width at half-maximum (FWHM) duration of 340 fs, and the chirp parameter (defined as in [21]) is +1.5. The first half-wave plate HWF1 is used to adjust the input power, and the second one, HWP2, allows us to align the polarization state to a neutral axis of the coupler. The PCF is spliced to the 90% output port of the coupler, with aligned neutral axes. The power was

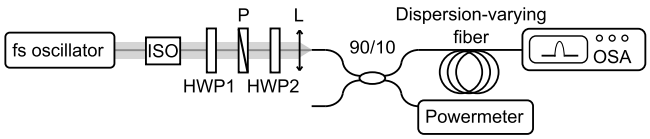

Fig. 2. Experimental setup. fs, femtosecond; ISO, optical isolator; L, lens; HWP, half-wave plates; P, polarizer; OSA, optical spectrum analyzer.

measured on the other output port, which allows a very accurate and very reproducible control of the power launched in the PCF during cutback experiments presented hereafter.

C. Spectral Domain Analysis

In a first round of experiments, we investigated the dynamics of the spectrum with fiber length. This was done with a cutback procedure, in which the output spectrum is recorded after cutting back the PCF every 50 cm. Figure 3(c) shows the result of this experiment performed in the 20 m long PCF described in Fig. 1 for a pump power of 75 W effectively launched into the PCF (by taking into account the coupling rate of the coupler and splice loss). In this section, we first focus on the 12 m long initial segment of the PCF [from 0 to the horizontal white dashed line in Fig. 3(c)]. It is thus made of a 7 m long uniform section followed by a 5 m long section in which the diameter decreases and then increases again [see Fig. 1(a)]. The processes occurring in the remainder of the fiber will be analyzed in the next section.

Figure 3(b) shows the output spectrum for a fiber length of 12 m. A soliton is ejected from the pump pulse and experiences Raman-induced SSFS. From 7 m, the SSFS increases because

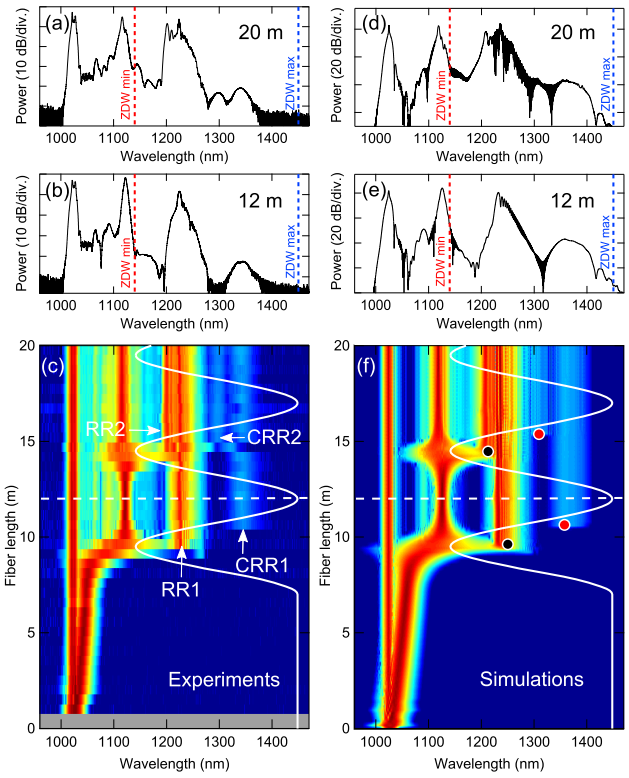

Fig. 3. (a), (d) Output spectrum after 20 m for a pump peak power of 75 W in (a) experiments and (d) simulations; (b), (e) output spectrum after 12 m for a pump peak power of 75 W in (b) experiments and (e) simulations. Red and blue dashed lines represent, respectively, the minimum and maximum ZDW. (c), (f) Dynamics of the spectrum formation versus fiber length in (c) experiments and (f) simulations. The white solid line represents the second ZDW, and the horizontal dashed line corresponds to a fiber length of 12 m. Black and red dots represent phase-matched wavelengths of RR obtained with Eq. (1) from the soliton when it reaches the second ZDW and from the first generated RR when it crosses the ZDW, respectively.

dispersion decreases [22], until it hits the decreasing ZDW (represented by the white line) at around 9 m. This results in the cancellation of the SSFS at 1120 nm and in the generation of a RR (labeled RR1 in Fig. 3) around 1230 nm, as expected from [6]. This RR, initially located in normal dispersion, crosses the increasing ZDW (at 10.4 m). Simultaneously, an *a priori* unexpected spectral feature appears at even longer wavelengths around 1340 nm. Such features may originate from the nonlinear interaction of Raman-shifted solitons with RRs [8–10,12] or with the residual pump radiation [23]. In the present case, however, this additional feature appears 1 m after the RR generation, which suggests that another mechanism is involved in the generation process of the 1340 nm spectral feature.

In order to understand the physical origin of this feature, we performed numerical simulations of the generalized nonlinear Schrödinger equation (GNLSE) [21], taking into account the full dispersion curve as well as Kerr and Raman nonlinearities. The pump pulse used in the simulations is the same as in experiments (340 fs Gaussian pulse, +1.5 chirp parameter, 75 W peak power). The fiber parameters are the same as described above. Numerical simulations were thus performed without any adjustable parameter. The dynamics of the process obtained from numerical simulations displayed in Fig. 3(f) shows excellent agreement with experiments. In particular, the black dot located at 9 m in Fig. 3(c) represents the solution of the phase-matching relation [Eq. (1)] for a soliton located at 1120 nm, in good agreement with simulations. Also, the appearance of the 1340 nm spectral feature is well reproduced, which allows us to study its physical origin more in detail with the help of numerical simulations in the time domain and numerical spectrograms.

D. Time Domain Analysis

In order to get further insight into this process, we numerically investigated the behavior of RR1 in the time domain. Figure 4 shows the simulated time domain evolution along the fiber corresponding to the spectral one shown in Fig. 3(f). As above, we focus our analysis here on the first 12 m of the fiber (the remaining section will be commented on hereafter). Figure 4(a) shows that, quite surprisingly, RR1 remains localized in the time domain, contrary to the usual RR1 observed in uniform fibers [6]. This is confirmed by the evolution of its peak power with fiber length, plotted in Fig. 4(b), and by the temporal profiles of RR1 shown in the right column of Fig. 4 for various fiber lengths. When RR1 enters the anomalous dispersion region at 10.4 m, its peak power is about 10 W. It then experiences a temporal compression, so that its peak power increases from 6 W at 11 m [Fig. 4(ϵ)] to 36 W at 12.1 m [Fig. 4(δ)], as a result of the change in the dispersion sign.

Having described spectral and temporal dynamics separately, we will now study their connections with the help of numerical spectrograms.

E. Spectro-Temporal Analysis

Figures 5(b) and 5(c) show the spectrograms corresponding to the simulation of Fig. 3(f), for fiber lengths of 10.4 and

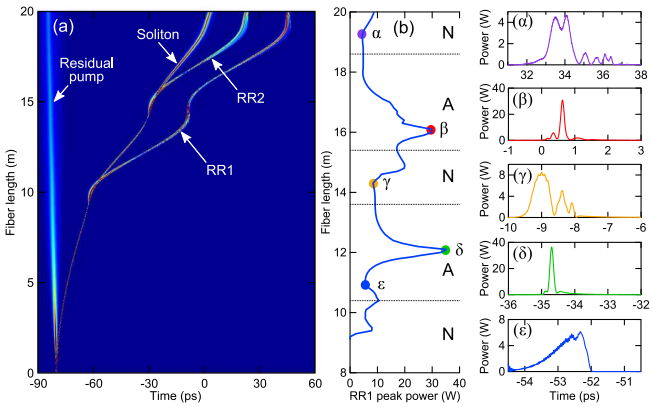

Fig. 4. (a) Simulated time domain evolution (in linear scale) versus fiber length corresponding to Fig. 3(f); (b) evolution of the peak power of RR1 with fiber length. Horizontal dotted lines depict locations where the RR1 experiences a change in dispersion sign (N, normal dispersion; A, anomalous dispersion). (α)–(ϵ) Simulated temporal profiles of RR1 at fiber lengths of 18, 16, 14.3, 12.1, and 11 m, respectively.

10.6 m, respectively, just around the point where the RR hits the ZDW. At 10.4 m [Fig. 5(a)], the RR, which has previously been generated, is located in the normal dispersion region, and additional spectral components appear on both sides of the soliton/RR pair. As we shall see hereafter, they originate from FWM between the soliton and the RR, as previously demonstrated in [8,9]. At 10.6 m [Fig. 5(c)], the RR (labeled RR1 above) crosses the increasing ZDW (depicted by the white horizontal dashed line). This results in the generation of an additional radiation (around 1340 nm) across the ZDW, which can be seen as a new RR generation from the previous RR1 located at 1230 nm. Indeed, the red dot located at 10.4 m in Fig. 3(f) represents the solution of the phase-matching relation [Eq. (1)] using RR1 as the solitonic pulse. Indeed, we demonstrate in the next section that RR1 actually contains a solitonic component. This whole process, which we call cascaded RR generation, is possible thanks to the high peak power of RR1 [Fig. 4(b)] when it crosses the ZDW, which is due to the dispersion-varying characteristics of the fiber. The spectral feature observed at 1340 nm thus originates both from FWM between the soliton and the RR and from the RR cascade because of the varying ZDW.

In order to confirm this, we performed numerical simulations in a fiber that has been designed so that the first generated RR does not cross the increasing ZDW [Fig. 5(d)]. The ZDW has the same evolution as in Fig. 1(a) over the first 10.4 m, and it is then constant for the remainder of the fiber in order to cancel out the change of the dispersion sign experienced by the RR. In this case, the RR always remains in the normal dispersion region. Corresponding spectrograms are displayed in Figs. 5(e) and 5(f) for fiber lengths of 10.4 and 10.6 m, respectively. The first one is identical to the top row for a fiber length of 10.4 m, i.e., the first RR is generated and a FWM process between the soliton and the RR appears. For a length of 10.6 m [Fig. 5(f)], the RR does not cross the ZDW and the cascaded RR is not observed. Figure 5(g) shows a comparison between the output spectra corresponding to these two cases [for the fiber profiles of Figs. 5(a) and 5(d)]. The spectra look very similar except around the 1340 nm radiation, which is much stronger in the fiber in Fig. 5(a) (real fiber). This is due to the fact that this peak [depicted by white-dashed circles in Figs. 5(c) and 5(f)] is to the result of two different mechanisms (FWM and cascaded RR), while only the FWM process takes place in the fiber in Fig. 5(d). In order to quantify the content of both processes to this spectral feature, it was numerically filtered and its energy was deduced by integrating the spectra in Fig. 5(g). It is found that the 1340 nm peak of the red curve in Fig. 5(g) (corresponding to the FWM process alone) represents only 0.6% of that of the black curve (corresponding to cascaded RR and FWM). This demonstrates that the cascaded RR process is largely predominant over the FWM in our experiments.

These numerical results, supported by experiments, therefore provide evidence for a new process in which a soliton emits a RR that remains temporally localized due to the change

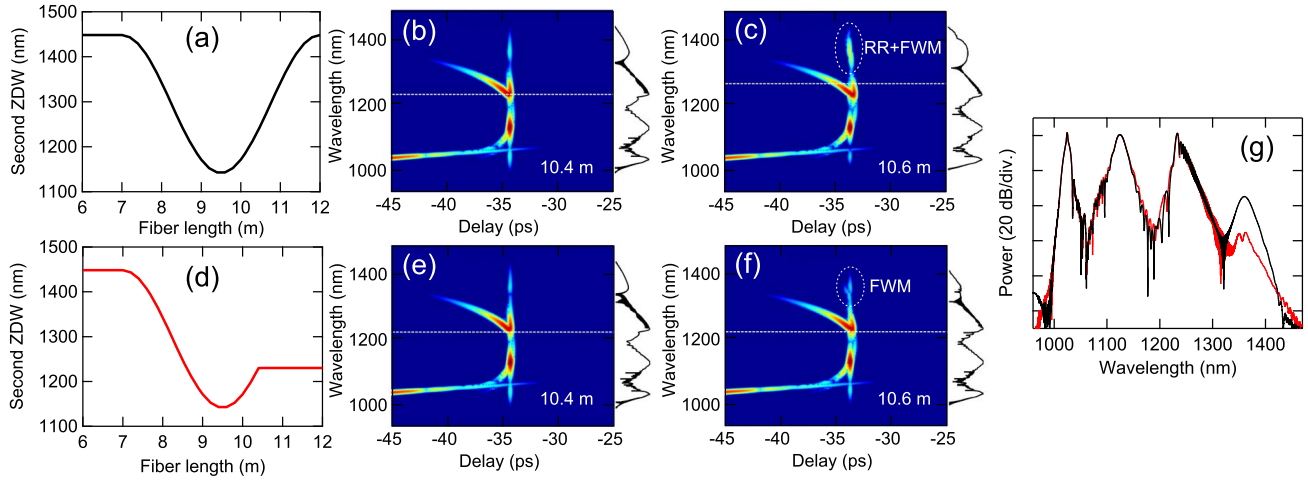

Fig. 5. Numerical spectrograms for fiber lengths of 10.4 and 10.6 m for the profiles displayed in (a) [(b) and (c)] (Media 1) and (d) [(e) and (f)]. Horizontal white-dashed lines depict the second ZDW. (g) Comparison between spectra obtained at 10.6 m in the profile of plots (a) (black line) and (d) (red line).

in the dispersion sign induced by the varying geometry along the fiber. Thanks to this property, the RR has a high enough peak power to generate its own cascaded RR when it crosses the ZDW.

3. EMISSION OF MULTIPLE RESONANT RADIATIONS

In this section, we investigate the soliton/RR dynamics in a much more complex scenario when the Raman-shifted soliton hits the ZDW a second time, i.e., for a longer propagation distance. Therefore, we consider and analyze here the results of Figs. 3(c) and 3(f) over the remaining part of the fiber length, i.e., until 20 m.

A. Spectral Analysis

Following the generation of the cascaded RR (labeled CRR1) around 1340 nm, and according to the process described in Section 2.C, the soliton duration strongly increases because of the varying dispersion map, which is why it becomes spectrally compressed. It does not experience any significant SSFS at this point, because the peak power is too low. When the ZDW decreases again from 12 m, the soliton temporally compresses, so that its spectrum broadens and hits the second ZDW again around its minimum value at 14.5 m. This leads to the generation of a new RR (labeled RR2) located at a slightly different wavelength than RR1, because the soliton wavelength is slightly different at the point where it hits the ZDW. The black dot located at 14.5 m represents the solution of the phase-matching relation [Eq. (1)] for the corresponding soliton wavelength. It is in very good agreement with the simulations, which confirms its origin. At 15 m, RR2 crosses the increasing ZDW which results in the generation of its own cascaded RR [labeled CRR2 in Fig. 3(c)], following the same mechanism as described above. The red dot located around 15 m in Fig. 3(f) shows the solution of Eq. (1) with RR2 as a solitonic pulse, in good agreement with the simulation result. Finally, after 20 m of propagation, the single fundamental soliton has directly generated two RRs, both of which have generated their own cascaded RR as observed in the output spectra of Figs. 3(a) and 3(d) (in the experiments and simulations, respectively).

B. Time Domain Analysis

The corresponding time domain map in Fig. 4(a) confirms that both RR1 and RR2 remain localized temporally, contrary to standard RRs generated in uniform fibers, which rapidly spread out in time. In particular, Fig. 4(b) shows that the peak power of RR1 increases when it is located in the anomalous dispersion region. In these regions and near the local maxima, RR1 is temporally compressed and its temporal profile resembles that of a soliton [Figs. 4(δ) and 4(β)]. However, in normal dispersion regions, RR1 tends to spread out in time and its shape is much more structured [Figs. 4(γ) and 4(α)], but it still has a peak power in the order of 10 W, which is enough to initiate the cascaded RR process. Cascaded RRs are not seen on Fig. 4(a) due to their reduced peak power as compared to RRs.

It can be demonstrated that during the propagation in the anomalous dispersion regime, RR1 and RR2 contain solitons, showing unequivocally the nonlinear nature of these waves. To prove this fact, we solve numerically the direct Zakharov–Shabat (ZS) scattering problem [24] by means of the Fourier collocation method [25] for some profiles of RR1 at different fiber lengths. In doing this we neglect for the moment the Raman and higher-order dispersive effects and we take a constant value of the second-order dispersion, evaluated at the corresponding fiber length. In this way, the GNLSE reduces to the integrable case, to which the inverse scattering transform applies. The discrete spectrum of the ZS operator is associated with solitons, whereas the continuous spectrum gives linearly dispersing waves (radiation). The total energy of a given pulse is proportional to the sum of two contributions: an integral over the continuous spectrum (radiation) and the sum of the imaginary parts of the discrete eigenvalues (solitons) of the ZS scattering problem [26]. We find that the field envelope of RR1 at $z = 12.1$ m [Fig. 4(δ)] contains one soliton that carries around 40% of the pulse energy, while at $z = 16$ m [Fig. 4(β)] the pulse still contains one soliton that carries around 60% of the total energy. Similar results are found for RR2. The solitonic part contained in the RR is ultimately the source of the observed cascaded RR.

C. Spectro-Temporal Analysis

Media 1 shows the evolution of the simulated spectrogram centered on RR1 with fiber length. The horizontal dashed line represents the second ZDW. This confirms that RR1 remains temporally localized and shows how its overall chirp changes sign over successive dispersion regions. It also confirms the solitonic nature of RR1 discussed above at various locations along the fiber (around 12 and 16 m).

4. DYNAMICS OF POLYCHROMATIC RESONANT RADIATIONS EMISSION

Increasing the pump power results in a higher peak power of the first ejected soliton, and thus to a more efficient SSFS. As a consequence, the soliton hits the ZDW before its minimum value, i.e., when it is still decreasing. This situation is illustrated in Fig. 6 for a pump peak power of 110 W, where Figs. 6(a) and 6(b) correspond to the experiments while Figs. 6(c) and 6(d) correspond to simulations. The soliton spectrum starts to overlap with the ZDW at about 9 m, i.e., at a point where it is still decreasing, and emits a RR. Then the soliton experiences a significant blueshift [16–18] as a result of the spectral recoil accompanying the RR emission combined with axially varying dispersion [17]. Figure 7 shows a close-up on the RR emission observed around 9 m in Fig. 6(d). The fiber ZDW (depicted by the white line) follows the blueshifting soliton in such a way that its spectrum keeps overlapping with the normal dispersion region throughout propagation until about 10 m. This results in a continuous emission of RRs (or polychromatic RR) following the phase-matching relation [Fig. 1] (depicted by the black line), similar to the numerical results reported in [19]. In the simulation of Fig. 7, the soliton goes from 1145 nm at

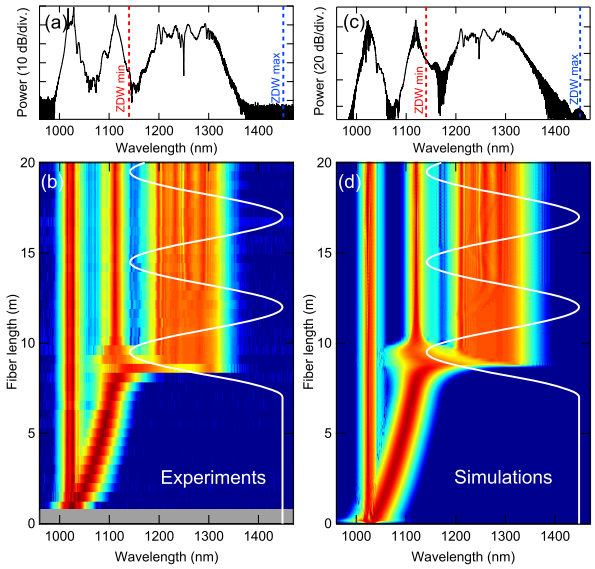

Fig. 6. (a), (c) Output spectrum after 20 m for a pump peak power of 110 W in (a) experiments and (c) simulations; (b), (d) dynamics of the spectrum formation versus fiber length in (b) experiments and (d) simulations. The white line represents the second ZDW. Red and blue dashed lines in (a) and (c) represent, respectively, the minimum and maximum ZDW.

8.8 m to 1115 nm at 9.4 m, which corresponds to the RRs located between 1325 and 1195 nm according to the phase-matching relation (black line), in excellent agreement with the simulated emission of RRs. This explains why the RR spectrum is polychromatic and finally spans more than 150 nm. After the emission of the polychromatic RR during its blueshift, the soliton does not have enough peak power left to experience SSFS again and hit the ZDW again. In our configuration, the emission of polychromatic RR is due to the fact that the soliton blueshift follows the decreasing ZDW, while in [19] it is the SSFS that allows it to follow the increasing ZDW.

The results of this section show how rich the dynamics of RR generation from a soliton in dispersion-varying optical fibers can be. They also provide the first experimental observation of the polychromatic RRs predicted in [19].

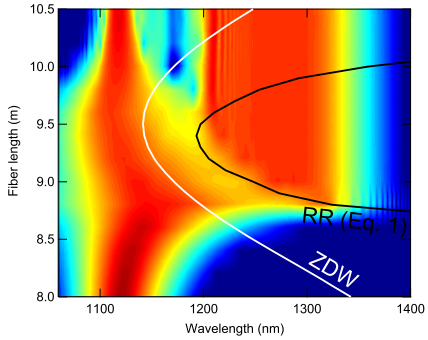

Fig. 7. Close-up on the RR emission observed around 9 m in Fig. 6(d). The white line represents the second ZDW. The black line represents the phase-matching relation given by Eq. (1).

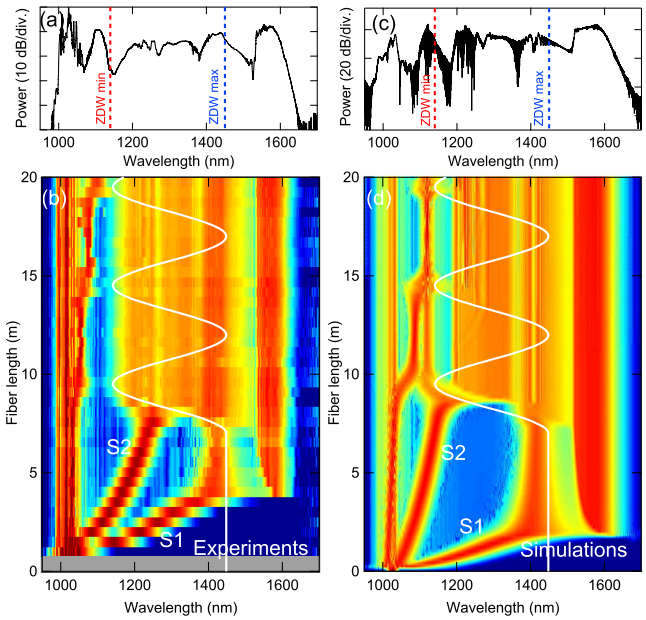

Fig. 8. (a) Experimental output spectrum after 20 m for a pump peak power of 380 W, (b) measured dynamics of the spectrum formation versus fiber length, (c) simulated output spectrum, and (d) simulated dynamics of the spectrum formation. The white line represents the second ZDW. Red and blue dashed lines in (a) and (c) represent, respectively, the minimum and maximum ZDW.

5. GENERATION OF A RESONANT RADIATION CONTINUUM

In a last set of experiments, we studied the dynamics of RR generation in the case in which two solitons hit the fiber ZDW at different points. This is achieved by increasing the pump peak power to 380 W. Figure 8(b) shows the spectrum evolution with the fiber length measured by successive cutbacks, while Fig. 8(d) corresponds to the numerical simulations. Experimentally, two main solitons are ejected from the breakup of the pump pulse. The first one, labeled S1, has the highest peak power and shortest duration and therefore experiences the most important SSFS. It reaches the second ZDW in the uniform section of the fiber (after 4 m), so that it emits a RR (centered around 1550 nm) similar to the case of Ref. [6]. As a consequence, the SSFS is cancelled and the soliton S1 keeps propagating until it hits the ZDW again, when it starts to decrease from 7 m. This results in the generation of another RR centered at 1440 nm. The second soliton, labeled S2, has a less important SSFS rate than S1 due to its lower peak power and longer duration. It reaches the second ZDW at 8 m, at a point where the ZDW is decreasing. The soliton then disappears and transfers all its energy to a polychromatic RR. Finally, the output spectrum [displayed in Fig. 8(a)] is mainly composed of various RRs generated along the fiber, which make a RR continuum between 1150 and 1650 nm. The simulations in Fig. 8(d) are in good agreement except for the fact that the soliton S2 hits the second ZDW closer to its minimum value, possibly due to the presence of a nonlinear chirp on the pump pulse induced by the input coupler at this high pump power. As a consequence, the RR emitted by

soliton S2 is less broad than in the experiments, which results in a more structured RR continuum [Fig. 8(c)].

6. SUMMARY

We have investigated experimentally and numerically the generation of RRs from a soliton in the vicinity of the second ZDW of dispersion-varying optical fibers. Several major and unprecedented features have been identified. First, we have observed and explained for the first time (to the best of our knowledge) a process in which a RR radiated from a soliton emits a new cascaded RR when crossing the evolving ZDW of the fiber. Second, we have provided first experimental results showing the emission of multiple RRs from a unique soliton in a dispersion-varying optical fiber, following the numerical work in [20]. Third, we have experimentally observed for the first time the generation of a polychromatic RR, as was previously numerically investigated in [19], leading to a RR continuum spanning over 500 nm.

The dynamics of RRs that we have highlighted here, and the fact that they do not spread out in time and remain temporally localized, might offer new perspectives for the development of fiber-based sources delivering two or even more ultrashort pulses with different wavelengths, which could be useful in stimulated Raman scattering microscopy, for instance.

More generally, our results show how the new degree of freedom brought by dispersion-varying optical fibers offers rich and complex dynamics of nonlinear effects and opens the door to a new way of thinking about nonlinear fiber optics.

FUNDING INFORMATION

Agence Nationale de la Recherche through the ANR TOPWAVE; French Ministry of Higher Education and Research; Nord-Pas de Calais Regional Council and Fonds Européen de Développement Régional (FEDER) Contrat de Projets Etat Région (CPER) 2007-2013; Campus Intelligence Ambiante (CIA).

REFERENCES

1. A. Hasegawa and M. Matsumoto, *Optical Solitons in Fibers* (Springer-Verlag, 2002).
2. P. Beaud, W. Hodel, B. Zysset, and H. Weber, "Ultrashort pulse propagation, pulse breakup, and fundamental soliton formation in a single-mode optical fiber," IEEE J. Quantum Electron. **23**, 1938–1946 (1987).
3. P. K. A. Wai, C. R. Menyuk, Y. C. Lee, and H. H. Chen, "Nonlinear pulse propagation in the neighborhood of the zero-dispersion wavelength of monomode optical fibers," Opt. Lett. **11**, 464–466 (1986).
4. N. Akhmediev and M. Karlsson, "Cherenkov radiation emitted by solitons in optical fibers," Phys. Rev. A **51**, 2602–2607 (1995).
5. J. M. Dudley, G. Genty, and S. Coen, "Supercontinuum generation in photonic crystal fiber," Rev. Mod. Phys. **78**, 1135–1184 (2006).
6. D. V. Skryabin, F. Luan, J. C. Knight, and P. St.J. Russell, "Soliton self-frequency shift cancellation in photonic crystal fibers," Science **301**, 1705–1708 (2003).
7. F. Biancalana, D. V. Skryabin, and A. V. Yulin, "Theory of the soliton self-frequency shift compensation by the resonant radiation in photonic crystal fibers," Phys. Rev. E **70**, 016615 (2004).
8. A. V. Yulin, D. V. Skryabin, and P. St.J. Russell, "Four-wave mixing of linear waves and solitons in fibers with higher-order dispersion," Opt. Lett. **29**, 2411–2413 (2004).
9. D. V. Skryabin and A. V. Yulin, "Theory of generation of new frequencies by mixing of solitons and dispersive waves in optical fibers," Phys. Rev. E **72**, 016619 (2005).
10. A. Efimov, A. Taylor, F. Omenetto, A. Yulin, N. Joly, F. Biancalana, D. Skryabin, J. Knight, and P. St.J. Russell, "Time-spectrally-resolved ultrafast nonlinear dynamics in small-core photonic crystal fibers: experiment and modelling," Opt. Express **12**, 6498–6507 (2004).
11. A. Efimov, A. V. Yulin, D. V. Skryabin, J. C. Knight, N. Joly, F. G. Omenetto, A. J. Taylor, and P. St.J. Russell, "Interaction of an optical soliton with a dispersive wave," Phys. Rev. Lett. **95**, 213902 (2005).
12. B. H. Chapman, J. C. Travers, S. V. Popov, A. Mussot, and A. Kudlinski, "Long wavelength extension of CW-pumped supercontinuum through soliton-dispersive wave interactions," Opt. Express **18**, 24729–24734 (2010).
13. E. Rubino, J. McLenaghan, S. C. Kehr, F. Belgiorno, D. Townsend, S. Rohr, C. E. Kuklewicz, U. Leonhardt, F. König, and D. Faccio, "Negative-frequency resonant radiation," Phys. Rev. Lett. **108**, 253901 (2012).
14. K. E. Webb, Y. Q. Xu, M. Erkintalo, and S. G. Murdoch, "Generalized dispersive wave emission in nonlinear fiber optics," Opt. Lett. **38**, 151–153 (2013).
15. M. Conforti and S. Trillo, "Dispersive wave emission from wave breaking," Opt. Lett. **38**, 3815–3818 (2013).
16. Z. Chen, A. J. Taylor, and A. Efimov, "Coherent mid-infrared broadband continuum generation in non-uniform ZBLAN fiber taper," Opt. Express **17**, 5852–5860 (2009).
17. A. C. Judge, O. Bang, and C. Martijn de Sterke, "Theory of dispersive wave frequency shift via trapping by a soliton in an axially nonuniform optical fiber," J. Opt. Soc. Am. B **27**, 2195–2202 (2010).
18. S. P. Stark, A. Podlipensky, and P. St.J. Russell, "Soliton blueshift in tapered photonic crystal fibers," Phys. Rev. Lett. **106**, 083903 (2011).
19. C. Milián, A. Ferrando, and D. V. Skryabin, "Polychromatic Cherenkov radiation and supercontinuum in tapered optical fibers," J. Opt. Soc. Am. B **29**, 589–593 (2012).
20. F. R. Arteaga-Sierra, C. Milián, I. Torres-Gómez, M. Torres-Cisneros, A. Ferrando, and A. Dávila, "Multi-peak-spectra generation with Cherenkov radiation in a non-uniform single mode fiber," Opt. Express **22**, 2451–2458 (2014).
21. G. Agrawal, *Nonlinear Fiber Optics*, 5th ed. (Academic, 2012).
22. A. Bendahmane, O. Vanvincq, A. Mussot, and A. Kudlinski, "Control of the soliton self-frequency shift dynamics using topographic optical fibers," Opt. Lett. **38**, 3390–3393 (2013).
23. M. Erkintalo, J. M. Dudley, and G. Genty, "Pump-soliton nonlinear wave mixing in noise-driven fiber supercontinuum generation," Opt. Lett. **36**, 3870–3872 (2011).
24. V. E. Zakharov and A. B. Shabat, "Exact theory of two-dimensional self-focusing and one dimensional self-modulation of waves in nonlinear media," Sov. Phys. JETP **34**, 62–69 (1972).
25. J. Yang, *Nonlinear Waves in Integrable and Nonintegrable Systems*, 1st ed. (SIAM, 2012).
26. S. Burtsev, R. Camassa, and I. Timofeyev, "Numerical algorithms for the direct spectral transform with applications to nonlinear Schrödinger type systems," J. Comput. Phys. **147**, 166–186 (1998).

Research Article Vol. 1, No. 4 / October 2014 / Optica 250

Optical magnetic mirrors without metals

Sheng Liu,[1,2,*] Michael B. Sinclair,[1] Thomas S. Mahony,[1,2] Young Chul Jun,[1,2,3] Salvatore Campione,[1,2,4] James Ginn,[1] Daniel A. Bender,[1] Joel R. Wendt,[1] Jon F. Ihlefeld,[1] Paul G. Clem,[1] Jeremy B. Wright,[1] and Igal Brener[1,2,5]

[1]Sandia National Laboratories, Albuquerque, New Mexico 87185, USA

[2]Center for Integrated Nanotechnologies, Sandia National Laboratories, Albuquerque, New Mexico 87185, USA

[3]Current address: Department of Physics, Inha University, Incheon 402-751, South Korea

[4]Department of Electrical Engineering and Computer Science, University of California Irvine, Irvine, California 92697, USA

[5]e-mail: ibrener@sandia.gov

*Corresponding author: snliu@sandia.gov

Received 30 June 2014; revised 14 August 2014; accepted 14 August 2014 (Doc. ID 214974); published 16 October 2014

The reflection of an optical wave from metal, arising from strong interactions between the optical electric field and the free carriers of the metal, is accompanied by a phase reversal of the reflected electric field. A far less common route to achieving high reflectivity exploits strong interactions between the material and the optical magnetic field to produce a "magnetic mirror" that does not reverse the phase of the reflected electric field. At optical frequencies, the magnetic properties required for strong interaction can be achieved only by using artificially tailored materials. Here, we experimentally demonstrate, for the first time to the best of our knowledge, the magnetic mirror behavior of a low-loss all-dielectric metasurface at infrared optical frequencies through direct measurements of the phase and amplitude of the reflected optical wave. The enhanced absorption and emission of transverse-electric dipoles placed close to magnetic mirrors can lead to exciting new advances in sensors, photodetectors, and light sources.

OCIS codes: (160.3918) Metamaterials; (300.6340) Spectroscopy, infrared; (300.6500) Spectroscopy, time-resolved; (320.7150) Ultrafast spectroscopy; (290.4020) Mie theory.

http://dx.doi.org/10.1364/OPTICA.1.000250

1. INTRODUCTION

Magnetic mirrors or high impedance surfaces were first proposed at microwave frequencies [1]. An important advantage of these mirrors is that a transverse-electric dipole placed close to the mirror surface is located at an antinode of the total (incident plus reflected) electric field and, hence, can absorb and emit efficiently [2]. In contrast, a dipole placed close to a metal surface experiences a node of the total electric field and can neither absorb nor emit efficiently. At microwave frequencies, these exceptional properties of magnetic mirrors have been utilized for smaller, more efficient antennas and circuits [3–6].

At optical frequencies, magnetic behavior can be achieved only through the use of artificially tailored materials and, as a result, relatively little work on optical frequency magnetic mirrors has been reported thus far. Recent investigations of magnetic mirror behavior at optical frequencies have utilized metallic building blocks such as fish-scale structures [7] and gold-capped carbon nanotubes [8]. However, the metals utilized in these approaches suffer from high intrinsic ohmic losses at optical frequencies. All-dielectric metamaterials, based upon subwavelength resonators, with much lower optical losses and isotropic optical response, have been used to demonstrate fascinating properties in a number of recent investigations [9–23]. In another recent work, magnetic mirror behavior was theoretically predicted for silicon dielectric resonators in the near infrared [24]. Although the reflection amplitude spectrum was measured in this work, no experimental phase measurements were achieved. In principle, this work is the same as our previous work [10] that showed only high reflectivity at the magnetic dipole resonance, which is a necessary

but not sufficient condition for magnetic mirror behavior. Moreover, the use of silicon as a resonator material does not result in a sufficiently small array spacing for effective medium behavior, particularly at oblique angles, as discussed in [10]. The benefit of using higher refractive index materials [tellurium (Te) in our work] is clear by comparing the reflectivity amplitude spectra of the silicon structure of [24] and the Te structure in this work: the Te resonators exhibit a much better spectral separation of the electric and magnetic dipole resonances. Recently, theoretical work [25,26] has also predicted nearly total omnidirectional reflection based upon the interplay among different resonant modes of high refractive index resonators. This is in strong contrast to the magnetic mirror behavior obtained in the effective medium limit, which does not depend on the coupling between different resonant modes. Therefore, we present here the first experimental demonstration of an optical magnetic mirror (OMM) using an all-dielectric metamaterial. Furthermore, none of these previous OMM demonstrations, including works that utilized metallic structures, were able to provide detailed temporal information about the optical fields, such as the resonant build-up of the response after transient excitation. In the present work, we overcome these limitations by using an OMM based on a subwavelength two-dimensional array of dielectric resonators fabricated from a low-loss high-permittivity dielectric material: Te. Furthermore, we utilize a phase-sensitive time-resolved optical technique to provide direct experimental proof of the magnetic mirror behavior. We also show that the electric-field standing-wave pattern for plane-wave illumination exhibits an antinode at the surface of the OMM, indicating that efficient coupling to transverse-electric dipoles placed close to the mirror surface should be possible.

2. RESULTS

A. Optical Magnetic Mirror Samples

Figure 1(a) shows a schematic of our magnetic mirror, which comprises a two-dimensional array of subwavelength Te cube resonators. The lowest frequency resonance of a high-permittivity cubic resonator exhibits a circular displacement current pattern, which yields magnetic dipole behavior [10,27], while the next higher resonance leads to a linear displacement current and, hence, electric dipole behavior. The large permittivity of Te [10,27,28] ensures that the dimensions of the resonator and array spacing are sufficiently subwavelength. Two-dimensional arrays of Te resonators were fabricated by depositing Te on a BaF_2 substrate, followed by e-beam lithography patterning and reactive ion etching. The resulting cube-like resonators exhibited a height of 1.7 μm and a base of ~1.5 μm × 1.5 μm (a slight overetching led to the deviation from perfect cube geometry). BaF_2 was selected as a substrate material due to its low reflective index (~1.4) and low loss throughout the IR spectral region. The large refractive index contrast between Te and BaF_2 allows for a high degree of confinement within the Te resonator and small leakage into the substrate [15]. The unit-cell spacing of the array was 3.4 μm for a ~45% duty cycle [10]. Figure 1(b) shows a scanning electron microscope (SEM) image of the fabricated OMM sample. Figure 1(c) shows the measured reflection spectrum of the sample (dotted black curve), which exhibits two reflection maxima that are close to the magnetic and electric dipole resonances [the electric-field patterns are shown as insets in Fig. 1(c)]. The wavelengths of the magnetic (8.95 μm) and electric (7.08 μm) dipole resonances do not precisely correspond to the transmission minima [29], but rather are determined by the loss maxima (i.e., absorption maxima) (see Section S1 of Supplement 1). This selection is also supported by numerical simulations, which show that the strongest dipole field intensities occur close to the wavelengths of maximum absorption (see Section S1 of Supplement 1).

B. Time-Domain Spectroscopy System

To directly measure both the amplitude and phase of the electric field of an optical wave reflected from the OMM, we utilize phase-locked time-domain spectroscopy (TDS) [30]. TDS has proven to be a powerful technique at terahertz frequencies [31–34] and has been recently extended to higher mid-infrared (mid-IR) frequencies [35,36]—a highly interesting frequency region covering vibrational and electronic resonances of molecular systems and solids [37,38]. Figure 2 shows

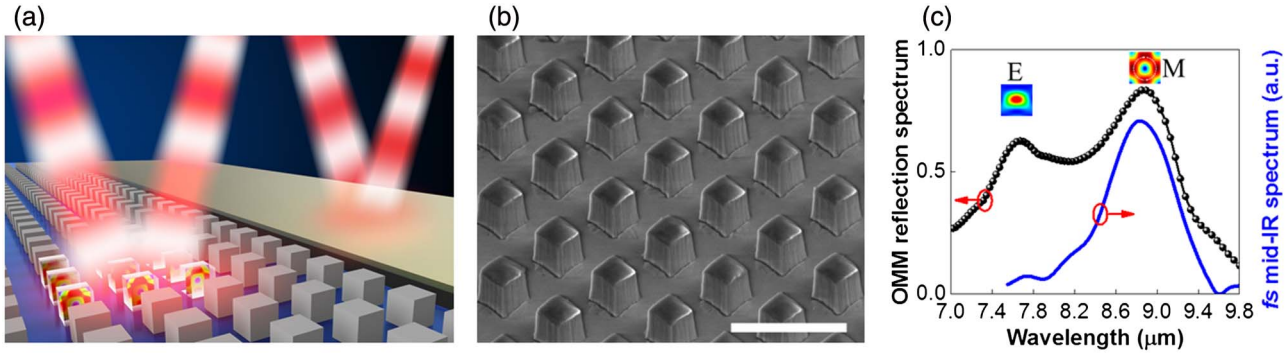

Fig. 1. Principle of all-dielectric OMMs. (a) The cubic dielectric resonators on the left side do not induce a phase shift of the reflected electric field at the magnetic resonance, but rather act as a dielectric magnetic mirror in the optical frequency range. In contrast, the gold surface on the right side (which serves as a reference surface) exhibits a 180 deg phase shift of the electric field upon reflection. (b) SEM image of the Te cube dielectric metasurface of our OMM. The scale bar corresponds to 5 μm. (c) The reflection spectrum (black-dotted curve) of the metamaterial sample in (b) shows two reflection maxima corresponding to the lowest (magnetic dipole) and the second lowest (electric dipole) resonances. The solid blue curve shows the spectrum of the femtosecond mid-IR pulses obtained by performing a Fourier transform of the measured electric field transients as discussed in Section 2.B.

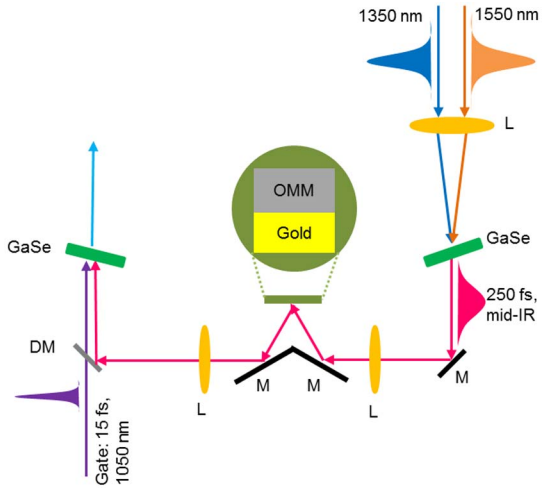

Fig. 2. Schematic of the TDS setup. We used a phase-locked TDS in the mid-IR to directly measure the phase shift of the reflected electric field from the OMM. Mid-IR pulses of 250 fs duration, produced by difference frequency mixing between ~1.35 and ~1.55 μm pulses, were focused by a ZnSe lens onto the OMM or gold surface. Another ZnSe lens was used to collect the reflected mid-IR beam. Gate pulses with a wavelength of 1.05 μm and duration of 15 fs were combined with the mid-IR pulses, using a dichroic mirror, and then focused into another GaSe crystal for phase-matched electro-optic sampling. DM, dichroic mirror; L, lens; M, mirror.

a simplified schematic of our stable-carrier-envelope-phase (CEP)-locked mid-IR TDS system. Briefly, an ultrafast fiber laser system was used to generate ~250 fs mid-IR pulses, tunable between 8.1 and 11 μm. The *p*-polarized pulses were focused onto either the OMM sample or a gold reference surface (which was deposited on top of the Te in an unpatterned region of the sample) at an incidence angle of 30 deg with ~10 deg of angular divergence in the focused beam. Thus, the incident radiation covered a range of angles from 25–35 deg. Care was taken to ensure that switching between the gold and OMM surfaces did not cause any spurious delay change (see Section S2 of Supplement 1). A synchronized 15 fs gate pulse output from the same fiber laser was used to measure the reflected infrared electric-field transients through phase-matched electro-optic sampling in a GaSe crystal [30,39]. The blue curve in Fig. 1(c) shows the spectrum of the femtosecond mid-IR pulses centered at ~8.9 μm obtained by performing a Fourier transform of the electric field transients acquired using the mid-IR TDS technique. More details of our TDS system can be found in Section S3 of Supplement 1, and in [17,40].

C. Phase of the Optical Electric Field Reflected from the Optical Magnetic Mirror

Figure 3(a) shows the measured electric field of the reflected pulses from the OMM (red line) and gold surface (blue line) when the central frequency of the incident pulse coincides with the magnetic dipole resonance of the Te resonators at 8.95 μm. For comparison, Fig. 3(b) is the simulated reflected electric field obtained using a commercial finite-difference time-domain (FDTD) simulator (FDTD Solutions by Lumerical Solutions Inc.), showing remarkable agreement between the

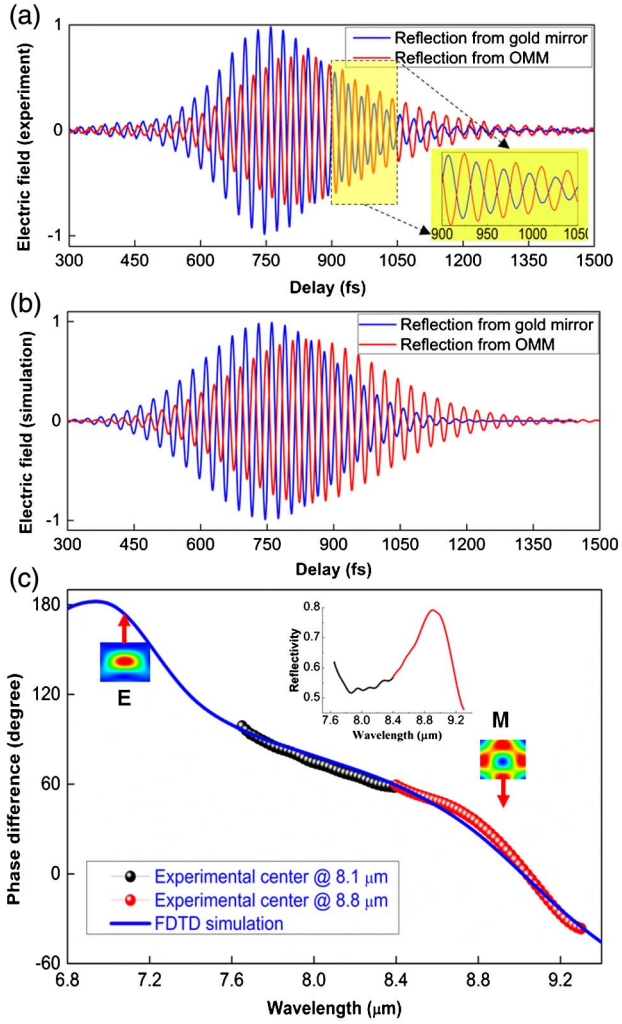

Fig. 3. Electric-field transients measured by TDS. (a) Experimental measurement of the electric field reflected from the gold surface (blue curve) and OMM (red curve) at the OMM magnetic resonance. The gold surface serves as a reference. (b) FDTD simulation of the reflected electric field from the gold surface (blue curve) and the OMM (red curve). Both experiment and simulation show that the electric-field fringes from the OMM are out-of-phase with those from the gold surface (i.e., a normal mirror). This unambiguously demonstrates the magnetic mirror behavior of the OMM. (c) Experimental and FDTD simulation results of the optical phase of the reflected wave. To cover a broader spectral range, two experimental data sets were obtained with the central frequency tuned to 8.8 and 8.1 μm. The inset is the reflectivity of the OMM derived from the Fourier transform of measured field transients.

experimental and simulation data. For both experiment and simulation, the phase of the reflection from the gold surface was referenced to a plane very close to the center of the cubic resonators, which is the plane that contains the radiating dipoles (see Section S4 of Supplement 1). Several features are noticeable in both the measured and simulated waveforms in Figs. 3(a) and 3(b). First, the amplitude of the red curve is slightly smaller than that of the blue curve, indicating that the reflectivity of the OMM is slightly smaller than that of the gold surface (which is close to a perfect mirror in the mid-IR). Second, the reflected field envelope from the OMM has a ~50 fs delay (approximately two optical periods) compared

to that from the gold surface due to the resonant interaction of the optical pulses with the metasurface resonators. Third, and most importantly, the electric-field fringes from the OMM are nearly phase-reversed with respect to the fringes from the gold reference (which are phase-reversed with respect to the incident field). Thus, the electric-field waveforms of Fig. 3(a) demonstrate that the field reflected from the OMM is in-phase with the incident field, which, combined with the high reflection amplitude, directly demonstrates magnetic mirror behavior at wavelengths around 9 μm. Due to the limited wavelength tuning range of the IR pulses, we further studied the phase shift at the electric dipole resonance using FDTD simulations only (see Section S5 of Supplement 1). These simulations show that the electric-field fringes from the OMM are in-phase with those from the gold surface at the electric dipole resonance, because the OMM acts as a normal mirror at this electric resonance frequency.

For a quantitative analysis of the phase difference between the electric fields reflected from gold and the OMM, we performed a Fourier transform of the measured field transients [Fig. 3(c)]. The time harmonic convention $\exp(-i\omega t)$ is implicitly assumed throughout the manuscript. To cover a broader spectral range, a second data set was obtained with the center frequency of the incident mid-IR pulses tuned to ~8.1 μm. The electric-field phase obtained from the FDTD simulation results is also plotted in Fig. 3(c) (blue curve) for comparison. Although the experimental data (red and blue circles) does not reach the electric dipole resonance frequency, it agrees very well with simulations over a wide wavelength region between 7.6 and 9.3 μm. We observe a ~180 deg phase difference between the magnetic and electric dipole resonances, further confirming the magnetic mirror behavior near 9 μm. The inset shows the reflectivity of the OMM calculated by the Fourier transform of the measured field transients. It agrees well with the spectra measured by Fourier transform infrared spectroscopy, exhibiting high reflectivity at the magnetic resonance around 8.9 μm. In addition, we measured another OMM sample made with a different fabrication technique, resulting in a smaller spectral separation between the electric and magnetic dipole resonances. For this sample, our mid-IR pulses are spectrally broad enough to cover both resonances at once (see Section S6 of Supplement 1). Once again, we observe an approximately ~180 deg phase difference between the two dipole resonances, which further demonstrates the OMM behavior at the magnetic dipole resonance. The fact that the behavior does not sensitively depend upon the separation of the electric dipole and magnetic dipole demonstrates that the magnetic mirror behavior does not rely on the coupling between these resonances. We would also like to stress that, due to the symmetric shape of our Te resonators [27], simulation results (not included here) show that the phase behavior is also insensitive to the incoming polarization up to an incidence angle of 45 deg.

To analyze the magnetic mirror behavior, we model each cubic resonator as an electric dipole and a magnetic dipole (whose polarizabilities are calculated via full-wave simulations) located at the center of the cube. We compute the amplitude and phase of the reflection coefficient of the two-dimensional array, including cross coupling between the electric and magnetic dipoles (see Section S4 of Supplement 1) using two-dimensional periodic dyadic Green's functions [41–43] and obtain very good agreement with full-wave simulations. Near the magnetic resonance, the magnetic dipole behavior dominates the optical response and magnetic mirror behavior is observed. In contrast, near the electric resonance, the electric dipole dominates and the array behaves like an electric mirror with an electric field phase shift of 180 deg upon reflection.

D. Emission Enhancement in the Optical Magnetic Mirror Near Field

When a transverse-electric dipole is placed in the near field of a conventional electric mirror, its emission is largely canceled by that of its image dipole [2,44–47]. In contrast, the image dipole produced by a magnetic mirror is in-phase with the original dipole and emission is allowed. Similarly, a transverse-electric dipole in very close proximity to an electric mirror finds itself at the node of the total electric field under plane-wave illumination and cannot efficiently absorb incoming radiation, whereas an electric dipole placed near a magnetic mirror is located at the antinode of the total electric field and can absorb efficiently. As a result, OMM behavior has been studied extensively at microwave frequencies for efficient, compact microwave circuits and antennas [3–6]. To demonstrate that these advantages can also be obtained at optical frequencies, we utilized FDTD simulations to generate maps of the total electric field at both the electric and magnetic resonance wavelengths of the OMM and compared them to the total field maps obtained for a conventional gold mirror. Figure 4(a) shows the standing-wave patterns obtained at the electric resonance wavelength of the OMM for both the OMM and a gold surface. As discussed previously, the gold surface is located at a height equivalent to the center of the dielectric resonators. At the electric resonance, the two standing-wave patterns show similar behavior, with an electric-field node located at the surface of both mirrors. The behavior is distinctly different at the OMM magnetic resonance wavelength [Fig. 4(b)], where an electric-field antinode is observed at the surface of the OMM. As expected, the gold mirror still exhibits a surface node at this wavelength. (Media 1 shows plane waves reflected from a gold surface and an OMM which are in-phase and out-of-phase at the electric and magnetic resonances, respectively.) Closer inspection of Fig. 4(b) shows that the total electric field exhibits some enhancement at the mirror surface, which is presumably due to the resonant nature of the OMM. Hence, at this wavelength, dipole absorbers/emitters placed in the immediate vicinity of the OMM surface are expected to interact strongly with the total field and efficiently absorb/emit electromagnetic energy. Indeed, we observe a large enhancement of dipole radiative emission when a transverse-electric dipole at the magnetic resonance wavelength is placed close to the OMM, as shown in Fig. 5. Using full wave simulation tools, the radiative decay rate is calculated by measuring the outgoing flux from a dipole source and normalizing it by the flux in free space. We calculate the normalized radiative decay rate of a transverse electric dipole oscillating at the magnetic resonance frequency as a function of the dipole–surface separation for

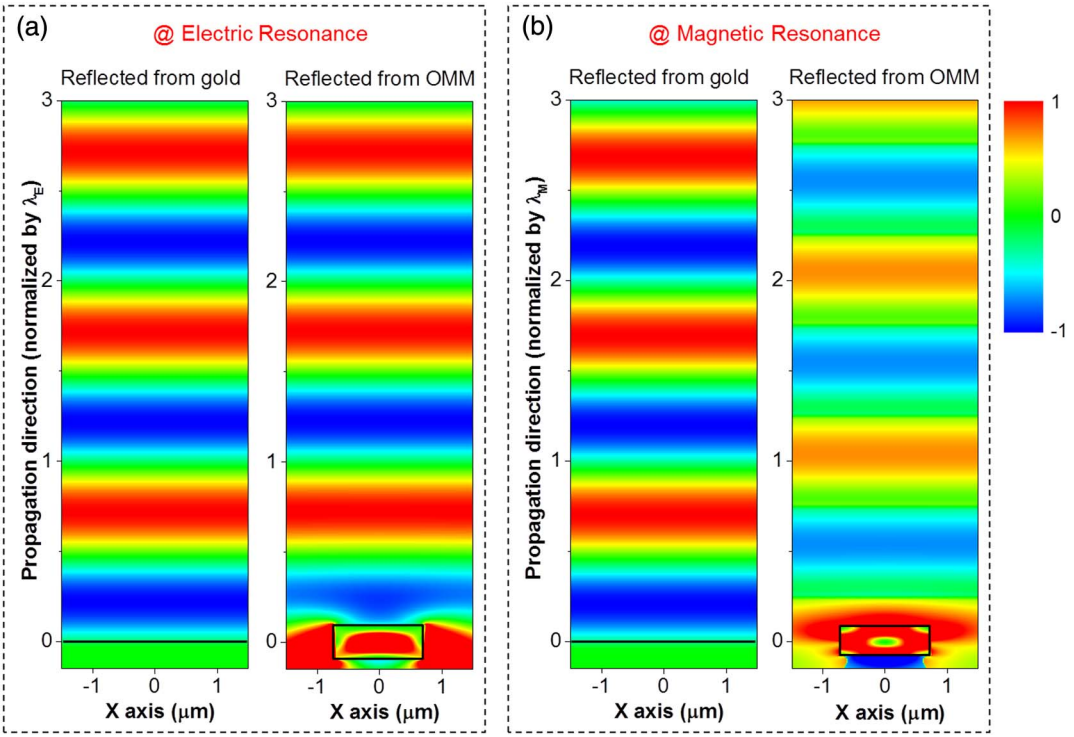

Fig. 4. Standing-wave patterns of light reflected from a gold mirror and an OMM at (a) the OMM electric resonance and (b) the OMM magnetic resonance. The OMM behaves like a conventional mirror at the electric resonance shown in (a) and behaves like a magnetic mirror at the magnetic resonance shown in (b) Media 1. The black lines and rectangles represent the gold–air interfaces and the boundaries of the Te cubic resonators, respectively. A node of the standing wave always occurs at the gold–air interface. In contrast, the top of the cubic resonator is at the node for the electric resonance and at the antinode for the magnetic resonance. All patterns share the same color scale bar on the right. Also note that the aspect ratio used for this figure causes the profile of the cubic resonator to appear as a rectangle.

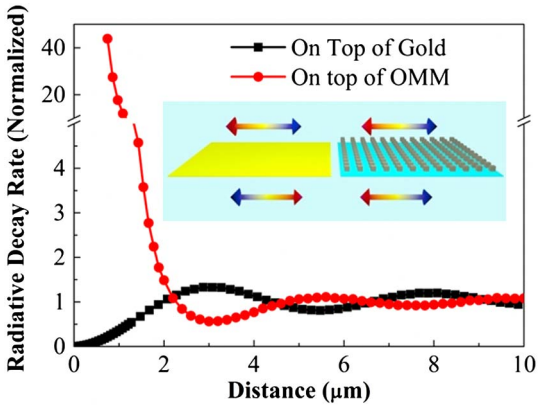

Fig. 5. Normalized radiative decay rate of a transverse-electric dipole oscillating at the magnetic resonance frequency as a function of the dipole–surface separation for both a 5 × 5 array approximating our OMM (red curve) and a gold surface (black curve). The distance of the dipole from the OMM is calculated using the center of the cubic resonator as distance "0," which is in agreement with our theoretical calculation (Section 4 of Supplement 1). First, the oscillatory dependence on distance is shifted by about half a period. Second, while the emission from the dipole is quenched very close to the gold surface, the dipole emission near the magnetic mirror is enhanced even for very small distances. Inset: a schematic of an electric dipole placed on top of a typical mirror and its reversed image dipole (left) and a schematic of an electric dipole on top of a dielectric magnetic mirror and its unreversed image dipole (right) at the magnetic dipole resonance.

both a 5 × 5 resonator array approximating our OMM and a gold surface. The behavior for these two cases is strikingly different: (i) the oscillatory dependence on distance is shifted by about half a period, which is a further confirmation of the magnetic mirror behavior of the OMM; (ii) while the emission from the dipole is quenched very close to the gold surface, the dipole emission rate near the magnetic mirror is enhanced even for very small distances. We also calculate the ratio of radiative decay rate to total decay rate to be ~53% when the transverse dipole is very close (10 nm) to the top surface of the Te resonators. The nonradiative loss is due to the nonzero imaginary part of the Te permittivity. However, the emission from the transverse dipole in the near field of the OMM is more complicated than what is expected from simple image dipole arguments, possibly due to coupling to higher order modes of the 5 × 5 array.

3. CONCLUSIONS

We experimentally demonstrated the OMM behavior of low-loss all-dielectric metasurfaces through direct measurements of the phase and amplitude of the reflected optical wave. We also showed that all-dielectric magnetic mirrors are good candidates for new types of infrared sensors, such as remotely interrogated chemical sensors in which molecular species adsorbed onto chemically selective layers on the mirror surface will interact strongly with the interrogating radiation and impart spectral

signatures on the reflected beam. In addition, these mirrors will be useful for compact and efficient thermal radiation sources in which thermal emitters are deposited directly on the mirror surface and the emitted thermal energy is efficiently coupled to the far field. Further, we envision that, through appropriate metasurface design, it should be possible to produce an admixture of magnetic mirror and electric mirror behaviors to achieve a pre-desired angular response for the amplitude and phase of reflected waves.

FUNDING INFORMATION

U.S. Department of Energy (DOE) (DE-AC04-94AL85000).

ACKNOWLEDGMENTS

This work was performed, in part, at the Center for Integrated Nanotechnologies, a U.S. Department of Energy, Office of Basic Energy Sciences user facility. Portions of this work were supported by the Laboratory Directed Research and Development program at Sandia National Laboratories. Sandia National Laboratories is a multi-program laboratory managed and operated by Sandia Corporation, a wholly owned subsidiary of Lockheed Martin Corporation, for the U.S. Department of Energy's National Nuclear Security Administration under contract DE-AC04-94AL85000. We thank Larry K. Warne for useful technical discussions.

See Supplement 1 for supporting content.

REFERENCES

1. D. Sievenpiper, Z. Lijun, R. F. J. Broas, N. G. Alexopolous, and E. Yablonovitch, "High-impedance electromagnetic surfaces with a forbidden frequency band," IEEE Trans. Microwave Theor. Tech. **47**, 2059–2074 (1999).
2. J. D. Jackson, *Classical Electrodynamics* (Wiley, 1999).
3. A. Erentok, P. L. Luljak, and R. W. Ziolkowski, "Characterization of a volumetric metamaterial realization of an artificial magnetic conductor for antenna applications," IEEE Trans. Antennas Propag. **53**, 160–172 (2005).
4. A. P. Feresidis, G. Goussetis, S. H. Wang, and J. C. Vardaxoglou, "Artificial magnetic conductor surfaces and their application to low-profile high-gain planar antennas," IEEE Trans. Antennas Propag. **53**, 209–215 (2005).
5. D. J. Kern, D. H. Werner, A. Monorchio, L. Lanuzza, and M. J. Wilhelm, "The design synthesis of multiband artificial magnetic conductors using high impedance frequency selective surfaces," IEEE Trans. Antennas Propag. **53**, 8–17 (2005).
6. A. Vallecchi, J. R. De Luis, F. Capolino, and F. De Flaviis, "Low profile fully planar folded dipole antenna on a high impedance surface," IEEE Trans. Antennas Propag. **60**, 51–62 (2012).
7. A. S. Schwanecke, V. A. Fedotov, V. V. Khardikov, S. L. Prosvirnin, Y. Chen, and N. I. Zheludev, "Optical magnetic mirrors," J. Opt. A Pure Appl. Opt. **9**, L1–L2 (2007).
8. H. Rostami, Y. Abdi, and E. Arzi, "Fabrication of optical magnetic mirrors using bent and mushroom-like carbon nanotubes," Carbon **48**, 3659–3666 (2010).
9. I. Staude, A. E. Miroshnichenko, M. Decker, N. T. Fofang, S. Liu, E. Gonzales, J. Dominguez, T. S. Luk, D. N. Neshev, I. Brener, and Y. Kivshar, "Tailoring directional scattering through magnetic and electric resonances in subwavelength silicon nanodisks," ACS Nano **7**, 7824–7832 (2013).
10. J. C. Ginn, I. Brener, D. W. Peters, J. R. Wendt, J. O. Stevens, P. F. Hines, L. I. Basilio, L. K. Warne, J. F. Ihlefeld, P. G. Clem, and M. B. Sinclair, "Realizing optical magnetism from dielectric metamaterials," Phys. Rev. Lett. **108**, 097402 (2012).
11. L. Shi, J. T. Harris, R. Fenollosa, I. Rodriguez, X. Lu, B. A. Korgel, and F. Meseguer, "Monodisperse silicon nanocavities and photonic crystals with magnetic response in the optical region," Nat. Commun. **4**, 1904 (2013).
12. S. Person, M. Jain, Z. Lapin, J. J. Sáenz, G. Wicks, and L. Novotny, "Demonstration of zero optical backscattering from single nanoparticles," Nano Lett. **13**, 1806–1809 (2013).
13. P. Moitra, Y. Yang, Z. Anderson, I. I. Kravchenko, D. P. Briggs, and J. Valentine, "Realization of an all-dielectric zero-index optical metamaterial," Nat. Photonics **7**, 791–795 (2013).
14. Y. H. Fu, A. I. Kuznetsov, A. E. Miroshnichenko, Y. F. Yu, and B. Luk'yanchuk, "Directional visible light scattering by silicon nanoparticles," Nat. Commun. **4**, 1527 (2013).
15. P. Spinelli, M. A. Verschuuren, and A. Polman, "Broadband omnidirectional antireflection coating based on subwavelength surface Mie resonators," Nat. Commun. **3**, 692 (2012).
16. L. Shi, T. U. Tuzer, R. Fenollosa, and F. Meseguer, "A new dielectric metamaterial building block with a strong magnetic response in the sub-1.5-micrometer region: silicon colloid nanocavities," Adv. Mater. **24**, 5934–5938 (2012).
17. M. K. Schmidt, R. Esteban, J. J. Sáenz, I. Suárez-Lacalle, S. Mackowski, and J. Aizpurua, "Dielectric antennas—a suitable platform for controlling magnetic dipolar emission," Opt. Express **20**, 13636–13650 (2012).
18. A. E. Miroshnichenko and Y. S. Kivshar, "Fano resonances in all-dielectric oligomers," Nano Lett. **12**, 6459–6463 (2012).
19. A. I. Kuznetsov, A. E. Miroshnichenko, Y. H. Fu, J. Zhang, and B. Luk'yanchuk, "Magnetic light," Sci. Rep. **2**, 492 (2012).
20. A. E. Krasnok, A. E. Miroshnichenko, P. A. Belov, and Y. S. Kivshar, "All-dielectric optical nanoantennas," Opt. Express **20**, 20599–20604 (2012).
21. J. M. Geffrin, B. García-Cámara, R. Gómez-Medina, P. Albella, L. S. Froufe-Pérez, C. Eyraud, A. Litman, R. Vaillon, F. González, M. Nieto-Vesperinas, J. J. Sáenz, and F. Moreno, "Magnetic and electric coherence in forward- and back-scattered electromagnetic waves by a single dielectric subwavelength sphere," Nat. Commun. **3**, 1171 (2012).
22. A. B. Evlyukhin, S. M. Novikov, U. Zywietz, R. L. Eriksen, C. Reinhardt, S. I. Bozhevolnyi, and B. N. Chichkov, "Demonstration of magnetic dipole resonances of dielectric nanospheres in the visible region," Nano Lett. **12**, 3749–3755 (2012).
23. K. Seo, M. Wober, P. Steinvurzel, E. Schonbrun, Y. Dan, T. Ellenbogen, and K. B. Crozier, "Multicolored vertical silicon nanowires," Nano Lett. **11**, 1851–1856 (2011).
24. J. Z. Hao, Y. Seokho, L. Lan, D. Brocker, D. H. Werner, and T. S. Mayer, "Experimental demonstration of an optical artificial perfect magnetic mirror using dielectric resonators," in *IEEE Antennas and Propagation Society International Symposium* (IEEE, 2012), pp. 1–2.
25. J. Du, Z. Lin, S. T. Chui, G. Dong, and W. Zhang, "Nearly total omnidirectional reflection by a single layer of nanorods," Phys. Rev. Lett. **110**, 163902 (2013).
26. C. J. Chang-Hasnain and W. Yang, "High-contrast gratings for integrated optoelectronics," Adv. Opt. Photon. **4**, 379–440 (2012).
27. S. Liu, J. F. Ihlefeld, J. Dominguez, E. F. Gonzales, J. E. Bower, D. B. Burckel, M. B. Sinclair, and I. Brener, "Realization of tellurium-based all dielectric optical metamaterials using a multi-cycle deposition-etch process," Appl. Phys. Lett. **102**, 161905 (2013).
28. Y. Fink, J. N. Winn, S. Fan, C. Chen, J. Michel, J. D. Joannopoulos, and E. L. Thomas, "A dielectric omnidirectional reflector," Science **282**, 1679–1682 (1998).
29. F. Capolino, A. Vallecchi, and M. Albani, "Equivalent transmission line model with a lumped X-circuit for a metalayer made of pairs of planar conductors," IEEE Trans. Antennas Propag. **61**, 852–861 (2013).
30. S. Liu, T. S. Mahony, D. A. Bender, M. B. Sinclair, and I. Brener, "Mid-infrared time-domain spectroscopy system with carrier-envelope phase stabilization," Appl. Phys. Lett. **103**, 181111 (2013).

31. N. Jukam, S. S. Dhillon, D. Oustinov, J. Madeo, C. Manquest, S. Barbieri, C. Sirtori, S. P. Khanna, E. H. Linfield, A. G. Davies, and J. Tignon, "Terahertz amplifier based on gain switching in a quantum cascade laser," Nat. Photonics **3**, 715–719 (2009).
32. J. Kroll, J. Darmo, S. S. Dhillon, X. Marcadet, M. Calligaro, C. Sirtori, and K. Unterrainer, "Phase-resolved measurements of stimulated emission in a laser," Nature **449**, 698–701 (2007).
33. B. Ferguson and X.-C. Zhang, "Materials for terahertz science and technology," Nat. Mater. **1**, 26–33 (2002).
34. H.-T. Chen, W. J. Padilla, J. M. O. Zide, A. C. Gossard, A. J. Taylor, and R. D. Averitt, "Active terahertz metamaterial devices," Nature **444**, 597–600 (2006).
35. Q. Wu and X. C. Zhang, "Free-space electro-optics sampling of mid-infrared pulses," Appl. Phys. Lett. **71**, 1285–1286 (1997).
36. R. Huber, A. Brodschelm, F. Tauser, and A. Leitenstorfer, "Generation and field-resolved detection of femtosecond electromagnetic pulses tunable up to 41 THz," Appl. Phys. Lett. **76**, 3191–3193 (2000).
37. R. Huber, F. Tauser, A. Brodschelm, M. Bichler, G. Abstreiter, and A. Leitenstorfer, "How many-particle interactions develop after ultrafast excitation of an electron-hole plasma," Nature **414**, 286–289 (2001).
38. G. Gunter, A. A. Anappara, J. Hees, A. Sell, G. Biasiol, L. Sorba, S. De Liberato, C. Ciuti, A. Tredicucci, A. Leitenstorfer, and R. Huber, "Sub-cycle switch-on of ultrastrong light-matter interaction," Nature **458**, 178–181 (2009).
39. A. Sell, A. Leitenstorfer, and R. Huber, "Phase-locked generation and field-resolved detection of widely tunable terahertz pulses with amplitudes exceeding 100 MV/cm," Opt. Lett. **33**, 2767–2769 (2008).
40. A. Benz, S. Campione, S. Liu, I. Montaño, J. F. Klem, A. Allerman, J. R. Wendt, M. B. Sinclair, F. Capolino, and I. Brener, "Strong coupling in the sub-wavelength limit using metamaterial nanocavities," Nat. Commun. **4**, 2882 (2013).
41. S. Steshenko, F. Capolino, P. Alitalo, and S. Tretyakov, "Effective model and investigation of the near-field enhancement and subwavelength imaging properties of multilayer arrays of plasmonic nanospheres," Phys. Rev. E **84**, 016607 (2011).
42. S. Campione, F. Mesa, and F. Capolino, "Magnetoinductive waves and complex modes in two-dimensional periodic arrays of split ring resonators," IEEE Trans. Antennas Propag. **61**, 3554–3563 (2013).
43. S. Campione, M. B. Sinclair, and F. Capolino, "Effective medium representation and complex modes in 3D periodic metamaterials made of cubic resonators with large permittivity at mid-infrared frequencies," Photon. Nanostr. Fundam. Appl. **11**, 423–435 (2013).
44. C. A. Balanis, *Antenna Theory: Analysis and Design* (Wiley, 2005).
45. E. Yablonovitch, "Inhibited spontaneous emission in solid-state physics and electronics," Phys. Rev. Lett. **58**, 2059–2062 (1987).
46. K. H. Drexhage, "Influence of a dielectric interface on fluorescence decay time," J. Lumin. **1–2**, 693–701 (1970).
47. W. L. Barnes, "Fluorescence near interfaces: the role of photonic mode density," J. Mod. Opt. **45**, 661–699 (1998).

Research Article Vol. 1, No. 4 / October 2014 / Optica 257

Nonredundant Raman imaging using optical eigenmodes

Sebastian Kosmeier,[1] Svetlana Zolotovskaya,[1] Anna Chiara De Luca,[1,2,*] Andrew Riches,[3] C. Simon Herrington,[3,4] Kishan Dholakia,[1] and Michael Mazilu[1]

[1]SUPA, School of Physics and Astronomy, University of St Andrews, North Haugh, KY16 9SS St Andrews, UK

[2]Institute of Protein Biochemistry, National Research Council, Via P. Castellino 111, 80131 Naples, Italy

[3]School of Medicine, University of St Andrews, North Haugh, KY16 9TF St Andrews, UK

[4]Medical Research Institute, University of Dundee, Ninewells Hospital Medical School, James Arrott Drive, DD1 9SY Dundee, UK

*Corresponding author: a.deluca@ibp.cnr.it

Received 8 July 2014; revised 10 September 2014; accepted 11 September 2014 (Doc. ID 216399); published 17 October 2014

Various forms of imaging schemes have emerged over the last decade that are based on correlating variations in incident illuminating light fields to the outputs of single "bucket" detectors. However, to date, the role of the orthogonality of the illumination fields has largely been overlooked, and, furthermore, the field has not progressed beyond bright field imaging. By exploiting the concept of orthogonal illuminating fields, we demonstrate the application of optical eigenmodes (OEis) to wide-field, scan-free spontaneous Raman imaging, which is notoriously slow in wide-field mode. The OEi approach enables a form of indirect imaging that exploits both phase and amplitude in image reconstruction. The use of orthogonality enables us to nonredundantly illuminate the sample and, in particular, use a subset of illuminating modes to obtain the majority of information from the sample, thus minimizing any photobleaching or damage of the sample. The crucial incorporation of phase, in addition to amplitude, in the imaging process significantly reduces background noise and results in an improved signal-to-noise ratio for the image while reducing the number of illuminations. As an example we can reconstruct images of a surface-enhanced Raman spectroscopy sample with approximately an order of magnitude fewer acquisitions. This generic approach may readily be applied to other imaging modalities such as fluorescence microscopy or nonlinear vibrational microscopy.

OCIS codes: (110.0110) Imaging systems; (170.3010) Image reconstruction techniques; (100.5070) Phase retrieval; (230.6120) Spatial light modulators; (180.5655) Raman microscopy.

http://dx.doi.org/10.1364/OPTICA.1.000257

1. INTRODUCTION

A generic challenge in all forms of imaging is to acquire information in a rapid, damage-free manner. In the optical domain, photo-damage can be an issue in numerous forms of biomedical methods, and furthermore the very manner of sample illumination is typically nonoptimal. In this context, structured illumination aims to engineer the excitation/illumination beams to achieve faster acquisition [1], higher resolution [2,3], or even three-dimensional imaging capabilities [4]. Structured illumination in combination with "bucket" detection (single detector acquisition) has gained popularity due to its inherent simplicity. Separately, illumination based upon nonredundant imaging relies on the use of structured light fields incident on a sample to detect its features by using the smallest number of illuminations, i.e., to achieve the fastest acquisition. This is normally not the case when considering a scanned Gaussian beam approach where the partial overlap between adjacent excitation spots leads to no additional information ("redundant"

measure) and to a decreased image resolution. Due to their orthogonality, optical eigenmodes (OEis) offer a natural set of fields that avoid any overlap in the probing the optical degrees of freedom of the sample [5,6]. Additionally, the experimental *in situ* determination of the OEis has the advantage of automatically taking into account all optical aberrations present in the system. It is therefore advantageous to use these OEis as structured illumination fields in the context of imaging.

Previously, we have developed a coherent indirect imaging technique [7] based on OEi fields. This paper demonstrates the first experimental application, to the best of our knowledge, of this approach to the case of imaging spontaneous Raman scattering. In particular, Raman scattering is a vibrational microscopy method offering a label-free imaging contrast mechanism capable of probing noninvasively the chemical composition of biological and inert materials at microscopic scales [8–12]. It has promise for many applications, yet has been hampered by long acquisition times, which in turn has resulted in researchers resorting typically to more complex nonlinear vibrational spectroscopy methods. Standard laser-scanning-based Raman spectroscopic imaging [13,14] allows the quantification of the chemical heterogeneity of a sample in terms of the spatial distribution of its molecular constituents. For these reasons, Raman imaging applications cover a wide range of scientific disciplines, such as pharmacology, biology, medicine, and material science [15–18]. Importantly, Raman imaging is useful to measure the pharmacokinetic properties of tablets as well as aid in authenticity evaluation, manufacturing processes, biomedical imaging, and even counterfeit product identification [19]. However, there exists a trade-off between the achievable scanning-based imaging speed and the spectral selectivity of such schemes. Raman spectroscopy is notoriously slow and not usually suitable for wide-field imaging purposes as the signals are very weak (only one photon in one million is Raman scattered). The required detection times are of the order of seconds to minutes for each pixel. As a result, an image of an area of tens of micrometers in length and width typically requires hours to acquire, making micro-Raman not suitable for rapid large-scale imaging of pharmaceutical tablets as an example. Various Raman imaging methodologies have been proposed to alleviate this issue. In point and line scanning Raman imaging [13,14,20,21] a circular or line-shaped laser beam raster scans the sample in two spatial dimensions with a Raman spectrum recorded at each position.

Other direct imaging techniques illuminate the sample using a number of laser spots or a wide-field laser beam. The resulting Raman signal is directly imaged on a filtered detector acquiring a single measurement. For example, in [22], the authors used a Hadamard mask to produce a structure illumination pattern on the sample to generate only a one-dimensional compressed Raman image. Additional wide-field Raman approaches include tunable detection band-pass filters and two-dimensional detectors [23–25]. However, this method discards the Raman scattered photons outside the wavelength detection band, rendering this approach spectrally inefficient. Recently, a multivariate hyperspectral Raman imaging (MHRI) approach has been introduced by Davis *et al.* based on a compressive spectral detection strategy [26]. Our method applies a nonredundant approach to the illumination side of the Raman imaging enabling a step change in the acquisition process for this modality. This nonredundant approach is equivalent to a compression in the number of measures when compared to a standard raster-scan method. This is due to the fact that the standard raster-scan approach inherently leads to an overlap between adjacent optical beams.

In our nonredundant Raman OEi imaging scheme, we illuminate the sample with a predetermined set of OEis. For each of the illuminations used, we measure the Raman spectrum from which we subsequently reconstruct the hyperspectral Raman image of the sample. An important outcome of this method is the adaptive resolution that can be achieved. Indeed, to increase the resolution, we do not need to rescan the sample with a finer step size, but simply continue to probe the sample with increasingly higher-order OEi illuminations. In effect, the higher the order of the OEi illumination, the finer the details probed by the OEi illumination. Furthermore, due to the nonredundant nature of OEi-based structured illumination, we realize a given imaging resolution using the smallest number of OEi probes possible. Similar arguments are also employed when considering compressive fluorescence imaging [27]. The sparsity of the sample allows it to be imaged using a small number of illuminations. Here, we restrict the number of illuminations such that the sparse degrees of freedom of the optical setup are used optimally for probing from the onset delivering a nonredundant version of compressive imaging. Interestingly, our approach is also similar to "computational ghost imaging" whereby known fields are used to illuminate a sample and the image is reconstructed using the scattering coefficients [28,29]. However, here the light is not shaped by a random mask created by a diffuser or spatial light modulator (SLM), but the illuminations correspond to a nonredundant set of orthogonal OEi beam profiles.

2. RESULTS

A. Determining the OEi

Figure 1(a) describes our experimental setup. Figure 1(b) shows the theoretical spatial field distribution of the first nine OEis $\mathbb{E}_\ell$ in the region of interest (ROI) [7,30]. We observe that as the order of the mode ℓ increases, finer details are accessed. In order to check the orthonormality relation, in the ROI, $\int_{\mathrm{ROI}} \mathbb{E}_k \mathbb{E}_l^* \mathrm{d}\sigma = \delta_{kl}$ of the experimentally implemented OEi, the complex product $\mathbb{E}_k \mathbb{E}_l^*$ is determined from four intensity acquisitions according to the polarization identity [31]. Each entry in the matrix in Fig. 1(c) corresponds to an orthonormality relation for a pair k, l. The matrix is almost diagonal, hence demonstrating orthonormality of the experimentally implemented modes in good approximation (for more details see Appendix A). Recall that the presence of optical aberrations precludes the use of theoretically calculated eigenmodes; however, in this case these eigenmodes can be experimentally determined [5] automatically accounting for any aberration and angular dependence.

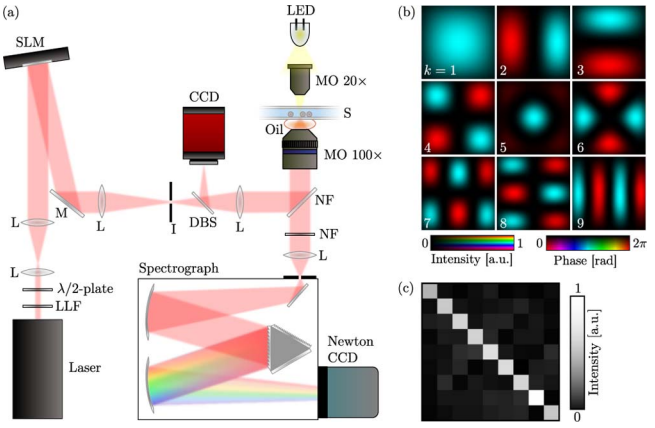

Fig. 1. (a) Experimental configuration for OEi Raman microscopy. LLF, laser line filter at 785 nm; L, lens; SLM, spatial light modulator; M, mirror; I, iris to filter out first diffraction order from SLM; DBS, dichroic beam splitter reflecting visible light and transmitting infrared light; CCD, CCD camera; NF, notch filters to transmit Raman scattered light into the spectrograph; MO, microscope objective; S, sample. (b) Spatial field distribution and (c) orthonormality matrix of the first nine OEis.

B. Raman OEi Imaging

As a first example, we imaged a sample consisting of a polystyrene bead in the top right corner of the ROI and a polymetacrylate (PMAA) bead in the lower left corner; both beads are 3 μm in diameter. Figure 2(b) shows a bright field image of the sample. Figures 2(c) and 2(d) depict raster-scan Raman images of the sample obtained by integrating the main polystyrene and PMAA peaks, respectively [shown in Fig. 2(a)]. In Fig. 2(e) the information from Figs. 2(c) and 2(d) is superimposed in a hyperspectral image, highlighting the polystyrene bead (red color) and the PMAA bead (in blue).

Following the raster scans, the same object was imaged with the OEi approach, using only the first $M = 4$ modes, where M was chosen such as to deliver a signal-to-noise ratio (SNR) comparable to the raster-scan image (SNR defined later). The results are shown in Figs. 2(f) and 2(g) with the reconstruction carried out for the polystyrene and PMAA peaks, respectively. Figure 2(h) depicts the hyperspectral Raman OEi image. Both beads are clearly reconstructed in agreement with the standard raster scans, hence demonstrating the functionality of the method and its nonredundant nature. Furthermore, we remark that the OEi images visually exhibit a lower background noise compared to the raster scans.

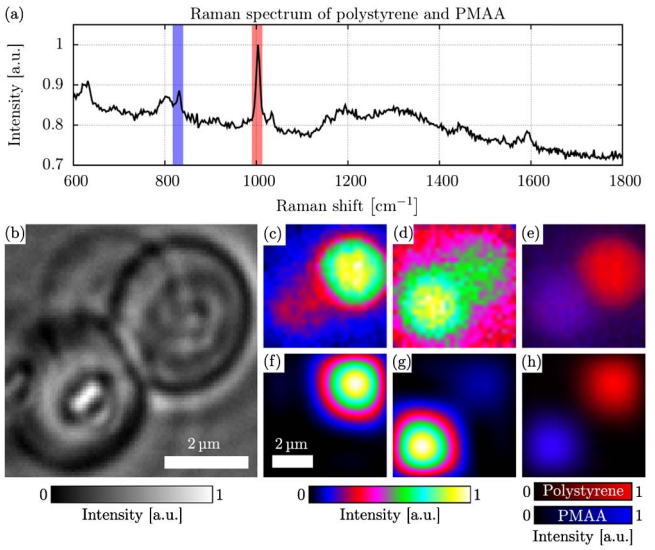

Fig. 2. (a) Spectrum for one polystyrene bead and one PMAA bead illuminated with the fourth eigenmode and 3 s acquisition time. The area of the PMAA peak is indicated in blue, while that of polystyrene is highlighted in red. (b) White-light image of the sample with a polystyrene bead in the top right corner and a PMAA bead in the lower left corner. (c), (d) Raman images obtained with 26 × 26 points raster scans. (f), (g) OEi Raman images corresponding to (c) and (d). (e) Graphical superposition of the intensity distributions in (c) and (d), showing the positions of the polystyrene bead (red) and the PMAA bead (blue). (h) Same as (e) for the OEi images.

C. Surface-Enhanced Raman Scattering OEi Imaging

In order to investigate the capabilities of the method to image samples with more highly resolved features, agglomerates of 200 nm gold nanoparticles were chosen as sample objects. The nanoparticles were deposited on a gold surface covered with an analyte, in our case dithiolated nanoparticle linkers [32,33]. The small gap of less than 2 nm between the gold surface and the gold particles enables a strong field enhancement, giving rise to surface-enhanced Raman scattering (SERS). Figure 3(a) shows a sketch of this arrangement with a gold sphere on the gold surface. As the object for the following experiments we chose a sample region with two agglomerates of particles. The scanning electron microscope (SEM) image in Fig. 3(b) shows an area of the sample, which is similar to the one we used for imaging. The actual object configuration is displayed in Fig. 3(c), which is a reflection of the reference wave E_{ref} from the sample surface. The nanoparticle agglomerates appear with low intensity due to scattering.

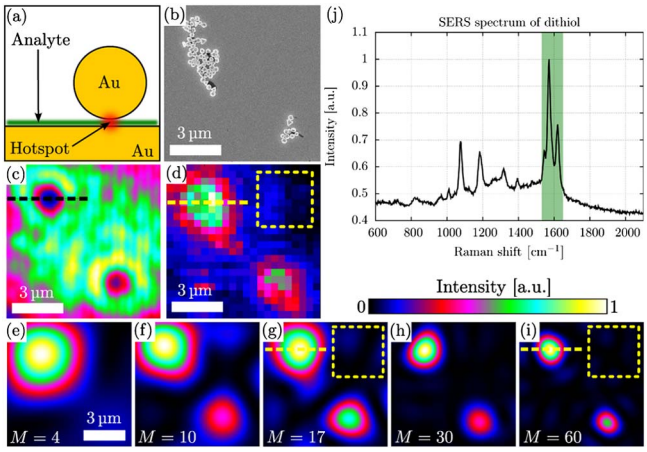

Fig. 3. (a) Schematic of the SERS sample: 200 nm gold particle on a gold surface coated with analyte dithiol. The hotspot between the gold layer and the sphere gives rise to a SERS signal. (b) SEM image of a sample area similar to the imaged one. (c) Reflected laser light from the 9 μm × 9 μm ROI chosen for imaging. Two agglomerates of gold particles are visible as dark spots. (d) SERS Raman raster scan of the sample plane. (e)–(i) OEi imaging reconstruction for $M = 4$ to $M = 60$ modes. (j) SERS spectrum of dithiol.

The main Raman peak of dithiolated nanoparticle linkers is located at a Raman shift of about 1600 cm^{-1} [Fig. 3(j), area of integration highlighted in green]. A SERS raster scan using 22 × 22 pixels results in the image shown in Fig. 3(d), revealing the SERS activity at the position of the gold particle agglomerates. The corresponding OEi-based images are depicted in Figs. 3(e)–3(i) for projection of $M = 4$ to $M = 60$ modes.

D. Signal-to-Noise Ratio

In Fig. 3, we observe visually that increasing the number M of the OEi used, the location and size of the SERS hotspots is reproduced with more accuracy. This effect can be quantified experimentally [Fig. 4(a)] and theoretically [Fig. 4(b)] by measuring the changes in the SNR and noise level as a function of the number of OEi illuminations used. The SNR is defined as the ratio between the maximum Raman peak, in the high signal region, and the average signal from the image region void of the Raman active medium where any measured signal can be associated with system noise. To determine the experimental SNR, we used the maximum Raman peak of the image divided by the mean value in the dotted squares in Figs. 3(d) and 3(i) for the raster scan and for the OEi image respectively. Note that, by adjusting the exposure time for each acquisition accordingly, the total laser power used to obtain both methods was identical. The results from the numerical simulation presented in Fig. 4(b) illustrate the case of a paraxial optical system consisting of a phase and amplitude mask for the SLM, an apertured lens modeling a generic finite optical system, and the imaging plane corresponding to the Fourier plane with respect to the SLM plane. The model takes into account noise in the system (beam pointing stability and detection) for both the determination and the subsequent use of the OEi for imaging. Multiple numerical realizations are shown to visualize the effect of noise.

E. Pharmaceutical Applications

Finally, the applicability of the Raman OEi imaging was investigated in a pharmaceutical context. In particular, the compound distribution of the well-known anticongestion and analgesic compound SUDAFED (Wrafton Laboratories Ltd.) was determined. Each capsule contains a microcrystal mixture of paracetamol (500 mg), caffeine (25 mg), and phenylephrine hydrochloride (6.1 mg). A white-light full-field image of the sample is shown in Fig. 5(a). The ROI of

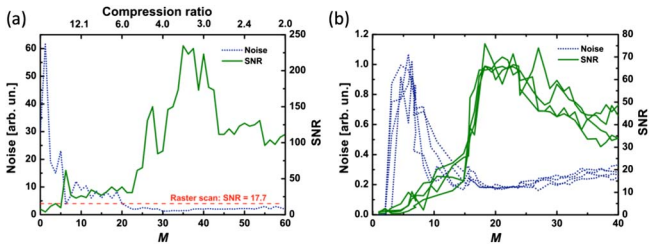

Fig. 4. (a) Experimental signal-to-noise ratio (SNR) and noise level as a function of the number of OEi illuminations. (b) Theoretical SNR and noise level as a function of the number of OEi illuminations for a paraxial optical stochastically system including CCD readout, SLM beam creation, and optical system noise.

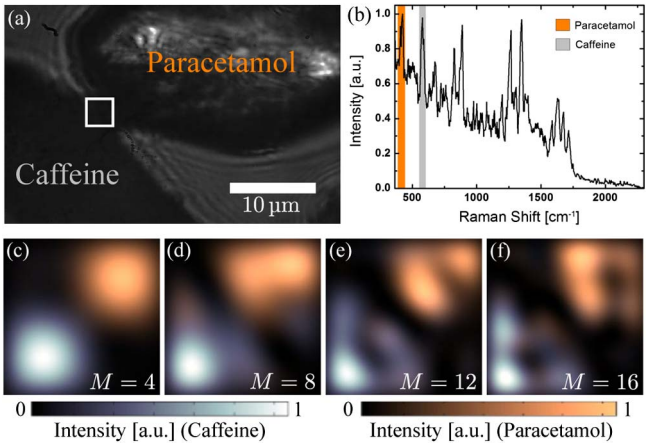

Fig. 5. (a) Full field of view image of a SUDAFED sample: a paracetamol crystal (top right corner) and a caffeine crystal (bottom left corner). The white square indicates the ROI. (b) Spectrum of the compound sample, in the ROI, illuminated with the 12th OEi mode, 5 s acquisition time, and 250 μm slit width. (c)–(f) Hyperspectral images of the ROI for different number M of OEis.

3.6 × 3.6 μm, marked with the white square, includes two adjacent microcrystals. Figure 5(b) shows a typical Raman spectrum of the two compounds illuminated simultaneously by $\ell = 12$ OEi. The reconstructions, based on the coupling coefficients of the Raman bands unique for each compound, are depicted in Figs. 5(c)–5(f) for $M = 4$ to $M = 16$ modes. It can be seen that two substances are clearly resolved.

3. DISCUSSION

The decomposition of the focal field into eigenmodes enables illumination of the object in the most nonredundant possible manner. The number of OEi illuminations (M) necessary is determined by the criteria chosen, such as resolution or SNR. This number can be determined either initially for an unknown sample by considering the optical coupling efficiency to each of the OEis or adaptively during the imaging process. Experimentally, hyperspectral Raman indirect imaging was shown for an object containing beads of different materials (Fig. 2) and hence different Raman signatures. In this case, we achieved a Raman image using only $M = 4$ OEis. In real terms, this corresponds to 16 illumination fields compared to $26 \times 26 = 676$ illuminations for the raster-scan methods [Fig. 2(d)] delivering a compression of more then 40 times. Additionally, the OEi imaging concept was applied to a SERS sample (Fig. 3) and compared to raster-scan imaging as the native Raman imaging modality. In this case, by comparing the raster-scan image with the $M = 17$ image in Fig. 3(g), which shows a similar reconstruction, we observe a sevenfold compression ratio. This compression ratio still delivers a large improvement versus the traditional raster-scan method, although this is not as high as in the case of beads due to the present reproducibility issues with SERS substrates. The compression ratio can be further improved by a factor of 4 when detecting the complex field in the image plane using a holographic approach [34] as opposed to the polarization identity [31].

A further advantage of the method presented here is the improvement in the SNR. If we look at the SERS experimental data (Fig. 3), for $M = 60$ modes we see good visual agreement of the OEi image [Fig. 3(i)] and the reference image [Fig. 3(c)] is observed. As for the images of the beads, the OEi images of the SERS sample exhibit a lower background than the raster scans. This visual impression was confirmed quantitatively in terms of the SNR [see Fig. 4(a)]. With a value of 17.7, the SNR in the raster scan is an order of magnitude lower compared to the value of 245 measured in the OEi image. Figure 4(a) also shows that increasing the number of OEi illuminations implies an increase of the SNR. A maximum (in this case at $M = 35$) is achieved when the noise level drops below a certain measurement resolution threshold (determined by considering the readout noise of the detector and its dynamic range). Additionally, each OEi mode is associated with an optical coupling efficiency (eigenvalue) linking the SLM beam generation plane to the imaging plane. As the OEi modes are ordered by decreasing eigenvalues, the larger the mode number, the more difficult it becomes to efficiently create the corresponding OEi beam. This can also be seen in the slight increase of the noise level in Fig. 4.

An important aspect of any imaging method is its resolution. We investigated this factor by measuring the full width at half-maximum of the larger of the two SERS clusters [dashed lines in Figs. 3(c), 3(d), 3(g), and 3(i)]. The optical image used as a reference image shows a width of $w_{\mathrm{ref}} = 1.58$ μm. The raster-scan image measures this particle agglomerate with a width of $w_{\mathrm{ras}} = 2.57$ μm. This deviation is attributed to the background noise and the 400 nm step width of the raster scan, which was chosen for a good compromise between SNR and spatial resolution. In contrast, the Raman OEi imaging scheme does not rely on probing the sample at discrete points, but uses a continuous wide-field sample illumination. As a result, the width $w_{\mathrm{OEi},M=60} = 1.30$ μm measured for the OEi image is in good agreement with the reference width w_{ref}. Further, adaptive resolution can be implemented using OEi illuminations. As shown in Figs. 3 and 5, it is possible to continuously increase the image resolution by illuminating the sample with increasing higher-order OEis without rescanning the sample.

It is by combining the SNR and resolution arguments that we can quantify the compression/nonredundancy level achieved by the OEi method discussed previously. Indeed, for determining the compression factor in the SERS case (Fig. 3), we look for the illumination containing the number of modes that produces the same spatial resolution as the raster scan. This is approximately the case for $M = 17$ in Fig. 3(g), for which $w_{\mathrm{OEi},17} = 2.70$ μm and SNR = 43.2. Compared to the 484 acquisitions for the raster scan (SNR = 17.7), the OEi image required $4 \times 17 = 68$ acquisitions; hence we achieve approximately a sevenfold compression, while the SNR is still a factor of 2.5 larger.

Finally, the applicability of the method for a practical task was shown by visualizing the compound distribution of a pharmaceutical sample. By increasing the number of illuminations to $M = 16$, in a ROI of 3.6×3.6 μm a resolution of $w_{\mathrm{OEi},16} = 0.9$ μm can be achieved, allowing us to visualize even small features. We believe that OEi-based indirect imaging in conjunction with Raman spectroscopy is a very promising concept for numerous real-world imaging applications.

The results demonstrate high potential of the method in pharmacology, for example, to detect counterfeit pharmaceuticals, monitor processes and products.

APPENDIX A

1. Optical Setup

The experimental implementation of OEi Raman imaging is depicted in Fig. 1(a): the expanded beam of a 1 W diode laser (TEC-420-0780-1000, Laser 2000, wavelength: 785 nm) is modulated by an SLM (LCOS-SLM X10468-02, Hamamatsu Photonics) and then coupled into a microscope objective (100 × /1.30 Oil UPlanFL N, Olympus). The SLM is used to encode phase and amplitude onto the incident beam in the first-order diffraction configuration filtered by the iris [35]. The Raman scattered light from the sample is collected in epi-configuration and transmitted into a spectrograph (Shamrock SR-303i-B, Andor) equipped with a cooled CCD detector (Newton CCD, Andor). Spectra are acquired with a 400 lines/mm grating blazed for 850 nm with a monochromator slit width of 250 μm and 5 s acquisition time. The slit size was chosen such that all Raman signal from the sample is collected while minimizing spectral resolution loss. An LED allows white-light illumination of the sample to capture transmission images on a conventional CCD camera (Basler pilot piA640-210gm, 648 × 488 pixel resolution, 7.4 μm pixel pitch).

2. Optical Eigenmodes Implementation

Regarding the imaging modality, we expand the concept of OEi imaging [7] to Raman spectroscopical imaging. This technique is based on the single bucket detector measure of the optical scattering from the imaged sample under orthogonal eigenmode illumination. Conceptually, in this instance we replace the single detector by a spectrometer [see Fig. 1(a)] and generalize the imaging technique to scattering and conjugate focal plane detection. To illustrate these points, let us consider a set of M OEis $\mathbb{E}_k$ (with $k = 1 \ldots M$) defining, in the sample plane, an intensity orthonormal set of optical fields

$$\int_{\mathrm{ROI}} \mathbb{E}_j^* \mathbb{E}_k \, \mathrm{d}\sigma = \delta_{jk}, \tag{A1}$$

where ROI stands for the surface of the ROI to be imaged. The OEis can be determined either experimentally or theoretically. The experimental determination of the OEis is taking into account the optical aberrations of the system and is equivalent to the measure of the optical transmission matrix between the SLM [see Fig. 1(a)] and the sample plane. However, this method is time consuming as the optical system itself needs to be experimentally characterized. If the optical setup allows for aberration-free, direct imaging and its optical transfer function is known, then it is possible to determine the set of OEis numerically. This approach is faster though at the expense of loss of flexibility. Here, depending on the particular experiment in question, we employ both of these approaches.

Figure 1(b) shows the precalculated OEis imaged after their propagation through the whole system, and Fig. 1(c) verifies experimentally their orthonormality defined by Eq. (A1).

3. Raman Imaging

The OEi imaging technique relies on the measure of the complex projection coefficients c_k corresponding to the optical overlap between the scattered field and the eigenmode illumination. These coefficients can be measured using multiple interferences between a reference beam and an OEi probe beam

$$c_k^*(\lambda) = \frac{1}{n}\sum_{p=0}^{n-1} e^{i\frac{2\pi}{n}p}\int_{\mathrm{ROI}} s_\lambda |E_{\mathrm{ref}} + e^{-i\frac{2\pi}{n}p}\mathbb{E}_k|^2 d\sigma$$
$$= \int_{\mathrm{ROI}} s_\lambda E_{\mathrm{ref}}^* \mathbb{E}_k d\sigma, \quad \textbf{(A2)}$$

where s_λ stands for the spatially dependent incoherent Raman intensity scattering efficiency, $n \geq 3$ defines the number of phase differences used to measure the OEi projection coefficients, λ is the detection wavelength defined by the spectrometer, and E_{ref} is the spatially dependent reference wave. In this paper, we used $n = 4$ measures for each projection coefficient accounting for the factor of four between the number of illuminations and number of probes.

Equation (A2) highlights the major difference between OEi imaging in the incoherent Raman case and the coherent OEi imaging technique [7]. In the coherent case, we measure the projection coefficient in the Fourier plane of the sample, which transforms the reference beam into a single proportionality coefficient, irrespective of the sample. The coefficients d_k in the coherent case are given by

$$d_k^*(\lambda) = \frac{1}{n}\sum_{p=0}^{n-1} e^{i\frac{2\pi}{n}p}\left|\int_{\mathrm{ROI}} T\left(E_{\mathrm{ref}} + e^{-i\frac{2\pi}{n}p}\mathbb{E}_k\right)d\sigma\right|^2$$
$$\propto \int_{\mathrm{ROI}} T\mathbb{E}_k d\sigma, \quad \textbf{(A3)}$$

where T stands for the spatially dependent field transmission coefficient of the sample. Equation (A3) shows that the coherent coefficients correspond to the projection coefficients of T on each of the OEis $\mathbb{E}_k$. Therefore, the reconstructed image using these coefficients visualizes the local transmission of the sample. On the other hand, we observe [Eq. (A2)] that the reconstructed image using incoherent scattering delivers the product between the local incoherent Raman scattering efficiency, s_λ, and the reference field, E_{ref}. Using a uniform illumination beam as a reference will deliver similar results in both cases. In our experiments, we therefore use a defocused Gaussian beam as a reference beam.

As outlined above, the OEi Raman imaging process requires the determination of the complex coupling coefficient c_k with respect to a Raman band of interest for each eigenmode $\mathbb{E}_k$ illumination. Exemplarily, Fig. 2(a) depicts a spectrum acquired for the illumination of a polystyrene bead and a PMAA bead with one of the eigenmodes, $\mathbb{E}_4$. The absolute value squared of the projection coefficients $|c_4|^2$ can be seen as the integral over the Raman peak of interest. In Fig. 2(a) the polystyrene peak is highlighted in red, while the PMAA peak is indicated in blue. Full phase and amplitude can be obtained using Eq. (A2) with at least three differential phase steps $n = 3$. In detail, both $\mathbb{E}_k$ and E_{ref} are simultaneously encoded on the SLM using random phase encoding [36].

After obtaining the coupling c_k for each mode $\mathbb{E}_k$, an OEi image T of the sample is formed by the superposition of the modes weighted with the corresponding coefficients:

$$T(\lambda) = \sum_{k=1}^{M} c_k(\lambda)\mathbb{E}_k, \quad \textbf{(A4)}$$

where T corresponds in reality to $s_\lambda E_{\mathrm{ref}}$; i.e., the reconstructed image detects the Raman scattering density illuminated by the reference beam. For comparison to the OEi images, a conventional raster-scan image can be acquired by deflecting a focused beam over the sample and capturing a Raman spectrum for each scanning position. Each pixel of the image is then formed by integration over the relevant spectral region.

FUNDING INFORMATION

Associazione Italiana per la Ricerca sul Cancro (Start-up Grant 11454); Engineering and Physical Sciences Research Council (EPSRC) (CR-UK/EPSRC/MRC/DoH (England) imaging programme); European Commission (FP7 ICT, contract no. 317744); Ministry of Education, Universities and Research (Italy) (FIR-project RBFR12WAPY).

ACKNOWLEDGMENTS

Sumeet Mahajan is acknowledged for the SERS sample and Kapil Debnath for providing SEM images of the sample. M. M., A. C. D. L., and K. D. developed and planned the project. M. M. performed the optical eigenmode theory and algorithm design. A. C. D. L. designed the optical setup. S. K. simulated the illumination eigenmodes and implemented the experimental imaging algorithms. S. K. and S. Z. performed the experimental work and data analysis. All authors contributed to the discussion of the results and writing of the paper.

REFERENCES

1. S. Abrahamsson, J. Chen, B. Hajj, S. Stallinga, A. Y. Katsov, J. Wisniewski, G. Mizuguchi, P. Soule, F. Mueller, C. D. Darzacq, X. Darzacq, C. Wu, C. I. Bargmann, D. A. Agard, M. Dahan, and M. G. Gustafsson, "Fast multicolor 3D imaging using aberration-corrected multifocus microscopy," Nat. Methods **10**, 60–63 (2012).
2. M. G. L. Gustafsson, "Surpassing the lateral resolution limit by a factor of two using structured illumination microscopy," J. Microsc. **198**, 82–87 (2000).
3. E. Mudry, K. Belkebir, J. Girard, J. Savatier, E. Le Moal, C. Nicoletti, M. Allain, and A. Sentenac, "Structured illumination microscopy using unknown speckle patterns," Nat. Photonics **6**, 312–315 (2012).
4. L. Shao, P. Kner, E. H. Rego, and M. Gustafsson, "Super-resolution 3D microscopy of live whole cells using structured illumination," Nat. Methods **8**, 1044–1046 (2011).
5. S. Kosmeier, A. C. De Luca, S. Zolotovskaya, A. Di Falco, K. Dholakia, and M. Mazilu, "Coherent control of plasmonic nanoantennas using optical eigenmodes," Sci. Rep. **3**, 1808 (2013).

6. X. Tsampoula, M. Mazilu, T. Vettenburg, F. Gunn-Moore, and K. Dholakia, "Enhanced cell transfection using subwavelength focused optical eigenmode beams," Photon. Res. **1**, 42–46 (2013).
7. A. C. De Luca, S. Kosmeier, K. Dholakia, and M. Mazilu, "Optical eigenmode imaging," Phys. Rev. A **84**, 021803 (2011).
8. V. Ciobota, E.-M. Burkhardt, W. Schumacher, P. Rosch, K. Kusel, and J. Popp, "Applications of Raman spectroscopy to virology and microbial analysis," Anal. Bioanal. Chem. **397**, 2929–2937 (2010).
9. P. R. Jess, M. Mazilu, K. Dholakia, A. C. Riches, and C. S. Herrington, "Optical detection and grading of lung neoplasia by Raman microspectroscopy," Int. J. Cancer **124**, 376–380 (2009).
10. E. Canetta, M. Mazilu, A. C. De Luca, A. E. Carruthers, K. Dholakia, S. Neilson, H. Sargeant, T. Briscoe, C. S. Herrington, and A. C. Riches, "Modulated Raman spectroscopy for enhanced identification of bladder tumor cells in urine samples," J. Biomed. Opt. **16**, 037002 (2011).
11. A. C. De Luca, S. Manago, M. A. Ferrara, I. Rendina, L. Sirleto, R. Puglisi, D. Balduzzi, A. Galli, P. Ferraro, and G. Coppola, "Non-invasive sex assessment in bovine semen by Raman spectroscopy," Laser Phys. Lett. **11**, 055604 (2014).
12. A. Jonas, A. C. De Luca, G. Pesce, G. Rusciano, A. Sasso, S. Caserta, S. Guido, and G. Marrucci, "Diffusive mixing of polymers investigated by Raman microspectroscopy and microrheology," Langmuir **26**, 14223–14230 (2010).
13. M. Delhaye and P. Dhamelincourt, "Raman microprobe and microscope with laser excitation," J. Raman Spectrosc. **3**, 33–43 (1975).
14. S. Schlücker, M. D. Schaeberle, S. W. Huffman, and I. W. Levin, "Raman microspectroscopy: a comparison of point, line, and wide-field imaging methodologies," Anal. Chem. **75**, 4312–4318 (2003).
15. S. Stewart, R. Priore, M. P. Nelson, and P. J. Treado, "Raman imaging," Annu. Rev. Anal. Chem. **5**, 337–360 (2012).
16. N. Gierlinger and M. Schwanninger, "The potential of Raman microscopy and Raman imaging in plant research," J. Spectrosc. **21**, 69–89 (2007).
17. G. Rusciano, A. C. De Luca, G. Pesce, and A. Sasso, "Raman tweezers as a diagnostic tool of hemoglobin-related blood disorders," Sensors **8**, 7818–7832 (2008).
18. D. Graf, F. Molitor, K. Ensslin, C. Stampfer, A. Jungen, A. C. Hierold, and L. Wirtz, "Spatially resolved Raman spectroscopy of single- and few-layer graphene," Nano Lett. **7**, 238–242 (2007).
19. M. N. Slipchenko, H. Chen, D. R. Ely, Y. Jung, M. T. Carvajal, and J.-X. Cheng, "Vibrational imaging of tablets by epi-detected stimulated Raman scattering microscopy," Analyst **135**, 2613–2619 (2010).
20. K. Hamada, K. Fujita, N. I. Smith, M. Kobayashi, Y. Inouye, and S. Kawata, "Raman microscopy for dynamic molecular imaging of living cells," J. Biomed. Opt. **13**, 044027 (2008).
21. A. F. Palonpon, J. Ando, H. Yamakoshi, K. Dodo, M. Sodeoka, S. Kawata, and K. Fujita, "Raman and SERS microscopy for molecular imaging of live cells," Nat. Protoc. **8**, 677–692 (2013).
22. P. J. Treado and M. D. Morris, "Hadamard transform Raman imaging," Appl. Spectrosc. **42**, 897–901 (1988).
23. G. J. Puppels, M. Grond, and J. Greve, "Direct imaging Raman microscope based on tunable wavelength excitation and narrow-band emission detection," Appl. Spectrosc. **47**, 1256–1267 (1993).
24. P. J. Treado, I. W. Levin, and E. N. Lewis, "High-fidelity Raman imaging: a rapid method using an acousto-optic tunable filter," Appl. Spectrosc. **46**, 1211–1216 (1992).
25. R. W. Havener, S.-Y. Ju, L. Brown, Z. Wang, M. Wojcik, C. S. Ruiz-Vargas, and J. Park, "High-throughput graphene imaging on arbitrary substrates with widefield Raman spectroscopy," ACS Nano **6**, 373–380 (2012).
26. B. M. Davis, A. J. Hemphill, D. C. Maltaş, M. A. Zipper, P. Wang, and D. Ben-Amotz, "Multivariate hyperspectral Raman imaging using compressive detection," Anal. Chem. **83**, 5086–5092 (2011).
27. V. Studer, J. Bobin, M. Chahida, H. S. Mousavia, E. Candes, and M. Dahane, "Compressive fluorescence microscopy for biological and hyperspectral imaging," Proc. Natl. Acad. Sci. USA **109**, E1679–E1687 (2012).
28. J. H. Shapiro, "Computational ghost imaging," Phys. Rev. A **78**, 061802 (2008).
29. Y. Bromberg, O. Katz, and Y. Silberberg, "Ghost imaging with a single detector," Phys. Rev. A **79**, 053840 (2009).
30. M. Mazilu, J. Baumgartl, S. Kosmeier, and K. Dholakia, "Optical eigenmodes; exploiting the quadratic nature of the energy flux and of scattering interactions," Opt. Express **19**, 933–945 (2011).
31. W. D. Montgomery, "Phase retrieval and the polarization identity," Opt. Lett. **2**, 120–121 (1978).
32. N. Guarrotxena, Y. Ren, and A. Mikhailovsky, "Raman response of dithiolated nanoparticle linkers," Langmuir **27**, 347–351 (2011).
33. L. Li, T. Hutter, A. S. Finnemore, F. M. Huang, J. J. Baumberg, S. R. Elliott, U. Steiner, and S. Mahajan, "Metal oxide nanoparticle mediated enhanced Raman scattering and its use in direct monitoring of interfacial chemical reactions," Nano Lett. **12**, 4242–4246 (2012).
34. P. Ferraro, S. De Nicola, A. Finizio, G. Coppola, S. Grilli, C. Magro, and G. Pierattini, "Compensation of the inherent wave front curvature in digital holographic coherent microscopy for quantitative phase-contrast imaging," Appl. Opt. **42**, 1938–1946 (2003).
35. J. Davis, D. Cottrell, J. Campos, M. Yzuel, and I. Moreno, "Encoding amplitude information onto phase-only filters," Appl. Opt. **38**, 5004–5013 (1999).
36. B. Katz, J. Rosen, R. Kelner, and G. Brooker, "Enhanced resolution and throughput of Fresnel incoherent correlation holography (FINCH) using dual diffractive lenses on a spatial light modulator (SLM)," Opt. Express **20**, 9109–9121 (2012).

optica

Extrinsic photodiodes for integrated mid-infrared silicon photonics

Richard R. Grote,[1,4,*] Brian Souhan,[1] Noam Ophir,[1] Jeffrey B. Driscoll,[1] Keren Bergman,[1] Hassaram Bahkru,[2] William M. J. Green,[3] and Richard M. Osgood, Jr.[1]

[1]Department of Electrical Engineering, Columbia University, 500 W. 120th Street, New York, New York 10027, USA

[2]College of Nanoscale Science and Engineering, State University of New York at Albany, 257 Fuller Road, Albany, New York 12203, USA

[3]IBM T. J. Watson Research Center, 1101 Kitchawan Rd., Yorktown Heights, New York 10598, USA

[4]Current affiliation: Department of Electrical and Systems Engineering, University of Pennsylvania, 200 S. 33rd Street, Philadelphia, Pennsylvania 19104, USA

*Corresponding author: rgrote@seas.upenn.edu

Received 4 August 2014; revised 12 September 2014; accepted 14 September 2014 (Doc. ID 220216); published 17 October 2014

Silicon photonics has recently been proposed for a diverse set of applications at mid-infrared wavelengths including spectroscopy, chemical and biological sensing, free-space communications, and nonlinear optics. While optical-to-electronic signal conversion is essential to these applications, on-chip photodetection remains an important and challenging task. In this Letter, we present room temperature operation of Zn^+-implanted Si waveguide photodiodes from 2.2 to 2.4 μm, with measured responsivities of up to 87 ± 29 mA/W and low dark currents of <10 μA. Photocurrent generation is achieved by transitions from dopant-induced sub-bandgap trap states located ≈0.58 eV above the valence band to the conduction band, resulting in a peak detection wavelength of ≈2.3 μm. The wavelength of operation can be increased by choosing a dopant with an appropriate trap level, opening the possibility for on-chip detection throughout the mid-infrared.

OCIS codes: (040.6040) Silicon; (040.5160) Photodetectors; (040.3060) Infrared; (130.3060) Infrared.

http://dx.doi.org/10.1364/OPTICA.1.000264

A diverse set of applications have been proposed for mid-infrared silicon photonics [1,2], the implementation of which require on-chip photodetectors. Dopant-based extrinsic photoconductors, which utilize absorption transitions from trap states within the bandgap of a host material such as Si and Ge, have long been used in planar geometries for mid-infrared detection [3]. Leveraging the dopant-induced sub-bandgap trap states used in bulk photoconductors for waveguide-integrated detectors offers simple processing, integration, and operation throughout the mid-infrared by appropriate choice of dopant. In particular, Si doped with Zn forms two trap levels ≈0.3 eV and ≈0.58 eV above the valence band [4,5], and has been utilized extensively for cryogenically cooled bulk extrinsic photoconductors [3,6]. Here, we demonstrate room temperature operation of Zn^+ implanted Si waveguide (SiWG) photodiodes (PDs) in the 2.2–2.4 μm wavelength range.

While a number of SiWG-integrated optoelectronic devices have been explored in this wavelength range, efficient photodetection is not easily achieved. Thus, spectral translation of mid-infrared signals to the telecom regime via four-wave mixing in SiWGs has been proposed for on-chip detection [7], which makes use of integrated PDs in the telecommunications wavelength range. However, this method requires a high-powered pump laser and long, on-chip waveguide lengths to achieve efficient wavelength conversion. Alternative solutions for on-chip mid-infrared detection have utilized heterogeneous integration of both narrow-bandgap semiconductors [8–11] and graphene [12] with SiWGs. Though viable PDs have been demonstrated, heterogeneous integration schemes present an inherent difficulty by imposing constraints on material quality and fabrication process compatibility.

Extrinsic detection presents a simple solution for high-performance on-chip mid-infrared PDs and alleviates the need for heterogeneous integration. These PDs can potentially be integrated into a standard CMOS process flow by adding

an ion implantation and annealing step after activation of the source and drain implants, and prior to the deposition of back-end dielectrics and interconnect metalization. Alternatively, this additional fabrication step can be performed as a post-process, as is done here. Indeed, CMOS-compatible SiWG PDs that utilize Si lattice defects have been demonstrated [13–16], though these detectors are limited in their processing thermal budget and spectral range of detection. However, the Si dopants used in bulk photoconductors cover a range of wavelengths from 1.5 to greater than 25 μm [Fig. 1(a)], while doped Ge bulk photoconductors operate out to wavelengths greater than 100 μm [3]. By leveraging the materials commonly found in Si photonics processes, dopant-induced transitions can be exploited for integrated PDs operating throughout the mid-infrared.

For the 2.2–2.4 μm wavelength range, Zn and Au dopants have been shown to produce a suitable trap-state level in Si [4], and planar photoconductive detectors based upon these dopants have been demonstrated [3,6]. While photoconductive detectors require liquid nitrogen cooling, it has very recently been shown that Si hyperdoped with Au can generate photocurrent up to a wavelength of 2.2 μm at room temperature with a Schottky contact configuration [17]. Since cooling is not required to eliminate dark current in diode-based detectors, room temperature operation is achieved with the PDs explored here as well. Although Au and Zn are generally not CMOS compatible, as they can diffuse into Si and adversely affect carrier mobility, the other dopants in Fig. 1(a) do not pose such a restriction. For the wavelength range explored here, Si:Se could be substituted for CMOS compatibility, and has been demonstrated for a SiWG PD operating at 1.55 μm [18].

Our Si:Zn PDs are based on a *p-i-n* diode fabricated in a 250-μm-long Si rib/ridge waveguide with 520 × 250 nm channel section and a 50-nm-doped Si ridge used to form ohmic contacts to Al, as shown in Figs. 1(b) and 1(c). The intrinsic region of the *p-i-n* diode corresponds to the channel section of the SiWG, and is implanted with 260 keV Zn^+ to form the *p*-Si:Zn-*n* PD. Two Zn^+ implantation doses are investigated, 10^{12} cm^{-2} and 10^{13} cm^{-2}, corresponding to estimated average Zn concentrations inside the channel section of the waveguide of $N_{Zn} = 4.5 \times 10^{16}$ cm^{-3} and $N_{Zn} = 4.5 \times 10^{17}$ cm^{-3}, respectively. Subsequent to implantation, the PDs are annealed in air at atmospheric pressure for a series of increasing temperatures, reaching a maximum of 350°C, and the responsivity was found to increase with each anneal.

The detection mechanism of our *p*-Si:Zn-*n* PDs is believed to be due to substitutional Zn atoms in the Si lattice, which act as a double acceptors and result in the two defect levels [Fig. 2(a)] with energy levels of $E_{d1} \approx E_v + 0.3$ eV and $E_{d2} \approx E_v + 0.58$ eV [4,5]. While the position of the Fermi level in the Si:Zn region is not known, the excess carrier concentration is below that of the *p* and *n* regions, ensuring that the Si:Zn region will be fully depleted with the application of a reverse bias voltage. Photon-induced transitions occurs between E_{d2} and the conduction band, which corresponds to a transition energy of $E_g - E_{d2} = 1.12$ eV – 0.58 eV = 0.54 eV, with a peak absorption wavelength of ≈2.3 μm. Photocurrent generation due to this transition is shown to be a single-photon process by the linearity measurements in Fig. 2(b). The presence of E_{d1} does not contribute to photocurrent generation in the wavelength range of interest; however, its presence should impact the thermally assisted repopulation rate of E_{d2} and thus the internal quantum efficiency, η_i, of the PD.

The responsivity, defined as $\Re = I_{ph}/P_{in}$, where I_{ph} is the photocurrent and P_{in} is the on-chip optical power entering the PD, is measured as a function of reverse bias voltage with 2.2 μm wavelength excitation [Fig. 3(a)]. The dependence of responsivity on bias voltage may be the result of avalanche

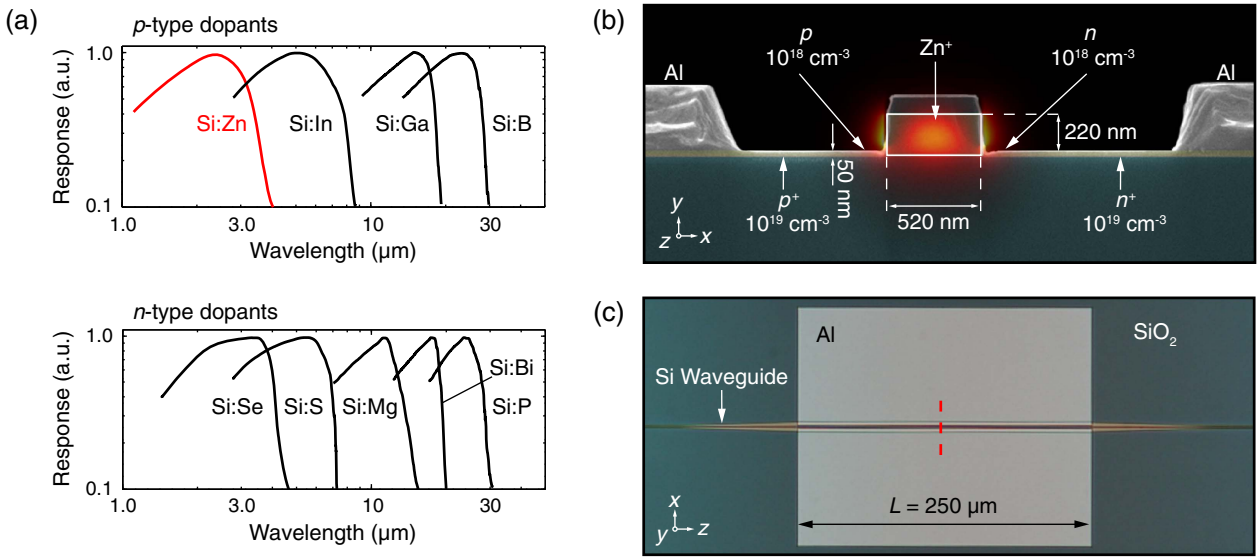

Fig. 1. (a) Normalized response of bulk silicon photoconductors for different dopants, re-plotted from [3]. Dopants are designated as either *p*-type or *n*-type depending upon whether the resultant trap state is closer to the valence band or conduction band, respectively. (b) False color scanning electron microscope (SEM) cross-section of the *p*-Si:Zn-*n* PD with finite element method calculated quasi-TE mode intensity at a wavelength of 2.3 μm superimposed. The waveguide has a 90 nm thick SiO_2 hardmask and 3 μm thick buried-oxide-layer substrate. (c) Top-view optical microscope image of the PD. The red dashed line indicates the position of the SEM cross-section shown in (b).

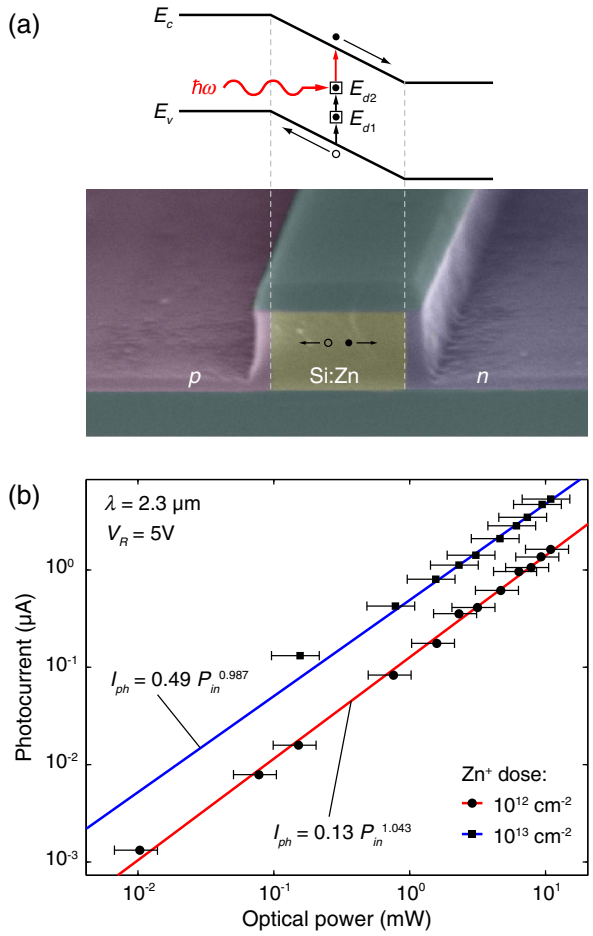

Fig. 2. (a) Band diagram of the *p*-Si:Zn-*n* PD with defect levels $E_{d1} \approx E_v + 0.3$ eV and $E_{d2} \approx E_v + 0.58$ eV in the Si:Zn region [4,5]. The doping profile is illustrated by the false-color SEM shown below. (b) Photocurrent I_{ph} versus input optical power P_{in} along with linear fits. The linear correspondence indicates a single-photon excitation process, and the slope is equal to the responsivity in mA/W at a wavelength of 2.3 μm with a reverse bias of 5 V. The higher implantation dose is shown for a 3 mm length PD.

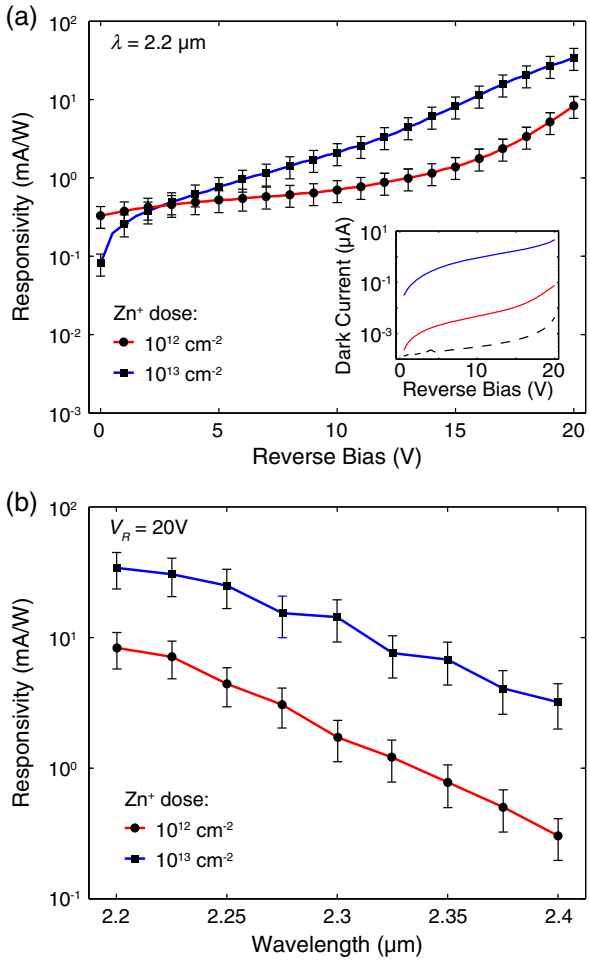

Fig. 3. (a) Responsivity as a function of reverse bias voltage. Inset, dark current as a function of reverse bias voltage for an unimplanted diode (black dashed line) and PDs with Zn^+ doses of 10^{12} cm^{-2} (red solid line) and 10^{13} cm^{-2} (blue solid line). (b) Responsivity as a function of wavelength. The decrease in responsivity with increasing wavelength is due to parasitic absorption in the contacts.

multiplication, which has previously been observed in similar SiWG *p-i-n* contact configurations [14], though trap-state population and excess carrier depletion may also play roles at low voltages. The dark current at 5 V reverse bias is measured to be 2.1 nA for the lower-dose PD, and increases to 43 nA for the higher-dose PD [Fig. 3(a), inset]. Though the dark current increases with bias voltage, it remains below 10 μA for all devices at the maximum reverse bias voltage of 20 V under which measurements were taken. From these measurements, the zero-bias noise equivalent power at 2.2 μm wavelength is determined to be 1.12×10^{-11} W/$\sqrt{\mathrm{Hz}}$ for the PD with a dose of 10^{12} cm^{-2} and 3.65×10^{10} W/$\sqrt{\mathrm{Hz}}$ for the PD with a dose of 10^{13} cm^{-2}.

The responsivity is largest at shorter wavelengths [Fig. 3(b)], reaching a maximum of 8.3 ± 2.6 mA/W and 34.1 ± 10.6 mA/W for doses of 10^{12} cm^{-2} and 10^{13} cm^{-2}, respectively, at a wavelength of 2.2 μm and a reverse bias of 20 V. For 3 mm length PDs, maximum responsivities of 87 ± 29 mA/W are measured under similar conditions (see Supplement 1). The decrease in responsivity with increasing wavelength is due to parasitic absorption from the contacts (free-carrier absorption in *p*, *n*-doped regions as well as the Al regions), which increases from >30% at 2.2 μm to >89% at 2.4 μm for a dose of 10^{12} cm^{-2}, and from >10% at 2.2 μm to >85% at 2.4 μm for a dose of 10^{13} cm^{-2}. The parasitic absorption has been determined by transmission measurements through an unimplanted diode with the same geometry, *p*, *n* doping, and contact metalization.

The modal absorption coefficient due to Zn^+ implantation (Fig. 4) is determined by transmission measurements with parasitic contact absorption being taken into account, and is found to peak at wavelengths of 2.325 μm (0.533 eV) and 2.250 μm (0.551 eV) for Zn^+ doses of 10^{12} and 10^{13} cm^{-2}, respectively. These peak absorption wavelengths correspond to the transition from E_{d2} to the conduction band shown in Fig. 2(a), and agree well with previously reported values of ≈0.54 eV [4,5].

Even with parasitic absorption taken into account, these measurements indicate that η_i is below 5%, which is

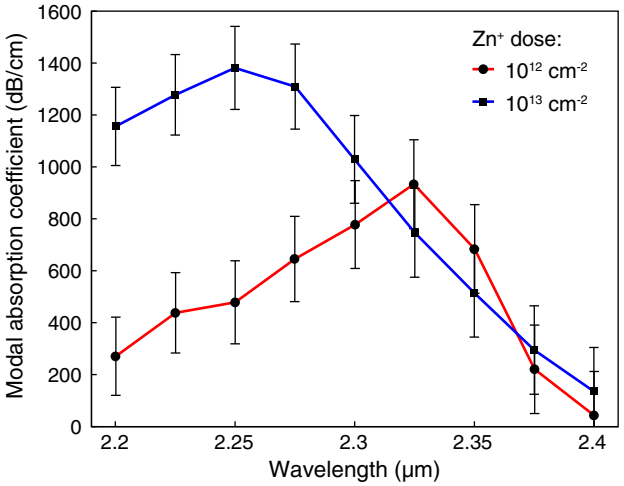

Fig. 4. Modal absorption coefficients due to Zn^+ implantation.

significantly lower than the reported values of $\eta_i = 20\%$ at a wavelength of 2.4 μm for Si:Zn bulk photoconductive detectors fabricated by diffusion doping [6]. Though diffusion doping of Zn in Si results in electrical activation by forming substitutional defects on Si lattice sites [6], activation of the Zn^+-implanted Si used here is not well characterized. For our PDs, the post-implantation annealing temperature was limited to 350°C to avoid reflow of the Al contacts, which is not high enough to fully activate Zn dopants and remove lattice damage caused by implantation [19]. Thus, there are two factors limiting η_i of the *p*-Si:Zn-*n* PDs: (1) Si lattice defects that remain after annealing, and (2) the fraction of implanted Zn atoms that have not been activated. The interstitial Zn atoms and Si defects are believed to contribute to optical scattering and increased carrier recombination. Though certain Si lattice defects and surface states can generate photocurrent from sub-bandgap photons, this is not believed to be the dominant mechanism in our devices. Indeed, measurements of Si^+-implanted SiWG PDs with identical geometry and similar dosages to the PDs explored here exhibit significantly different characteristics in the 2.2–2.4 μm wavelength range, and do not display a peak in their absorption coefficient at the transition energy associated with Si:Zn [16].

Our results illustrate the potential for silicon photonic extrinsic photodiodes operating at mid-infrared wavelengths. The use of dopants for trap-state engineering in diode configurations allows for the design of on-chip PDs with device parameters such as dark current, internal quantum efficiency, and peak detection wavelength being controlled through adjustments to the trap-state levels and populations. Beyond photodetection, trap-state transitions can emit photons under the proper conditions [20], creating the prospect for on-chip waveguide-integrated sources and detectors operating throughout the mid-infrared wavelength band.

FUNDING INFORMATION

National Science Foundation (NSF) (DGE-1069420); U.S. Department of Energy (DOE) (DE-AC02-98CH10886).

ACKNOWLEDGMENTS

The authors thank M. W. Geis and S. J. Spector at MIT Lincoln Laboratory for samples and fabrication advice, and S. Mann for a careful reading of the manuscript. The authors acknowledge support from the Columbia Optics and Quantum Electronics IGERT under NSF grant DGE-1069420. This research was carried out in part at the Center for Functional Nanomaterials, Brookhaven National Laboratory, which is supported by the U.S. Department of Energy (DOE), Office of Basic Energy Sciences, under Contract No. DE-AC02-98CH10886.

See Supplement 1 for supporting content.

REFERENCES

1. R. Soref, Nat. Photonics **4**, 495 (2010).
2. X. Liu, R. M. Osgood, Jr., Y. A. Vlasov, and W. M. J. Green, Nat. Photonics **4**, 557 (2010).
3. N. Sclar, Prog. Quantum Electron. **9**, 149 (1984).
4. A. G. Milnes, *Deep Impurities in Semiconductors* (Wiley-Interscience, 1973).
5. S. Weiss, R. Beckmann, and R. Kassing, Appl. Phys. A **50**, 151 (1990).
6. N. Sclar, Solid-State Electron. **24**, 203 (1981).
7. X. Liu, B. Kuyken, G. Roelkens, R. Baets, R. M. Osgood, Jr., and W. M. J. Green, Nat. Photonics **6**, 667 (2012).
8. N. Hattasan, A. Gassenq, L. Cerutti, J.-B. Rodriguez, E. Tournié, and G. Roelkens, IEEE Photon. Technol. Lett. **23**, 1760 (2011).
9. A. Gassenq, N. Hattasan, L. Cerutti, J. B. Rodriguez, E. Tournié, and G. Roelkens, Opt. Express **20**, 11665 (2012).
10. G. Roelkens, U. Dave, A. Gassenq, N. Hattasan, C. Hu, B. Kuyken, F. Leo, A. Malik, M. Muneeb, E. Ryckeboer, S. Uvin, Z. Hens, R. Baets, Y. Shimura, F. Gencarelli, B. Vincent, R. Loo, J. Van Campenhout, L. Cerutti, J.-B. Rodriguez, E. Tournié, X. Chen, M. Nedeljkovic, G. Mashanovich, L. Shen, N. Healy, A. C. Peacock, X. Liu, R. M. Osgood, Jr., and W. M. J. Green, Opt. Mater. Express **3**, 1523 (2013).
11. P. T. Lin, V. Singh, J. Wang, H. Lin, J. Hu, K. Richardson, J. D. Musgraves, I. Luzinov, J. Hensley, L. C. Kimerling, and A. Agarwal, Opt. Mater. Express **3**, 1474 (2013).
12. X. Wang, Z. Cheng, K. Xu, H. K. Tsang, and J.-B. Xu, Nat. Photonics **7**, 888 (2013).
13. M. W. Geis, S. J. Spector, M. E. Grein, J. U. Yoon, and T. M. Lyszczarz, in *Handbook of Silicon Photonics*, L. Vivien and L. Pavesi, eds. (CRC Press, 2013), pp. 518–535.
14. J. J. Ackert, A. S. Karar, D. J. Paez, P. E. Jessop, J. C. Cartledge, and A. P. Knights, Opt. Express **21**, 19530 (2013).
15. D. J. Thomson, L. Shen, J. J. Ackert, E. Huante-Ceron, A. P. Knights, M. Nedeljkovic, A. C. Peacock, and G. Z. Mashanovich, Opt. Express **22**, 10825 (2014).
16. B. Souhan, R. R. Grote, C. P. Chen, H. S. Huang, J. B. Driscoll, M. Lu, A. Stein, H. Bakhru, K. Bergman, W. M. J. Green, and R. M. Osgood, Jr., "Si^+-implanted Si-wire waveguide photodetectors for the mid-infrared," Opt. Express, article id: 222026 (to be published).
17. J. P. Mailoa, A. J. Akey, C. B. Simmons, D. Hutchinson, J. Mathews, J. T. Sullivan, D. Recht, M. T. Winkler, J. S. Williams, J. M. Warrender, P. D. Persans, M. J. Aziz, and T. Buonassisi, Nat. Commun. **5**, 3011 (2014).
18. X. Mao, P. Han, L. Gao, Y. Mi, S. Hu, Y. Fan, C. Zhao, and Q. Wang, IEEE Photon. Technol. Lett. **23**, 1517 (2011).
19. J. Gyulai, O. Meyer, R. Pashley, and J. Mayer, Radiat. Eff. **7**, 17 (1971).
20. J. M. Herman III and C. T. Sah, J. Appl. Phys. **44**, 1259 (1973).

optica

Coherent random walks in free space

Toni Eichelkraut,[1] Christian Vetter,[1] Armando Perez-Leija,[1] Hector Moya-Cessa,[2] Demetrios N. Christodoulides,[3] and Alexander Szameit[1,*]

[1]Institute of Applied Physics, Friedrich-Schiller-Universität Jena, Max-Wien-Platz 1, 07743 Jena, Germany

[2]Instituto Nacional de Astrofsica, Optica y Electronica, Coordinacion de Optica, Luis Enrique Erro No. 1, 72840 Tonantzintla, Puebla, Mexico

[3]CREOL, The College of Optics and Photonics, University of Central Florida, Orlando, Florida 32816, USA

*Corresponding author: alexander.szameit@uni-jena.de

Received 16 July 2014; revised 1 September 2014; accepted 15 September 2014 (Doc. ID 216859); published 17 October 2014

Two-dimensional continuous time quantum random walks (CTQRW) are physical processes where quantum particles simultaneously evolve in different permissible directions within discrete graphs. In order to force the quantum walkers (QWs) to evolve in such a fashion, one generally requires periodic potentials. Here, we demonstrate that two-dimensional CTQRW can be generated in free space by properly tailoring the initial wave functions. We analytically show that within a certain spatial region the arising probability distribution quantitatively resembles the probability pattern exhibited by a QW traversing a periodic lattice potential. These theoretical predictions were experimentally verified using classical laser light, appropriately shaped by a spatial light modulator. Expanding the presented results to the case of multiple walkers may open new possibilities in quantum information technology using bulk optics.

OCIS codes: (270.0270) Quantum optics; (270.1670) Coherent optical effects.

http://dx.doi.org/10.1364/OPTICA.1.000268

Classical random walks are ubiquitous in various research fields such as physics, biology, and finance theory [1–4]. In most of these disciplines, classical random walks are among the most powerful mathematical tools used for developing advanced algorithms [3]. Within the framework of quantum mechanics, where the inherent superposition principle and entanglement enable parallelization, random walks of quantum particles may surpass the potential offered by their classical counterpart [5–7]. In that vein, for instance, computational algorithms based on quantum random walks have been presented to overcome several fundamental problems more efficiently [8].

In essence, one-dimensional (1D) continuous time quantum random walks (CTQRWs) can be implemented via tunneling of quantum particles between adjacent sites in discrete systems [9]. In other words, the wave dynamics occurring in coupled systems, such as crystalline structures and periodic photonic lattices, is essentially equivalent to quantum walks of single particles [2,6,10]. In fact, CTQRWs have been demonstrated using different physical platforms ranging from nuclear magnetic resonance [11] and optical resonators [12] to evanescently coupled waveguide lattices [13]. Additionally, an approach to extend the concept of CTQRWs to some other physical setting where the so-called quantum walkers (QWs) can freely evolve might be of interest. That is, provided the fact that such free evolution—in the absence of any external potential—would exhibit a dynamical behavior comparable to a CTQRW.

In this Letter, we demonstrate that CTQRWs can be realized in free space through the spatial evolution of a single QW whose initial wave function ψ is appropriately shaped so as to exhibit the highest probability amplitude around the origin. We experimentally demonstrate our theoretical findings by using paraxial optical beams. Evidently, the usage of such classical beams to explore the propagation dynamics of point-like quantum particles is possible since both phenomena are mathematically described by the same equation. This, in turn, makes our approach suitable for the realization of random walks using different quantum particles, including electrons and single photons [14]. For instance, the feasibility of tailoring electron wave packets is by now possible employing nanoscale holograms [15].

Since the terms quantum random walk and coherent random walk can be used synonymously [6], and because our experiments were conducted using classical light, throughout our Letter we refer to coherent random walks (CRWs). To study the spatial evolution of a general wave function envelope $\psi(x, y, z)$, we consider the paraxial wave equation

$$\left(i\frac{\partial}{\partial z}+\frac{1}{2k}\nabla_{\perp}^{2}\right)\psi=0, \tag{1}$$

which can be derived from first principles for both quantum particles and light beams. Here, we use $\nabla_{\perp}^{2}=\partial^{2}/\partial x^{2}+\partial^{2}/\partial y^{2}$; z is the propagation distance and $k=2\pi/\lambda$ is the wave number. As previously mentioned, the evolution of quantum particles and classical light follows the same mathematical description. Thus, Eq. (1) is equivalent to the Schrödinger equation, which describes the temporal evolution of free particles. In fact, the temporal evolution can also be mapped to a spatial propagation; for instance, this formalism has been successfully used in Ref. [15] to study the generation of electron Airy beams.

We start our analysis with the initially *localized* wave function envelope

$$\psi(x,y,0)=N\mathrm{e}^{-(x^{2}+y^{2})/2\sigma^{2}}J_{n}(\alpha x)J_{n}(\alpha y), \tag{2}$$

which is symmetric around the origin ($x=y=0$), and $J_n(\alpha x)$ represents a Bessel function of the first kind of order n. Note that the Gaussian apodization guarantees the requirement of finite energy, while N provides the necessary normalization. Importantly, the Bessel profiles introduced here are not azimuthally symmetric as the usual diffraction-free Bessel beams. Following the approach reported in Refs. [16,17], one can show that the evolution dynamics of such initially Gaussian-apodized Bessel envelopes is analytically described by

$$\psi(x,y,z)=N\prod_{s\in\{x,y\}}\left(1-\frac{iz}{k\sigma^{2}}\right)^{-1/2}\exp\left[\frac{-2ks^{2}+i\alpha^{2}\sigma^{2}z}{4(k\sigma^{2}-iz)}\right]\times\sum_{l=-\infty}^{\infty}(-i)^{l}J_{n+2l}(A(s,z))J_{l}(B(z)). \tag{3}$$

Here, we have $A(s,z)=\alpha k\sigma^{2}s/(k\sigma^{2}-iz)$ and $B(z)=\alpha^{2}(z+iz^{2}/(k\sigma^{2}-iz))/(4k)$, with s taking the place of x and y, respectively.

Of particular interest for our work is the case where the initial probability amplitude is given by

$$\psi(x,0)=N\exp[-x^{2}/2\sigma^{2}]J_{0}(\alpha x). \tag{4}$$

In this 1D scenario, the arising probability distribution within a parabolic region in the (x,z) plane (depicted in Fig. 1) resembles not only qualitatively but quantitatively [18] the probability pattern exhibited by a QW traversing a uniform periodic potential [9,13]. This is true, despite the fact that the evolution takes place in free space, i.e., a lattice potential is not present at all.

In order to analytically derive the evolution dynamics of the initial wave function as given in Eq. (4), we consider the case of a very broad Gaussian envelope ($k\sigma^{2}\gg z;\sigma\gg x$) apodizing a Bessel profile of order zero, as given in Eq. (4), such that the evolution dynamics can be approximated by

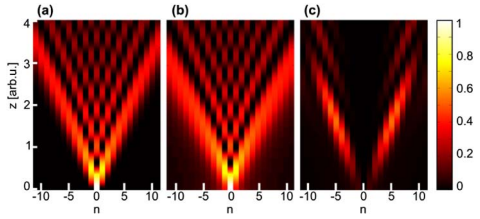

Fig. 1. Theoretical probability evolution. (a) Probability distribution $|\psi_{\mathrm{lattice}}(n,z)|^{2}$ expected for a quantum walker traversing a uniform lattice, where the lattice sites are labeled by n. (b) Calculated free space probability density, $|\psi_{\mathrm{fs}}(x_n,z)|^{2}$, plotted for the different transverse positions $x_n=n\pi/\alpha$. (c) The difference $|\psi_{\mathrm{fs}}(x_n,z)-\psi_{\mathrm{lattice}}(n,z)|^{2}$.

$$\psi(x,z)=\sum_{l=-\infty}^{\infty}(-i)^{l}J_{2l}(\alpha x)J_{l}\left(\frac{\alpha^{2}z}{4k}\right). \tag{5}$$

Note that Eq. (5) is only valid within a finite transverse window and for a certain propagation distance, both determined by the apodization envelope ($k\sigma^{2}\gg z;\sigma\gg x$). From Eq. (5), one can readily see that at $x=0$, the evolution is simply given by $\psi(x=0,z)=J_{0}(\alpha^{2}z/4k)$, which is identical to the probability amplitude of a single QW in the excited site of a uniform lattice [10,13]. Furthermore, for every $x_m=m\pi/\alpha$, m being an integer, one can show [18] that the evolution equation Eq. (5) becomes

$$\psi(x_m,z)=(-i)^{m}J_{m}(\alpha^{2}z/4k), \tag{6}$$

which is mathematically identical to the probability amplitude described by a QW along the mth site within a periodic lattice [10,13]. To be precise, Eq. (6) is a good approximation within the aforementioned parabolic region bounded by $z>z_m\approx 16k(m^{2}+2m+1)/\alpha^{2}$ [18].

In Fig. 1, we illustrate these effects by comparing the probability pattern of a QW traversing a periodic potential, given by Eq. (6), and the probability distribution corresponding to a single QW propagating in free space described by Eq. (5). In order to have a meaningful comparison between $|\psi_{\mathrm{lattice}}(n,z)|^{2}$ and $|\psi_{\mathrm{fs}}(x_n,z)|^{2}$, it is important to be aware of the fact that $|\psi_{\mathrm{lattice}}(n,z)|^{2}$ is a probability distribution, whereas $|\psi_{\mathrm{fs}}(x,z)|^{2}$ is a probability density. Consequently, in Fig. 1, we actually plot $\int_{x_n-\Delta x/2}^{x_n+\Delta x/2}|\psi_{\mathrm{fs}}(x,z)|^{2}\mathrm{d}x\approx|\psi_{\mathrm{fs}}(x_n,z)|^{2}\Delta x$, where we integrate over a very small transverse distance. For brevity, we omitted the Δx in the caption of Fig. 1. Note that in an experiment, the transverse width Δx is associated with the detector width. Figure 1(c) depicts the difference between both space-evolved wave functions, $|\psi_{\mathrm{fs}}-\psi_{\mathrm{lattice}}|^{2}$. It is well perceived that within the specified region the deviation between both propagation patterns, which includes their respective phases, is almost negligible.

In order to experimentally verify our theoretical findings, we have shaped the amplitude and phase of a collimated light beam using a spatial light modulator (SLM). The corresponding setup is shown in Fig. 2. In order to generate the desired input field in the $z=0$ plane, we implement its Fourier transform $\tilde{\psi}(\xi,\eta)=\mathrm{FT}[\psi]$ on the SLM. In general, the field at the SLM plane can be written as $\tilde{\psi}(\xi,\eta)=M(\xi,\eta)\exp[i\phi(\xi,\eta)]$,

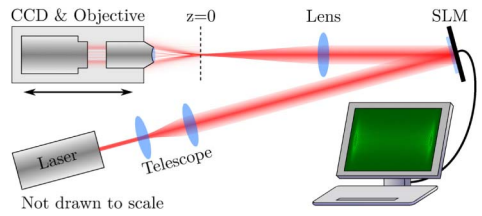

Fig. 2. Experimental setup consisting of a Helium Neon laser ($\lambda = 633$ nm), telescope for beam expansion, spatial light modulator (Holoeye Pluto VIS) for amplitude and phase modulation, spherical lens ($f = 300$ mm) for Fourier transformation, microscope objective (10× Olympus Plan Achromat) for imaging, and movable CCD camera (Basler Ace 1600-20gm).

where $M(\xi,\eta)$ and $\phi(\xi,\eta)$ represent the amplitude and phase distribution, respectively. Following [19], any complex function, such as $\tilde{\psi}(\xi,\eta)$, can be obtained by applying a phase-only modulation given by

$$\chi(\xi,\eta) = \exp[iM(\xi,\eta)[\phi(\xi,\eta) + \phi_G(\xi,\eta)]]. \quad (7)$$

Importantly, the imposed periodic phase $\phi_G(\xi,\eta) = 2\pi(\xi,\eta)/d$ acts as a grating that separates the different diffraction orders. When Fourier transforming the beam using a spherical lens and postselecting the first diffraction order, the desired field distribution is obtained at $z = 0$. In our case, we set $d = 64$ μm and the focal length of the lens to $f = 300$ mm. The three-dimensional intensity distribution of the light was recorded using a 10× microscope objective and a CCD camera mounted on a movable linear stage. The propagation distance under study was chosen to be $\Delta z = 2.5$ cm.

For the creation of a 1D free space CRW, we generate the initial field distribution given by Eq. (4) with $\alpha = 125$ mm^{-1} and $\sigma = 0.13$ mm. The experimental propagation pattern over the (x, z) plane is shown in Fig. 3(b) along with the actual camera images of the intensity distribution at $z = 0$ cm and $z = 2.5$ cm on bottom and top, respectively. Note the good agreement between the experimental data, Fig. 3(b), and our theoretical predictions, Fig. 3(a). This is possible since for the chosen experimental parameters, $\sigma = 0.13$ mm, the propagation distance under consideration falls within the established limits, that is, $z \ll k\sigma^2$ and $k\sigma^2 = 18$ cm. To quantitatively assess the agreement between the observed and the theoretically expected results, in Fig. 3 we superimpose both intensity patterns. Figure 3(c) depicts the intensity distribution in the initial plane for $y = 0$. The intensity contrast between the central maximum and the first side minimum, for instance, is $I_{max}/I_{min} \approx 143$, whereas no emphasis has been laid on maximizing this ratio. Moreover, to fully quantify the agreement between theory and experiment, we calculated the coefficient of determination which, for the values depicted in Fig. 3(c), is $R^2 = 0.9915$. Figure 3(d) shows the longitudinal intensity distribution along z at $x_0 = 0$ and $x_1 = \pi/\alpha \approx 25$ μm, as well as the theoretically predicted Bessel patterns. From this graph one can clearly see that the most pronounced difference between the experimentally observed evolution and the Bessel pattern is found at x_1 for $z \approx 0$ whereas, for larger propagation distances, the deviation decreases.

We would like to emphasize that single-photon CRWs can be realized in our setup by replacing the continuous wave laser with a single-photon source and scanning the transverse position x_m using photon-counting detectors.

Another interesting scenario occurs when a linear superposition of two transverse Bessel profiles of order zero, $\psi(x, 0) = \exp[-x^2/2\sigma^2](J_0(\alpha x) + J_0(\alpha x - n\pi))$, is considered as initial wave envelope. In this case, the arising probability distribution corresponds to a situation where a single QW is initially prepared in a coherent superposition of states. In this setting, the initial wave function features two main lobes separated by a transverse distance of $\Delta x = n\pi/\alpha$. In Fig. 4, this process is depicted for the specific case of $n = 2$. In addition, in [18], it is shown that within a certain region the dynamics obeyed by the QW propagating in free space is indeed identical to the one exhibited by a QW being simultaneously launched into two sites of a periodic lattice. The experimental results presented in Fig. 4(b) were obtained analogously to the single excitation case.

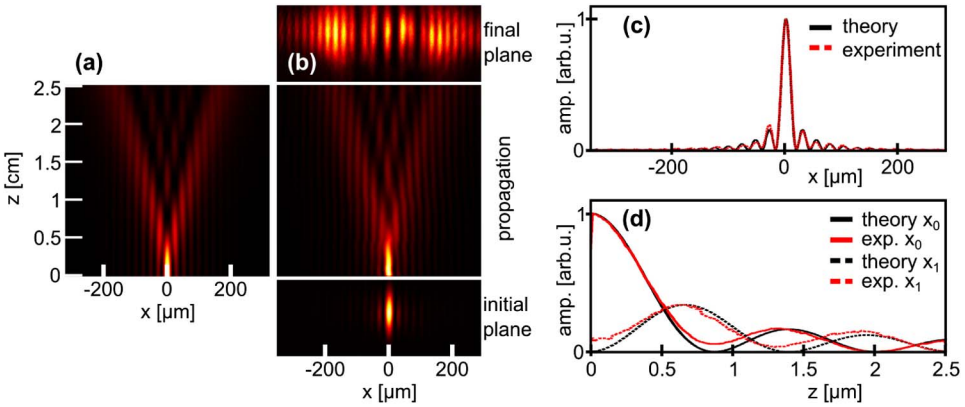

Fig. 3. Theoretical and experimental comparison for a 1D CRW in free space. (a) Theoretical free-space probability evolution corresponding to the initial wave profile given by Eq. (4) using the parameters $\alpha = 125$ mm^{-1} and $\sigma = 0.13$ mm. (b) Bottom, experimental intensity envelope as produced in our setup at $z = 0$ cm. Center, recorded intensity evolution of the light beam at the plane $y = 0$. Top, final intensity pattern after a propagation distance of $z = 2.5$ cm. (c) Comparison between theoretical and experimental intensity distribution in the initial plane at $y = 0$. (d) Comparison between theoretical and experimental intensity evolution at two different transverse positions. $x_0 = 0$ and $x_1 = \pi/\alpha \approx 25$ μm.

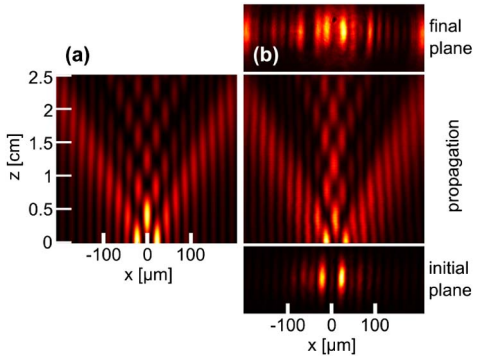

Fig. 4. Theoretical and experimental comparison for a 1D CRW in a coherent superposition of states. (a) Theoretical free-space probability evolution of the initial wave function $\psi(x,0) = \exp[-x^2/2\sigma^2](J_0(\alpha x) + J_0(\alpha x - 2\pi))$ using the parameters $\alpha = 145\ \mathrm{mm}^{-1}$ and $\sigma = 1$ mm. (b) Bottom, experimental initial intensity profile. Center, top view of the intensity evolution. Top, intensity pattern recorded after a propagation distance of $z = 2.5$ cm.

Finally, in order to demonstrate the potentiality of this approach for the realization of 2D free space CRWs, we consider the experimental propagation of the initial field profile given by

$$\psi(x,y,0) = \exp[-(x^2+y^2)/2\sigma^2]J_0(\alpha x)J_0(\alpha y). \quad (8)$$

To do so, we tune the SLM such that $\alpha = 310\ \mathrm{mm}^{-1}$ and $\sigma = 0.13$ mm. The experimental propagation dynamics are presented in Fig. 5, where now the intensity pattern resembles the probability distribution of a QW evolving through a 2D square lattice. Figures 5(a)–5(c) show the experimental intensity patterns registered at three planes perpendicular to the propagation direction. These observations fully confirm our theoretical predictions depicted in Figs. 5(d)–5(f). The

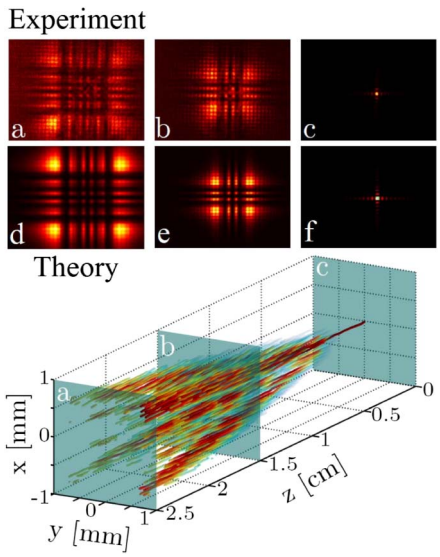

Fig. 5. Experimental results for a 2D CRW. Top row, experimental images taken with a CCD camera. Central row, theoretical intensity evolution. Bottom row, stitched image from all camera images, showing the 2D CRW of a "single excitation."

3D picture at the bottom of Fig. 5 shows the experimental evolution of the registered light spots where the intensity is a local maximum. We emphasize again that the evolution takes place in free space and no lattice potential is present.

In conclusion, we have demonstrated theoretically and experimentally that CRWs can be generated in the absence of any periodic environment, e.g., in the bulk of a uniform material or even in free space. We performed experiments using classical light beams that resemble a probability distribution of QWs as if a lattice potential were present. With current technology, we foresee that experiments will soon be feasible using real quantum particles, in particular photons and electrons (see, e.g., [15]). As CTQRWs carry the potential of substantially accelerating computation schemes [2,8], our results may open new possibilities in quantum information technology using bulk optics. However, this potential can only be fully tapped by expanding the presented results to the case of multiple walkers.

FUNDING INFORMATION

Deutsche Forschungsgemeinschaft (DFG) (NO462/6-1); German Ministry of Education (ZIK 03Z1HN31); German-Israeli Foundation for Scientific Research and Development (GIF) (1157-127.14/2011); Thuringian Ministry for Education, Science and Culture (11027-514).

See Supplement 1 for supporting content.

REFERENCES AND NOTES

1. Y. Aharonov, L. Davidovich, and N. Zagury, Phys. Rev. A **48**, 1687 (1993).
2. J. Kempe, Contemp. Phys. **44**, 307 (2003).
3. V. M. Kendon, Phil. Trans. R. Soc. A **364**, 3407 (2006).
4. P. L. Knight, E. Roldán, and J. E. Sipe, Phys. Rev. A **68**, 020301 (2003).
5. A. M. Childs, Phys. Rev. Lett. **102**, 180501 (2009).
6. O. Mulken and A. Blumen, Phys. Rep. **502**, 37 (2011).
7. T. Kitagawa, M. A. Broome, A. Fedrizzi, M. S. Rudner, E. Berg, I. Kassal, A. Aspuru-Guzik, E. Demler, and A. G. White, Nat. Commun. **3**, 882 (2012).
8. P. W. Shor, SIAM J. Comput. **26**, 1484 (1997).
9. H. B. Perets, Y. Lahini, F. Pozzi, M. Sorel, R. Morandotti, and Y. Silberberg, Phys. Rev. Lett. **100**, 170506 (2008).
10. Y. Bromberg, Y. Lahini, R. Morandotti, and Y. Silberberg, Phys. Rev. Lett. **102**, 253904 (2009).
11. J. A. Jones, Prog. Nucl. Magn. Reson. Spectrosc. **59**, 91 (2011).
12. D. Bouwmeester, I. Marzoli, G. P. Karman, W. Schleich, and J. P. Woerdman, Phys. Rev. A **61**, 013410 (1999).
13. A. Peruzzo, M. Lobino, J. C. F. Matthews, N. Matsuda, A. Politi, K. Poulios, X.-Q. Zhou, Y. Lahini, N. Ismail, K. Woerhoff, Y. Bromberg, Y. Silberberg, M. G. Thompson, and J. L. O'Brien, Science **329**, 1500 (2010).
14. J. E. Sipe, Phys. Rev. A **52**, 1875 (1995).
15. N. Voloch-Bloch, Y. Lereah, Y. Lilach, A. Gover, and A. Arie, Nature **494**, 331 (2013).
16. A. Perez-Leija, F. Soto-Eguibar, S. Chavez-Cerda, A. Szameit, H. Moya-Cessa, and D. N. Christodoulides, Opt. Express **21**, 17951 (2013).
17. G. Dattoli and A. Torre, J. Opt. Soc. Am. B **31**, 2214 (2014).
18. See Supplement 1 for a complete rigorous analysis.
19. J. A. Davis, D. M. Cottrell, J. Campos, M. J. Yzuel, and I. Moreno, Appl. Opt. **38**, 5004 (1999).